CENTRO DE INVESTIGACIÓN Y DE ESTUDIOS AVANZADOS
DEL INSTITUTO POLITÉCNICO NACIONAL

UNIDAD ZACATENCO
DEPARTAMENTO DE FÍSICA

"El hadrón B^+ como herramienta para investigar las modificaciones nucleares en colisiones pPb y para explorar nueva física a través del decaimiento raro $B^+ \rightarrow \mu^+\mu^-K^+$ en colisiones pp a $\sqrt{s} = 13$ TeV"

Tesis que presenta

Horacio Crotte Ledesma

para obtener el Grado de

Doctor en Ciencias

en la Especialidad de

Física

Director de tesis: Dr. Heriberto Castilla Valdez

Ciudad de México Noviembre, 2024

CENTER FOR RESEARCH AND ADVANCED STUDIES OF THE NATIONAL POLYTECHNIC INSTITUTE

UNIT ZACATENCO
PHYSICS DEPARTMENT

"The B^+ hadron used as a probe to investigate nuclear modifications in pPb collisions and to explore new physics through the rare decay $B^+ \rightarrow \mu^+\mu^-K^+$ in pp collisions at $\sqrt{s}$ = 13 TeV"

by

Horacio Crotte Ledesma

In order to obtain the

Doctor of Science

degree, speciality in

Physics

Advisor: Ph. D. Heriberto Castilla Valdez

Mexico City November, 2024

Agradecimientos

Agradezco profundamente a todas las personas que me apoyaron y contribuyeron de diversas formas en la realización de esta tesis.

En primer lugar, al Dr. Heriberto Castilla Valdez, por permitirme aprender, desarrollar y realizar análisis físicos en colisiones de partículas a altas energías. Su apoyo constante me abrió las puertas a un área de la ciencia que antes desconocía.

A los doctores Sergio Armando Tomás Velázquez, Omar Gustavo Miranda Romagnoli, Eduard De La Cruz Burelo y Antonio Ortiz Velásquez, por su apoyo y disposición al formar parte del comité sinodal.

A los doctores Iván Heredia de la Cruz, Irais Bautista Guzmán, Jhovanny Andrés Mejía Guisao, Rogelio Reyes Almanza y Gabriel Artemio Ayala Sánchez, por sus valiosas discusiones, que impulsaron el avance de los diferentes análisis físicos realizados en el grupo del Cinvestav en CMS.

Al grupo de física del mesón B del experimento CMS, por permitirme ser parte del equipo de Trigger y aprender detalles organizativos esenciales para el desarrollo de los grupos.

A mis compañeros y profesores del Departamento de Física del Cinvestav, por crear un ambiente de trabajo excepcional.

A mi querida familia, que siempre me brindó su apoyo incondicional. A mis padres, Rosaura Ledesma Rosales y Horacio Crotte Franco, a mis abuelos Alicia Franco Quintero, Martha Rosales Torres y Alfredo Ledesma Vargas, así como a todos mis tías, tíos, primas y primos. Muchas gracias por todo.

A mis amigos, quienes me han acompañado en este largo camino desde la licenciatura. Especialmente a mi esposa Marcela García Hernández, le estoy profundamente agradecido por su incondicional apoyo a lo largo de todo este proceso.

Finalmente, me gustaría expresar mi agradecimiento al Consejo Nacional de Humanidades, Ciencias y Tecnologías (CONAHCYT) por el apoyo económico que hizo posible esta investigación.

Resumen

El mesón $B^{\pm}$ está compuesto por un quark up y un quark bottom, con una masa de aproximadamente 5.279 GeV y una vida media del orden de 1.6 ps. Los decaimientos del mesón $B^{\pm}$ que producen muones son particularmente adecuados para su estudio en colisionadores hadrónicos, como el Solenoide Compacto de Muones (CMS) en el Gran Colisionador de Hadrones (LHC). Los decaimientos que resultan en un estado final compuesto por un par de muones y un $K^{\pm}$ pueden ocurrir a través de un estado intermedio. Específicamente, se puede formar un mesón $c\bar{c}$ que decae en un par de muones, lo que conduce al mismo estado final. Los canales resonantes, que proceden a través de una resonancia intermedia, se producen a tasas aproximadamente dos órdenes de magnitud más altas que los canales no resonantes. Utilizamos el canal de decaimiento $B^{\pm} \to K^{\pm} J/\Psi(\mu^{-}\mu^{+})$ para estudiar las modificaciones nucleares en colisiones protón-plomo. Estas modificaciones nucleares son útiles para investigar los efectos de colectividad que surgen de la formación de Plasma de Quarks y Gluones en colisiones de iones pesados. Por otro lado, el canal no resonante tiene gran importancia ya que es una corriente neutra que cambia de sabor. Suprimido al nivel árbol en el Modelo Estándar, estos decaimientos raros son herramientas valiosas para la búsqueda de Física Más Allá del Modelo Estándar. Hemos analizado las distribuciones angulares de este decaimiento y extraído dos parámetros que son conocidos con alta precisión teórica. Esta medición contribuye a la comprensión de las llamadas Anomalías de Sabor, que fueron reportadas por primera vez por la colaboración LHCb a finales de la década de 2010.

Abstract

The $B^{\pm}$ meson is composed of an up and a bottom quark, with a mass of approximately 5.279 GeV and a lifetime on the order of 1.6 ps. Decays of the $B^{\pm}$ meson that produces muons are particularly well-suited for study in hadronic colliders, such as the Compact Muon Solenoid at the Large Hadron Collider. Decays resulting in a final state consisting of a pair of muons and a $K^{\pm}$ can occur through an intermediate state. Specifically, a $c\bar{c}$ meson can be formed and decay into a pair of muons, leading to the same final state.

The resonant channels, which proceed through an intermediate resonance, are produced at rates approximately two orders of magnitude higher than the non-resonant channels. We used the $B^{\pm} \to K^{\pm} J/\Psi(\mu^{-}\mu^{+})$ decay channel to study nuclear modification in proton-lead collisions. These nuclear modifications are useful for probing collectivity effects arising from the formation of Quark-Gluon Plasma in heavy-ion collisions.

On the other hand, the non-resonant channel holds great importance as a flavour-changing neutral current. Suppressed at the tree level in the Standard Model, these rare decays are valuable tools for searching Physics Beyond the Standard Model. We have analyzed the angular distributions of this decay and extracted two parameters that are known with high theoretical precision. This measurement contributes to understanding the so-called Flavour Anomalies, which were first reported by the LHCb collaboration in the late 2010s.

Contents

List of Figures

List of Tables

Chapter 1

Introduction

The Standard Model (SM) of particle physics describes the matter in the universe as being composed of fermions, whose interactions are mediated by bosons. Fermions are divided into two categories: quarks and leptons. Quarks experience both the electroweak interaction and the strong force, while leptons are influenced only by the electroweak interaction.

Leptons and quarks are further organized into three generations or families. Each family consists of two types of leptons and two types of quarks. Among the leptons, one has a charge of -1 (electron-like), while the other is neutral (a neutrino). For the quarks, one has charge 2/3 (up-type) and the other -1/3 (down-type). With the exception of neutrinos, particles from higher generations have greater mass than those in lower generations.

The heaviest and most recently discovered family consists of the tau and tau neutrino on the lepton side, and the top and bottom quarks on the quark side. Due to its large mass, the top quark cannot hadronize, making the bottom quark the heaviest quark capable of forming bound states.

The first observation of b hadrons occurred at Fermilab in 1977, when bound states of bottom and anti-bottom quarks, known as Upsilon mesons, were detected decaying into a pair of muons. Upsilon mesons decay mainly into pairs of charged B^+ and neutral B^0 mesons.

The SM has been remarkably successful, with its predictions verified across a wide range of energies, from a few electron volts up to the TeV scale. One of the most precise results of the SM predictions is the decay widths of the Z and W bosons. The theoretical precision is about 0.008%, and the experimental measurements have a precision of less than 1%, with both results in complete agreement.

However, despite the success of the SM, certain phenomena, such as neutrino oscillations and the presence of dark matter, remain unexplained. This has driven the search for "new physics," which focuses on two main areas: precision measurements (the intensity frontier) and the direct observation of unpredicted particles (the energy frontier). Although no direct evidence for new physics has been found, precision measurements continue to be essential for refining and challenging the Standard Model.

A key player in precision measurements is the B^+ meson. One important example is the flavor-changing neural current decay $b \to s\ell\ell$, which has been central to studies of potential violations of lepton flavor universality. Research in this area has revealed some tensions with the SM, increasing interest in more detailed studies of this decay. While rare decays

like this are important, the charmonium decay $B^+ \to K^+ J/\psi(1S)$serves as a benchmark for normalization and validation in these studies.

Moreover, this decay is significant because it is produced in large quantities, and its decay products —muons and kaons— are easily detected in particle detectors such as the Compact Muon Solenoid. Their large masses and early production make them ideal tools for studying the early stages of heavy ion collisions and probing the quark-gluon plasma (QGP), which permeated the universe in its first few microseconds.

Chapter 2

The Standard Model

The Standard Model (SM) of particle physics is a theory that describes the fundamental particles and the forces that govern them. It accounts for the electromagnetic, weak, and strong forces explaining the interactions of elementary particles such as quarks, leptons, and gauge bosons.

One of its key achievements is predicting the existence of the Higgs boson, which was discovered in 2012 [1, 2] and explains how particles acquire mass. The model has been rigorously tested through experiments, accurately predicting various observables like cross-sections and particle masses.

The SM unifies quantum mechanics, special relativity, and field theory to form a quantum field theory, where fundamental particles are treated as excitations of their respective fields. Fermions, which follow Fermi-Dirac statistics, are matter particles, while bosons, governed by Bose-Einstein statistics, act as force carriers. Particles with semi-integer spin (1/2, 3/2, ...) are classified as fermions, and bosons have integer spin (0, 1, ...). Figure 2.1 illustrates the particles in the SM, with fermions displayed on the left and bosons on the right.

At the most fundamental level, all matter in the universe is composed of fermions, while fundamental bosons mediate the forces between these particles.

2.1 Fermions

Elementary fermions, the building blocks of matter, are divided into two categories: quarks and leptons; all of which have spin 1/2. Quarks form bound known as hadrons with protons and neutrons, key components of the atomic nuclei, being examples of hadrons. There are six different *flavors* of quarks, grouped into three families: up and down, charm and strange, and top and bottom. Each successive family is heavier than the previous one. Quarks also have fractional electric charges, with the up-type quarks (u,c,t) having a charge of +2/3, and the down-type quarks (d, s, b) having a charge of -1/3.

A distinctive feature of quarks is their possession of another type of charge known as color charge. Color charge is related to the strong force in a similar manner to how the electric charge is tied to the electromagnetic force. There are three types of color charges: red, green, and blue, and the combination of all three colors makes a color-neutral or "uncolored" state. In nature, only color-neutral combinations are observed. For example, mesons consist of

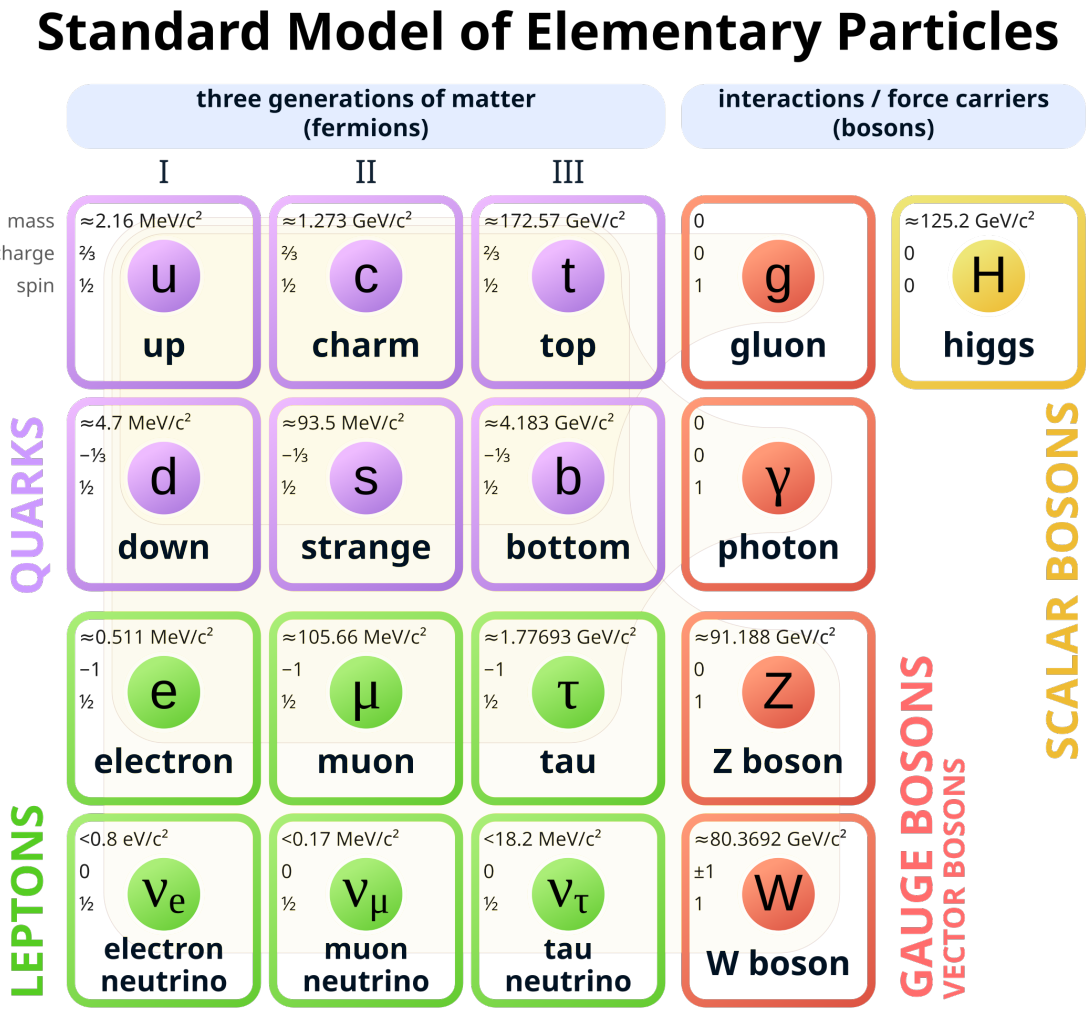

Figure 2.1: Elementary particles of the Standard Model. Two main categories are described at the top. On the left, fermions, with spin 1/2, can be further classified as quarks and leptons. Quarks form bound states called hadrons, protons, and neutrons are examples of them. There are neutral and charged leptons, charged leptons are the electron, muon, and tau, and the neutrinos conform to the neutral sector. On the right, bosons with integer spin, are the force mediators.

a quark and an anti-quark paired with the correct color and anti-color combination, while baryons consist of three quarks, each with a different color. Quantum chromodynamics (QCD) is the quantum field theory that describes the strong interactions between colored particles.

Particles composed of quarks are collectively known as hadrons. The most common hadrons are protons and neutrons which are made from the lightest quarks. A proton consists of two up quarks and one quark down (uud), while a neutron consists of one up quark and two down quarks (udd).

Quantum Chromodynamics (QCD) has two important regimes. At lower energies, quarks

are confined into bound "hadronic" states. The strong interaction at low energies increases with distance, effectively limiting the size of hadrons to approximately 1 femtometer (1 fm). However, at high energies, the strength of the strong force decreases, a phenomenon known as asymptotic freedom, discovered independently by Gross and Wilczek [3], and Politzer [4] in 1973.

Asymptotic freedom suggests that at extreme temperatures or densities, such as those expected in the core of neutron stars, hadrons may be so close together that they lose their individuality, resulting in a deconfined state of matter composed of colorful states. This state is known as quark-gluon plasma (QGP) in analogy with the "electromagnetic" plasma.

The other type of fermions are leptons, which include both a charged and a neutral sector. The charged leptons are the electron, muon, and tau, while neutrinos come in three flavors: the electron neutrino, muon neutrino, and tau neutrino. Neutrinos were originally predicted to be massless in the Standard Model (SM); however, the discovery of neutrino oscillations—where neutrinos change flavors—indicated that they must have a non-zero mass. This discovery led to extensions of the SM to account for neutrino masses.

Both quarks and leptons interact via the weak force, which is responsible for processes such as beta decay, where a neutron decays into a proton, electron, and its anti-neutrino. At the quark level, this involves the transition of a down quark into an up quark. This ability to change flavor is unique to the weak interaction. Finally, since neutrinos are chargeless, they do not interact electromagnetically, unlike charged leptons and all quarks.

2.2 Bosons

The force carriers in the Standard Model are bosons with spin 1. The gluon is the force carrier of the strong force; it is massless but carries color charge, meaning it not only mediates the strong interaction but also participates in it. The photon is the mediator of the electromagnetic (EM) force. Since the photon is a neutral particle, it does not interact with itself through the EM interaction. Being massless, the photon allows the EM interaction to have an infinite range.

The weak force is mediated by the Z^0 and $W^{\pm}$ bosons. Unlike the photon and gluon, the weak bosons are massive, with masses around 80 times that of the proton. These large masses limit the range of weak interaction. Interactions mediated by the Z^0 boson are called neutral current interactions, where only momentum, spin, and energy are transferred. In contrast, interactions mediated by the $W^{\pm}$ bosons involve the transfer of electric charge and it is responsible for the flavor changes.

The only fundamental boson with spin 0 in the SM is the Higgs boson. Discovered in 2012 by the CMS and ATLAS collaborations, the Higgs boson was the final missing piece of the SM. It plays a crucial role by explaining how fundamental particles acquire mass through their interactions with the Higgs field, via the Higgs mechanism [5].

2.3 Standard Model Predictions

The main experimental observables for particle physics are the cross-section σ, which describes the production of particles, and the decay rate Γ, which describes the decay of particles. Both of these can be calculated using the S-matrix, which gives the probability amplitude for a system transitioning from an initial state $|i\rangle$ to a final state $|f\rangle$. The probability amplitude is given by:

$$\langle f|\mathrm{S}|\mathrm{i}\rangle \tag{2.1}$$

With the help of the Dyson series, the S-matrix can be expanded perturbatively if the Hamiltonian H of the interaction is known:

$$\mathrm{S} = 1 - \mathrm{i}\int \mathrm{d}^4\mathrm{x}_1 \mathrm{H}(\mathrm{x}_1) + \frac{(-\mathrm{i})^2}{2!}\int \mathrm{d}^4\mathrm{x}_1\mathrm{d}^4\mathrm{x}_2 \mathrm{T}\{\mathrm{H}(\mathrm{x}_1), \mathrm{H}(\mathrm{x}_2)\} + ... \tag{2.2}$$

Finally, the appropriate observable for a given interaction (cross section or decay width) is proportional to the magnitude of the S matrix element:

$$d\Gamma \propto |\langle f|\bar{S}|i\rangle|^2, \tag{2.3}$$

In practice, the branching fraction $\mathcal{B}$ is measured rather than the decay width. They are related by:

$$\mathcal{B}(i \to f) = \frac{\Gamma(i \to f)}{\Gamma(i, \mathrm{Total})} \tag{2.4}$$

where $1/\Gamma(i, \mathrm{Total}) = \tau$ is the lifetime of the initial state or particle.

A practical way to compute and visualize particle interactions is through Feynman diagrams, which represent perturbative contributions to transition amplitudes. Each component of the diagram—such as arrows, lines, and vertices—corresponds to elements in the integral that define a perturbative term of the probability amplitude, allowing for the calculation of observables up to a given order in the perturbation series.

The simplest diagrams, like the one shown in Figure 2.2, are called tree-level diagrams, and correspond to the first term in the Dyson series. Higher-order corrections are represented by internal loops, which depict additional internal interactions without altering the initial and final states. An example of a higher order will be shown in the following sections. The intermediate states in these diagrams are described by virtual particles, which are excitations of the same field but exist only temporarily, as allowed by the uncertainty principle. Virtual particles can emerge from the vacuum for short time scales, potentially having different masses, while conserving energy and momentum during the interactions they mediate.

The development of the Standard Model has involved the contributions of many scientists over several decades, with its theoretical framework guided by experimental observations. A notable example of how high-energy physics experiments have shaped the SM is the study of transitions between particles that change flavour without altering charge, known as the Flavour Changing Neutral Currents (FCNC).

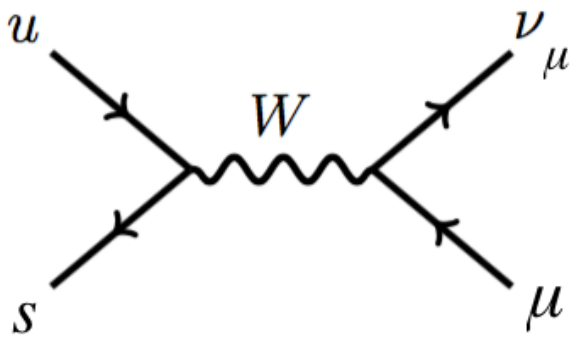

Figure 2.2: Feynnman diagram representing the lowest order of perturbation theory for a weak interaction between two quarks. Time flows from left to right, therefore, it depicts the decay of a meson with quark content (su) to a muon and its neutrino.

2.4 Quark Gluon Plasma

Shortly after the discovery of the asymptotic freedom in QCD, it was suggested that, under extreme densities or temperatures, matter might behave like a soup of quarks rather than hadronic states [6, 7], giving rise to a new state of matter.

One of the first suggestions that this might occur was in the study of neutron stars, where densities greater than nuclear density are expected in the core. At such extreme densities, nuclei could be so closely packed that their individual properties may become indistinguishable, potentially leading to the presence of quark-gluon states.

Although these densities have not yet been achieved in laboratories, heavy ion collisions have been used to explore the high-temperature regime where the formation of new matter is possible. Studies by the HotQCD collaboration demonstrated that the transition from hot QCD matter, such as quark-gluon plasma (QGP), to normal hadronic matter proceeds via a continuous crossover [8], rather than a first-order transition. The pseudo-critical temperature, at which color degrees of freedom begin to emerge rapidly, is estimated to be around $T_C \approx 160$ MeV [9, 10]. To put this into perspective, 1 eV corresponds to approximately 11.6 $\times$ 10^3 Kelvin, illustrating the extreme nature of these temperatures.

Finally, Figure 2.3 shows the QCD phase transition as studied by lattice QCD. The crossover occurs at small baryon chemical potential, which corresponds to conditions achievable in heavy ion colliders.

Findings from the RHIC collaboration at Brookhaven, as well as from ALICE and CMS at the LHC during its first run, suggest that fluid hydrodynamics [11] is important for understanding the dynamics of heavy ion collisions at high energy. The anisotropies observed in the production of low p_T particles imply the existence of a collective flow, where particles follow a hydrodynamic pressure gradient due to the initial collision [12].

The current hydrodynamic model of these collisions, and its evolution over the few femtoseconds (fm/c) that the so-called "fireball" exists, is depicted in Figure 2.4. This model indicates that data from RHIC is compatible with a fluid having an initial temperature between 300 and 600 MeV [13], well above the pseudo-critical temperature. Figure 2.4 shows two ultra-relativistic heavy ions colliding, where the ions resemble discs due to Lorentz con-

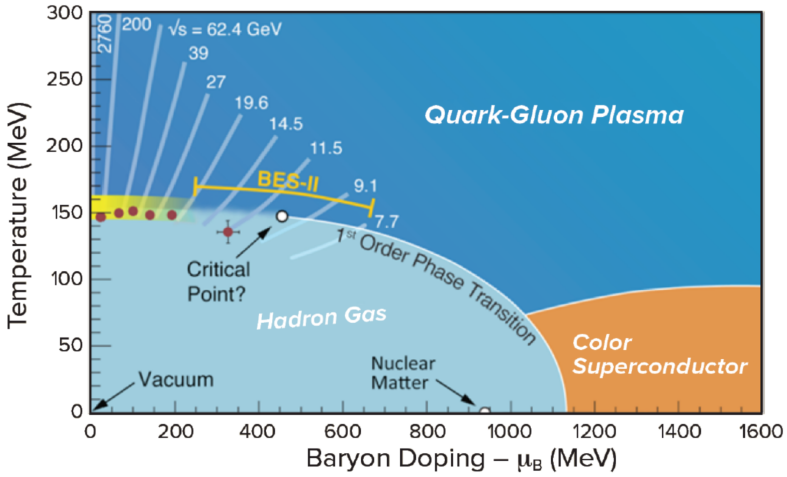

Figure 2.3: An illustration of the current understanding of the phase diagram of QCD as a function of temperature and baryon dopping, the excess of quarks over antiquarks, parametrized by the chemical potential for baryon number μ_B.

traction. Each ion has a radius of around 7 fm and a width of approximately 1fm/γ.

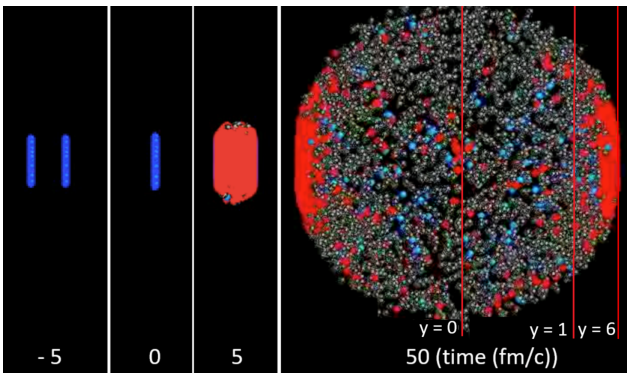

Figure 2.4: Snapshots of a central 2.76 TeV PbPb collision at different times (different horizontal slices of the space-time picture on the left) with hadrons (blue and grey spheres) as well as QGP (red) [14].

Not all collisions are head-on. If we consider the colliding nuclei to be composed of A nucleons, we can call the nucleons that do not encounter any other nucleon as "spectators", those that do not interact are referred to as "spectators," while those that do interact are called "participants". The spectator nucleons continue traveling down the beam pipe, while the number of participants is conserved, expressed as $N_{spec} + N_{part} = A_L + A_R$, where $A_{L,R}$ is the number of nucleons for the type of ion on the Left (Right) side of the colliding beams, respectively. The total number of binary nucleon-nucleon encounters can be much larger than the number of participating nucleons, especially in the most central collisions.

Although N_{coll} cannot be measured directly, they can be estimated using theoretical methods, such as the Glauber Model [15], which is based on Monte Carlo simulations. However, the number of collisions is only determined on average and calssified by centrality.

Centrality is a measure of the impact parameter of an A+A collision, with centrality classes defined as percentages of other quantities, such as energy deposition in forward calorimeters or charged particle multiplicity at central rapidity. For example, events with the highest 10% of charged particle counts correspond to the 10% most central collisions.

Other signatures of collective effect are the correlations between particles that are widely separated in rapidity and are observed [16], studies on dijets that suggest that at more central collisions an imbalance of the leading jet and subleading jet becomes pronounced [17], and the suppression of high p_T particles with respect to pp collisions [18].

These signatures quantify the modifications due to the formation of a medium, or collective effects, by comparing the results from nucleus-nucleus collisions with those expected from the superposition of independent nucleon-nucleon incoherent interactions, known as "binary scaling." For a given class of nucleus-nucleus (A+A) collisions, and the average number of inelastic nucleon-nucleon (N+N) collisions, the nuclear modification factor is defined as the ratio:

$$R_{AA}(p_T) = \frac{dN^{AA}/dp_T}{< N_{coll} > dN^{pp}/dp_T}, \tag{2.5}$$

where dN^{xx}/dp_T is the number of jets, high p_T particles, or other type of specified particle, and $< N_{coll} >$ is typically obtained via the Glauber method.

In the absence of nuclear modifications, the ratio R_{AA} would be equal to 1; meaning that any deviation from 1 indicates the presence of nuclear medium effects.

Studies on smaller systems were planned to fully characterize the modification factors, with intriguing results. Effects similar to those seen in heavy ion collisions have also been observed in smaller systems, such as proton-nucleus (p+A) and proton-proton (p+p) collisions.

In Chapter 4 we describe the search for nuclear modifications in the production of the B+ meson in pPb collisions at $\sqrt{s_{NN}} = 8.16 TeV$ at the CMS detector, using a novel method to obtain $< N_{coll} >$ not involving the Glauber method.

2.4.1 Flavour Changing Neutral Currents

In the late 1960s, the study of neutral and charged kaons (with quark content $d\bar{s}$, $u\bar{s}$ respectively) posed a theoretical challenge. The decay $K^+ \to \mu^+\nu_\mu$ was well understood, and even its charge asymmetry was studied in great detail [19]. The Feynman diagram for this decay, which involves the exchange of a virtual W^+ boson producing a lepton and its neutrino, was used as an example of a tree-level Feynman diagram in Figure 2.2.

On the other hand, the neutral counterpart $K^0 \to \mu^+\mu^-$ was not observed. This decay cannot occur at tree level, as the Z^0 boson does not change flavor and the W^+ boson changes charge. Therefore, the first non-zero perturbative contribution to the decay width involves more than one virtual particle, making this decay rarer than the charged decay. Figure 2.5 shows the Feynman diagram representing this decay, known as a W-box diagram. Since there is a change of flavor between quarks or leptons, it is known as a flavor-changing neutral current (FCNC) decay.

As depicted in 2.5, the FCNC decay of the neutral kaon is mediated by several virtual particles; two W bosons, a neutrino, and an up or a charm quarks. At the time, the quark

model contained only the lightest quarks, (u, d, s), and no evidence for a fourth quark existed. Then, in October 1970, Glashow, Iliopoulos, and Maiani [20] introduced the mechanism to explain the suppression of this neutral-current process relative to its charged counterpart. This mechanism, now-called GIM mechanism, required a fourth type of quark, the charm quark. The contribution of this new quark to the neutral current decay would cancel out with the contribution of the up quark explaining the observed suppression of the neutral current decay. In today's terms, the charm quark field was considered "new physics".

Four years after the GIM paper was published, two different groups independently announced the observation of a signal consistent with a $c\bar{c}$ meson was announced by two different groups [21, 22]. Although the groups proposed different names for the particle, today we honor both by calling it the J/Ψ meson.

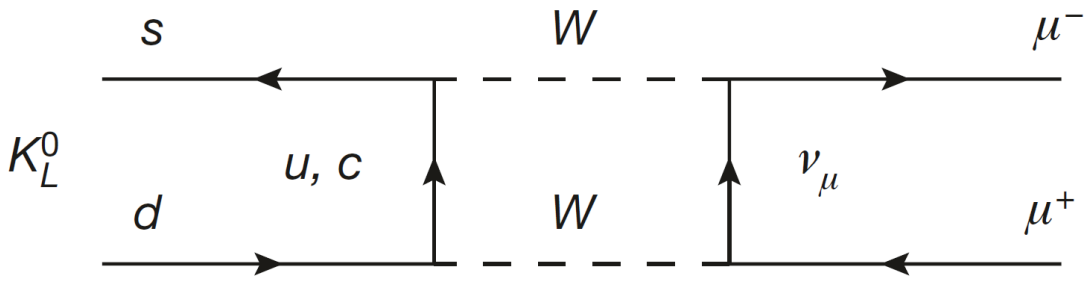

Figure 2.5: Feynman diagrams depicting the decay $K_L^0 \to \mu^+\mu^-$. The strange quark (s) and the down quark (d) that make up the K_L^0, a superposition of K^0 and $\bar{K^0}$, interact via the weak force involving two virtual W bosons, either a virtual up quark (u) or a virtual charm quark (c), and a muon neutrino (ν_μ). The outcome is a muon and its antiparticle.

2.5 Rare decays of b hadrons

Before the discovery of the J/Ψ meson, the study of neutral kaons shed light to another puzzle: the decay of neutral kaons into three pions, which indicated a violation of the charge-parity (CP) conservation. CP violation refers to the asymmetry between the behavior of particles and antiparticles under the combined transformations of charge conjugation (C), which swaps particles with antiparticles, and parity (P), which reflects spatial coordinates.

At the time, the existing current quark model could not explain the observed CP violation. In 1973, Kobayashi and Maskawa [23] proposed a 6-quark model to explain the CP violation of the weak interaction.Although it was initially considered just another theoretical proposal, the observation of mesons consistent with the charm quark gave weight to the model. This lead to the discovery of the b-quark at Fermilab in 1977 [24] via the Υ particle (a $b\bar{b}$ meson) decaying to a dimuon $\mu^+\mu^-$.

The introduction of the six-quark model expanded the Cabibbo matrix into what is now known as the Cabibbo-Kobayashi-Maskawa (CKM) matrix. This matrix quantifies the transition probabilities between different quark flavors. Equation 2.6 presents the most recent experimental values for the CKM matrix elements (rounded to one significant figure in the uncertainties), provided by the PDG booklet [25],

$$|V_{\mathrm{CKM}}| = \begin{pmatrix} |V_{ud}| & |V_{us}| & |V_{ub}| \\ |V_{cd}| & |V_{cs}| & |V_{cb}| \\ |V_{td}| & |V_{ts}| & |V_{tb}| \end{pmatrix} = \begin{pmatrix} 0.9744 \pm 0.0002 & 0.2250 \pm 0.0007 & 0.00373 \pm 0.00009 \\ 0.2249 \pm 0.0007 & 0.9735 \pm 0.0002 & 0.0418 \pm 0.0007 \\ 0.0086 \pm 0.0002 & 0.0411 \pm 0.0007 & 0.99912 \pm 0.00003 \end{pmatrix} \tag{2.6}$$

During the 1980s, experiments like ARGUS and CLEO expanded the study of B hadrons. Some key results from these experiments include the measurement of branching fractions of B mesons, the determination of CKM matrix elements, and the study of both inclusive and exclusive decays of B hadrons. One particularly relevant observation to this thesis is the exclusive decay of B mesons into charmonium states, such as $\mathrm{B}^+ \to \mathrm{K}^+\mathrm{J}/\psi(1\mathrm{S})$which was observed with a very clean signal though with only a handful of events [26, 27].

In the 1990s, two dedicated colliders, known as B-factories [28] were built in Japan (Belle) and the USA (BABAR) to produce large quantities of B mesons. These colliders produced mesons containing b-quarks at rates 4 to 5 orders of magnitude higher than their predecessors (e.g., CLEO), enabling the study of rare decays of B hadrons.

B hadrons primarily decay via the flavor-changing charged current (FCCC) $b \to (c, u)W$ with the decays to charm quarks being more frequent due to the structure of the CKM matrix. As previously discussed, the FCNC decays, are much rarer because they do not occur at the tree level. As a result, transitions such as $b \to s$ and $b \to d$, are supressed, making them sensitive probes of the Standard Model (SM) and potential indicators of new physics.

The $b \to s$ transition, is accompanied by the production of two leptons, and the decay is described by various contributions, including the so-called penguin diagram, (described in Figure 2.6), and W box diagrams shown in Figure 2.5. Belle and BABAR provided measurements on these FCNC decays, and their observations were in agreement with the SM predictions [29, 30], with experimental uncertainties of up to 30%, and theoretical uncertainties up to 20%.

B factories are well suited for measuring inclusive decays, such as $\mathrm{B} \to \mathrm{X_s}\ell^+\ell^-$ where ℓ is a lepton and X_s is a system containing at least one strange hadron. In particular, electrons and muons can be measured simultaneously with comparable efficiencies. However, detectors in hadronic colliders like LHCb and CMS face more challenges in measuring electrons compared to muons due to the crowded track environment. While this doesn't prevent these experiments from conducting B-physics research, it complicates the study of inclusive measurements and decays with electrons in the final state.

In 2014, LHCb produced some intriguing results in the study for Lepton flavor Universality (LFU) [31]. The test for lepton flavor universality in the $\mathrm{B}^+ \to \mathrm{K}^+\ell^+\ell^-$ decay showed some tension with the very precise SM prediction of 1, with an uncertainty less than 1%. LFU states that all leptons couple equally to the electroweak force, meaning that the branching fractions for $\mathrm{B}^+ \to \mathrm{K}^+\ell^+\ell^-$ should be the same for both electrons and muons. The R_K parameter measures the ratio of the branching fractions.

LHCb with significantly smaller experimental uncertainty than those from Belle [32] and BABAR [33], more than twice as small. The result from LHCb deviated with respect to the SM around 2.5 σ as shown in Figure 2.7, illustrating the status of the measurements in 2014.

This report was followed by other measurements on exclusive decays of B hadrons to

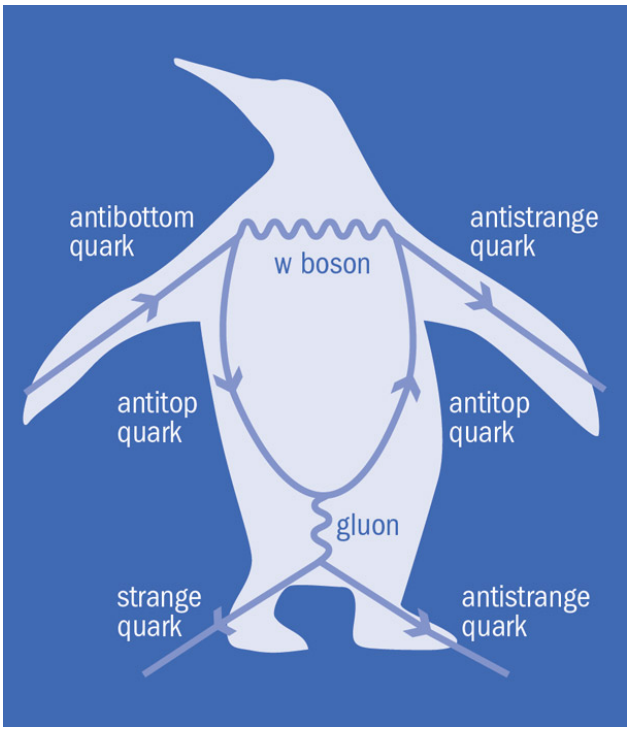

Figure 2.6: One-loop processes describing the flavor changing neutral current decay $b \to s\ell\ell$. The name was coined by John Ellis after losing a bet playing darts.

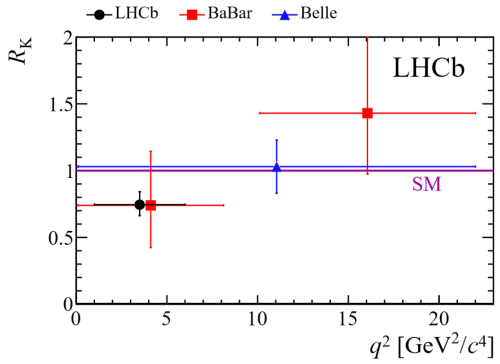

Figure 2.7: Status of the measurement of R_K parameter back in 2014, when LHCb reported its first measurement.

final states with muons [34–36]. The branching ratio was measured as a function of the squared dimuon invariant mass (q^2). Although no clear evidence of new physics was found, the repeated pattern of tension across different decays, as shown in Figure 2.8, provides a strong motivation for new and more precise measurements to understand these effects.

The source of the anomalies in $b \to s\ell\ell$ branching fractions and LFU observables remains unclear. If new particles were involved in these decays, they would likely modify both the decay rates and the angular distribution of the decay products. To investigate this, LHCb performed analyses of the angular distribution of particles produced in B^0 and $B^\pm$ decays with dimuon final states.

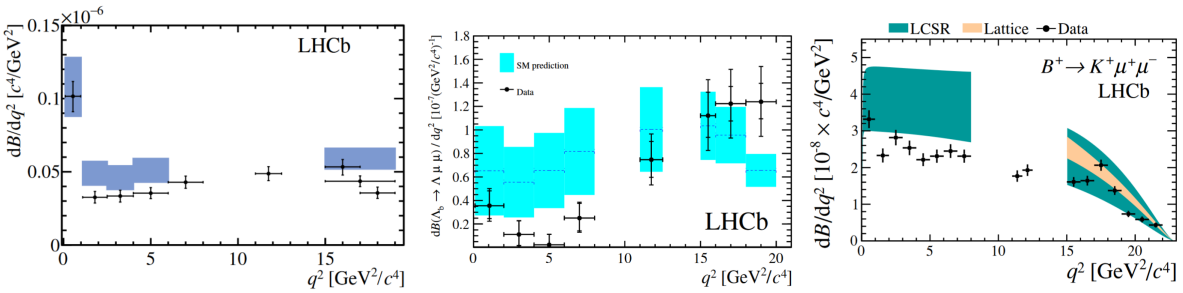

Figure 2.8: Some of the flavor anomalies reported by the LHCb collaboration in 2014-2015. The measured branching fraction of the channels $B^0 \to K^*(892)^0\mu^+\mu^-$ (left), $\Lambda_b^0 \to \Lambda\mu^+\mu^-$ (middle), and $B^+ \to K^+\mu^+\mu^-$(right). Exhibit pattern of being smaller than SM predictions.

2.5.1 Angular Analyses

The angular analysis that indicated some tension with SM predictions is the angular analysis of the rare b decay: $B^0 \to K^{*0}(K^+\pi^-)\mu^+\mu^-$. The initial paper from LHCb in 2013 [37] described the decay by q^2, the squared mass of the dimuon system, and three angles $\vec{\Omega} = (\cos\theta_l, \cos\theta_K, \phi)$, the depiction of the angles is shown in Figure 2.9.

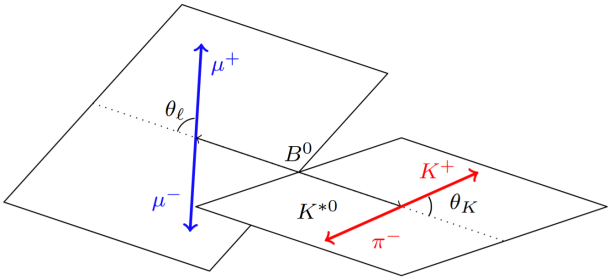

Figure 2.9: θ_K and θ_{ell} definitions for the B^0 decay. The angle ϕ is the angle between the plane containing the μ^+ and μ^- and the plane containing the kaon and pion from the K^{*0}.

The angular distribution of the decay can be written as:

$$\begin{aligned}\frac{1}{\mathrm{d}(\Gamma+\bar{\Gamma})/\mathrm{d}q^2}\frac{\mathrm{d}^4(\Gamma+\bar{\Gamma})}{\mathrm{d}q^2\,\mathrm{d}\Omega} = \frac{9}{32\pi}\Bigg[&\frac{3}{4}(1-F_L)\sin^2\theta_K + F_L\cos^2\theta_K \\ &+ \frac{1}{4}(1-F_L)\sin^2\theta_K\cos 2\theta_\ell \\ &- F_L\cos^2\theta_K\cos 2\theta_\ell + S_3\sin^2\theta_K\sin^2\theta_\ell\cos 2\phi \\ &+ S_4\sin 2\theta_K\sin 2\theta_\ell\cos\phi + S_5\sin 2\theta_K\sin\theta_\ell\cos\phi \\ &+ \frac{4}{3}A_{\mathrm{FB}}\sin^2\theta_K\cos\theta_\ell + S_7\sin 2\theta_K\sin\theta_\ell\sin\phi \\ &+ S_8\sin 2\theta_K\sin 2\theta_\ell\sin\phi + S_9\sin^2\theta_K\sin^2\theta_\ell\sin 2\phi\Bigg]. \end{aligned} \tag{2.7}$$

Finally, a set of observables, called P'_X was defined to cancel out the leading $B^0 to K^{*0}$ form-factor uncertainties. Those are built from F_L and S_{3-9}. All of the parameters were consistent with SM predictions except P'_5:

$$P'_5 = \frac{S_5}{\sqrt{F_L(1-F_L)}} \tag{2.8}$$

The initial report presented the plot shown in Figure 2.10. This measurement was confirmed, by CMS [38], Belle [39], ATLAS [40] , and LHCb [41] with more data. Although the overall trend is the same, uncertainties have not reached the precision wanted to claim an inconsistency with SM, more precise measurements are needed.

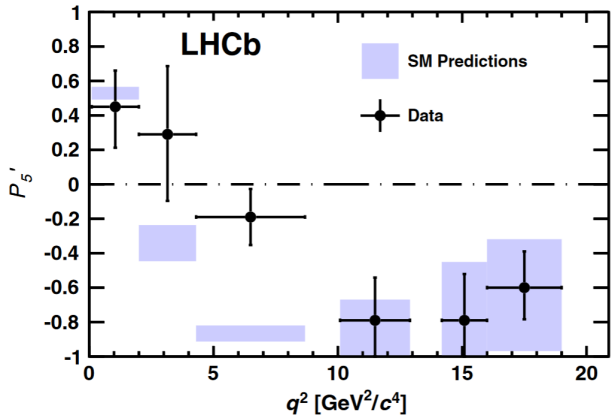

Figure 2.10: Initial measurement by LHCb of the optimized P'_5, that cancel out the uncertainties of the hadronic form factors. Only one q^2 presents a deviation from the SM, and it happened in one parameter out of the 20 measured. However, the statistical significance of such deviation is not negligible.

The FCNC decay for the charged B meson, $B^+ \to K^+\mu^+\mu^-$, can be described in terms of the angular distributions as well, and since it is a 3-particle final state, only one angle can be used to define its angular distribution.

In this case, the parametrization was introduced by Bobeth *et. al.* [42], where two parameters are introduced, the A_{FB} and F_H parameters. F_H is a measure of the contribution from (pseudo)scalar and tensor amplitudes to the decay width in the approximation that muons are massless, and A_{FB}, the forward-backward asymmetry of the dimuon system. In the SM, A_{FB} is zero and F_H is suppressed by m^2_{ell}[43].

Previous measurements have been consistent with the SM with uncertainties on the order of 10^{-1} using data from Run 1. With increasing statistics, an updated analysis is desired to verify the compatibility with the SM. In Chapter 5 we describe the measurement of these angular parameters using data from CMS during Run 2.

Chapter 3

The Compact Muon Solenoid at the Large Hadron Collider

3.1 The Large Hadron Collider

The Large Hadron Collider (LHC) is a two-ring superconducting-hadron accelerator operated by the European Organization for Nuclear Research, known as CERN. It is installed in a 26.7 km tunnel constructed for the previous CERN machine, the Large Electron-Positron Collider (LEP), at a depth ranging from 50 to 175 meters on the French-Swiss border. It is designed to accelerate protons at nearly the speed of light by a series of superconducting radiofrequency (RF) cavities and dipole magnets to bend the path of the particles. The protons are accelerated in two beams circulating in opposite directions. Each beam contains a large of bunches ranging from tens up to several thousands, and each bunch contains on the order of 10^{11} protons.

The acceleration of protons at LHC involves a succession of machines to achieve increasingly higher energies. The starting point is a bottle of hydrogen gas, where the protons are obtained by ionizing the hydrogen atoms with an electric field. The protons are then accelerated at a Linear Accelerator (Linac) to be injected in the Proton Synchrotron Booster (PSB), the Proton Synchrotron (PS), and the Super Proton Synchrotron (SPS) to achieve an energy of 450 GeV. Finally, the beam of protons is injected to the two beam pipes of the LHC, circulating in opposite directions. Beams reach an energy of 6.5 TeV in around 20 minutes, and when the maximum energy is obtained, the two beams are brought into collision inside four detectors; ALICE, ATLAS, CMS, and LHCb. Figure 3.1 shows schematically the accelerator complex.

In addition to the collision energy, and of particular importance, is the luminosity L, from which the number of events per second produced is obtained as:

$$N_{event} = L\sigma_{event} \tag{3.1}$$

where σ_{event} is the cross-section for the type of events under study. The machine luminosity depends only on beam parameters and can be written as [45]:

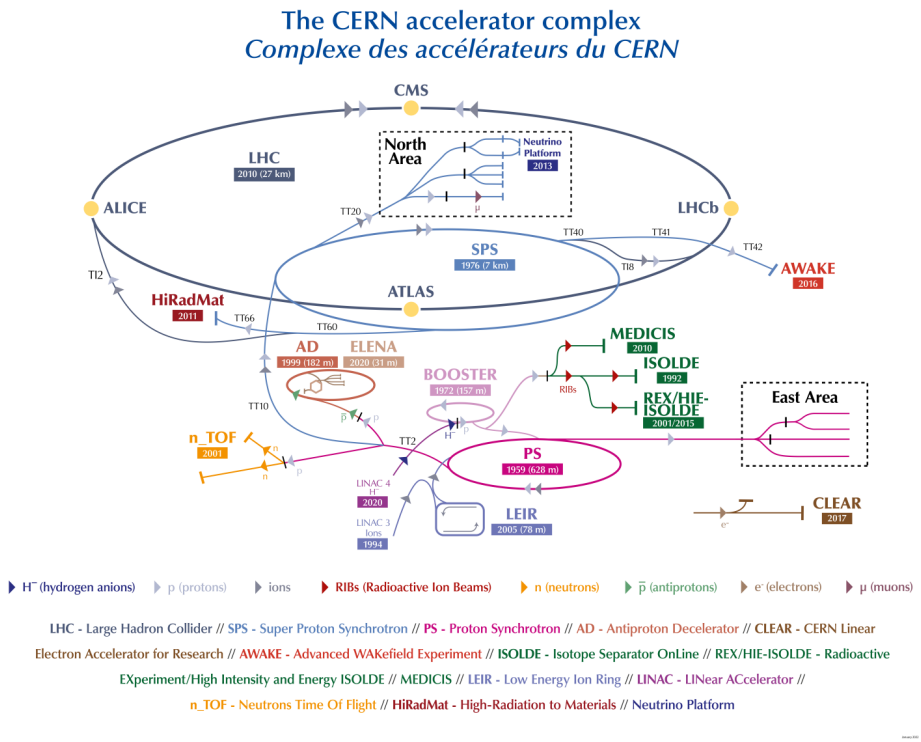

Figure 3.1: The CERN accelerator complex layout in 2022 [44].

$$L = \frac{N_b^2 n_b f_{rev} \gamma_r}{4\pi \epsilon_n \beta^*} F \tag{3.2}$$

where N_b is the number of particles per bunch, n_b the number of bunches per beam, f_{rev} the revolution frequency, γ_r the relativistic gamma factor, ϵ_n the normalized transverse beam emittance, β^* the beta function at the collision point, and F a geometric reduction factor due to the crossing angle at interaction point. The normalized transverse beam emittance and the beta function are two quantities that describe the transverse size of the beam [46].

The LHC started its Run 1 operations in 2010 at an energy of $\sqrt{s} = 7$ TeV, later increasing to $\sqrt{s} = 8$ TeV. By the end of Run 1 in 2012, it had provided a total integrated luminosity of about 30 fb^{-1}. The LHC then entered a two-year Long Shutdown (LS1) for upgrades and maintenance, resuming with Run 2 in 2015. During Run 2, which lasted from 2015 to 2018, the LHC operated at $\sqrt{s} = 13$ TeV with a 25 ns bunch spacing, delivering a total luminosity of 160 fb^{-1}. The next Long Shutdown (LS2) started in 2019, and the LHC was reactivated for Run 3 in 2022, with $\sqrt{s} = 13.6$ TeV.

Although protons are the main participants in the accelerator complex, heavy ions can also be accelerated at the LHC. For instance, Pb ions, which can be obtained from a source of vaporized lead, follow identical LHC injection chains as protons, except for the first two accelerators; the pp Linac is replaced by heavy ion Linac3 and the PSB by the Low Energy Ion Ring (LEIR) [47].

During Run2, three different collision modes were exploited using different beam configurations:

- $Pb - Pb$ collisions in 2015 and 2018 at a beam energy of 6.37 TeV,
- $p - Pb$ in 2016 at beam energies of 4 and 6.5 TeV,
- and a special run, single-day, of $Xe - Xe$ collisions in 2017 [48].

The center-of-mass energy for heavy ion collisions is related to the beam energy (E_b) as:

$$\sqrt{s} = 2\sqrt{\frac{Z_1 Z_2}{A_1 A_2}} E_b \tag{3.3}$$

where Z and A are the charge and mass numbers of the two beams. Therefore, for the 2016 pPb collisions, Z1=1, A_1=1, A_2=208, and Z_2=82, the center of mass energy is 8.16 TeV.

Figure 3.2 shows the integrated luminosity delivered to CMS during stable beams for (top) pp collisions at nominal center-of-mass energy, and (bottom) for heavy ion collisions, only for Run 2.

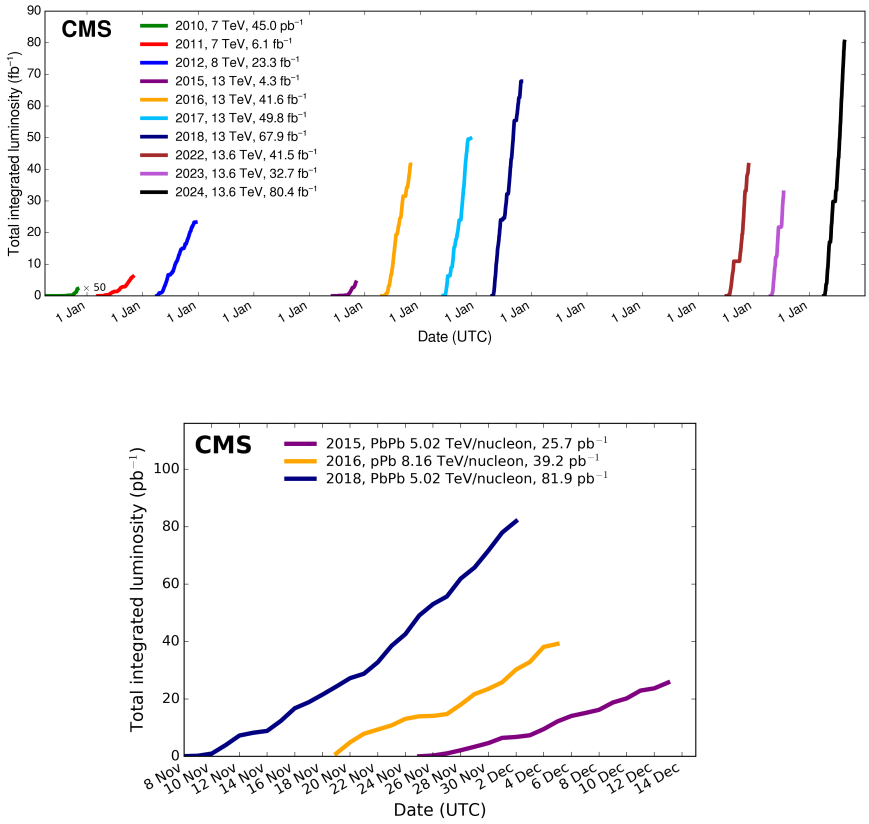

Figure 3.2: Top, delivered luminosity versus time for 2010-2012, 2015-2018, and 2022-2023 (pp data only). Bottom, delivered luminosity versus time for the Run 2 heavy ion collisions. [49].

3.2 The Compact Muon Solenoid

The Compact Muon Solenoid (CMS) is a general-purpose particle detector, located at the LHC. The detector was mainly designed to search for the Higgs boson, which was discovered in 2012. However, a variety of physics phenomena can be studied with the multipurpose detector such as precision measurements of the SM particles, flavor physics, heavy-ion physics, and searches for new physics beyond SM. The dimensions of the detector are 16 meters in height, 21 meters in length, and weighs 14000 tonnes.

The coordinate system used by the CMS detector (and other detectors around the LHC) originates at the nominal collision point. The z-axis is aligned with the beam pipe, while the y-axis is pointing vertically upward, and finally, the x-axis is pointing radially inward toward the center of the LHC. The azimuthal angle and pseudo-rapidity are used to describe the position and kinematic variables of the particles instead of the classical Cartesian coordinate system. The azimuthal angle ϕ is measured from the x-axis in the $x-y$ plane. The polar angle is measured from the z-axis. Pseudo-rapidity is defined in terms of the polar angle θ as $\eta = -\ln\tan\frac{\theta}{2}$. Momentum, and energy measured transverse to the beam direction, denoted by p_T and E_T are computed from the x and y components. Figure 3.3 depicts the CMS geometry with the center at the nominal Interaction Point.

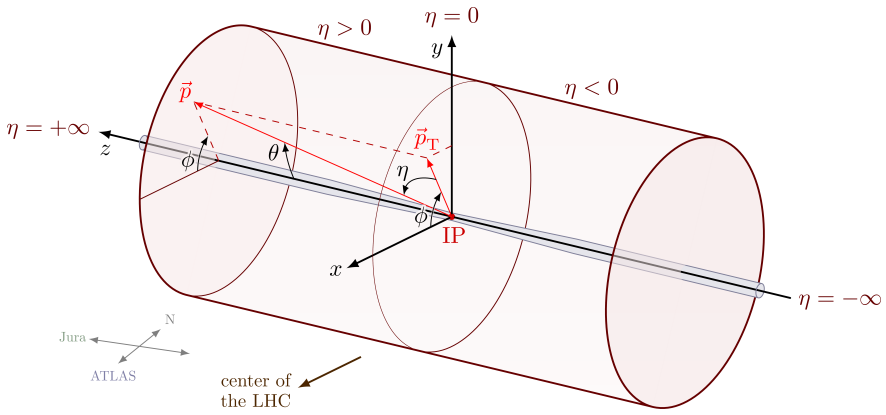

Figure 3.3: Coordinate system for the CMS detector.

The CMS comprises several subdetectors which will be discussed in detail in the following pages. A schematic drawing of the CMS detector and its subdetectors is shown in Figure 3.4.

The main feature of the CMS detector is a superconducting solenoid with an internal diameter of 6 meters and a length of 12.5 meters that generates a magnetic field of 3.8 T. Inside the magnetic volume there are located the tracker system, composed of the most inner detector: the silicon pixel, followed by the strip silicon tracker. The next big layer is the calorimetry system, which is composed of a lead tungstate crystal electromagnetic calorimeter (ECAL), and a brass and scintillator hadron calorimeter (HCAL). Forward calorimeters extend the pseudorapidity (η) coverage provided by the barrel and endcap detectors. Outside the superconducting solenoid, the muon system is found. The muon system is comprised of three types of gas-ionization detectors embedded in the steel flux-return yoke. In the barrel region ($|\eta| < 1.2$) drift tube chambers (DT) are used, in both endcaps, cathode strip

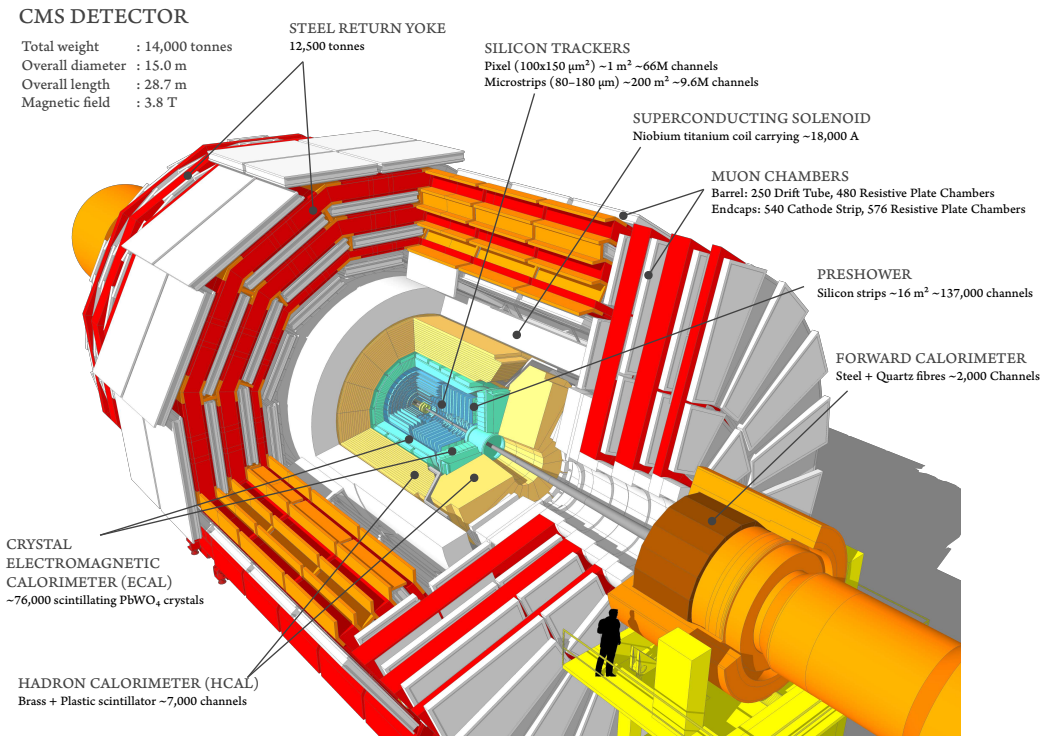

Figure 3.4: Schematic drawing of the CMS detector [50].

chambers (CSC) are deployed covering a range up to $|\eta| < 2.4$. In addition, resistive plate chambers (RPC) are used in both the barrel and the endcap regions.

A two-tiered trigger system is used to select *interesting* events. The first-level (L1) trigger involves custom hardware processors and uses coarse, but fast, information from the calorimetry and muon systems to select events at a rate of around 110 kHz with a latency of 4 μs. The second level, known as the high-level trigger (HLT), comprises a cluster of commercial processors running an optimized version of the full event reconstruction software. The initial output rate for HLT during Run 1 was around 100 Hz but has increased on Run3 up to several kHz.

Finally, the CMS software and computing systems are an integral component of the collaboration, and cover a broad range of activities including the storage, access, reconstruction, and analysis of data; as well as the support of a distributed computing infrastructure for physicists developing these tasks. The CMS computing model is highly distributed, with a primary "Tier-0" center at CERN being supplemented by Tier-1 and Tier-2 computing centers at national laboratories and universities worldwide.

An exhaustive description of the CMS detector can be found in the Technical Design Report [51] and in the update report [52].

3.2.1 Solenoid Magnet

The superconducting solenoid magnet provides the structural support of the whole detector, and its inner magnetic field of 3.8 T is capable of bending the trajectory of charged particles

with a good resolution (down to the order of 1%). During its development, the requirement for a good momentum resolution, without making stringent demands on the spatial resolution and keeping a compact detector, led to the choice of its high magnetic field.

The magnetic system is comprised of a NbTi superconducting solenoid cooled down with liquid helium to a temperature of 4.2 K, and a magnetic flux return yoke made of construction steel containing up to 0.17% carbon and up to 1.22% manganese, as well as small amounts of silicon, chromium, and copper divided in multi-layer barrel and endcap sections [53].

One of the most important benefits of the magnetic field of 4 T is to enable an efficient L1 trigger. The CMS muon trigger relies on two independent measurements in the muon system, and lowering the intensity of the magnetic field by a fourth means a reduced momentum resolution that increases the L1 rate by about 70%. Additionally, the inner tracking system benefits from the high magnetic field; when changing from 3 to 4T, occupancy decreases in the inner tracker by more than 40% [54], making it easier to distinguish between different particles.

3.2.2 Inner Tracking System

The inner tracking system is composed of pixel and strip detectors. It is crucial to measure the momentum particles and build a picture of what happened at the heart of the collision by measuring the trajectories of the particles and interpolating them to primary vertices.

Silicon Pixel

The silicon pixel detector is the innermost part of the CMS sub-detectors. It provides three-dimensional space points close to the LHC collision point, allowing for high-precision tracking and vertex reconstruction. The original pixel detector consisted of three barrel layers at radii 44, 73, and 102 mm and two endcap disks at distances of 345 and 465 mm from the interaction point. However, due to the increased luminosity of the LHC and updates on the beam pipe, the installation of the CMS Phase-1 pixel detector took place during the technical stop of the LHC in 2016/2017.

This update improved the original features of the pixel detector, by increasing the number of barrel layers to four at radii of 29, 68, 109, and 160 mm, and three disks on each endcap at distances of 291, 396, and 516 mm from the center of the detector. A comparison of the original and updated pixel detector is shown in Figure 3.5.

The CMS Phase-1 pixel detector is built from 1856 segmented silicon sensor modules, where 64% (1184) of those are used in the barrel pixel detector (BPIX) and 36% (672) modules are used for the forward disks. Each module consists of a sensor with 160 $\times$ 416 pixels, and the standard pixel size is 100 $\times$ 150 μm^2 [55].

Strip Pixel

The silicon strip tracker, together with the pixel detector, measures the trajectories of the charged particles up to a pseudo rapidity of $|\eta| < 2.5$. The layout of the complete inner tracking system (pixel and strips) is shown in Figure 3.6.

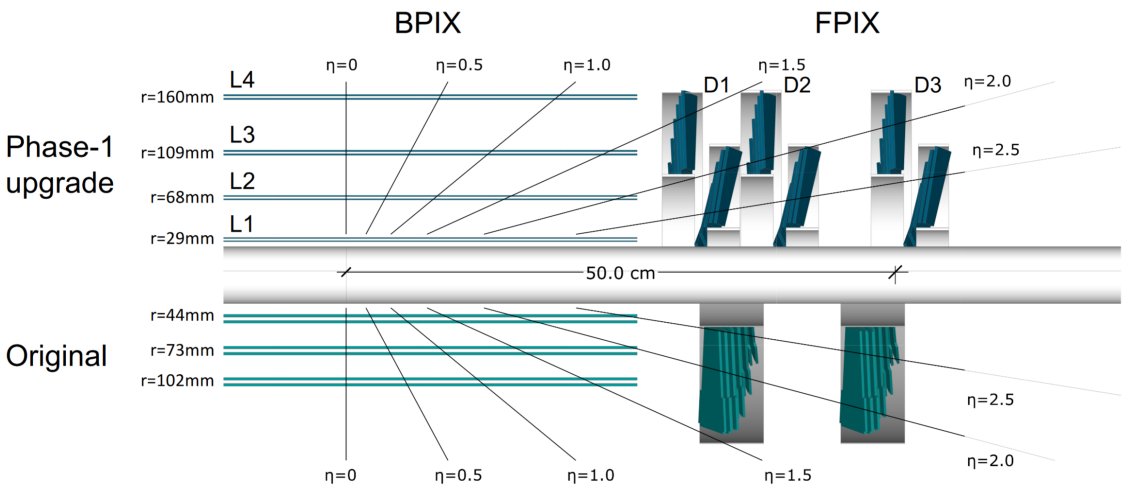

Figure 3.5: A comparison of the CMS Phase-1 pixel detector to the original detector layout in longitudinal view [55].

The strip tracker is composed of four sectors. In the inner part, the tracker inner barrel (TIB) is composed of four layers complemented with three tracker inner disks (TID). The outer part has six layers in the tracker outer barrel (TOB) and the forward regions are covered by tracker end caps (TEC). Each TID is composed of three rings, and each TEC is composed of up to seven rings.

The silicon strip tracker has in total of 9.3 million silicon micro-strips that cover 198 m^2 of active silicon area distributed over 15148 modules. And throughout all years of operation sensors were exchanged and the fraction of bad detector components was stable during Run 1 and Run 2.

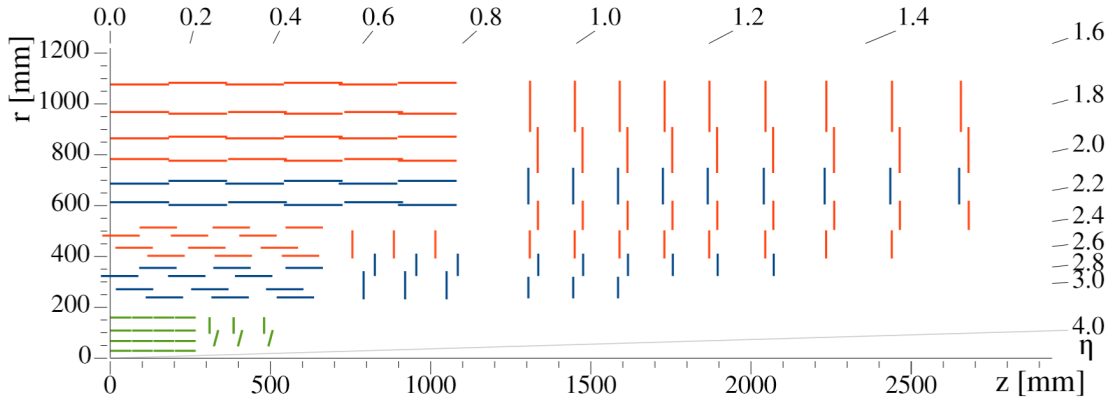

Figure 3.6: Sketch of one-quarter of the Phase-1 CMS tracking system in r-z view. The pixel detector is shown in green, while single-sided and double-sided strip modules are depicted as red and blue segments, respectively. [56].

3.2.3 Calorimetry System

Just after the silicon tracker system, we find the calorimetry subdetectors. Two types of detectors are placed, the Electromagnetic (ECAL) and Hadronic (HCAL) calorimeters. The electromagnetic calorimeter is used to measure the energy of charged particles, in particular photons and electrons. The hadronic calorimeter is responsible for measuring the energy of the hadrons passing the ECAL.

Electromagnetic Calorimeter

The Electromagnetic Calorimeter (ECAL) is responsible for measuring the energy of electrons and photons, this is done by using lead lead tungstate (PbWO4) crystals. The crystals were manufactured as truncated pyramids which produce electromagnetic shower as charged particles and photons pass through. The scintillation is captured by photomultipliers glued to the back of the crystals. The ECAL is composed of a barrel and endcap parts with a total of 75 848 crystals [57], and in front of the encdap portions.

The barrel part covers the pseudorapidity $|\eta| < 1.479$, and is located at a radius of 1290 mm of the nominal interaction point. Crystals in the barrel have a front face measuring approximately 22×22 mm^2, and a length of 230 mm. The crystals form a grid in the $\eta - \phi$ space with a granularity of $\Delta\eta(\Delta\phi) = 0.0174(1°)$.

The endcap component lies 3170 mm from the interaction point, the front face dimensions of the crystals are about 15% larger than those of the barrel crystals, have a length of 220 mm, and are arranged in a square $x - y$ array.

As in the barrel, the crystals in the endcap are tilted, in a direction that increases the average depth of ECAL seen by a shower. Figure 3.7 shows the layout of the barrel and endcap portions of the ECAL.

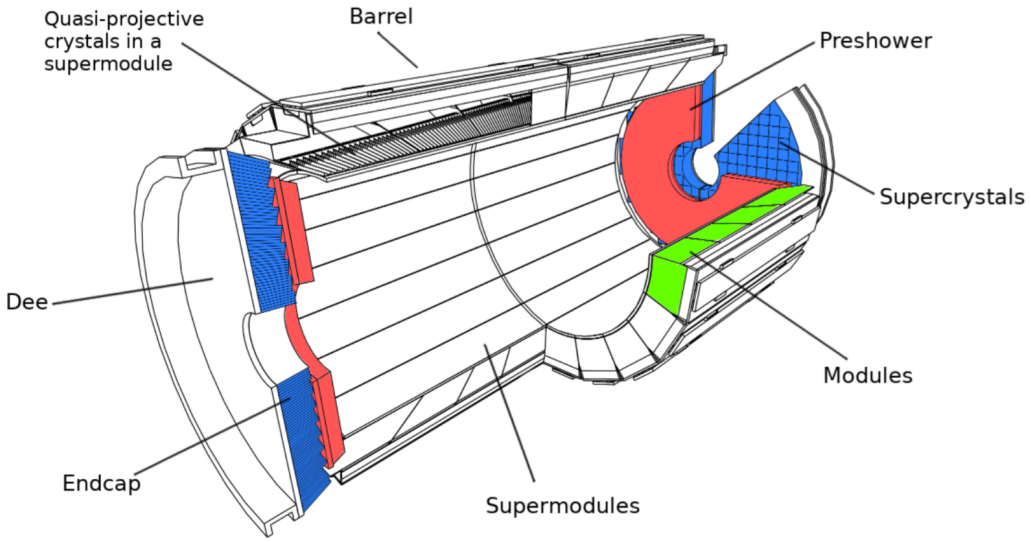

Figure 3.7: ECAL layout in CMS. [58].

3.2.4 Hadron Calorimeter

In contrast to the ECAL, the hadron calorimeter is a sampling calorimeter. This means that the dense material producing the particle shower alternates with another material that measures the deposited energy. In the HCAL the dense material is a brass alloy (70% Copper and 30% Zinc) [51]. When a particle hits a brass layer, an interaction can occur producing numerous secondary particles. These particles interact with the alternating plastic scintillator layers, producing blue-violet light. Within each tile, wavelength-shifting optical fibers, with a diameter of less than 1mm, absorb this light. These fibers shift the blue-violet light into the green region of the spectrum, and clear optic cables then carry the green light away to readout boxes located within the HCAL volume.

The CMS hadron calorimeter (HACL) shown in Figure 3.8 is composed of four subdetectors: hadron barrel (HB), hadron endcap (HE), hadron forward (HF), and hadron outer (HO).

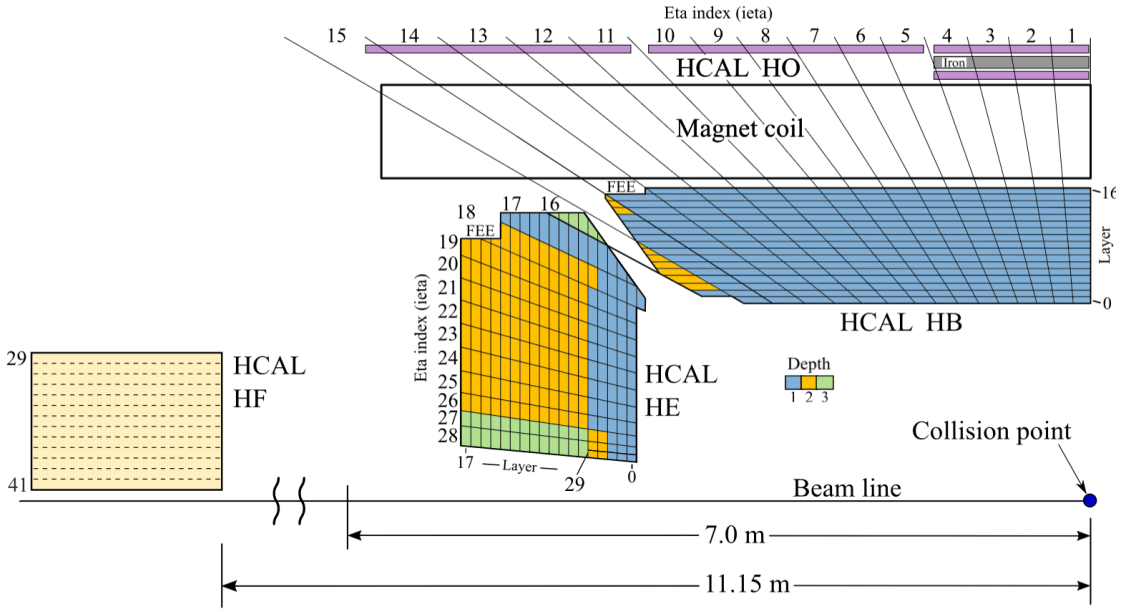

Figure 3.8: HCAL layout in CMS. [59].

The hadron barrel goes from an inner radius of 1777 mm to an outer radius of 2876.5 mm, it is composed of 17 plastic scintillator layers alternating with brass and stainless steel plates. While the brass plates have been discussed, the stainless steel plates are used for structural strength. Plastic fibers send the signal from the scintillator layers to hybrid photodetectors (HPDs) in the original design or silicon photomultipliers (SiPMs) after the upgrades.

Finally, the hadron forward (HF) is structurally different than the HB and the HE. It is a 1.65 m sampling calorimeter of steel absorber and quartz fibers. Its front face is located at 11.2 m from the interacting point. In this case, the signal originates from Cerenkov light emitted in the quartz fibers, which is then channeled by the fibers to photomultipliers.

3.2.5 Muon System

Muons can penetrate large depths of matter before being absorbed, and they are not stopped by the CMS calorimetry system, that is why chambers to detect muons are placed at the very edge of the experiment where they are the only particles likely to register a signal. Outside the volume enclosed by the solenoid the muon system, depicted in Figure 3.9, is composed of three different gaseous detectors.

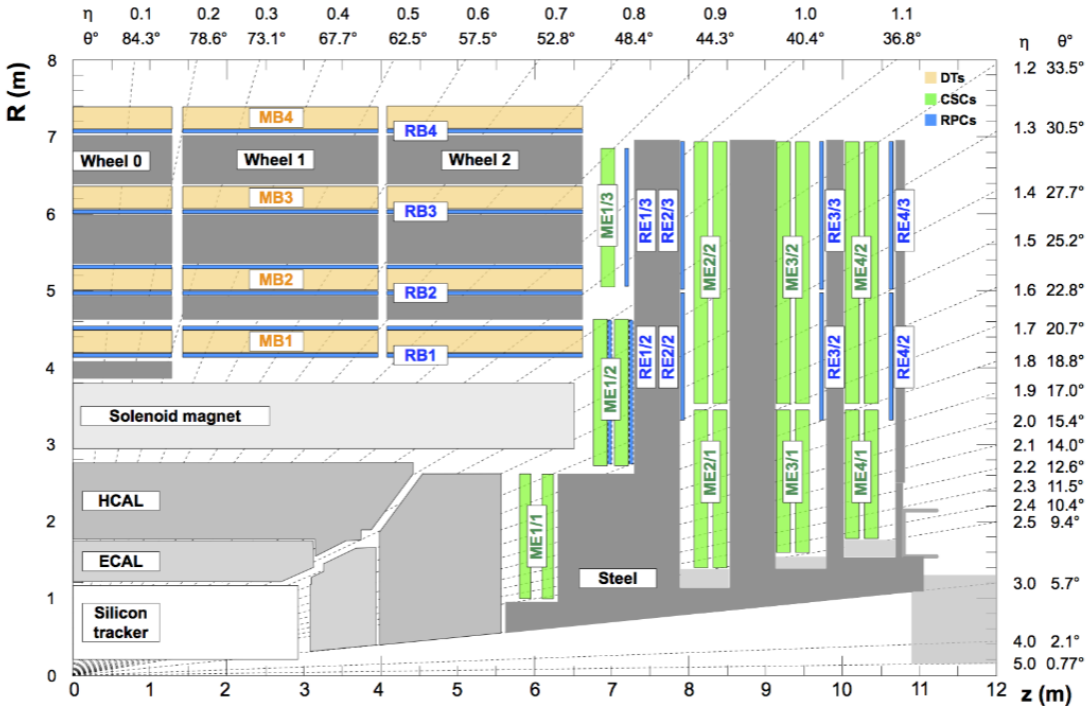

Figure 3.9: An R-z cross-section of a quadrant of the CMS detector. The interaction point is at the lower left corner. The locations of the various muon stations and the steel flux-return disks (dark areas) are shown. The DT stations are labeled MB ("Muon Barrel") and the CSCs are labeled ME ("Muon Endcap"). RPCs are mounted in both the barrel and endcaps of CMS, where they are labeled RB and RE, respectively [60].

Drift Tubes

Drift Tubes (DT) are located in the barrel region ($|\eta| < 1.2$) where the muon rate, neutron-induced background, and residual magnetic field are low. The basic cell of a DT is a rectangular drift cell with a transverse size of 4.2×1.3 cm^2 containing a stretched wire within a gas volume. When a particle passes through the volume, it knocks electrons off the atoms of the gas. These electrons drift to the anode producing a signal that is later amplified and produces a measurable charge pulse.

Cathode Strip Chambers

Cathode Strip Chambers (CSC) are used in the endcaps covering a region up to $|\eta| < 2.4$. In this region, the conditions are different, muon rate, neutron-induced background, and magnetic fields are high. The CSCs consist of arrays of positively-charged anode wires crossed with negatively-charged copper cathode strips within a gas volume. Just like the Drift Tubes, CSC exploits the phenomena of knock-off electrons from the gas atoms due to the interaction with passing particles. In this case, both the positive ion and the knocked-off electron contribute to the measured signal to characterize the passing muons.

Resistive Plate Chambers

In addition to the DTs and CSCs, Resistive Plate Chambers (RPC) are used in both, the barrel and the endcap regions. RPCs consist of two parallel plates, a positively-charged anode, and a negatively-charged cathode, both made of a very high resistivity plastic material and separated by a thin gas volume. The voltage between the resistive plate is high enough to produce a large number of secondary electrons, which is known as avalanche mode.

There are 1846 muon chambers: 250 DTs, 540 CSCs, and 1056 RPCs. With a spatial resolution from 50 μm (CSCs) up to 1.3 cm (RPCs), and time resolution from 2 ns (DTs) to 1.5 ns (RPCs). The muon system provides redundant and fast identification of muons and their momenta.

3.2.6 Trigger and Data Acquisition

During its operation, the LHC provides two highly energetic proton beams with a train structure of empty and filled wagons, or bunches. The LHC provided around 2400 bunches at its maximum capacity during Run 2, each bunch traversing the 26.7 km accelerator with a revolution frequency of around ($3\times10^8/26.7\times10^8 =$) 11.235 kHz. With these conditions, one expects a bunch crossing, and therefore collisions, with a rate around 27 MHz. The typical event weighs around 2 MB [61], therefore, to save all the information from each collision, CMS would be storing more than 50 TB of data per second. Storing around 8 hours a day for several weeks result impractical.

However, most of the events are "not interesting" in the sense that the most common events provide little new information, to solve this problem, CMS employs a two-tiered trigger system to select the most "interesting" events.

L1

The first level (L1) is implemented in custom hardware processors and electronics. It relies on the calorimeter and muon systems, which provide coarse information to create candidates for jets, e/γ, and muons, as well as calculations of energy sums. Around one hundred algorithms conform to what is known as the L1 menu, these algorithms perform selections to keep a fraction of the incoming events. Algorithms of single objects as well as multiobjects are used to select, for example, events with two muons whose transverse momentum is greater than 3 GeV each. Any event that passes at least one algorithm from the L1 menu is accepted.

The selection is done in around 3 μs, and the output rate of events from the L1 system is approximately 100 kHz. Figure 3.10 shows a diagram of the CMS Level-1 trigger system, and how the data is combined from the different subdetectors.

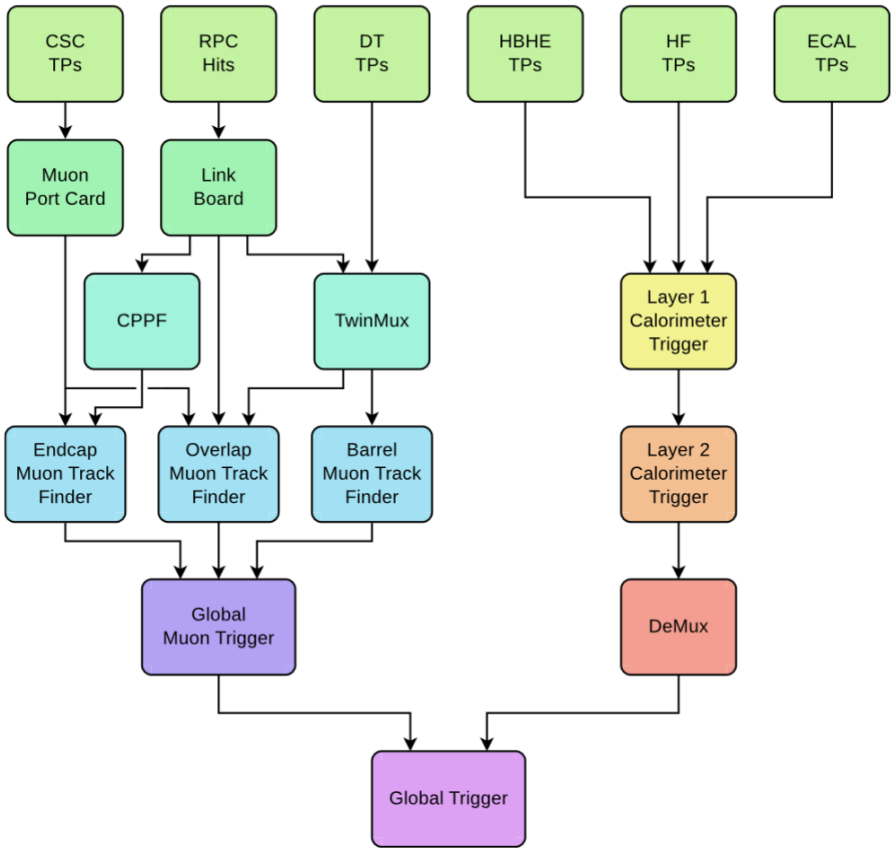

Figure 3.10: Diagram of the upgraded CMS Level-1 trigger system during Run 2. Labels in the diagram correspond to trigger primitives (TPs), concentration preprocessing and fan-out (CPPF), and demultiplexing card (DeMux) [62].

HLT

The second level, or high-level trigger (HLT), runs on a farm of commercial computer nodes. It improves the resolution and purity of the physics objects from events selected by the L1 system.

The HLT is built around the concept of "paths" to structure its workflow. These paths are sequences of algorithmic steps designed to reconstruct physics objects and make selections based on specific physics requirements. Paths from the HLT menu can share several steps therefore reducing the computation time, in addition, the menu is optimized to make fast decisions and reject events as soon as possible before more intensive steps are made (e.g. tracking).

The reconstruction modules and selection filters of the HLT use the same software framework that is also used for offline simulation, reconstruction, and analysis: the CMS software (CMSSW).

Data sets are defined as a set of paths for similar physics processes, therefore each dataset is filled with events passing a logical OR of a set of trigger paths from the HLT menu.

The total of the HLT menu stores around 1 kHz of events that are then transported by the data acquisition system (DAQ) to the different tiers of computing, starting from the first layer located at CERN (T0) which is later transferred at T1 and T2 tiers. T1 tiers are large-size clusters that reconstruct the events using the most precise, yet computationally expensive, version of algorithms in the CMSSW software. T2 tiers are smaller clusters in terms of computational power which can be used as clusters for reconstruction, but their main usage is data storage. The data is stored in a file booking type service, where the data is available for anyone certified by the collaboration. The data is stored under the object-oriented programming paradigm using the CERN's ROOT framework.

Dataformats

Different formats of data are used in CMS. The most basic is a format called RAW, which contains all information from each subdetector, for example, it contains all clusters pixel hits, energies from the calorimetry system, and positions in the whole tracker. All accepted events stored by the HLT menu, are saved as C++ objects. These objects contain candidates for electrons, tracks, muons, jets, and have their own set of methods to be manipulated with, and own attributes achievable with the CMSSW software. Objects can be further processed and stored in different data formats like the AOD, MINIAOD, and NANOAOD formats.

The AOD format was the first used in CMS, after Run1 it became evident that a lighter version would be needed. Run 2 introduced the MINIAOD, where the information of a given event was reduced. Finally, at the end of Run2, the NANOAOD data format was introduced, it represents a change of paradigm on the AOD family since it is no longer needs the CMSSW software to interact with it, it can be used in a stand-alone way and readable with popular programming languages such as python.

The information loss in this last step is an issue for BPH since a re-calibration of the tracks considering a secondary vertex (trademark of B decays) improves significatively the resolution of the kinematic variables of the B hadrons and its decay products.

Therefore, customized NanoAODs were produced by including the information on the kinematic vertex fits to secondary vertices. An example of this was the BParking NanoAOD which was used for the CMS measurement of the LFU test on the R_K. The BParking dataset was stored in 2018 using the parking strategy, meaning that it was collected during 2018 and processed afterward. The paths used to collect this dataset were single muon paths with thresholds in the transverse momenta and on the significance of the impact parameter.

During Run 3, the CMS experiment implemented an additional data collection strategy known as Scouting. This approach stores reduced event information with a resolution comparable to the HLT. For B-Physics studies, both Parking and Scouting for B-Physics was driven by three sets of triggers based on single, double and triple muon paths. The core of the Run 3 datasets consists of dimuon events, as illustrated in Figure 3.11, which shows the expected dimuon contributions to the dataset for the three main trigger paths.

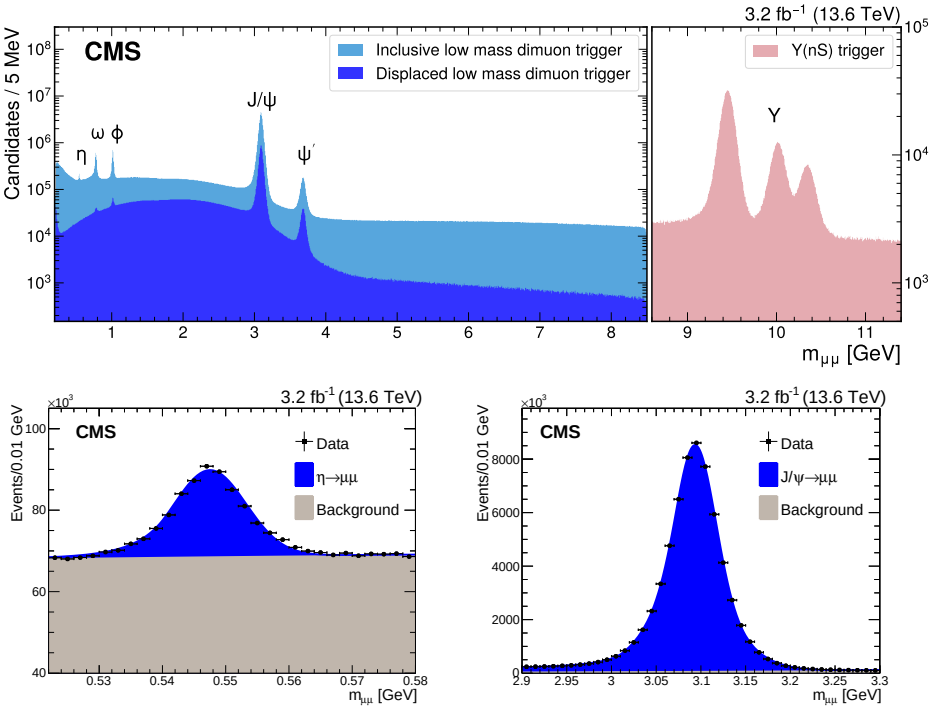

Figure 3.11: Dimuon mass spectra obtained from data recorded in 2022 during Run 3, corresponding to $L_{int} = 3.2$ fb^{-1}. In the range $2m_{\mu}^{PDG} < m_{\mu\mu} < 8.5$ GeV, the light blue distribution represents the subset of dimuon events triggered by the inclusive low-mass trigger algorithm, while the dark blue distribution shows the subset of dimuon events triggered by the displaced low-mass trigger path. These two paths work as the main triggers for B-Physics during Run3. In the range $8.5 < m_{\mu\mu} < 11.5$ GeV, dimuon events are instead triggered by the HLT paths targeting the $\Upsilon(nS)$ resonances, which are shown by the pink distribution. On the bottom we show the dimuon invariant mass distributions in the η (left) and J/Ψ (right) mass regions, as obtained from data recorded by the inclusive low-mass dimuon trigger algorithm. [63]

Chapter 4

Search for nuclear modification of the B^+ meson production in pPb collisions at $\sqrt{s_{NN}} = 8.16$ TeV

4.1 Introduction

This chapter describes the use of the $B^+ \to K^+ J/\psi(1S)$decay as a probe for nuclear modifications in pPb collisions. Small collision systems such as pPb and pp, are being studied to understand the collective effects observed in heavy ion collisions. In this analysis, events are categorized by their charged-particle multiplicity. While previous studies have reported a monotone dependency between centrality and charged-particle multiplicity [64], in the present analysis, we define an observable, R_{HL}, to quantify the effect of the B meson production across low to high multiplicity classes.

The R_{HL} observable is a ratio of the cross-sections for low to high multiplicity classes. In this case, the numerator and denominator are scaled with the corresponding number of binary nucleon-proton collisions. This scaling allows us to benchmark medium effects to an independent superposition of nucleon-proton collisions. While the number of binary nucleon collisions is typically estimated by the Glauber model, the present analysis implements a novel approach based on the production of the Z^0 boson in the same events. This approach relies on the lack of charge color of the Z^0 boson; since it is not strongly interacting, the presence of a medium should not modify its production in different multiplicity classes. Therefore, it provides an effective measure of the ratio of the average number of binary collisions for the corresponding multiplicity classes.

The selection of events, extraction of yields, and evaluation of the cross-section of the B^+ and Z^0 production, as well as the measurement of the R_{HL} observable are described in the following sections. In addition, we discuss the different sources of uncertainty affecting this measurement, providing a unique measurement of nuclear modifications without input from Glauber model.

4.2 Motivation

In the presence of extreme density or temperatures, Quantum Chromodynamics (QCD) matter could transition into a different state of matter broadly called the quark-gluon plasma (QGP) [6, 7]. Within this state, quarks and gluons, traditionally confined within particles such as protons and neutrons, become "deconfined". They are no longer bound and can move freely resulting in the formation of a highly energetic and dense medium characterized by strong interactions.

The long-held view that the quark-gluon plasma could only be formed in heavy-ion collisions faces a significant challenge. Recent observations of phenomena typically associated with QGP, such as elliptic flow and long-range correlations, in smaller systems like pPb and even pp collisions, force us to re-evaluate our understanding of collectivity generation in these systems [65–69].

There are recent measurements in high-multiplicity pPb collisions that exhibit strong collective flow, similar to what is observed in heavy-ion collisions [70, 71]. This suggests that collectivity might emerge under specific conditions even in smaller collision systems, potentially due to the creation of a localized, hot, and dense system – a "mini-QGP" [72, 73]. However, definitively determining the nature of this hot, dense system, if any, formed in high-multiplicity pPb collisions needs further investigation.

Heavy quarks, with their unique properties, are invaluable tools for studying QGP [74–76]. Produced early in the collision, they experience the entire lifetime of the medium, allowing them to probe its properties throughout its evolution.

Their large mass minimizes distortions arising from final-state interactions with other particles. Additionally, perturbative QCD enables precise calculations of their initial production rates. By studying how the medium affects heavy quarks (energy loss, fragmentation), the properties of the medium can be determined.

The b hadron production cross-section measurements from the LHCb experiment in pPb collisions reveal a suppression of b hadron production compared to pp collisions [77].

These measurements suggest an influence from the nuclear environment on their production mechanism.

This chapter explains the measurement of the differential production cross-section of the B^+ meson as a function of the meson transverse momentum (p_T), and for events with different charged-particle multiplicities. In addition, it presents a measurement of the ratio of nuclear modification factors ($R_{\rm pPb}$) for different multiplicity classes. In this analysis, we measure the differential cross-sections of B^+ states, which are given by

$$\frac{d\sigma}{dp_T} = \frac{1}{2}\frac{1}{\Delta p_T}\frac{N(p_T)}{\epsilon\,\mathcal{B}\mathcal{L}}\,, \text{ and} \tag{4.1}$$

$$\frac{d\sigma}{dp_T|_{(N_{trk})}} = \frac{1}{2}\frac{1}{\Delta p_T}\frac{N(p_T, N_{\rm trk})}{\epsilon\,\mathcal{B}\mathcal{L}}\,, \tag{4.2}$$

where $N(p_T)$ and $N(p_T, N_{\rm trk})$ are the measured yields of the B^+ meson as function of p_T and the charged-particle multiplicity. $\mathcal{B}$ is the product of the world-average results for the $B^+ \to K^+ J/\psi(1S)$and $J/\Psi \to \mu^+\mu^-$ branching fractions, $(1.026 \pm 0.031) \times 10^{-3}$ and $(5.961 \pm 0.033) \times 10^{-2}$ [78], respectively. ϵ is the total efficiency for B^+ candidates. $\mathcal{L}$ is

the integrated luminosity. The factor of two in the denominator reflects the choice used to quote the cross-section for a single charge (taken to be the B^+), whereas $N(p_T)$ includes both charge states. The yields of the B^+ meson (charge conjugate states are assumed throughout this note) candidates are extracted using an unbinned maximum-likelihood fit to the reconstructed invariant mass distributions. The cross sections are measured in bins of transverse momentum, in different charged-particle multiplicity. We use the decay mode $B^+ \to K^+ J/\psi(1S)$, with $J/\Psi \to \mu^+\mu^-$.

The inclusive measured differential cross section $d\sigma/dp_T$ is compared to Fixed Order Next-to-Leading Log (FONLL) calculations [79–81].

The effect of the nuclear medium on B^+meson production is examined through the R_{HL} variable conceptually defined as:

$$R_{HL} = \frac{\langle N_{coll}\rangle|_{low}}{\langle N_{coll}\rangle|_{high}} \frac{(d\sigma/dp_T)|_{high}}{(d\sigma/dp_T)|_{low}}, \tag{4.3}$$

where, $\langle N_{coll}\rangle$ is the average number of incoherent nucleon-nucleon collisions in the events of a certain multiplicity class, $d\sigma/dp_T$ is the differential cross section as a function of the p_T at high (numerator) and low (denominator) multiplicity.

Since the production of the Z bosons is expected to scale with the number of binary collisions and be void of final-state medium effects, the ratio of Z boson cross section in the same high- and low-multiplicity event classes provides experimental means to determine the scaling factor of Eq. 4.3. The experimental equivalent of Eq. 4.3 can be expressed as:

$$R_{HL} = \frac{(d\sigma^{B^+}/dp_T)|_{high}}{(d\sigma^{B^+}/dp_T)|_{low}} \Bigg/ \frac{(d\sigma^{Z}/dp_T)|_{high}}{(d\sigma^{Z}/dp_T)|_{low}} \tag{4.4}$$

with $d\sigma/dp_T$ for the Z bosons measured from the same pPb data set.

The measurement uses events produced in pPb collisions at a center-of-mass energy of $\sqrt{s} = 8.16$ TeV. This sample was collected by the CMS experiment in 2016, corresponding to an integrated luminosity of $175nb^{-1}$ [82].

4.3 Data samples

For this analysis, we use data corresponding to the 2016 pPb collisions. The primary dataset is called PADoubleMuon, which was collected with a set of double muon HLT paths. In particular, we used the data collected by the HLT_PAL1DoubleMuOpen_v1 trigger. This trigger path is seeded by an L1 algorithm that only requires two L1 muons with a minimal requirement on the quality of the pattern of hits in the muon chambers. The requirements at the HLT level are very soft, requiring both muons to be inside the detector acceptance region: $|\eta| < 2.5$, finally, during the data-taking period, this path was run un-prescaled, meaning that it stored the entirety of events that it accepted.

We used the prompt reconstruction processing (PARun2016C-PromptReco-v1) in the AOD format: /PADoubleMuon/PARun2016C-PromptReco-v1/AOD. The dataset was processed using CMSSW_8_0_30 and the offline Global Tag 80X_dataRun2_v19. The luminosity sections were selected based on the certified list; and validated by the different

Detector Performance Groups (DPGs) and Physics Object Groups (POGs), through the use of JSON files:

- /afs/cern.ch/cms/CAF/CMSCOMM/COMM_DQM/certification/Collisions16/13TeV/HI/Cert_285479-285832_HI8TeV_PromptReco_pPb_Collisions16_JSON_NoL1T_MuonPhys.txt,
  for the pPb collision runs (285952-286496)
- /afs/cern.ch/cms/CAF/CMSCOMM/COMM_DQM/certification/Collisions16/13TeV/HI/Cert_285952-286496_HI8TeV_PromptReco_Pbp_Collisions16_JSON_NoL1T_MuonPhys.txt,
  for the Pbp collision runs (285479-285832).

Table 4.1 lists the integrated luminosity (L_{int}) recorded for the trigger, and computed with the CMS official tool, `brilcalc`.

Table 4.1: Integrated luminosity.

Year	Collision	L_{int} nb^{-1}
2016	pPb	62.65
2016	Pbp	111.92
	Total luminosity	174.57

4.3.1 Monte Carlo

The simulation, or Monte Carlo, samples used in this analysis followed the same reconstruction steps as the data in $pPb(Pbp)$ collisions. The intented use for the simulation samples is two-fold: to study the efficiencies, *e.g.* reconstruction and selection, and to perform cross-checks of potential detector effects.

Monte Carlo (MC) samples of $pPb(Pbp)$[1] collisions are generated in this analysis for efficiency studies, analysis selection, and cross-checks of other potential detector effects. The simulation samples are of three different types: the minimum bias hadronic interactions in heavy ions are modeled by EPOS, important to obtain a more realistic number of charged particles in heavy-ion, or small systems, collisions. The signal sample is $B^+ \to J/\Psi(\mu^+\mu^-)K^+$, needed to obtain signal efficiencies. Finally, a partially reconstructed background is modeled with Non-prompt J/Ψ samples. The samples are produced with the detector conditions during the collection of data, and are listed in Table 4.2 below.

4.4 Signal reconstruction and selection

The B meson candidates are reconstructed by combining selected muons coming from the J/Ψ decay with a track. In the following, we describe the event selection requirements, for tracks, muons, and J/Ψ selection, as well as the process to reconstruct B^+ candidates.

[1] Although we have two datasets one with collisions pPb and another with Pbp, we refer to both with pPb as it is done in the other analyses.

Table 4.2: MC samples for 8.16 TeV *pPb* and *Pbp* collisions with EPOS generator.

Generator	Dataset
EPOS	/ReggeGribovPartonMC_EposLHC_pPb_4080_4080_DataBS/pPb816Summer16DR-MB_80X_mcRun2_pA_v4-v2/AODSIM
EPOS	/ReggeGribovPartonMC_EposLHC_PbP_4080_4080_DataBS/pPb816Summer16DR-MB_80X_mcRun2_pA_v4-v2/AODSIM
PYTHIA+EVTGEN	/BPlusToJpsiK_pThat5_pPb-Embed_8p16TeV_TuneCUETP8M1_Pythia8_EvtGen/pPb816Summer16DR-80X_mcRun2_pA_v4-v2/AODSIM
PYTHIA+EVTGEN	/BPlusToJpsiK_pThat5_Pbp-Embed_8p16TeV_TuneCUETP8M1_Pythia8_EvtGen/pPb816Summer16DR-80X_mcRun2_pA_v4-v2/AODSIM
PYTHIA+EVTGEN	/NonPromptPsi1S2S_pPb-EmbEPOS_8p16TeV_Pythia/pPb816Summer16DR-pPbEmb_80X_mcRun2_pA_v4-v2/AODSIM
PYTHIA+EVTGEN	/NonPromptPsi1SPsi2S_PbP-EmbEPOS_8p16TeV_Pythia/pPb816Summer16DR-PbPEmb_80X_mcRun2_pA_v4-v2/AODSIM

4.4.1 Event selection

There are several background sources to the inelastic hadronic collisions. Examples of this background are beam-gas collisions and beam-scraping events, as well as ultra-peripheral collisions, which are dominated by electromagnetic interactions. To remove those sources of background, several offline selections are applied to each event:

- `Primary Vertex Filter`: Events are required to have at least one reconstructed primary vertex. The primary vertex is formed by two or more associated tracks and is required to have a distance from the nominal interaction region of less than 25 cm along the beam axis and less than 2 cm in the transverse plane.

- `Beam-scraping Filter`: the beam scraping background events are characterized by large multiplicities observed in the tracker without any sign of a common origin of the tracks within the CMS Detector. The filter removes events where the number of reconstructed tracks, passing the high-purity requirement, is larger than 10, but the fraction of good-quality tracks is lower than 25%.

- `Offline HF coincidence`: at least one tower on each side of the forward calorimeters with energy greater than 3 GeV/c.

- `Overlapping Vertex Filter`: applied to reduce the contamination from multiple interactions per bunch crossing, the filter was produced, studied, and recommended by the Heavy Ion Tracking Group. Given an order of the primary vertices by their number of associated tracks, this filter imposes conditions on the distance between the first to the second primary vertices (dz=1.0 cm). The track content of the second primary vertex must be grater than a threshold, which varies inversely with dz; 4-22 tracks, 1.0-0.0 cm [83]. The filter name is "olvFilter_pPb8TeV_dz1p0".

4.4.2 Muon selection

Acceptance

The muons are selected with the acceptance cuts defined by the double muon trigger (HLT_PAL1DoubleMuOpen_v1).

The acceptance region is defined by the blue line in Fig. 4.1 and described in Table 4.3.

$\lvert\eta\rvert$	p_T [GeVc]
$0 < \lvert\eta\rvert < 0.3$	$p_T > 3.4$
$0.3 < \lvert\eta\rvert < 1.1$	$p_T > 3.3$
$1.1 < \lvert\eta\rvert < 2.1$	$p_T > 5.5 - 2\lvert\eta\rvert$
$2.1 < \lvert\eta\rvert < 2.4$	$p_T > 1.3$

Table 4.3: Muon acceptance

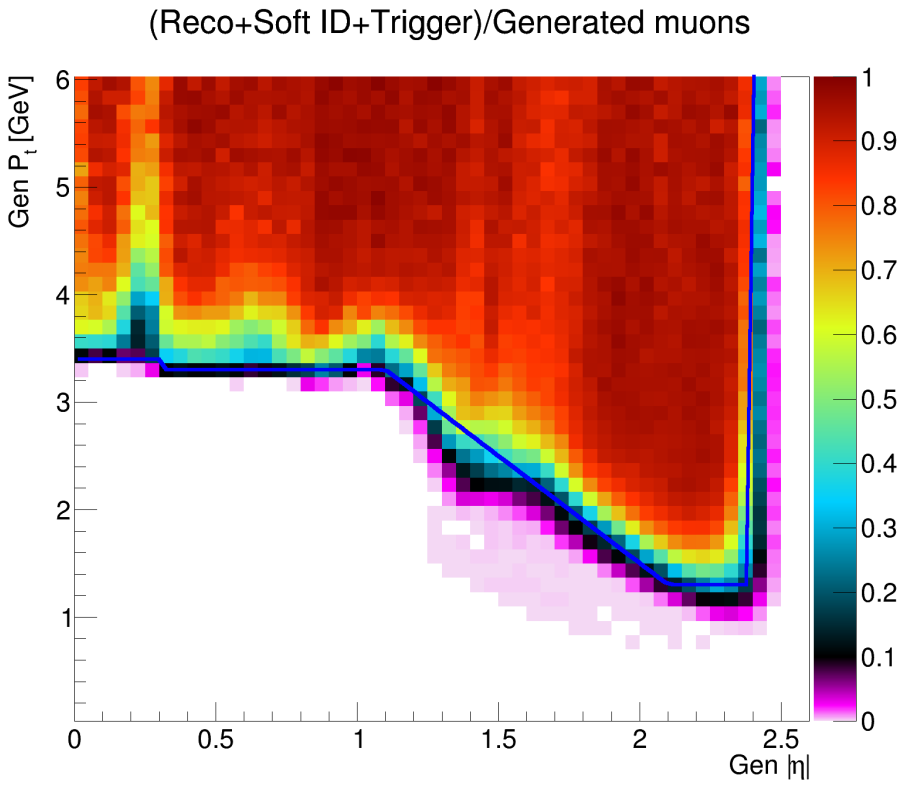

Figure 4.1: Muon acceptance cut for the analysis (blue line).

Muon ID

The *Soft Muon* selection, approved by the Muon-POG, uses the following requirements: the track identified by the tracker is matched with at least one segment in any muon station, in both x and y coordinates (*TMOneStationTight*); the track needs to qualify as *high-purity* and must include more than five hits in the tracker layers, at least one of them being in a pixel layer; the impact parameter of the single muons, with respect to the primary vertex, must be smaller than 0.3 cm in the transverse plane, and smaller than 20 cm along the beam axis.

The offline reconstruction requires two oppositely charged muons matching those that triggered the detector readout.

4.4.3 J/Ψ selection

Opposite charge pairs of muon candidates are combined to form the J/Ψ candidates, which are selected in the analysis if they have an invariant mass between 2.9 and 3.3 GeV, and absolute rapidity of less than 2.4. The dimuon vertex fit must have a χ^2 probability larger than 1%. The mass distributions for different p_T bins are shown in Fig.4.2.

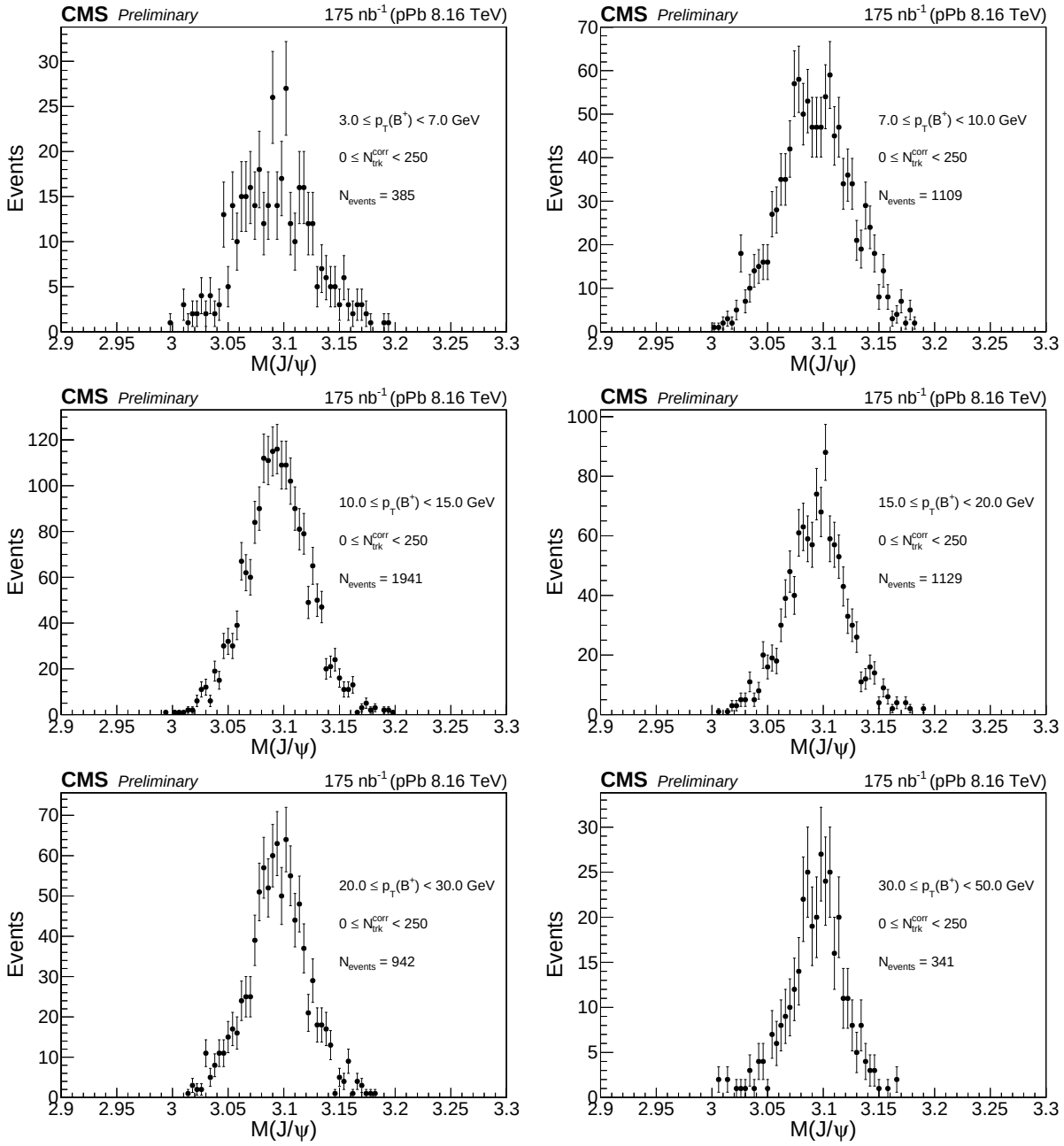

Figure 4.2: J/Ψ mass distribution for the different p_T bins.

4.4.4 B^+ selection

The B^+ candidates are reconstructed by combining the dimuon with a track, assumed to be a kaon.

As the muons are those that triggered the detector readout, there is only a J/Ψ candidate per event and all the multiplicity of B^+ candidates comes from the additional track (kaon). Hereafter, this track is denoted as K^+ for the $B^+ \to K^+ J/\Psi$ decay mode. Only tracks that pass *high-purity* requirements are used.

The B^+ candidate is obtained by performing a kinematic fit, constraining the dimuon invariant mass to be the world-average J/Ψ mass [78], and then imposing a common vertex on the dimuon and kaons tracks. The primary vertex (PV) with the highest multiplicity is used as recommended by HIN group [84].

The transverse decay length of the B hadron is computed as the distance between the PV and the B hadron vertex (assumed to be, respectively, the B meson production and decay vertices).

The chosen PV is refitted removing all tracks from the B candidate, if they were associated with the PV.

The charged tracks, K^+, are required to have at least 11 tracker hits (strips and pixels together), relative uncertainty on the track p_T, (trkPtError/trkPt) < 0.1, and must have $|\eta| < 2.4$, and p_T of the charged tracks K^+ have to be greater than 1.0 GeV. The p_T of the B hadrons is required to be between 3 and 50 GeV.

The B hadrons must have a rapidity of $|y| < 1.8$, a decay length larger than seven times its uncertainty, and a vertex χ^2 probability greater than 7%. When multiple B hadron candidates are found in the same event, only the one with the highest fit χ^2 probability is selected (using MC, it was found that the probability of picking the correct candidate based on the highest χ^2 probability is correct approximately 98% of the times).

The selection criteria are optimized using the figure of merit of the significance $efficiency/\sqrt{Background}$, which does not rely on signal normalization.

Events from sidebands in data are used to estimate the background, and the $B^+ \to K^+ J/\Psi$ simulated sample is used to measure the signal reconstruction efficiency.

The mass distributions of the B meson candidate for different p_T bins are shown in Fig.4.3.

4.4.5 Z boson selection

The Z boson reconstruction and selection requirements, which were followed from Ref. [63], required a pair of opposite sign Tight ID muons, with p_{T} greater than 15 GeV for the leading muon (*i.e.* with the highest p_{T}), and greater than 10 GeV to the other. A kinematic vertex fit is done to the muon pair. The χ^2 of the fit divided by the number of degrees of freedom must be smaller than 20, this ensures that the two tracks originate from the same vertex, thus reducing the contribution from non-compatible muons.

To suppress the background contributions due to muons originating from hadrons, muons are required to be isolated, based on the p_{T} sum of the charged-particles tracks around the muon. Isolations sums are evaluated in the (η, ϕ) plane around the lepton candidate with

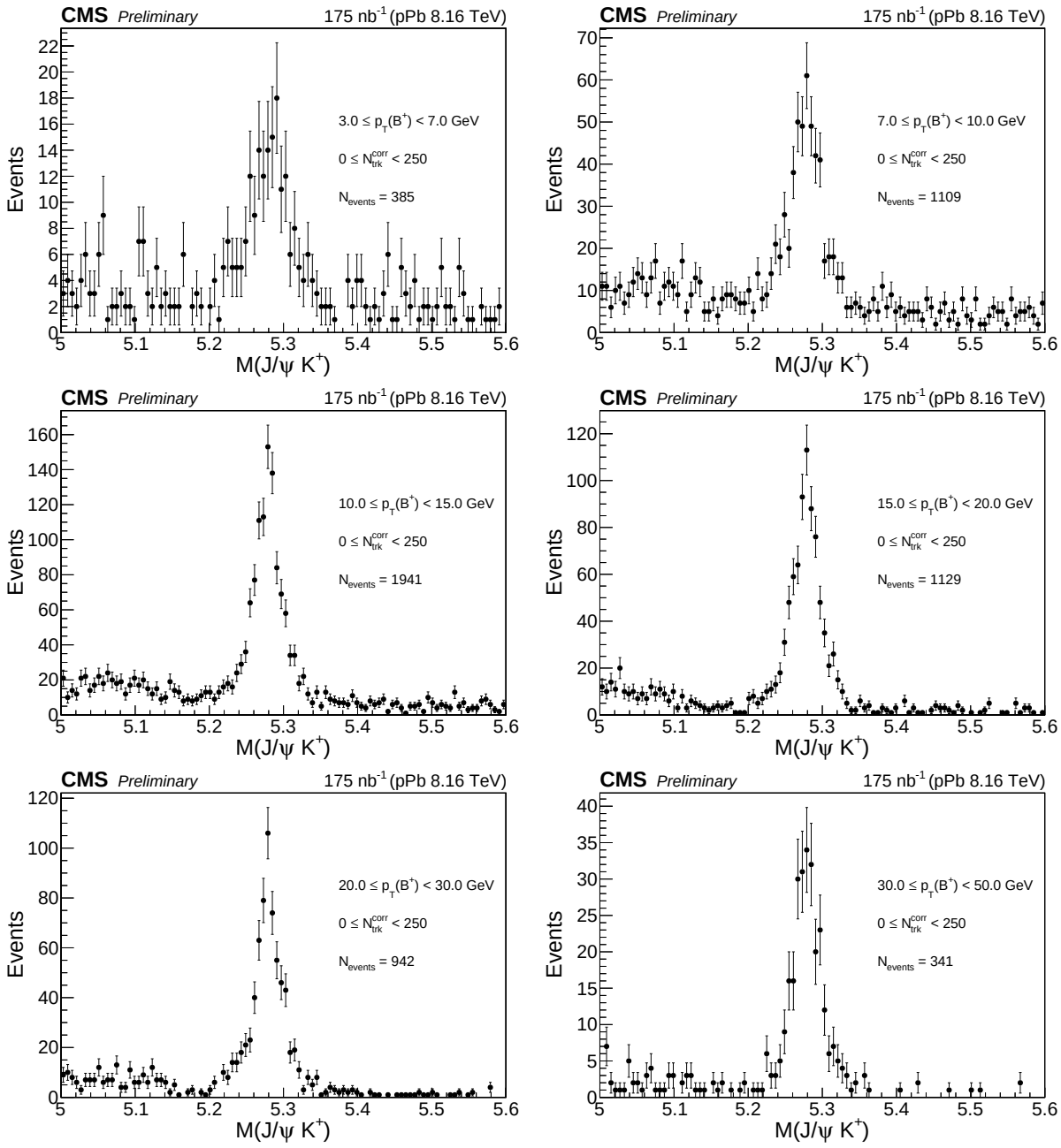

Figure 4.3: $J/\Psi K^+$ mass distribution for the different p_T bins.

$\Delta R < 0.3$. The relative isolation I_{rel}, obtained by dividing this isolation sum by the muon p_{T} is required to be below 0.2.

Finally, the contribution from lepton pairs produced through photon interactions is reduced by requiring at least one HF calorimeter tower with more than 3 GeV of total energy on either side of the interaction point.

4.4.6 Signal Extraction using unbinned maximum likelihood estimations

The B^+ yields are extracted using unbinned maximum likelihood estimations to the reconstructed $J/\Psi K^+$ invariant mass distributions. The default fit function for the signal is the sum of two Gaussian functions with a common mean and different widths. The widths are fixed to the values obtained from a fit performed to the $J/\Psi K^+$ invariant mass in the pure-signal MC sample. The default fit function for the combinatorial background is an exponential function. The $J/\Psi K^+$ invariant mass distribution has an additional background contribution; the partially reconstructed $B^+ \to J/\Psi K^+ X$ decays that contribute to the left part of the $J/\Psi K^+$ invariant mass distribution are modeled with an error function, its parameters are fixed to the values obtained from a fit performed to the invariant mass distribution in the non-prompt J/Ψ MC sample.

The dataset is examined both with respect to transverse momentum and multiplicity. The binning was chosen to have enough data for a robust maximum likelihood estimation and to have similar statistical uncertainties as much as possible. The distributions and the results of each fit are shown in the next subsections. The numerical results from the fits can be seen in Table 4.8.

4.4.7 Invariant mass distributions on Transverse Momentum Bins

In order to perform the measurement of cross sections as a function of transverse momentum, yields must be extracted in the corresponding bins. The bins used to examine the p_T dependence of the yields are defined by the boundaries of: 3, 7, 10, 15, 20, 30, and 50 GeV . In Fig.4.4 the $J/\Psi K^+$ mass distribution and the pulls of the fit for all p_T bins are displayed. Besides, in Fig. 4.5 the $J/\Psi K^+$ mass distribution and the pulls of the fit for all multiplicity classes are displayed.

4.4.8 Definition of charged-particle multiplicity

The charged-particle multiplicity is the average number of charged particles produced in a collision. In the simulation, at the generation level, the charged-particle multiplicity ($N_{\rm trk}^{\rm gen}$) is defined as charged stable particles with $|\eta| < 2.4$ and $p_T > 0.4\,\text{GeV}$. In data and the simulation after reconstruction of generated events, the charged-particle multiplicity $N_{\rm trk}$ is defined using primary tracks, i.e., tracks coming from the PV and satisfying the high-purity criteria [85]. To improve track quality and ensure the primary tracks, the following is required: impact parameter significance less than 3, measured with respect to the PV, both along the beam axis, $d_z/\sigma(d_z)$, and transverse, $d_T/\sigma(d_T)$, to the beam direction; relative p_T uncertainty, $\sigma(p_T)/p_T$, must be less than 10%; and to ensure high tracking efficiency and to reduce the rate of misreconstructed tracks, $|\eta| < 2.4$ and $p_T > 0.4\,\text{GeV}$. Figure 4.7 shows the $N_{\rm trk}$ distribution of the events selected in this analysis.

Track reconstruction implies that the detector effect is present, so to get the actual number of charged particles a tracking efficiency correction is needed. Then each reconstructed track is weighted by the inverse of the efficiency factor, $\epsilon_{\rm trk}(\eta, p_T)$, as a function of the track pseudorapidity and transverse momentum. The efficiency weighting factor accounts

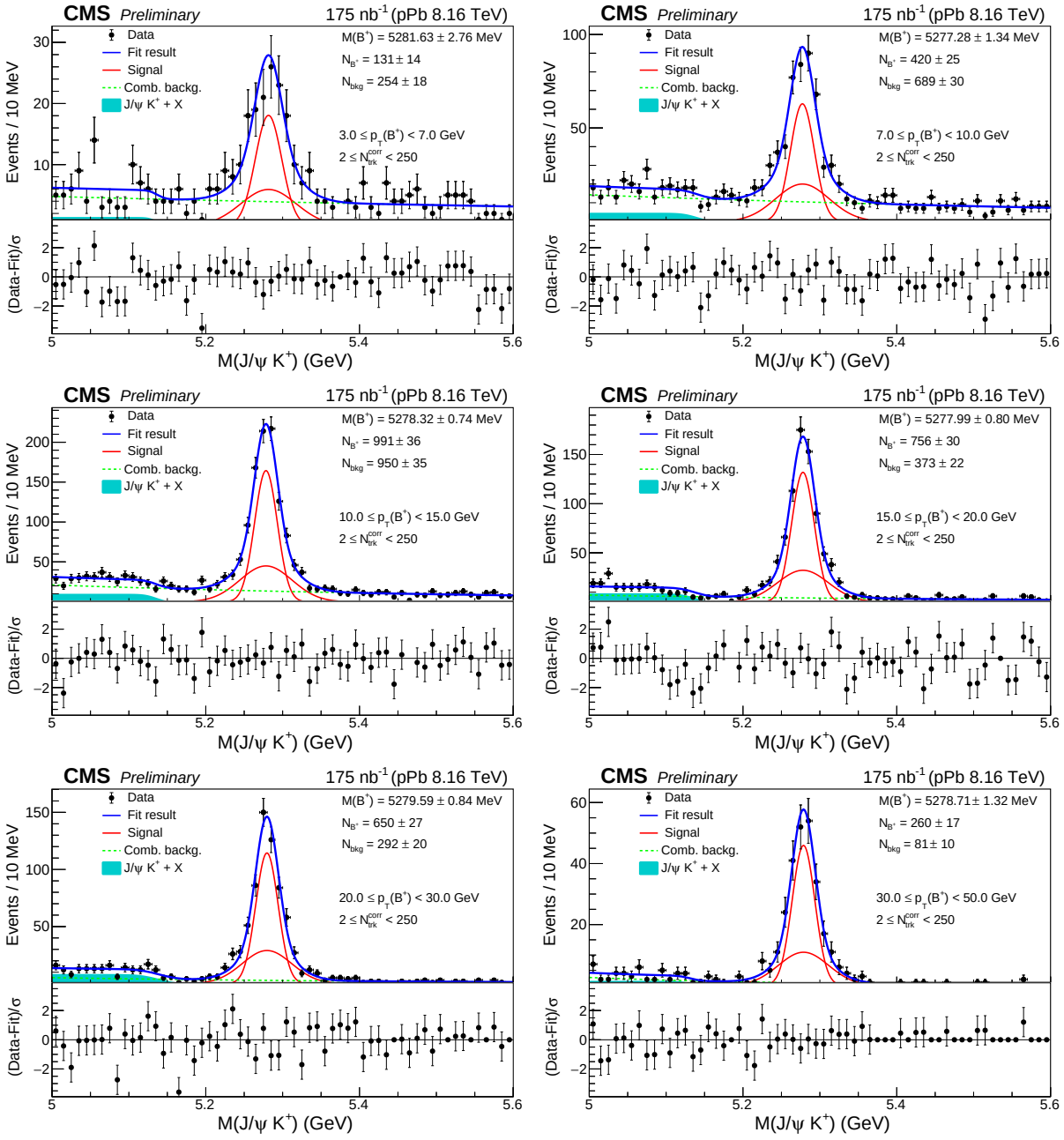

Figure 4.4: Fits performed to the B^+candidates in transverse momentum bins. The signal is modeled with the sum of two Gaussian functions with a common mean and different widths. The combinatorial background component is fit to an exponential distribution, this component tends to drop at increasing p_T . The contribution of partially reconstructed decays is modelled by an error function.

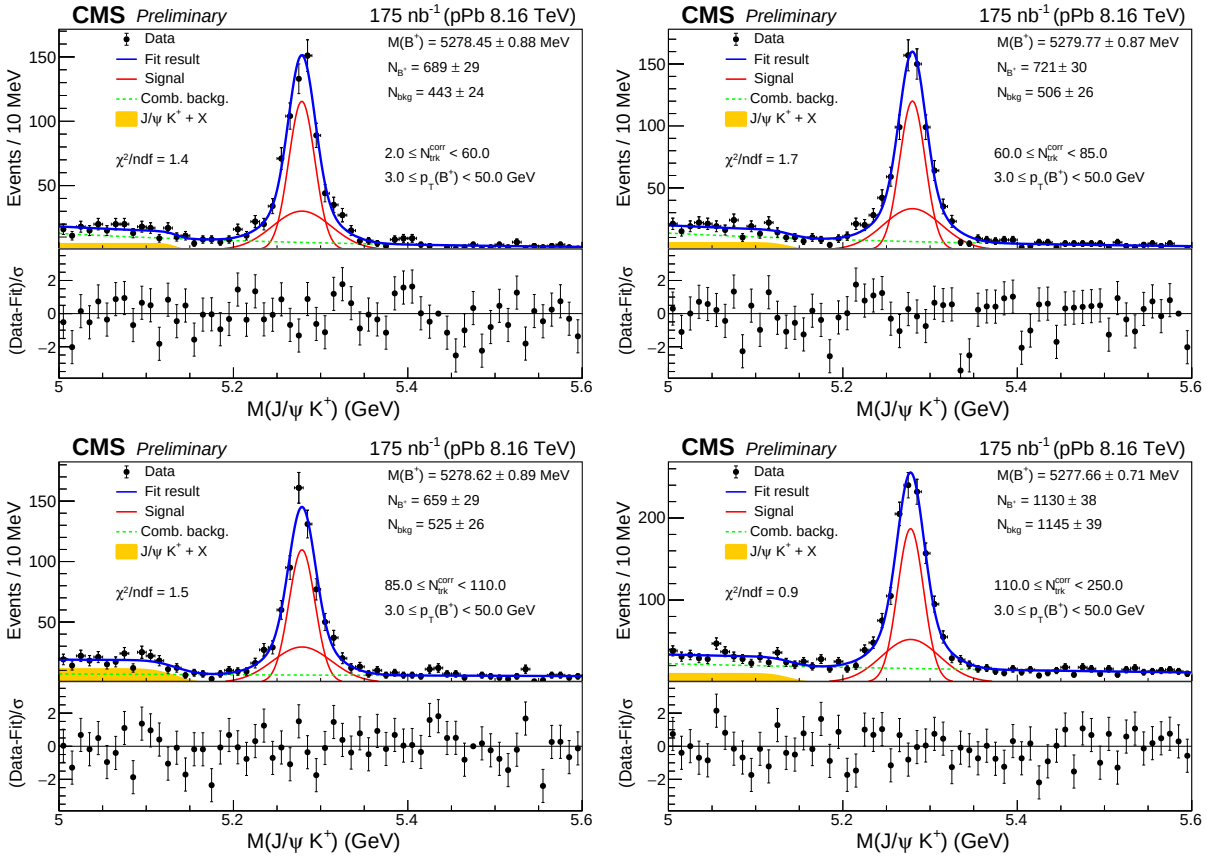

Figure 4.5: Fits performed to the B^+candidates in multiplicity classes. The signal is modeled with the sum of two Gaussian functions with a common mean and different widths. The combinatorial background component is fit to an exponential distribution. The contribution of partially reconstructed decays is modeled by an error function.

for the detector acceptance $A(\eta, p_{\mathrm{T}})$, the reconstruction efficiency $E(\eta, p_{\mathrm{T}})$, and the fraction of misidentified tracks or the fake rate, $F(\eta, p_{\mathrm{T}})$,

$$\epsilon_{\mathrm{trk}}(\eta, p_{\mathrm{T}}) = \frac{AE}{1-F}\,, \tag{4.5}$$

where E is the ratio of reconstructed tracks associated to simulated tracks (simulated in GEANT) over the total number of simulated tracks, *recoToSimTracks/SimTracks*; F is the ratio of reconstructed tracks not associated with simulated tracks over the total number of reconstructed tracks *NotRecoToSimTracks/recoTracks*. To compute these ratios we use a private MC sample with the same conditions as the official one, we consider the *general-tracks* collection, and the CMSSW tools `associateRecoToSim` and `associateSimToReco` [86].

Finally for each (η, p_{T}) bin, we count the numbers *recoToSimTracks/SimTracks* or *NotRecoToSimTracks/recoTracks* for $E(\eta, p_{\mathrm{T}})$ and $F(\eta, p_{\mathrm{T}})$, respectively. The details on the studies of $\epsilon_{\mathrm{trk}}(\eta, p_{\mathrm{T}})$ have been documented in Refs. [87, 88], and they are not repeated in this note, since it follows the same prescription. Figure 4.6 shows the reconstruction efficiency and the fraction of misidentified tracks as a function of η and p_{T} of each track.

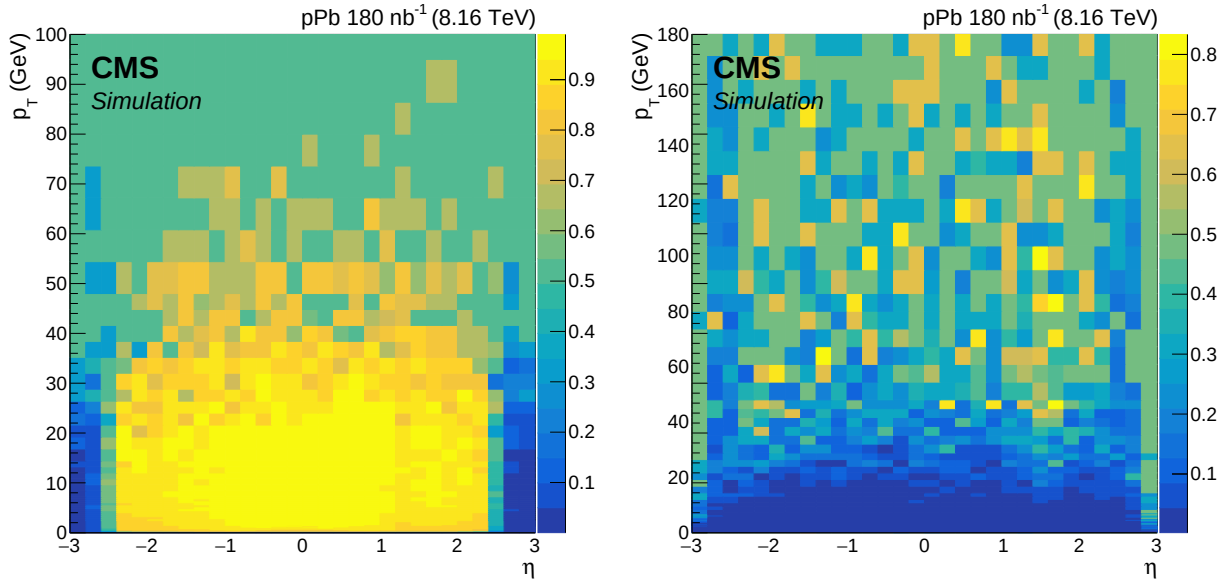

Figure 4.6: Reconstruction efficiency $E(\eta, p_{\mathrm{T}})$ (left) and the fraction of misidentified tracks $F(\eta, p_{\mathrm{T}})$ (right). The values were computed from MC samples.

In this method, GEANT runs on all generator-level particles satisfying minimal cuts on their p_{T} and the distance of their decay vertex from the beam line. The resulting tracks, plus any additional ones produced by GEANT (due to material interactions or K^0 decays etc.), are compared to the hits associated with the track itself at RECO level. The technique leaves a limitation on the method, not all true charged particles can be associated with a track detected in the tracker, however, the method is efficient enough to capture most charged particles.

Data are divided into classes based on $N_{\rm trk}$. The quantity $N_{\rm trk}^{\rm corrected}$is the corresponding multiplicity corrected in the same kinematic region ($|\eta| < 2.4$ and $p_{\rm T} > 0.4$). The fraction of the total multiplicity found in each interval and the average number of tracks both before and after accounting for the corrections are listed in table 4.4. Figure 4.8 shows the compatibility of the two distributions, pPb and Pbp data samples, with a Kolmogorov-Smirnov test. The uncertainty in the corrected average value is evaluated from the uncertainty in the tracking efficiency, which is 2.4% [89, 90]. In addition, comparison for $N_{\rm trk}$, $N_{\rm trk}^{\rm corrected}$ and $N_{\rm trk}^{\rm gen}$, in both MC samples pPb (left) and Pbp (right), are shown on Fig. 4.9.

Table 4.4: Fraction of the full event sample for each multiplicity class. The last two columns show the observed and corrected multiplicities, respectively, of charged particles with $|y| < 2.4$ and $p_T > 0.4$ GeV/c. Systematic uncertainties are given for the corrected multiplicities, while statistical uncertainties are negligible.

Multiplicity class (N_{trk})	Fraction(%)	N_{trk}	$N_{trk}^{corrected}$
$2 \leq N_{trk} < 250$	100.0	88	102 ± 2
$2 \leq N_{trk} < 60$	27.5	42	49 ± 1
$60 \leq N_{trk} < 85$	24.1	72	84 ± 2
$85 \leq N_{trk} < 110$	20.6	96	112 ± 3
$110 \leq N_{trk} < 250$	27.7	140	163 ± 4

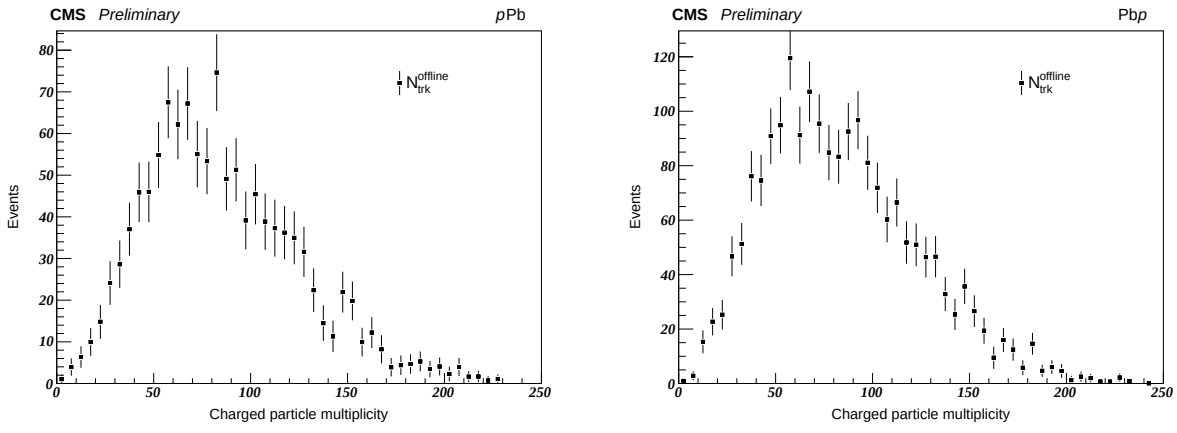

Figure 4.7: $N_{\rm trk}$ distribution of the events selected in this analysis, for pPb (left) and Pbp (right) samples.

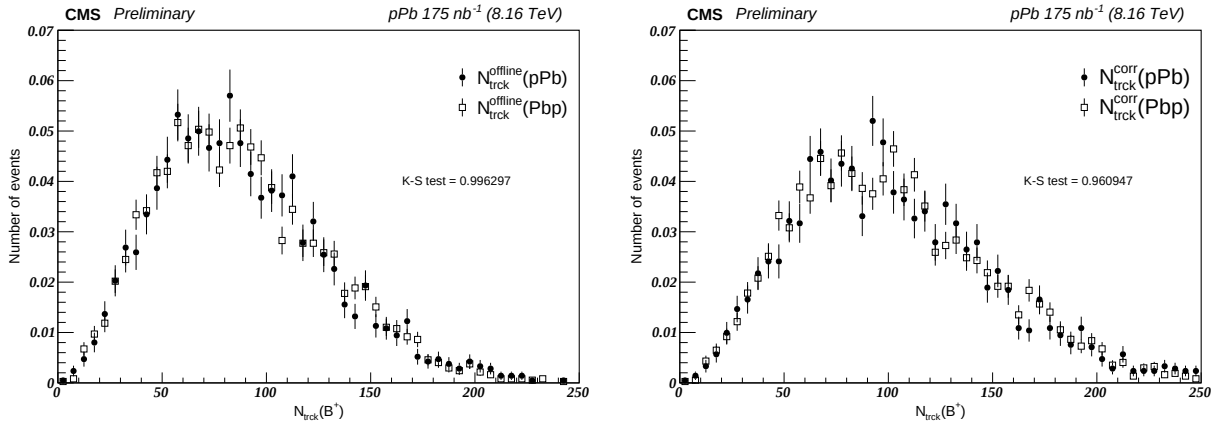

Figure 4.8: N_{trk} distribution of the events selected in this analysis, for pPb and Pbp , both before (left) and after (right) accounting for the corrections.

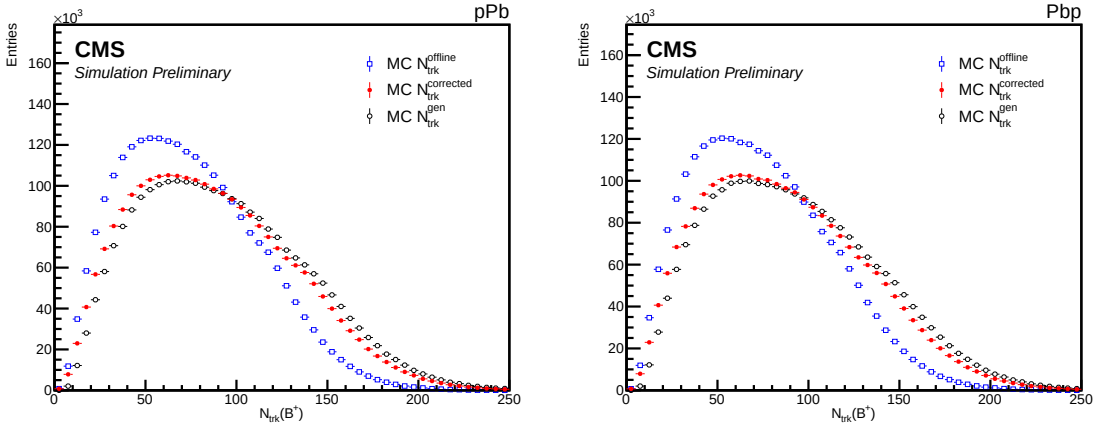

Figure 4.9: Number of tracks distribution showing N_{trk}, $N_{\mathrm{trk}}^{\mathrm{corrected}}$ and $N_{\mathrm{trk}}^{\mathrm{gen}}$ in both MC samples pPb (left) and Pbp (right).

During the analysis review, it was recommended by the spectra group to compare the observed and corrected multiplicity with HIN-21-012 analysis which uses the same dataset. We changed our multiplicity of classes to allow a direct comparison. The statistical uncertainties have been not considered. Except for the lowest multiplicity class, where the statistical uncertainty could be relevant, we observe that $N_{\mathrm{trk}}^{\mathrm{corrected}}$ are compatible within errors for both analyses as shown in table 4.5.

Table 4.5: Observed and corrected charged-particle multiplicity with tracks satisfying $|y| < 2.4$ and $p_T > 0.4$ GeV/c. Systematic uncertainties are given for the corrected multiplicities, while statistical uncertainties are negligible.

	B meson RpA results		HIN-21-012 results	
Multiplicity class (N_{trk})	N_{trk}	$N_{trk}^{corrected}$	N_{trk}	$N_{trk}^{corrected}$
$2 < N_{trk} \leq 20$	15	18 ± 0.4	12	11 ± 0.4
$20 < N_{trk} \leq 40$	32	38 ± 1	36	36 ± 1
$40 < N_{trk} \leq 60$	51	60 ± 1	60	60 ± 1
$60 < N_{trk} \leq 80$	70	82 ± 2	82	82 ± 2
$80 < N_{trk} \leq 100$	90	105 ± 3	105	107 ± 3
$100 < N_{trk} \leq 150$	122	142 ± 3	137	140 ± 2
$150 < N_{trk} \leq 200$	168	196 ± 5	191	198 ± 5
$200 < N_{trk} \leq 250$	213	248 ± 6	246	256 ± 6

4.4.9 Distributions on Transverse Momentum and Multiplicity Classes

Multiplicity classes are defined by the boundaries at values: 2, 60, 85, 110, and 250. In Figs. 4.10, 4.11, 4.12, and 4.13 the $J/\Psi K^+$ mass distribution and the pulls of the fit in all p_T and multiplicity classes are displayed.

4.5 Data and Monte Carlo comparison

4.5.1 Tag & Probe Corrections

We improve the efficiency by using a data-driven method of Tag and Probe (TnP) and scale factors (SFs), which are derived from the efficiency ratio between the data and the MC in the J/ψ analysis for each muon (https://twiki.cern.ch/twiki/bin/viewauth/CMS/HIMuonTagProbe).

The TnP SFs are applied as a weight to MC RECO candidates in order to correct the efficiency. In this analysis, we use the 2016 pPb TnP header file located at this github repository: https://github.com/CMS-HIN-dilepton/MuonAnalysis-TagAndProbe/blob/80X_HI/macros/tnp_weight_lowPt.h, which is used to determine the SF of each MC muon based on its kinematics (p_T and η).

Then, we multiply them together:

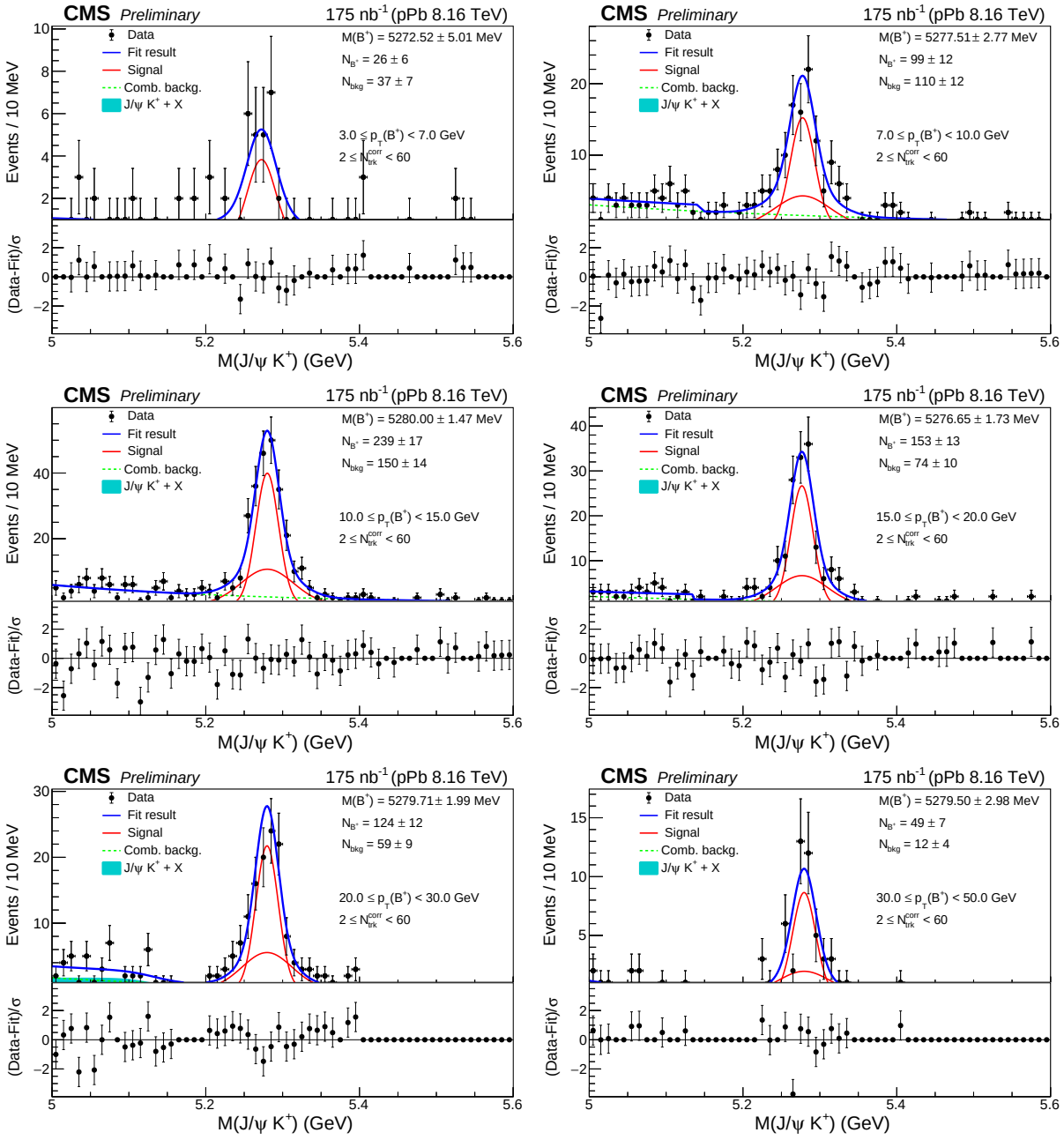

Figure 4.10: Fits performed to the B$^+$candidates in transverse momentum bins in the 2-60 multiplicity bin. The signal is modelled with the sum of two Gaussian functions with a common mean and different widths. The combinatorial background component is fit to an exponential distribution. The contribution of partially reconstructed decays is modelled by an error function.

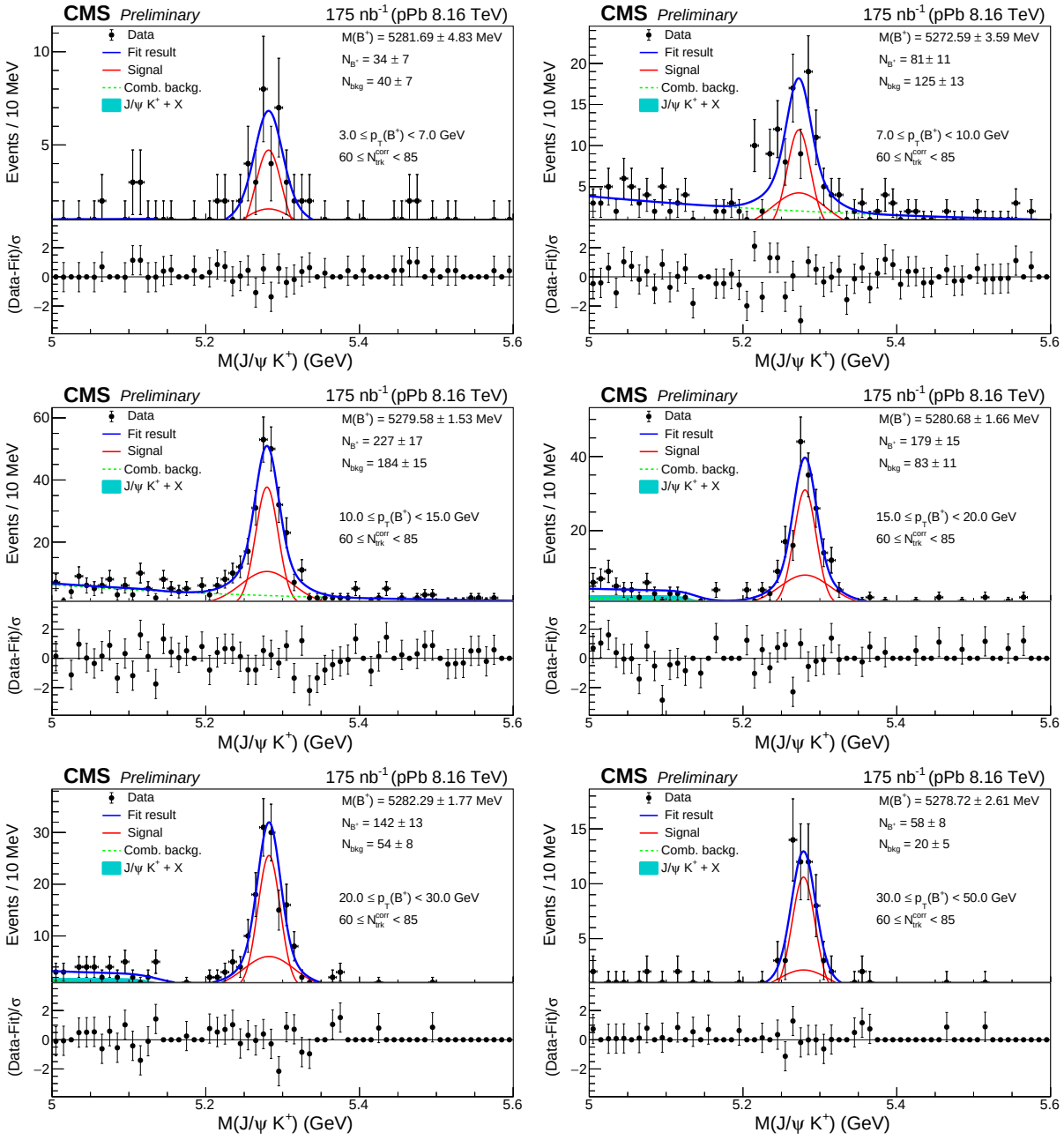

Figure 4.11: Fits performed to the B^+candidates in transverse momentum bins in the 60-85 multiplicity bin. The signal is modeled with the sum of two Gaussian functions with a common mean and different widths. The combinatorial background component is fit to an exponential distribution. The contribution of partially reconstructed decays is modeled by an error function.

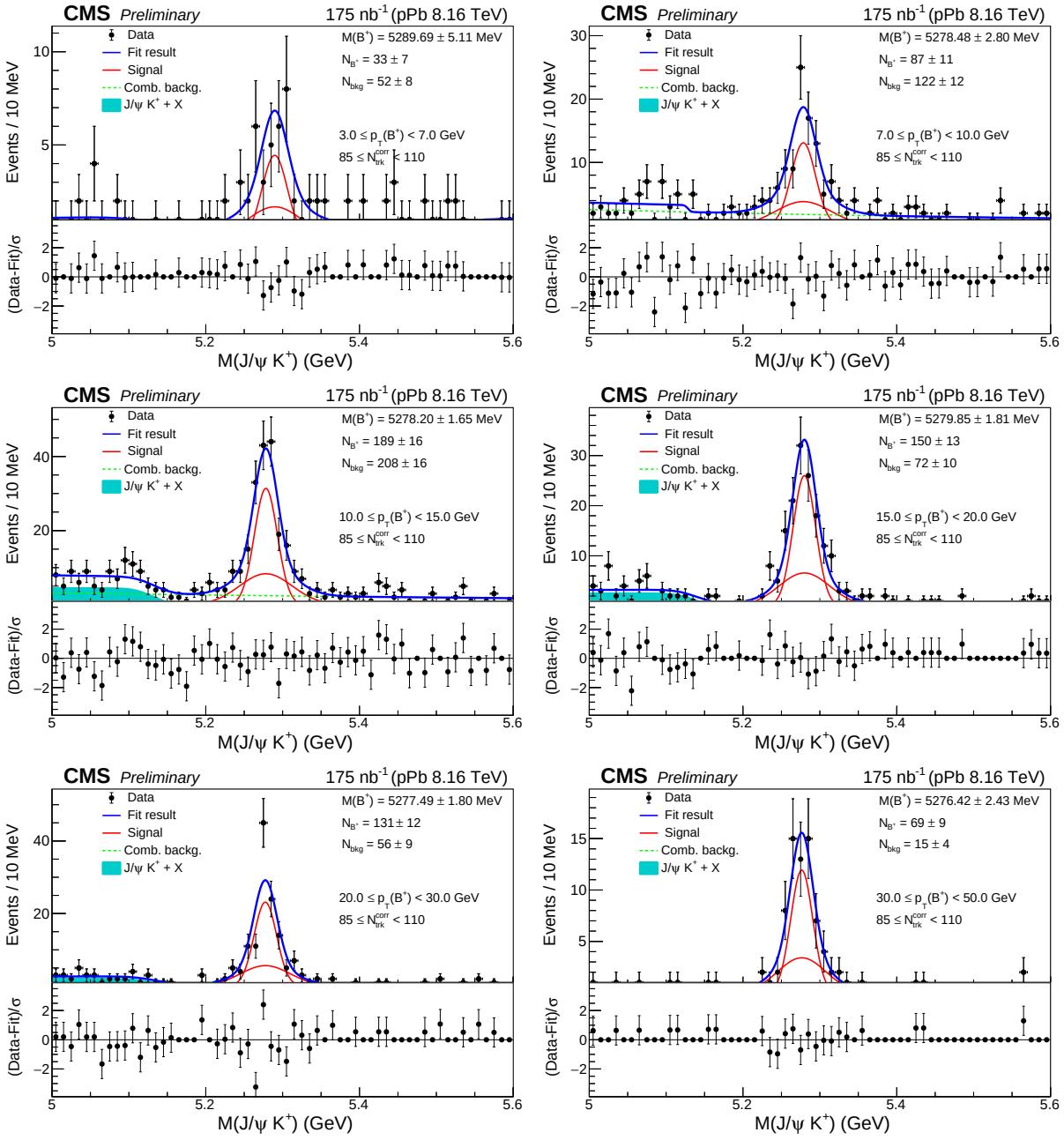

Figure 4.12: Fits performed to the B^+candidates in transverse momentum bins in the 85-110 multiplicity bin. The signal is modeled with the sum of two Gaussian functions with a common mean and different widths. The combinatorial background component is fit to an exponential distribution. The contribution of partially reconstructed decays is modeled by an error function.

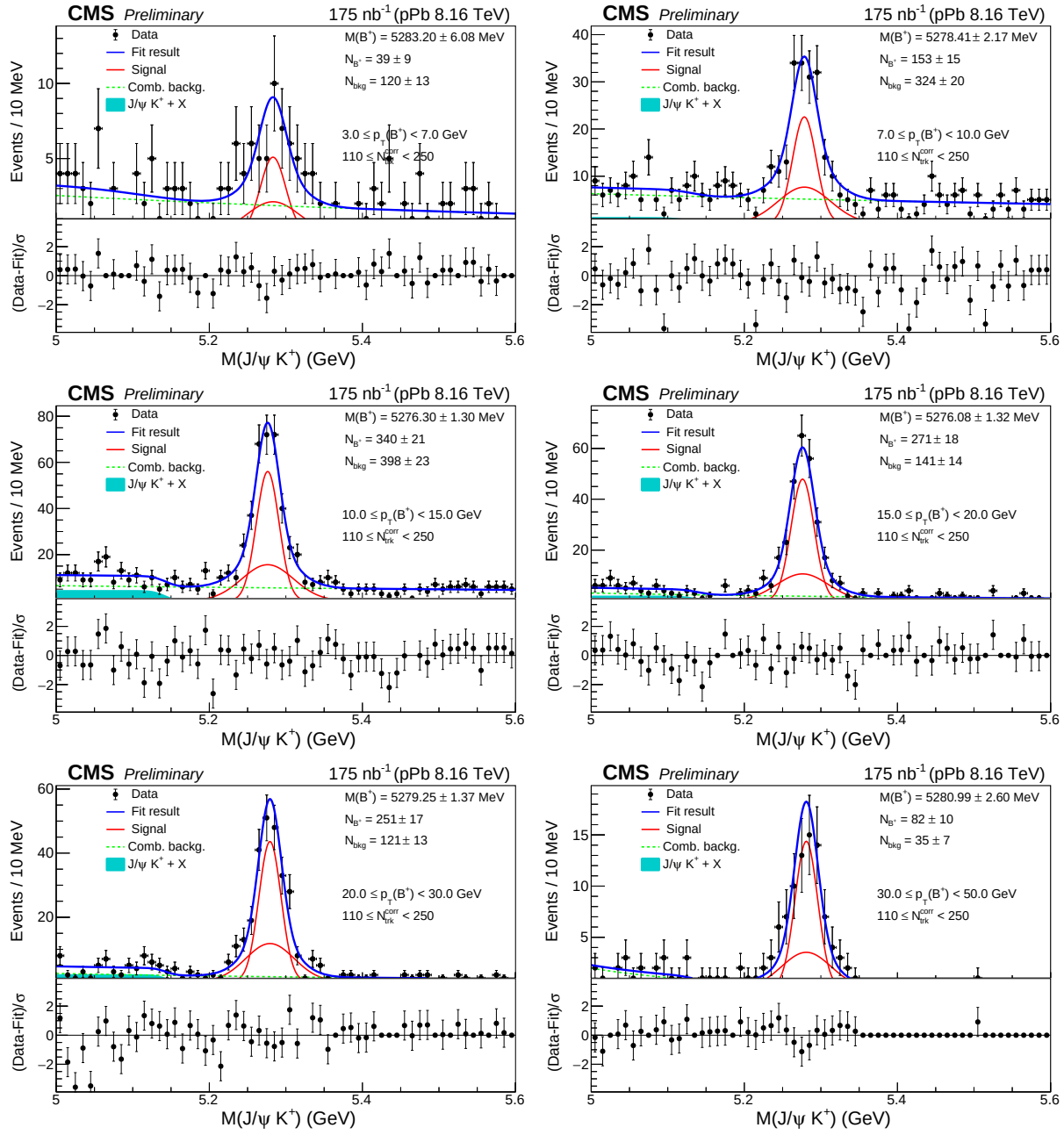

Figure 4.13: Fits performed to the B$^+$candidates in transverse momentum bins in the 110-250 multiplicity bin. The signal is modeled with the sum of two Gaussian functions with a common mean and different widths. The combinatorial background component is fit to an exponential distribution. The contribution of partially reconstructed decays is modeled by an error function.

$$SF_{\mu^+\mu^-} = SF^{\mu^+} \times SF^{\mu^-}, \tag{4.6}$$

Finally we use the $SF_{\mu^+\mu^-}$ as a weight to the MC for efficiency correction. The TnP weighted efficiency is the nominal and quote the deviation of the SF up and down as the TnP systematic uncertainties.

4.5.2 Reweighting

The kinematic distributions of both transverse momentum and rapidity for the objects involved in the reconstruction of $B^+ \to K^+\mu^+\mu^-$ pPb and Pbp candidates are shown in figures 4.14 and 4.15, respectively.

From the candidate selection described in Section 4.4 and from $J/PsiK^+$ invariant mass distribution fit in data, the data distributions are background subtracted by the sPlot technique.

Discrepancies between data and MC are found mainly in the $J/PsiK^+$ p_T and rapidity distributions. Then, those p_T and rapidity distributions of the $B^+ \to K^+\mu^+\mu^-$ candidates (after the weight coming from TnP procedure) are reweighted as shown in Fig. 4.16.

Iterative correction

A first approach towards a multivariate reweighting was proposed by Alexander Tulupov and Sergey Polikarpov in the internal analysis note AN-2017/256. Here we reproduced the method. The algorithm's idea is to create histograms of weights per variable. These single-variable weights are obtained by Eq. 4.7, where (i) is the i-th iteration, j is the j-th bin, var is one of the variables that are to be reweighed, and α is a tunable parameter, whose value given by the rule of thumb is equal to 1 / Number of Variables. The initial value of ω^i can be set to any available weights or, as default, use weights equal to 1.

$$\omega^{(i)}_{j,var} = \frac{RD_{j,var} - \alpha MC_{j,var}}{MC_{j,var}} \tag{4.7}$$

The weight histograms are then interpolated using a cubic-spline. By doing this single-variable weights per event can be obtained, *i.e.* $\omega^{(i)}_{j,var} \to \omega(x)^{(i)}_{var}$. The total weight (per-event) of the i-th iteration is calculated by the product of all single-variable weights as in Eq. 4.8 . The process is repeated until all variables have met a previously defined χ^2 p_{val} threshold.

$$\prod_{vars} \omega(x)^{(i)}_{var} = \omega(x)^{(i)}_{total} \tag{4.8}$$

After the reweighting procedure, the rapidity distributions of MC sample match those of data samples.

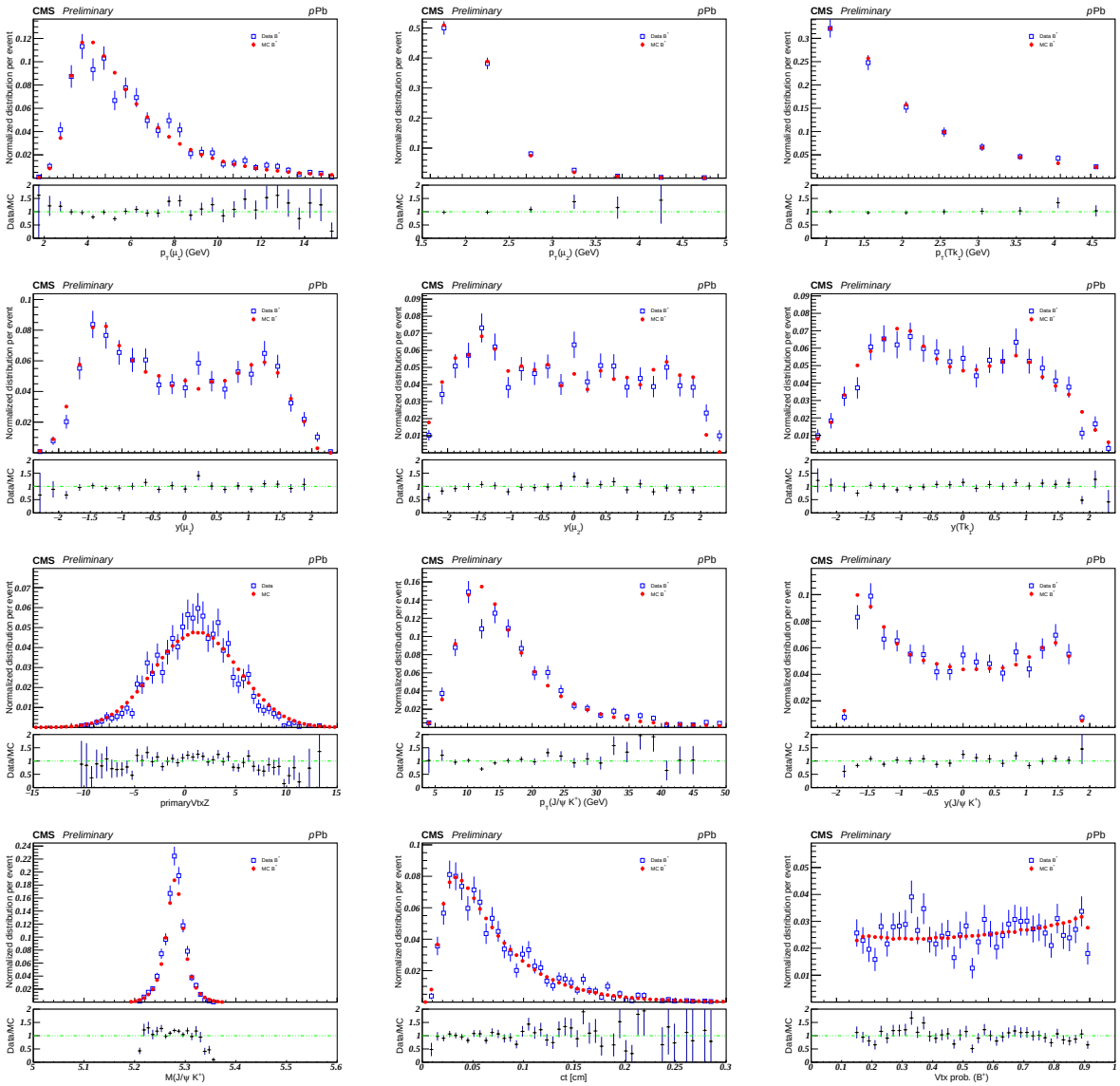

Figure 4.14: Transverse momentum, (pseudo)rapidity, and other distributions in both data and MC samples of the objects used to reconstruct $B^+ \to K^+\mu^+\mu^-$ candidates in pPb samples.

4.6 Efficiency Determination

To estimate the real number of B^+ mesons produced in pPb collisions, the efficiency of to the reconstruction and the selection criteria is needed. In this chapter, efficiency correction is discussed.

Correction based on a Tag and Probe method is performed with muons on data and MC, this method is discussed in section 4.5.1, as well as the tracking efficiency in section 4.8. In addition, the discrepancies between data and MC are effectively removed by the reweighting procedure described in section 4.5 and shown in Fig. 4.16.

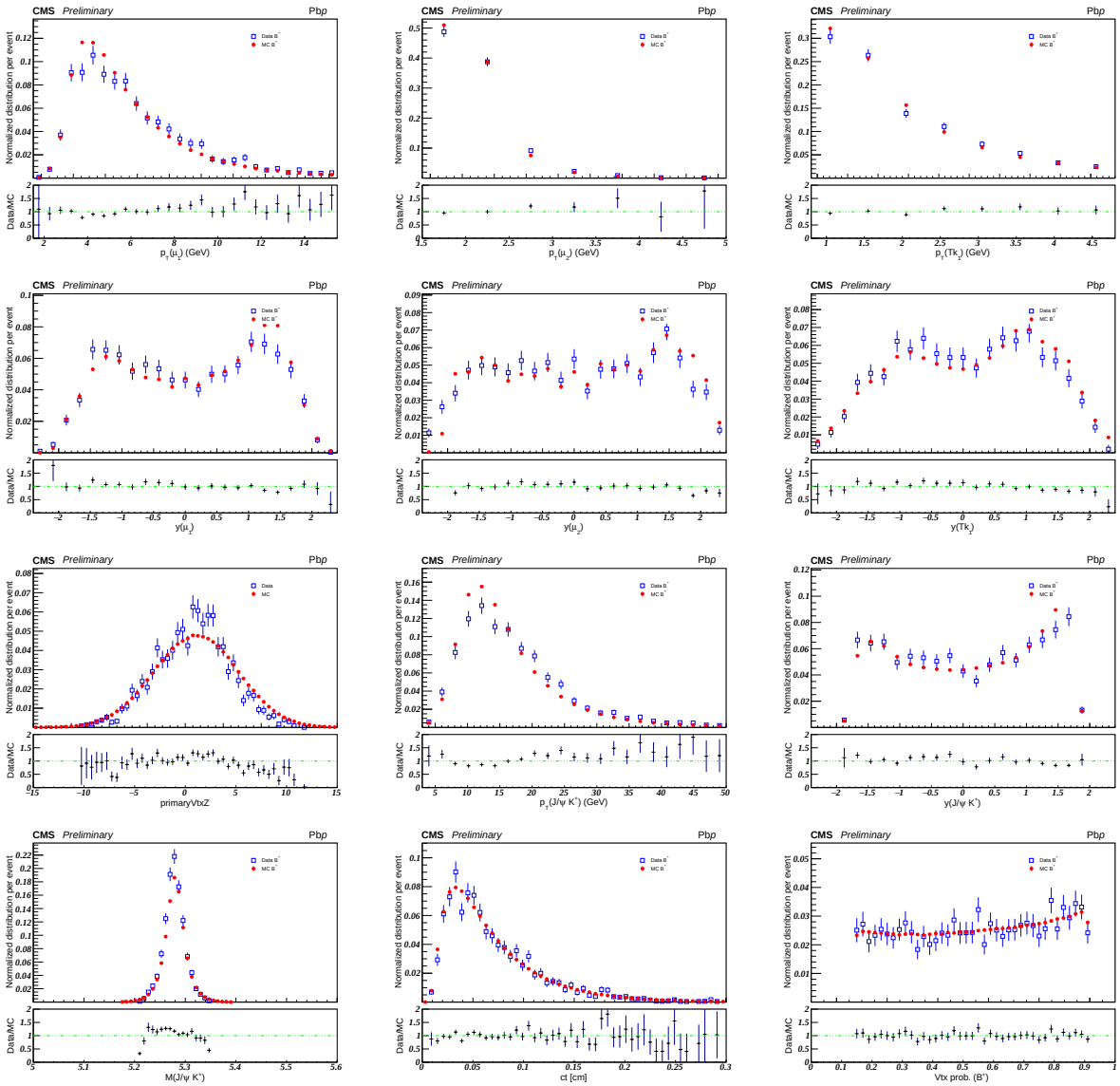

Figure 4.15: Transverse momentum, (pseudo)rapidity, and other distributions in both data and MC samples of the objects used to reconstruct $B^+ \to K^+\mu^+\mu^-$ candidates in Pbp samples.

Efficiency is determined as the number of reconstructed B meson events after the full selection divided by the number of generated B meson decays in the fiducial region of the analysis: $3 < p_T(B) < 50$ GeV and $|y(B)| < 1.8$. This definition includes both the acceptance and offline selection. To determine the efficiency two MC samples per channel are used:

- A first sample with gen-level only production of $B^+ \to K^+\mu^+\mu^-$ decays without any prefiltering cuts.
- A second sample with pre-filter cuts at gen-level: $|\eta(\mu)| < 2.5$, $|\eta(K)| < 2.5$, $p_T(\mu) > 1.5$ GeV and $p_T(K) > 0.4$ GeV.

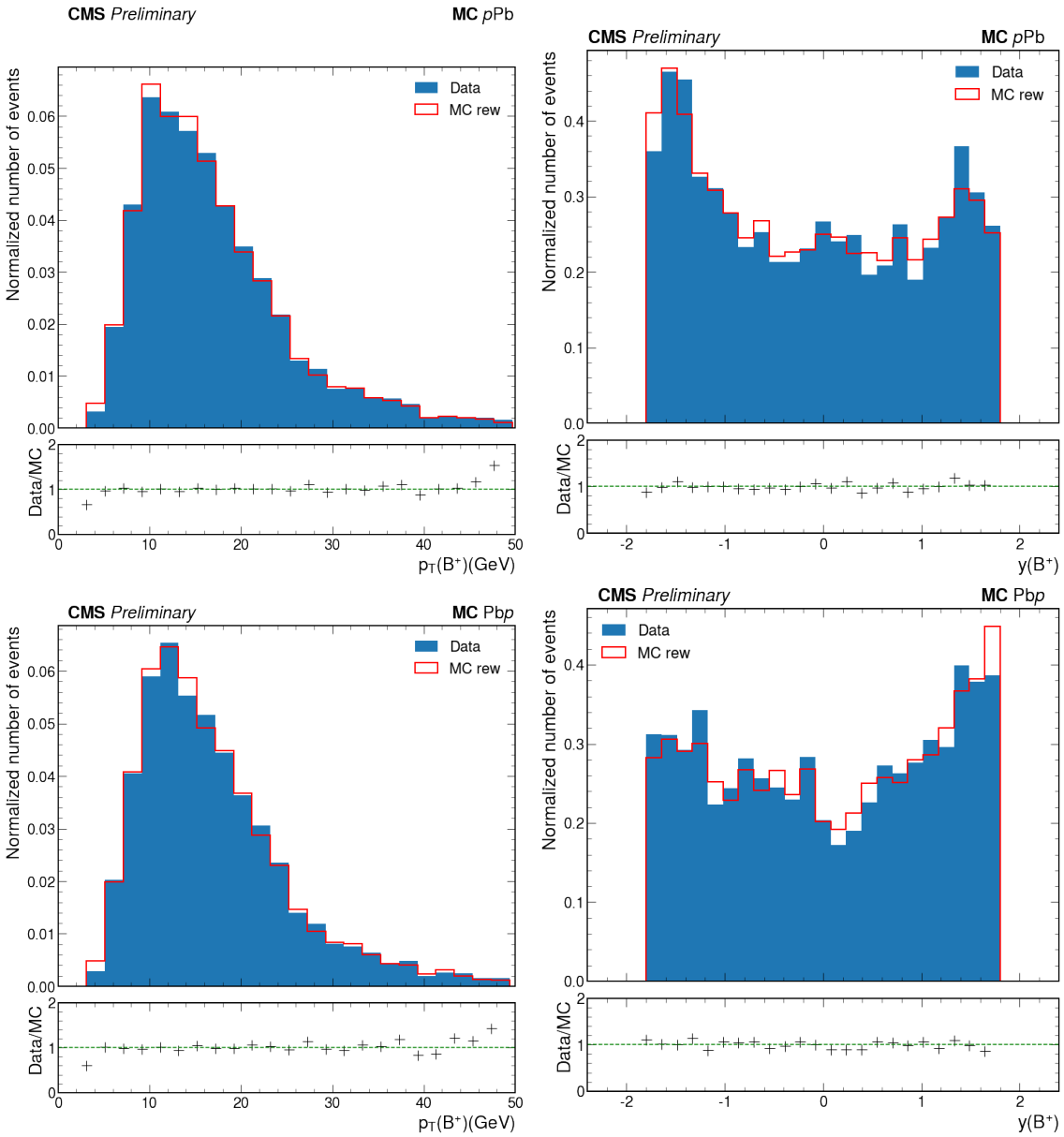

Figure 4.16: The p_T (left) and rapidity (right) distributions of both pPb (top) and Pbp (bottom) samples are shown. The data is shown in blue, while (reweighted) MC samples are shown in red.

The efficiency is split into two terms: the *pre-filter* efficiency (ϵ_1) and the efficiency of reconstruction (ϵ_2). The former measures the efficiency of the generator *pre-filter* (acceptance) using the sample without any cuts, whereas the latter measures the reconstruction and event selection efficiency after the pre-filter selection (second sample). The product of this pair of efficiencies ($\epsilon = \epsilon_1 \times \epsilon_2$) is considered as the total efficiency and it is computed in the relevant bins to the measurement.

In the following subsections each component of the efficiency is shown and described.

The bins of interest for this analysis are the efficiency and multiplicity, we followed a similar procedure to calculate the efficiency in the same bins of these variables in which the cross sections are estimated.

4.6.1 Acceptance

The efficiency at generator level is an estimate of the effect of acceptance in the counting of b candidates for the present measurement. The number of events passing the pre-filter cuts is divided by the number of events generated as described in section **??**. Efficiency for p_T bin i, which is $c < p_T(B^+) < d$, is defined as:

$$\epsilon_1^i = \frac{N(\mathrm{B^+ \to J/\Psi K^+}\ |\mathrm{y}^{\mathrm{gen}}_{\mathrm{B^+}}| < 1.8, \mathrm{c} < \mathrm{p}^{\mathrm{gen}}_{\mathrm{T}}(\mathrm{B^+}) < \mathrm{d}, \text{filter cuts})}{N(\mathrm{B^+ \to J/\Psi K^+}\ |\mathrm{y}^{\mathrm{gen}}_{\mathrm{B^+}}| < 1.8, \mathrm{c} < \mathrm{p}^{\mathrm{gen}}_{\mathrm{T}}(\mathrm{B^+}) < \mathrm{d})} \tag{4.9}$$

The equation shows prefilter efficiency for $\mathrm{B^+ \to J/\Psi K^+}$. Figure 4.17 shows the pre-filter efficiency ϵ_1 as a function of gen-level b meson p_T. The corresponding results for (p_T, $N^{\mathrm{gen}}_{\mathrm{trk}}$) bins are also shown in Appendix A.

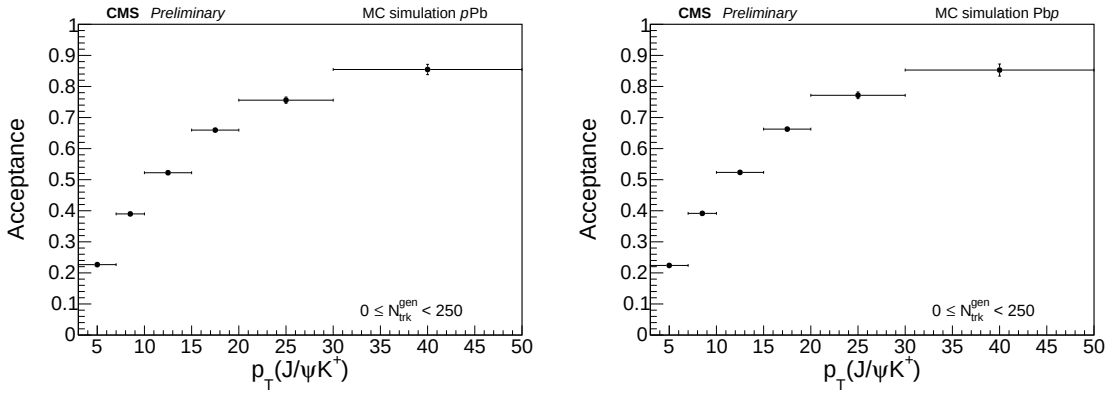

Figure 4.17: The efficiency dependencies at generator level are shown for pPb (left) and Pbp (right) samples in p_T bins. Generator level efficiency is defined as the ratio of events passing pre-filter cuts to the number of generated events.

4.6.2 Reconstruction Efficiency

The second component of the total efficiency is estimated from MC samples that are generated with the pre-filter cuts already applied. The ratio of the number of reconstructed events after the full selection with respect to the number of generated decays in the appropriate binning is the so called reconstruction efficiency. Reconstruction efficiency for p_T bin i, which is $c < p_T(\mathrm{B^+}) < \mathrm{d}$, is defined as:

$$\epsilon_2^i = \frac{N(\mathrm{B^+ \to J/\Psi K^+}, |\mathrm{y}^{\mathrm{reco}}_{\mathrm{B^+}}| < 1.8, \mathrm{c} < \mathrm{p}^{\mathrm{reco}}_{\mathrm{T}}(\mathrm{B^+}) < \mathrm{d}, \text{filter cuts, full selection})}{N(\mathrm{B^+ \to J/\Psi K^+}, |\mathrm{y}^{\mathrm{gen}}_{\mathrm{B^+}}| < 1.8, \mathrm{c} < \mathrm{p}^{\mathrm{gen}}_{\mathrm{T}}(\mathrm{B^+}) < \mathrm{d}, \text{filter cuts})} \tag{4.10}$$

The equation shows efficiency of reconstruction for $B^+ \to J/\Psi K^+$. The dependencies on p_T are shown in Fig. 4.18. The corresponding results for (p_T, N_{trk}^{gen}) bins are also shown in Appendix A.

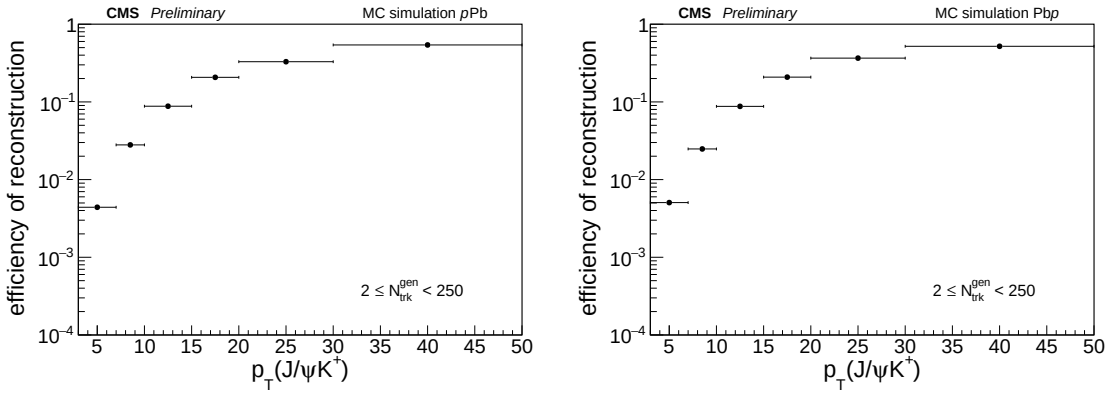

Figure 4.18: The reconstruction efficiency dependencies are shown for pPb (left) and Pbp (right) samples in p_T bins. Reconstruction efficiency is defined as the ratio of reconstructed events in a sample of MC events that include pre-filter cuts with respect to the number of generated events in the same sample.

4.6.3 Total Efficiency

The product of the gen-level efficiency and reconstruction efficiency ($\epsilon = \epsilon_1 \times \epsilon_2$) is the total efficiency used in the measurement and for p_T bins can be observed in Fig. 4.19. Figure 4.20 shows the efficiency before and after applying the reweighting procedure, tables 4.6 and 4.7 show the computed values for each component of the total efficiency. The results for (p_T, N_{trk}^{gen}) are also displayed in detail in Appendix A.

Table 4.6: The numerical values obtained for the prefilter efficiency, the reconstruction efficiency and the total efficiency are shown in the table as transverse momentum bins of the B^+ candidates, in pPb collisions.

p_T (B^+) (GeV)	Pre-Filter	Reco	Total
3 – 7	0.22658 ± 0.00134	0.00440 ± 0.00002	0.00100 ± 0.00001
7 – 10	0.38985 ± 0.00268	0.02797 ± 0.00006	0.01091 ± 0.00008
10 – 15	0.52236 ± 0.00385	0.08804 ± 0.00013	0.04599 ± 0.00035
15 – 20	0.65958 ± 0.00740	0.20728 ± 0.00033	0.13672 ± 0.00155
20 – 30	0.75591 ± 0.01007	0.32932 ± 0.00053	0.24893 ± 0.00334
30 – 50	0.85463 ± 0.01656	0.54133 ± 0.00111	0.46263 ± 0.00901

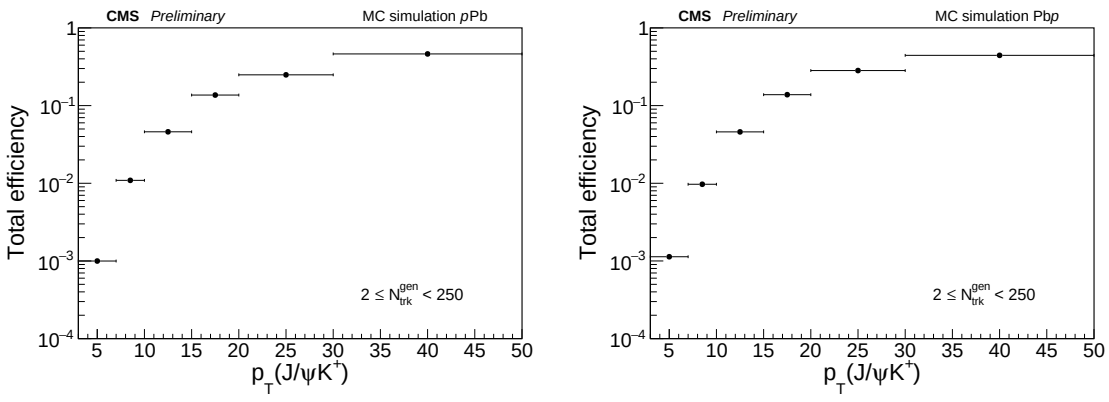

Figure 4.19: The total efficiency distributions are shown for pPb (left) and Pbp (right) samples in p_T bins. The total efficiency is defined as the product of generator level efficiency with reconstruction efficiency.

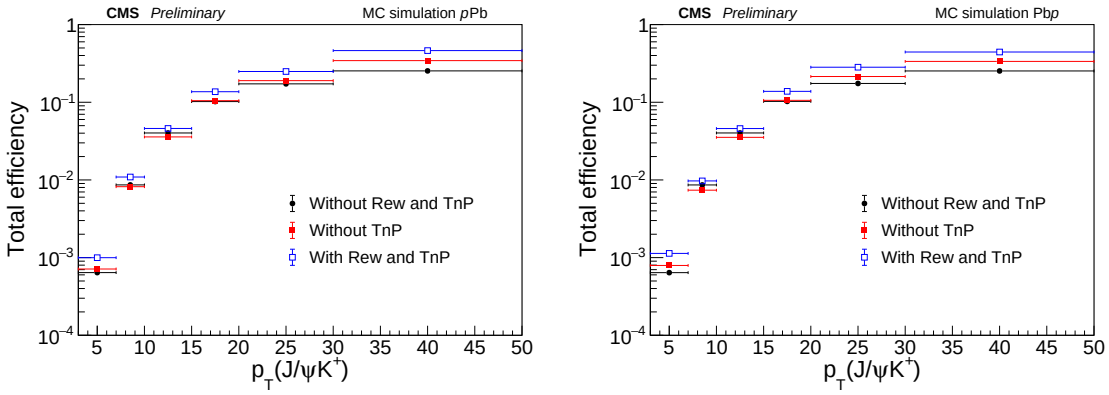

Figure 4.20: The total efficiency distributions are shown for pPb (left) and Pbp (right) samples in p_T bins. The efficiency distributions are shown before and after applying the reweighting procedure.

4.7 Cross Sections

The observable of interest is the differential cross section:

$$\frac{\mathrm{d}\sigma}{\mathrm{dp_T}} = \frac{1}{2}\frac{1}{\Delta p_T}\frac{N(p_T)}{\epsilon \mathcal{BL}} \tag{4.11}$$

$$\frac{\mathrm{d}\sigma}{\mathrm{dp_T}|_{(\mathrm{N_{trk}^{corrected}})}} = \frac{1}{2}\frac{1}{\Delta p_T}\frac{N(p_T, N_{\mathrm{trk}}^{\mathrm{corrected}})}{\epsilon\, \mathcal{BL}}\,, \tag{4.12}$$

Using the raw yields obtained and the efficiency computed, the results are displayed in Tables 4.8 for transverse momentum. The efficiency column shows the average efficiency

Table 4.7: The numerical values obtained for the prefilter efficiency, the reconstruction efficiency and the total efficiency are shown in the table as transverse momentum bins of the B^+ candidates, in Pbp collisions.

p_T (B^+) (GeV)	Pre-Filter	Reco	Total
3 – 7	0.22398 ± 0.00146	0.00506 ± 0.00002	0.00113 ± 0.00001
7 – 10	0.39157 ± 0.00293	0.02481 ± 0.00006	0.00971 ± 0.00008
10 – 15	0.52347 ± 0.00422	0.08765 ± 0.00013	0.04588 ± 0.00038
15 – 20	0.66276 ± 0.00809	0.20852 ± 0.00032	0.13820 ± 0.00170
20 – 30	0.77160 ± 0.01073	0.36626 ± 0.00054	0.28261 ± 0.00395
30 – 50	0.85285 ± 0.01944	0.52011 ± 0.00110	0.44358 ± 0.01015

weighted according to the integrated luminosity of the periods (pPb and Pbp). From Figure 4.9 it is observed that N_{trk}^{gen} and $N_{trk}^{corrected}$ are equivalent to each other.

Therefore, to show the differential cross section in data at different charged-particle multiplicity, the $N_{trk}^{corrected}$ values are used unless otherwise stated.

The corresponding results for (p_T , $N_{trk}^{corrected}$) bins are also shown in Appendix B.

Table 4.8: The raw yields obtained and efficiencies computed are shown with their respective statistical uncertainties. The value of $d\sigma/dp_T$is computed directly from these results. For $d\sigma/dp_T$, just the yield error propagation is present.

p_T (GeV)	B^+ Yield	B^+ Efficiency	$d\sigma/dp_T(\mu b/GeV)$
3 – 7	131 ± 14	0.00108 ± 0.00001	1422.79 ± 157.19
7 – 10	420 ± 25	0.01014 ± 0.00006	647.10 ± 38.61
10 – 15	991 ± 36	0.04592 ± 0.00027	202.10 ± 7.24
15 – 20	756 ± 30	0.13767 ± 0.00122	51.41 ± 2.02
20 – 30	650 ± 27	0.27052 ± 0.00280	11.25 ± 0.47
30 – 50	260 ± 17	0.45042 ± 0.00727	1.35 ± 0.09

4.7.1 Transverse momentum spectra

As complementary information, the p_T spectra of B^+ meson is shown in Fig. 4.21 for the four multiplicity classes.

4.8 Systematic Uncertainties

The results so far includes only statistical uncertainties. Several sources of systematic uncertainties have been considered for the cross section measurement, coming from different inputs in Eqns. 4.11. In Tables 4.10 for p_T bins, and Tables 4.12, 4.13, 4.14, and 4.15 for (p_T ,$N_{trk}^{corrected}$) bins the various sources and their contributions are summarized.

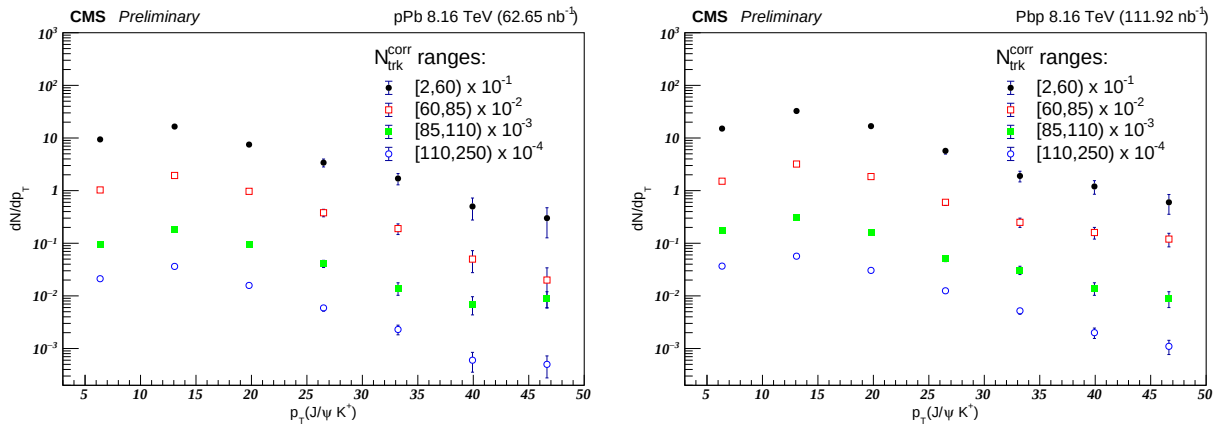

Figure 4.21: The p_{T} spectra of B^{+} particles. Results are shown for the four multiplicity classes, for pPb (left) and Pbp (right) samples.

The total systematic uncertainty is obtained by the sum in quadrature of the individual uncertainties. The details of each contribution are discussed below.

4.8.1 Overall scale related to the cross section calculation

There are two dominant sources of systematic uncertainties in this category: (1) product of the world-average results for the branching fractions (2) the uncertainty related to luminosity measurement.

Systematic uncertainty associated with exclusive B decay chain branching fractions are calculated using the uncertainty of each decay listed in PDG, it is found to be 3.1% [78]. In addition, one of the dominant sources of systematic uncertainty, in most momentum bins, is originating from the uncertainty on the estimation of the integrated luminosity of 3.5% [82]. We keep these sources of uncertainty separate when quoting the final results.

4.8.2 Signal and Background Models

The uncertainties for the cross section measurements due to the estimation of the B^{+} yield has been evaluated by varying the probability density functions (pdfs) used in the maximum likelihood (ML) fit, for signal and background separately. The systematic uncertainty related to the choice of the signal fit model is evaluated by testing different models. For instance, when modeling the signal, we have changed the nominal signal model, which consists of a sum of a pair of Gaussian distributions with a common mean and different widths fixed from MC.

A systematic uncertainty is computed by letting the mean and widths to floated in the fit. Other two alternative signal models were considered: firts model is Johnson's S_{U} distribution [91]. Second model is a Student's t function [92].

The largest deviation in the measured yields from its baseline value is taken as a systematic uncertainty. The systematic uncertainty is estimated as the difference between the

yields obtained by varying the model.

We studied the systematic uncertainty due to the combinatorial background mass modeling, where we used an exponential distribution as nominal pdf. We have changed this shape to a Chebyshev polynomial of degree one.

On the other hand, the partially reconstructed $B^+ \rightarrow J/\Psi K^+, X$ background is fitted with an error function, and its parameters are fixed from MC. A systematic uncertainty is computed by letting the error function parameters to floated in the fit.

The observed differences, sum in quadrature, in the measured B^+ yields are quoted as systematic uncertainty due to the background model.

In addition, the fitting procedure was tested using randomly generated event samples, of sizes corresponding to the number of measured events, reflecting the nominal likelihood probability distribution functions and fitted parameters. No significant fit biases were found in the central values and uncertainties.

4.8.3 Monte Carlo

Monte Carlo Size

Given the finite nature of the Monte Carlo samples used, a systematic uncertainty is computed from the efficiency. In other words, the statistical uncertainty of the efficiency is taken as a systematic uncertainty in the cross section measurements. The results are summarized in Tables 4.6 and 4.7.

Multiplicity correction

After observing the MC variables in Fig. 4.9, a small difference was observed between $N_{\rm trk}^{\rm corrected}$ and $N_{\rm trk}^{\rm gen}$, in both MC samples pPb (left) and Pbp (right). In order to consider the effect that this difference could have, in the normalized multiplicity dependence ratios measurement, a reweighting procedure was explored.

The idea is as follows: we want to see the result if we correct $N_{\rm trk}^{\rm corrected}$(data)) event by event by multiplying it by $N_{\rm trk}^{\rm corrected}/N_{\rm trk}^{\rm gen}$ (from the MC, Fig. 4.9). In this way, from the difference between the two results, we could evaluate a systematic uncertainty related to the procedure of multiplicity correction. Now, we have the weighted yields. Nevertheless, we need not only the weighted yields but also the average of the weighted multiplicity in all the multiplicity classes.

The effects of this procedure are summarized in Table 4.9 and showed in Figure 4.22.

This systematic is relevant in the ratios of the cross section, shown in Figure 4.26 (Right).

4.8.4 Tracking

In the determination of the cross section, the track reconstruction in the decay of B^+ meson may induce a systematic uncertainty, due to the track efficiency determination. To take into account this effect, the systematic uncertainties related to tracking efficiency or track reconstruction can be evaluated based on the method described in the D meson analysis

Table 4.9: Cross-section values, nominal(CS) and after multiplicity correction (weighted CS). Weighted multiplicity average, the nominal ratio, and the weighted ratio.

Multiplicity Class	CS	Weighted CS	Weighted Avg N_{trk}	Ratio	Weighted Ratio
2 – 60	47.674	41.362	42.200		
60 – 85	45.329	44.656	82.842	0.555	0.550
85 – 110	41.917	42.606	113.889	0.385	0.382
110 – 250	66.334	78.450	188.051	0.418	0.426

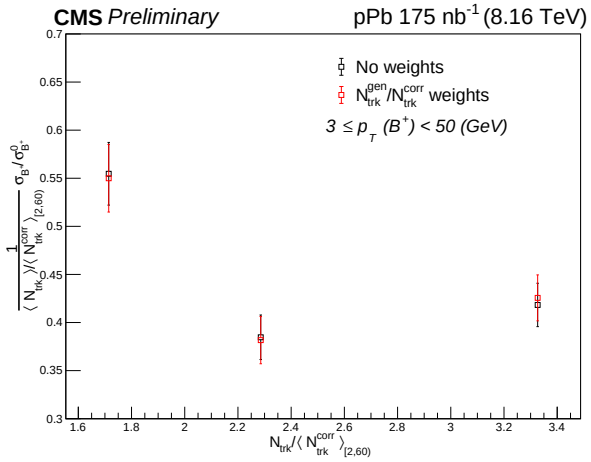

Figure 4.22: The scaled Ratio $\sigma^{\mathrm{B}^+}/\sigma_0^{\mathrm{B}^+}$ is shown in p_{T} bins. The error bars correspond to the statistical uncertainty.

(CMS DP-2018/050). The current standard value of tracking efficiency uncertainty for one track is 2.4% per track. This is global to all p_{T} and multiplicity selections in our analysis.

4.8.5 Muon Systematic Efficiencies using the Tag and Probe method

The systematic uncertainty of the charged hadron tracking efficiency was determined, based on Muon performance studies in 2016 pPb data (https://twiki.cern.ch/twiki/pub/CMS/HIMuonTagProbe/TnP_pPb2016_lowPt_instructions_v2.pdf). TnP method 4.5.1 is used to estimate the single-muon tracking, identification and trigger efficiencies on both data and MC.

Differences between data and MC efficiencies are quantified by the scale factors (SF), taking the ratio of data/MC and used to correct the efficiency from MC truth in the final results.

We use the TnP weighted efficiency as the nominal and quote the deviation of the SF up and down as the TnP systematic uncertainties.

Besides, we have considered the variation of the weights of the reweighting process (see section 4.5), however, it is negligible compared to that of the TnP weights, which is the

dominant uncertainty.

Table 4.10: Systematic uncertainties on $d\sigma/dp_T$ from alternative B^+ fitting strategies described in the text. The total systematic uncertainty is the sum in quadrature of the individual uncertainties. Statistical uncertainty is shown too.

p_T (GeV)	B^+ signal	Bu bkg	MC size	Tracking	Tag and Probe	Total Systematic uncertainty (%)	Statistical uncertainty (%)
3 – 7	4.7	0.57	0.9	2.4	0.04	5.4	11.0
7 – 10	1.1	0.45	0.6	2.4	0.29	2.8	6.0
10 – 15	2.1	1.30	0.6	2.4	1.25	3.7	3.6
15 – 20	1.5	0.33	0.9	2.4	3.97	5.0	3.9
20 – 30	3.3	0.57	1.0	2.4	8.15	9.2	4.2
30 – 50	0.8	0.35	1.6	2.4	14.23	14.5	6.5

Table 4.11: Systematic uncertainties on $d\sigma/dp_T$ from alternative B^+ fitting strategies described in the text. The total systematic uncertainty is the sum in quadrature of the individual uncertainties. Statistical uncertainty is show too.

N_{trk}^{corr}	B^+ signal	B^+ bkg	MC size	Tracking	Tag and Probe	Total Systematic uncertainty (%)	Statistical uncertainty (%)
2 – 60	2.6	0.7	0.6	2.4	0.4	3.7	4.2
60 – 85	1.6	0.6	0.7	2.4	0.5	3.1	4.1
85 – 110	0.1	0.6	0.7	2.4	0.5	2.6	4.3
110 – 250	1.9	2.3	0.5	2.4	0.6	4.0	3.4

4.9 Results

4.9.1 Differential cross-section $d\sigma/dp_T$

The results of the measurement of the differential cross-section, $d\sigma/dp_T$, for the fiducial kinematic region $3 < p_T(B) < 50$ GeV and $|y(B)| < 1.8$ are displayed in Fig. 4.23 for pPb and Pbp samples. Besides, for both samples together the results are displayed in Fig. 4.24 and the systematic uncertainties on Table 4.10. In the same plot, the pp FONLL reference at the same energy (See appendix **??** for more details) are superimposed. Besides, Table 4.16 shows the cross section value, error from pPb+Pbp data and FONLL pp reference.

4.9.2 Normalized multiplicity dependence

To study the differences in the pattern for the B^+ meson production the $\sigma^{B^+}/\sigma_0^{B^+}$ is defined as

Table 4.12: Systematic uncertainties on $d\sigma/dp_T$from alternative B^+ fitting strategies described in the text, for samples in (p_T , $N_{trk}^{corrected}$) bins, with $2 \leq N_{trk}^{corrected} < 60$. The total systematic uncertainty is the sum in quadrature of the individual uncertainties. Statistical uncertainty is shown too.

p_T (GeV)	B^+ signal	Bu bkg	MC size	Tracking	Tag and Probe	Total Systematic uncertainty (%)	Statistical uncertainty (%)
3 – 7	12.9	2.09	1.0	2.4	0.04	13.4	23.3
7 – 10	6.1	1.76	1.1	2.4	0.30	6.8	11.8
10 – 15	0.7	2.16	1.2	2.4	1.31	3.7	7.0
15 – 20	2.7	0.81	1.8	2.4	4.08	5.8	8.7
20 – 30	13.2	10.06	2.2	2.4	8.39	18.9	9.7
30 – 50	0.4	6.32	3.8	2.4	14.33	16.3	14.7

Table 4.13: Systematic uncertainties on $d\sigma/dp_T$from alternative B^+ fitting strategies described in the text, for samples in (p_T , $N_{trk}^{corrected}$) bins, with $60 \leq N_{trk}^{corrected} < 85$. The total systematic uncertainty is the sum in quadrature of the individual uncertainties. Statistical uncertainty is shown too.

p_T (GeV)	B^+ signal	Bu bkg	MC size	Tracking	Tag and Probe	Total Systematic uncertainty (%)	Statistical uncertainty (%)
3 – 7	4.7	1.24	0.9	2.4	0.04	5.5	20.1
7 – 10	10.2	4.36	1.2	2.4	0.29	11.4	13.3
10 – 15	2.0	3.12	1.3	2.4	1.23	4.8	7.4
15 – 20	4.3	1.80	1.9	2.4	4.07	6.9	8.2
20 – 30	6.1	3.42	2.3	2.4	8.29	11.4	8.9
30 – 50	3.1	0.78	3.1	2.4	14.81	15.7	13.7

Table 4.14: Systematic uncertainties on $d\sigma/dp_T$from alternative B^+ fitting strategies described in the text, for samples in (p_T , $N_{trk}^{corrected}$) bins, with $85 \leq N_{trk}^{corrected} < 110$. The total systematic uncertainty is the sum in quadrature of the individual uncertainties. Statistical uncertainty is shown too.

p_T (GeV)	B^+ signal	Bu bkg	MC size	Tracking	Tag and Probe	Total Systematic uncertainty (%)	Statistical uncertainty (%)
3 – 7	11.4	2.47	1.0	2.4	0.04	11.9	21.5
7 – 10	0.4	2.86	1.2	2.4	0.29	4.0	12.6
10 – 15	0.7	0.73	1.3	2.4	1.20	3.2	8.2
15 – 20	0.6	0.61	2.0	2.4	3.84	5.0	8.8
20 – 30	1.3	1.02	2.4	2.4	7.86	8.7	9.3
30 – 50	0.6	3.51	4.3	2.4	13.16	14.5	12.5

Table 4.15: Systematic uncertainties on $d\sigma/dp_T$from alternative B^+ fitting strategies described in the text, for samples in (p_T , $N_{trk}^{corrected}$) bins, with $110 \leq N_{trk}^{corrected} < 250$. The total systematic uncertainty is the sum in quadrature of the individual uncertainties. Statistical uncertainty is shown too.

p_T (GeV)	B^+ signal	Bu bkg	MC size	Tracking	Tag and Probe	Total Systematic uncertainty (%)	Statistical uncertainty (%)
3 – 7	16.7	2.07	0.8	2.4	0.04	17.0	22.7
7 – 10	8.2	11.56	1.0	2.4	0.30	14.4	10.0
10 – 15	6.7	3.01	1.0	2.4	1.24	7.9	6.3
15 – 20	2.2	0.31	1.5	2.4	3.90	5.3	6.6
20 – 30	1.3	1.08	1.7	2.4	8.05	8.7	6.8
30 – 50	3.1	4.48	2.4	2.4	14.39	15.8	11.8

Table 4.16: Summary table of the pT-differential cross sections of B^+ in pPb collisions at $\sqrt{s_{NN}} = 8.16$ TeV.

pt (GeV)	$d\sigma/dp_T$ ($\mu b\ GeV^{-1}$)	stat. error ($\mu b\ GeV^{-1}$)	sys. error ($\mu b\ GeV^{-1}$)	$d\sigma/dp_T$(FONLL) ($\mu b\ GeV^{-1}$)	FONLL error ($\mu b\ GeV^{-1}$)
3 – 7	1422.79	157.19	76.09	1275.39	+806.48 -677.37
7 – 10	647.10	38.61	17.66	494.46	+289.87 -191.16
10 – 15	202.10	7.24	7.04	167.28	+85.55 -56.31
15 – 20	51.41	2.02	2.55	52.51	+22.57 -15.70
20 – 30	11.25	0.47	1.03	12.83	+4.39 -3.29
30 – 50	1.35	0.09	0.20	1.57	+0.39 -0.32

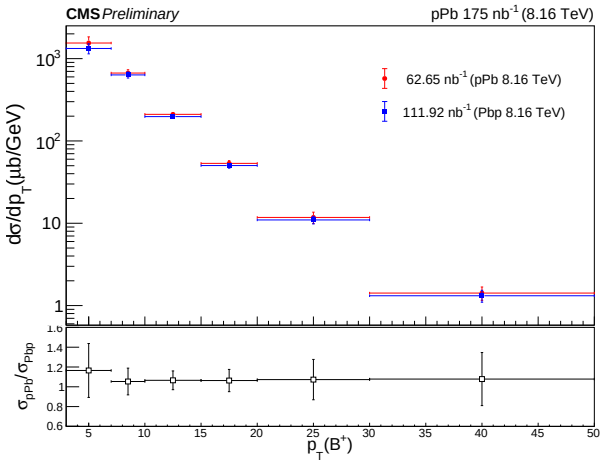

Figure 4.23: The B^+ differential cross-section $d\sigma/dp_T$is shown in transverse momentum bins for pPb and Pbp. The inner error bars correspond to the sum in quadrature of each systematic uncertainty computed and the statistical uncertainty. Besides, the ratio is shown in the bottom panel.

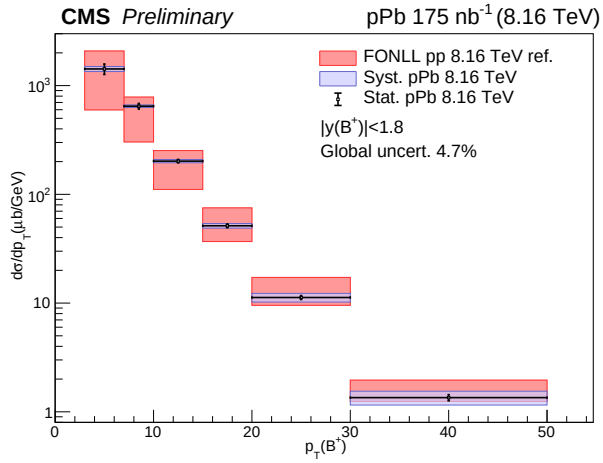

Figure 4.24: The B^+ differential cross-section $d\sigma/dp_T$is shown in transverse momentum bins. The inner error bars correspond to the statistical uncertainty. The blue error bars (boxes) correspond to the sum in quadrature of each systematic uncertainty computed. The red error bars (boxes) correspond to the FONLL calculation uncertainty.

$$\sigma_{B^+}/\sigma^0_{B^+}(p_T, N_{\rm trk}) = \frac{d\sigma^{B^+}_{pPb}/dp_T|_{(N_{\rm trk})}}{d\sigma^{B^+}_{pPb}/dp_T|_{(N^0_{\rm trk})}} \tag{4.13}$$

where $d\sigma^{B^+}_{pPb}/dp_T$ is the differential cross section of the B^+ meson production as a function of p_T . In the numerator this differential cross section is evaluated in a given multiplicity class with $N_{\rm trk}$ measured tracks, while in the denominator it is evaluated in the lowest multiplicity

class ($N^0_{\rm trk}$) in 2–60 range where no medium or collective effects are expected, it is also to have an equal number of events in all multiplicity classes.

The normalized multiplicity dependence of $\sigma^{\rm B^+}/\sigma_0^{\rm B^+}$ is shown for the six intervals of $p_{\rm T}$ in Figure 4.25.

This figure shows the ratio $\sigma^{\rm B^+}/\sigma_0^{\rm B^+}$ scaled by (1/multiplicity density) vs multiplicity density, where the (denominator)average charged-hadron multiplicity density is taken from the lowest multiplicity bin in our case (2-60). Besides, Figure 4.26 shown as function of the normalized multiplicity: (Left) the scale $\rm B^+$ differential cross-section for all the transverse momentum ranges (Right) scale Ratio of cross sections $\sigma^{\rm B^+}/\sigma_0^{\rm B^+}$ in full transverse momentum range.

In addition, in Figures 4.27 and 4.28 the corresponding $\sigma^{\rm B^+}/\sigma_0^{\rm B^+}$ factor of $\rm B^+$, is presented as a function of the transverse momentum. In the case of Figure 4.28 it is scaled by 1/multiplicity density. The production cross-section shows a trend to be suppressed in pPb high multiplicity collisions when compared to the low multiplicity bin as a reference.

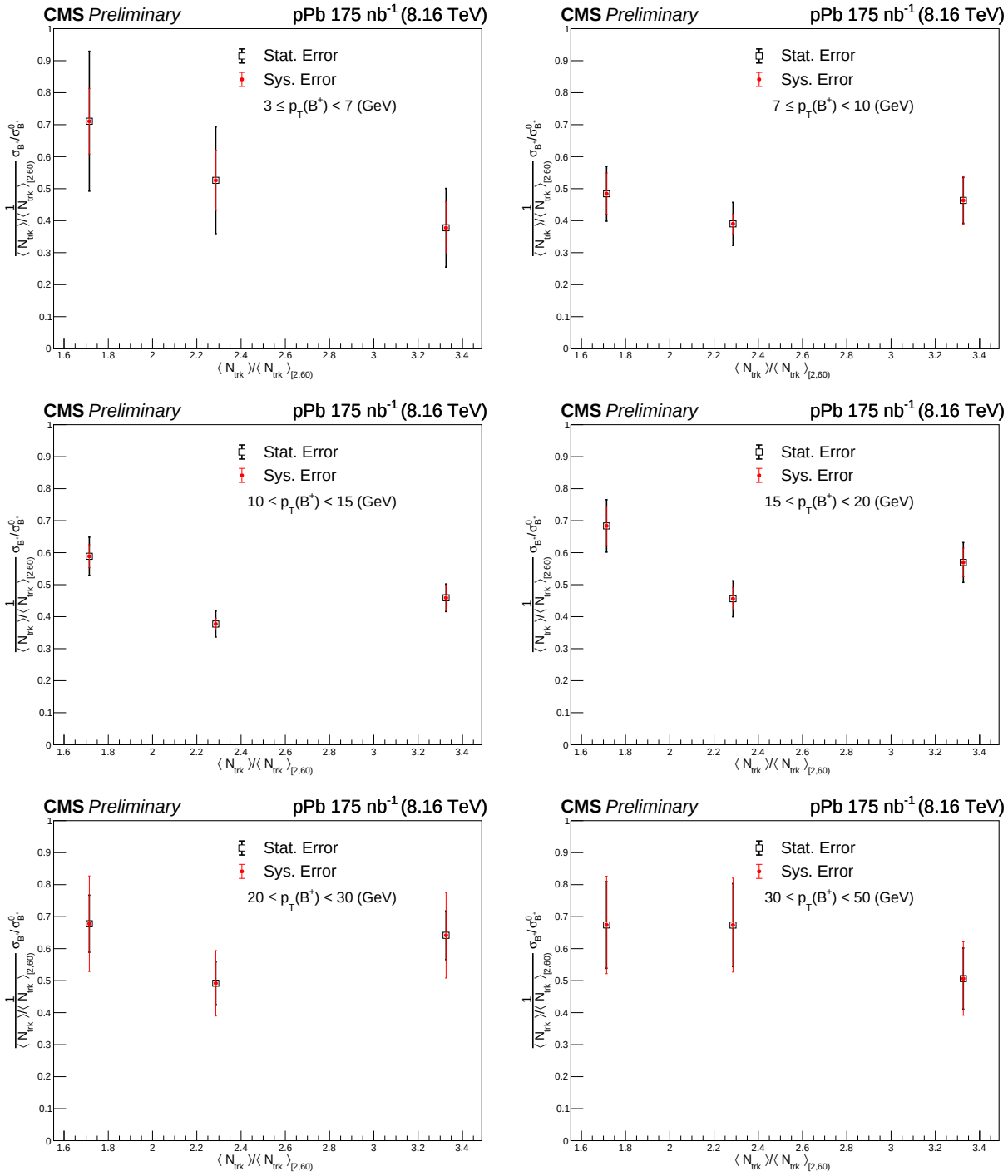

Figure 4.25: Scaled ratio of cross sections $\sigma^{\mathrm{B}^+}/\sigma_0^{\mathrm{B}^+}$ versus normalized multiplicity in the different transverse momentum ranges.

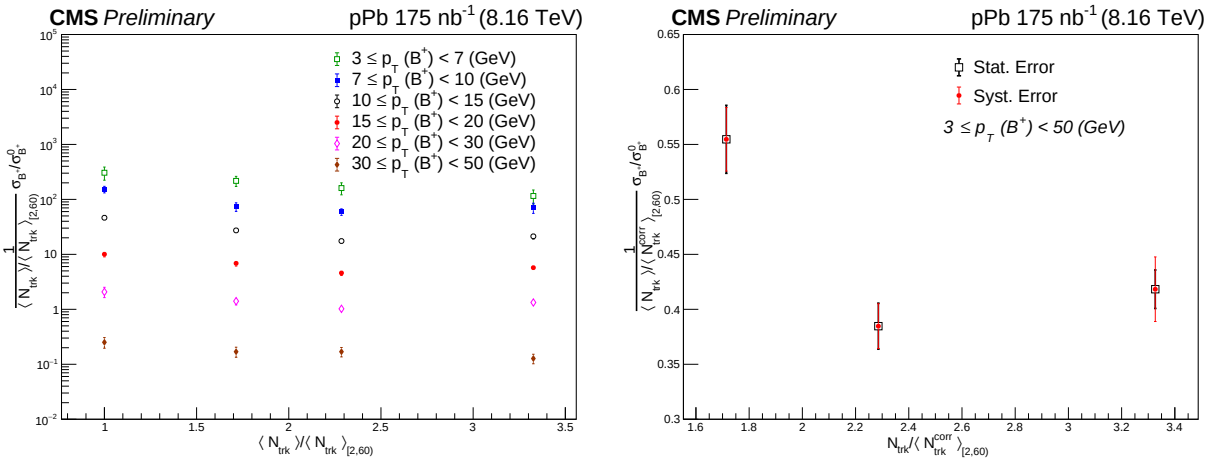

Figure 4.26: (Left) the scale B^+ differential cross-section is shown in normalized multiplicity for all the transverse momentum ranges. (Right) scale Ratio of cross sections $\sigma^{B^+}/\sigma_0^{B^+}$ in full transverse momentum range. The error bars correspond to the sum in quadrature of each systematic uncertainty computed and the statistical uncertainty.

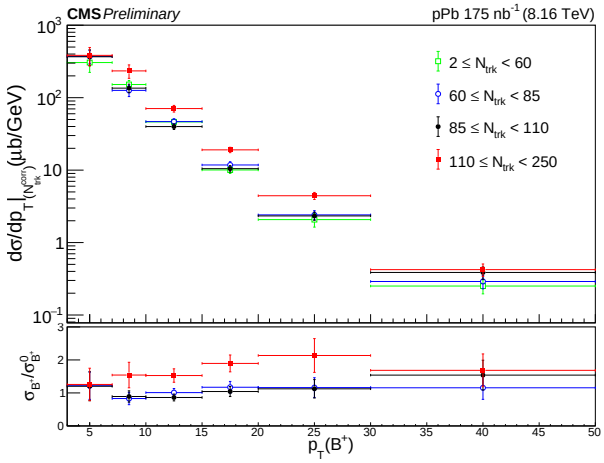

Figure 4.27: In top panel the B^+ differential cross-section is shown in p_T bins for the different multiplicity classes. Besides, the $\sigma^{B^+}/\sigma_0^{B^+}$ is shown in the bottom panel.

4.9.3 Double ratio of the nuclear modification factors

As mentioned in the introduction, the primary focus of this analysis is the ratio of nuclear modification factors, as indicated by Equation 4.4. The right-hand side of that equation is the product of a factor that depends on the centrality of the collision times the cross-section ratio.

This factor is referred to as the geometrical factor ($GF_{\mathrm{N_{ch}}}$), and it can be determined using the measured $Z \to \mu^-\mu^+$ cross-section (see Fig. **??**) in pPb collisions as a probe.

In other words, we can measure the ratio of nuclear modification factors ($R^{\mathrm{Z}}_{\mathrm{pPb}}$) for the

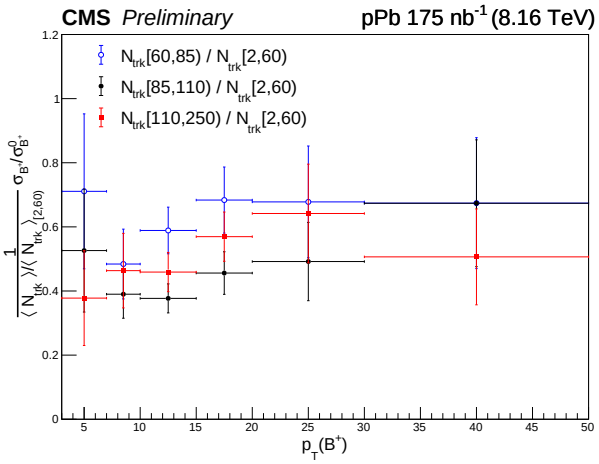

Figure 4.28: The scaled Ratio $\sigma^{\mathrm{B}^+}/\sigma_0^{\mathrm{B}^+}$ is shown in p_{T} bins. The error bars correspond to the sum in quadrature of each systematic uncertainty computed and the statistical uncertainty.

Z boson, and given the expectation that this ratio should be unity for the Z boson [93–96], the $GF_{\mathrm{N_{ch}}}$ can be determined.

Using the expression in Eq. 4.4 for the Z boson, we can write:

$$R^{\mathrm{Z}}_{\mathrm{pPb}}|_{N_{\mathrm{ch}}} \Big/ R^{\mathrm{Z}}_{\mathrm{pPb}}|_{\mathrm{low}} = GF_{\mathrm{N_{ch}}} \frac{\sigma^{\mathrm{Z}}|_{N_{\mathrm{ch}}}}{\sigma^{\mathrm{Z}}|_{\mathrm{low}}} \tag{4.14}$$

Even more, if the Eq. 4.4 is divided by the Eq. 4.14 the factors $GF_{\mathrm{N_{ch}}}$ are canceled, leaving behind only a double ratio between the B^+ meson and Z boson cross sections.

Since Eq. 4.14 should be unity the ratio of the nuclear modification factor of the B^+ meson is obtained.

In Fig. 4.29 the left plot shows the ratio of the nuclear modification factor as a function of p_{T} (B^+), while the right plot represents it as a function of the multiplicity density for the full range of the B^+ meson p_{T} .

Results on the nuclear modification factor ratio as a function of p_{T} and of charged-particle density show to be consistent with one at the current level of accuracy, therefore no medium effect can be claimed.

4.10 Conclusions

The measurement of the differential cross section $\mathrm{d}\sigma/\mathrm{dp_T}$for B^+ meson in pPb collisions at a center-of-mass energy of $\sqrt{s} = 8.16 TeV$ is presented. The data correspond to an integrated luminosity of 175 nb^{-1} collected by the CMS experiment at the LHC. The $\mathrm{B}^+ \rightarrow \mathrm{K}^+\mathrm{J}\Psi$ decays are used to measure the cross-section of the B^+ production, the results shown in Fig 4.24 is in excellent agreement with the FONLL predictions.

In addition, the dependence of the B+ cross-section on charged-particle multiplicity classes has been measured for the first time in pPb collisions, is shown in Fig 4.27.

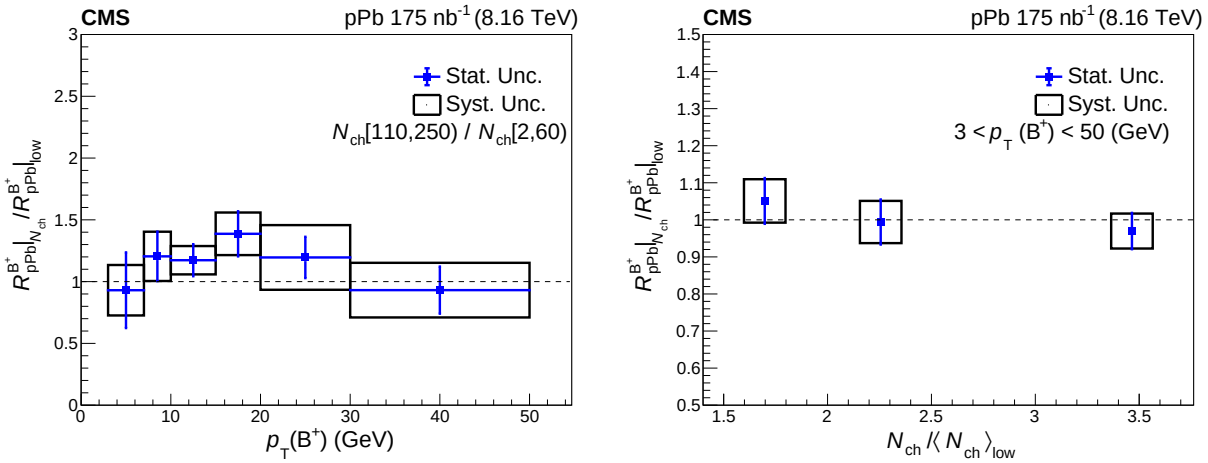

Figure 4.29: The ratio of the nuclear modification factors for B^+ in p_T bins for the highest and lowest multiplicity classes (left), and in the full p_T range and as a function of the multiplicity density (right). The error bars correspond to the statistical uncertainty, and the boxes represent the sum in quadrature of systematic uncertainties.

This measurement reveals a rising trend in the B^+ production cross section with increasing charged-particle multiplicity. Finally, the ratio of nuclear modification factors is also presented in Fig. 4.29, using a geometrical factor obtained from the same ratio measured for the Z boson.

The measurement was performed by using a novel approach without dependence on the overlap function TAA by using electroweak Z bosons. The approach presented in this work can be used to estimate possible medium effects for other small systems where TAA can not be defined directly by centrality. The result is consistent with unity, providing no evidence for medium effects in the B^+ production as a function of the charged-particle multiplicity at the present level of accuracy. This serves as a useful result for potential future studies on medium effects in b quark production in high-multiplicity events in pPb collisions.

Chapter 5

Angular Analysis of the decay $B^+ \to K^+\mu^+\mu^-$

5.1 Introduction

The angular distribution of the $B^+ \to K^+\mu^+\mu^-$gives us access to two parameters, namely A_{FB} and F_H. The A_{FB} parameter describes the asymmetry of the dimuon system, and F_H represents the contribution from the scalar, pseudo-scalar, and tensor amplitudes to the decay width. Both parameters are measured in bins of the dimuon mass squared (q^2). While the A_{FB} is predicted to be zero within the Standard Model, the F_H parameter depends on the dimuon mass squared (q^2). The measurement of these parameters provides insights into the This chapter describes the procedure we implemented to obtain the angular distribution, estimate its backgrounds, and extract the angular parameters. We also describe an implementation of the Feldman-Cousins method used to obtain 2D confidence contours in the A_{FB}-F_H plane by considering the boundaries defined by the non-negativeness of the decay width. In addition, we describe a set of sources of systematic uncertainties, considered for this analysis, being dominated by the statistical uncertainties provided by the methods described previously.

5.1.1 Motivation

The decay $B^+ \to K^+\mu^+\mu^-$is a flavor-changing neutral current (FCNC) process of the kind $b \to s\ell^+\ell^-$, (where ℓ is a lepton). This process is forbidden at the tree level and can only occur at higher orders in the Standard Model. Such decay is very sensitive to potential Physics beyond the Standard Model since it proceeds at the lowest order in SM via either a γ/Z diagram or a W^+W^- box diagram as shown in Figure 5.1, but new undiscovered heavy particles can play a role in these loops and modify the SM predictions.

5.1.2 Angular Distribution and Observables

Angular distributions are studied to retrieve the forward-backward asymmetry of the muons A_{FB}, and the contribution from (pseudo)scalar and tensor amplitudes to the decay width

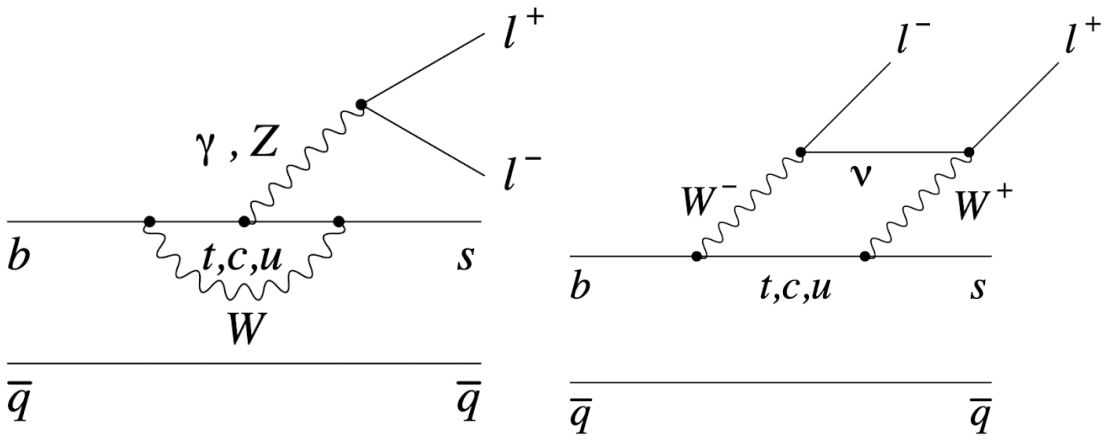

Figure 5.1: Electroweak diagrams.

F_H.

The decay rate of $B^+ \to K^+\mu^+\mu^-$as a function of $\cos\theta_l$ is given by Equation 5.1 [42], where θ_l is the angle between the direction of the μ^- (μ^+) and the direction of the K^+ (K^-) measured in the dimuon system center of mass. Figure 5.2 depicts the definition of this angle.

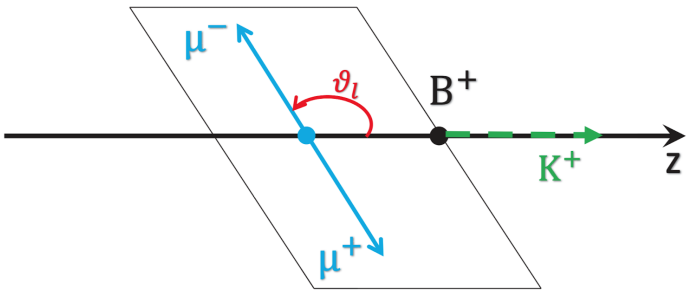

Figure 5.2: Graphical definition of θ_l.

$$\frac{1}{\Gamma_l}\frac{d\Gamma_l}{d\cos\theta_l} = \frac{3}{4}(1-F_H)(1-\cos^2\theta_l) + \frac{1}{2}F_H + A_{FB}\cos\theta_l. \tag{5.1}$$

For equation 5.1 to be physical, it should be positive for all lepton angles. Therefore, A_{FB} and F_H must satisfy, at least two conditions. This conditions can be obtained by comparing the equation 5.1 evaluated at 0 and ± 1 :

$$0 \leq F_H \leq 3, \tag{5.2}$$

$$|A_{FB}| \leq \frac{F_H}{2}. \tag{5.3}$$

These boundaries split the parameter space into two regions. However, the simple three-point evaluation does not provide the real allowed region for the parameters. A numerical

evaluation of the Equation 5.1 (which must be positive for all lepton angles) gives us a more constrained (true) physical region. The true un-physical and allowed regions can be seen in Figure 5.3.

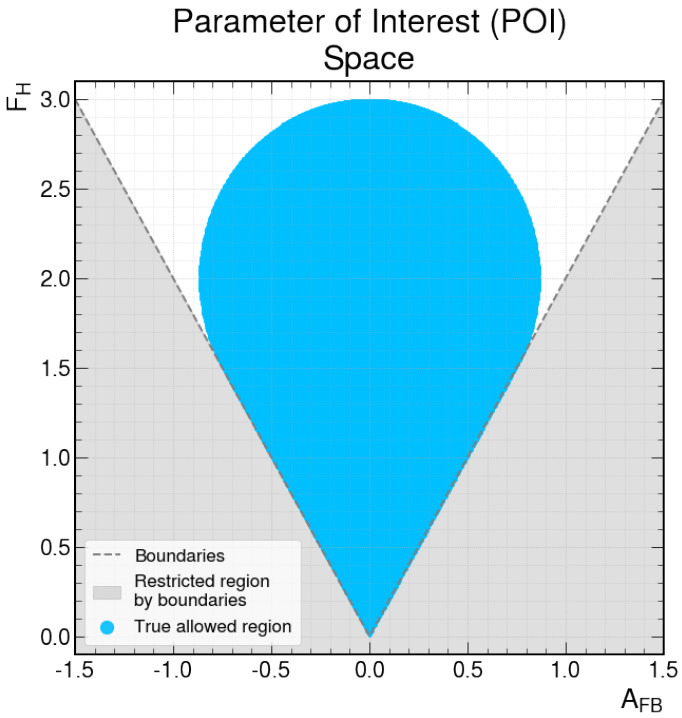

Figure 5.3: Physical constraints for the angular parameters in the differential decay width.

5.1.3 q^2 Binning

The differential decay rate in Equation 5.1 shows an integrated version of a double differential in the squared dimuon mass (q^2) and the lepton angle ($\cos\theta_l$). The integral goes from a q^2_{min} to a q^2_{max}.

Therefore, the parameters of interest A_{FB} and F_H are measured in each q^2 bin defined in Table 5.1.

The SM prediction for F_H is of the order of m^2_μ/q^2[42], and A_{FB} vanishes in $B \to K\ell^+\ell^-$ decays[97]. The values reported by flavio[98] can be seen in Table 5.1.

5.1.4 Blinding Strategy

The blinding strategy used in this analysis hides the fitted values of the parameters of interest in data. However we are not blinding the mass and angular projections on the signal region, this serves two purposes, one is to ensure having a good fit, and the other is to use the information of the yields to get an estimation of uncertainties.

The statistical and systematic uncertainties depend on the value of the parameters of interest, and we use an injection Monte Carlo (MC) sample to get an estimation. This injection sample involves a combination of a toy MC derived from the 2D background probability

Table 5.1: Binning on the dimuon invariant mass with A_{FB} and F_H predictions obtained from flavio version 2.4.0

Bin Number	q^2 Range $(\text{GeV})^2$	q Range (GeV/c^2)	$< F_H >_{flavio}$	$< A_{FB} >_{flavio}$
0	1.10 - 2.00	1.05 - 1.41	0.04460 ± 0.00031	0
1	2.00 - 4.30	1.41 - 2.07	0.02299 ± 0.00028	0
2	4.30 - 8.68	2.07 - 2.95	0.01173 ± 0.00030	0
3 (J/Ψ)	8.68 - 10.09	2.95 - 3.18	-	-
4	10.09 - 12.86	3.18 - 3.59	0.00718 ± 0.00032	0
5 ($\Psi(2S)$)	12.86 - 14.18	3.59 - 3.77	-	-
6	14.18 - 16.0	3.77 - 4.0	0.00633 ± 0.00034	0
7	16.0 - 18.0	4.0 - 4.24	0.00638 ± 0.00041	0
8	18.0 - 22.0	4.24 - 4.69	0.00792 ± 0.00063	0
9	1.10 - 6.0	1.05 - 2.45	0.02390 ± 0.00034	0
10	1.10 - 22.0	1.05 - 4.30	0.01263 ± 0.00041	0
11	[1.10, 8.68], [10.09, 12.86], [14.18, 22]	[1.05, 2.95] ,[3.18, 3.57], [3.77, 4.69]	0.03328 ± 0.00068	0

density function, coupled with a 2D sample extracted from the official signal MC dataset, both samples, signal and background, have the same size as the corresponding yields obtained from the mass projections on data.

5.1.5 Previous Measurements

The most recent measurements of the angular analysis of $B^+ \to K^+\mu^+\mu^-$decay have been conducted by the LHCb and CMS collaborations [99, 100], using data collected from proton-proton collisions at center-of-mass energies of 7 and 8 TeV. Both analyses performed a binned measurement on q^2 and measured the parameters A_{FB} and F_H.

While the LHCb analysis employed a finer binning strategy, and was limited by statistical uncertainties, the CMS analysis used a coarser binning, with statistical uncertainties dominating over systematic uncertainties in almost all bins. The presentation of results also differed between the two experiments: LHCb's results were presented as intervals, whereas CMS's results were reported as best-fit values with asymmetric uncertainties. The detailed results can be found in Tables 5.2 and 5.3.

Previous studies by Belle [101], BaBar [102], and CDF [103] also measured similar angular parameters. Belle and CDF adopted a different parametrization for the decay width, limiting their analysis to the forward-backward asymmetry and performed the analysis using the same binning. On the other hand, BaBar employed the same parametrization as CMS and LHCb, with a small difference in the naming, the parameter for the contribution from scalar and pseudoscalar amplitudes is called F_S, instead of F_H. However, only 3 q^2 bins were reported. The results are summarized in Tables 5.4 and 5.5.

q^2 Range [(GeV/c^2)^2]	F_H (stat.)	F_H (syst.)	A_{FB} (stat.)	A_{FB} (syst.)
0.10-0.98	[+0.01, +0.20]	± 0.03	[-0.09, -0.01]	± 0.01
1.10-2.00	[+0.00, +0.21]	± 0.03	[+0.00, +0.10]	± 0.01
2.00-3.00	[+0.05, +0.30]	± 0.03	[+0.01, +0.11]	± 0.01
3.00-4.00	[0.00, +0.04]	± 0.02	[-0.02, +0.01]	± 0.01
4.00-5.00	[0.00, +0.09]	± 0.03	[-0.01, +0.05]	± 0.01
5.00-6.00	[0.00, +0.14]	± 0.02	[-0.04, +0.04]	± 0.01
6.00-7.00	[0.00, +0.08]	± 0.02	[-0.01, +0.04]	± 0.01
7.00-8.00	[0.00, +0.03]	± 0.03	[-0.02, +0.02]	± 0.01
11.00-11.75	[+0.06, +0.23]	± 0.03	[+0.03, +0.12]	± 0.01
11.75-12.50	[+0.00, +0.10]	± 0.02	[+0.00, +0.05]	± 0.01
15.00-16.00	[+0.06, +0.20]	± 0.02	[-0.10, -0.03]	± 0.01
16.00-17.00	[+0.00, +0.12]	± 0.02	[-0.05, +0.00]	± 0.01
17.00-18.00	[+0.01, +0.16]	± 0.02	[-0.06, +0.00]	± 0.01
18.00-19.00	[+0.05, +0.23]	± 0.02	[-0.03, +0.05]	± 0.01
19.00-20.00	[0.00, +0.10]	± 0.04	[-0.02, +0.05]	± 0.02
20.00-21.00	[0.00, +0.14]	± 0.04	[-0.01, +0.07]	± 0.02
21.00-22.00	[+0.04, +0.41]	± 0.05	[+0.03, +0.19]	± 0.02

Table 5.2: LHCb (2014) [99] results on the angular analysis of $B^+ \to K^+\mu^+\mu^-$.

q^2 Range [(GeV/c^2)^2]	F_H	A_{FB}
1.00-2.00	$0.08^{+0.22}_{-0.19} \pm 0.05$	$0.21^{+0.29}_{-0.21} \pm 0.39$
2.00-4.30	$-0.04^{+0.12}_{-0.12} \pm 0.07$	$0.85^{+0.34}_{-0.31} \pm 0.14$
4.30-8.68	$0.00^{+0.04}_{-0.04} \pm 0.02$	$0.01^{+0.02}_{-0.01} \pm 0.04$
10.09-12.86	$0.00^{+0.05}_{-0.05} \pm 0.05$	$0.01^{+0.02}_{-0.01} \pm 0.06$
14.18-16.00	$0.01^{+0.06}_{-0.05} \pm 0.02$	$0.03^{+0.03}_{-0.03} \pm 0.07$
16.00-18.00	$0.04^{+0.05}_{-0.04} \pm 0.03$	$0.07^{+0.06}_{-0.07} \pm 0.07$
18.00-22.00	$0.05^{+0.05}_{-0.04} \pm 0.02$	$0.10^{+0.06}_{-0.10} \pm 0.09$

Table 5.3: CMS (2008) [100] results on the angular analysis of $B^+ \to K^+\mu^+\mu^-$.

q^2 Range [(GeV/c^2)^2]	F_S	A_{FB}
0.1-8.41	0	$-0.49^{+0.51}_{-0.99} \pm 0.18$
> 10.24	0	$0.26^{+0.23}_{-0.24} \pm 0.03$
> 0.1	$0.81^{+0.58}_{-0.61} \pm 0.46$	$0.15^{+0.21}_{-0.23} \pm 0.08$

Table 5.4: BaBar (2006) [102] results on the angular analysis of $B^+ \to K^+\mu^+\mu^-$.

q^2 Range [(GeV/c^2)^2]	A_{FB} (Belle)	A_{FB} (CDF)
0.00-2.00	$0.06^{+0.32}_{-0.35} \pm 0.02$	$0.13^{+0.42}_{-0.43} \pm 0.07$
2.00-4.30	$-0.43^{+0.38}_{-0.40} \pm 0.09$	$0.32^{+0.15}_{-0.16} \pm 0.05$
4.30-8.68	$-0.20^{+0.12}_{-0.14} \pm 0.03$	$0.01^{+0.13}_{-0.10} \pm 0.01$
10.09-12.86	$-0.21^{+0.17}_{-0.15} \pm 0.06$	$-0.03^{+0.11}_{-0.10} \pm 0.04$
14.18-16.00	$0.04^{+0.32}_{-0.26} \pm 0.05$	$-0.05^{+0.09}_{-0.11} \pm 0.03$
16.00-23.00	$0.02^{+0.11}_{-0.08} \pm 0.02$	$0.09^{+0.17}_{-0.13} \pm 0.03$

Table 5.5: Belle (2009) [101] and CDF (2011) [103] results on the angular analysis of $B^+ \to K^+\mu^+\mu^-$.

5.2 Data and Simulation Samples

5.2.1 Data Samples

This analysis is performed on the B Parked dataset (also known as *ParkingBPH*), recorded during the 2018 pp run, but reconstructed and processed afterward.

The dataset is divided into 4 eras (A, B, C, and D). Eras A and B are subdivided into 6 and eras C and D into 5 parts. There are approximately 10^{10} events in this dataset. The format used by this analysis is the centrally produced MiniAOD. We perform a reconstruction and a preselection of these datasets to produce NanoAOD tuples. The NanoAOD format is produced with a customized version of the BParkingNANO code which can be found in this GitLab repository. This NanoAOD producer uses the global tag (a set of instructions describing in detail the geometry and status of the CMS detector) 102X_dataRun2_v11, and is later discussed in Section 5.3.1.

Certified data by the DQM (Data Quality Monitoring) team is used. This is done through a JSON file that indicates the luminosity blocks marked as good for physics. The JSON file used for this analysis can be accessed here: https://cms-service-dqmdc.web.cern.ch/CAF/certification/Collisions18/13TeV/ReReco/Cert_314472-325175_13TeV_17SeptEarlyReReco2018ABC_PromptEraD_Collisions18_JSON.txt.

Table 5.6: Dataset names, and the corresponding luminosity for the ParkingBPH Eras. The * in the dataset names run from 1 to 6 (5) for eras A and B (C and D).

Era	Dataset	Recorded Luminosity
Run2018A	/ParkingBPH*/Run2018A-05May2019-v1/MINIAOD	4.64 fb^{-1}
Run2018B	/ParkingBPH*/Run2018B-05May2019-v2/MINIAOD	4.93 fb^{-1}
Run2018C	/ParkingBPH*/Run2018C-05May2019-v1/MINIAOD	5.51 fb^{-1}
Run2018D	/ParkingBPH*/Run2018D-05May2019promptD-v1/MINIAOD	26.50 fb^{-1}
	Sum	41.58 fb^{-1}

The integrated luminosity of each dataset is calculated with the officially recommended tool from the luminosity group, BRILCALC [104]. By following the instructions provided by the group, we obtained the information displayed in Table 5.6.

5.2.2 MC Simulation Samples

Two different signal MC samples are used. One is simulated with the BTOSLLBALL model, and the other on simple PHSP model, both implemented in EVTGEN . The BTOSLLBALL model implements the form factors calculated by P. Ball et. al. [97], and produces angular distributions that follow SM predictions. The second type, the one decayed using the Phase Space (PHSP) model, has the advantage of producing flat distributions on the angular observable, which aids us in modeling the detection and selection efficiency.

While the PHSP simulation is intended for efficiency purposes, the BTOSLLBALL, which follows more realistic distributions, is used for assessing the efficiency and optimizing the

signal selection in data.

Additional official samples for the resonant channels $B^+ \to K^+ J/\psi(1S)(\mu^-\mu^+)$and $B^+ \to K^+\psi(2S)'(\mu^-\mu^+)$were used for the optimization and validation of the analysis in these control channels. This study is discussed in detail in Section 5.7.2.

To asses the effect of the $B^+ \to \pi^+\mu^+\mu^-$, we used an appropiate sample along with its J/Ψ counterpart.

All MC samples are generated with PYTHIA version 8 [105], and particles containing b quarks are decayed with the EVTGEN package [106].

All stable particles are passed through the CMS detector simulation based on GEANT 4, then, minimum bias samples are added to the event to represent the pileup as seen on the data.

Finally, the same reconstruction and selection algorithm applied to data (Section 5.3) is also applied to all Monte Carlo samples.

Table 5.7: Official Monte Carlo datasets. The number of completed events and filter efficiency values were taken from the McM web page.

Process	Filters	Completed events	ϵ_{filter}	McM	DAS
$B^+ \to K^+\mu^+\mu^-$BTOSLLBALL	Mu filter	40 665 765	0.012 ± 0.001	link	link
$B^+ \to K^+\mu^+\mu^-$BTOSLLBALL	Kinematic relaxed cuts	9 925 123	0.289 ± 0.004	link	link
$B^+ \to K^+\mu^+\mu^-$PHSP	Mu filter	37 588 442	0.012 ± 0.001	link	link
$B^+ \to K^+\mu^+\mu^-$PHSP	Kinematic relaxed cuts	9 987 860	0.271 ± 0.004	link	link
$B^+ \to K^+ J/\psi(1S)(\mu^-\mu^+)$	Mu filter	15 134 486	0.064 ± 0.002	link	link
$B^+ \to K^+ J/\psi(1S)(\mu^-\mu^+)$	No filters	2 985 972	0.6739 ± 0.005	link	link
$B^+ \to K^+\psi(2S)'(\mu^-\mu^+)$	Mu filter	10 164 669	0.0671 ± 0.005	link	link
$B^+ \to K^+\psi(2S)'(\mu^-\mu^+)$	No filters	3 031 009	0.671 ± 0.005	link	link
$B^+ \to \pi^+\mu^+\mu^-$	–	–	–	link	link
$B^+ \to J/\Psi\pi^+$	–	–	–	link	link

5.2.3 Trigger

The trigger menu used to record the *ParkingBPH* dataset, required the presence of a single, displaced muon [107]. At L1, the triggering μ requires $|\eta| < 1.5$ and a p_T threshold from 12 to 7 GeV . In addition to the requirements of the L1 seed, HLT also requires thresholds on the significance of the muon's track impact parameter ($IP/\sigma_{IP} = IP_{sig}$).

The set of HLT paths used in this analysis has the following naming scheme: HLT_MuX_IPY. Where X(Y) stands for the $p_T(IP_{sig})$ threshold. The complete integrated luminosity collected by each HLT path used in this analysis can be found in Table 5.8.

The idea behind this trigger structure is that the events firing any of these paths can be thought of as a pp interaction where a pair of b quarks is produced, one of them decaying as $b \to \mu X$. This one will identify the tag side. On the other side, named signal-side, the B meson decays freely, *i.e.* it is unbiased. However, after analyzing the data, the majority of

Table 5.8: Total recorded luminosity in fb^{-1} for each HLT path used in this analysis. Luminosity by path should not be summed since they are not exclusive partitions.

Path Name	Run2018A	Run2018B	Run2018C	Run2018D	Total
HLT_Mu7_IP4	0.000	0.365	0.150	6.415	6.930
HLT_Mu8_IP3	0.442	0.718	0.010	0.404	1.574
HLT_Mu8_IP5	0.000	0.000	0.000	8.251	8.251
HLT_Mu8_IP6	0.000	0.000	0.000	8.251	8.251
HLT_Mu8p5_IP3p5	0.316	0.000	0.000	0.000	0.316
HLT_Mu9_IP4	0.000	0.000	0.000	0.002	0.002
HLT_Mu9_IP5	0.000	1.367	2.691	16.822	20.881
HLT_Mu9_IP6	4.638	4.323	3.831	20.769	33.361
HLT_Mu10p5_IP3p5	0.316	0.000	0.000	0.000	0.316
HLT_Mu12_IP6	0.000	2.673	5.508	26.505	34.686
Total Recorded Luminosity	4.638	4.932	5.508	26.505	41.583

reconstructed B mesons fall on the tag side. That is why we will consider only these types of events.

5.3 Event Selection

The process $B^+ \to K^+\mu^+\mu^-$, was reconstructed in its fully final charged state. The charge conjugates are implied throughout the analysis unless otherwise stated.

First of all, events are required to pass any of the displaced single muon HLT triggers described in Section 5.2.3. Events are manipulated to select and create candidates for muons, dimuons, kaons, and finally B mesons. This is done using a customized version of the BParkingNano code (NanoAOD producer) developed for the lepton flavor universality test via the $R(K)$ measurement.

5.3.1 Overview of the NanoAOD producer.

The NanoAOD production starts by selecting a set of muons and identifying possible triggering muons (μ_{trg}). Muons from the `slimmedMuons` container, here we find muons with $p_T > 5\,\text{GeV}$ or muons reconstructed by the Particle Flow algorithm.

All of these muons are considered for trigger matching. This matching is based on the `triggerObjectMatch` method of the `PAT` muons. If no selected muons are matched to a trigger object, the event is then discarded.

Selected muons are used as input for a dimuon producer. We do a kinematic vertex fit for two opposite sign muons, and we keep them if their tracks are compatible; *i.e.* they come from the same vertex.

The K^+candidates are selected from all charged hadron candidates of the Particle Flow algorithm. Minimum requirements are applied on the distance in the z-axis concerning the closest trigger muon. And a minimum number of pixels and strip hits.

Finally, each dimuon and kaon candidates are iterated to produce B meson candidates. All combinations of dimuons and kaons are considered. A final kinematic vertex fit is done for the $\mu\mu K^+$ triplet where soft requirements are imposed on the produced candidate.

The output is a NanoAOD format that contains several candidates per event and is accessible using simple the ROOT framework alone. The previous procedure and following selections are applied equally to Data and MC samples.

5.3.2 Selected Muons

All muons are taken from the `slimmedMuons` container, and trigger objects from the `slimmedPatTrigger` container.

Triggering Muon

For each muon, the `triggerObjectMatch` method is evaluated with every HLT path of the form `HLT_MuX_IPY_part*`. If more than one reco muon was matched to the same HLT object, a selection based on the minimum ΔR is performed to eliminate the multiple matches.

Selected Muons

The selected muons collection, which is used for the subsequent reconstruction, consist of all the triggering and non-triggering muons that comply with the threshold ($dz < 1.0$ cm) *w.r.t.* any triggering muon.

5.3.3 Dimuon Selection

Dimuon candidates are formed with two oppositely charged `Selected Muons`.

A `KinematicVertexFit` is applied to those muon pairs satisfying the following conditions:

- 0 GeV/$c^2 < m(\mu\mu) < 5$ GeV/c^2 ;
- $p_T(\mu_1) > 1.5$ GeV/c : leading muon transverse momentum higher than 1.5 GeV/c ;
- $\Delta z(\mu^+, \mu^-) < 1$ cm ;
- $\Delta R(\mu^+, \mu^-) > 0.03$.

Those candidates with a successful vertex fit will be considered for the B meson reconstruction. They also have to satisfy these conditions on the vertex fit output:

- Secondary Vertex probability $> 1 \times 10^{-5}$

5.3.4 K^+ Candidates

Hadron tracks are selected from the `packedPFCandidates` container, each particle flow candidate is checked to have track details `hasTrackDetails` and a `|pdgId| = 211` corresponding to all charged hadrons. The pre-selection cuts applied to the tracks are:

- $|\eta| < 2.5$;
- $\Delta R(K^+, \mu_{trg}) > 0.03$;
- $\Delta z(K^+, \mu_{trg}) < 1\,\text{cm}$

Then, these selected candidates are considered as K^+meson candidates throughout the reconstruction procedure, and the mass of the charged kaon is assigned when needed.

5.3.5 B^+ Meson Selection

To produce a B^+candidate, each combination of a dimuon and K^+candidate is considered. If the B^+candidate satisfies:

- $p_T > 3.0\,\text{GeV}/c$;
- $\min(\Delta R(K^+, \mu^+, \mu^-)) > 0.03$;
- $4.0\,\text{GeV}/c^2 < m(B^+) < 7.0\,\text{GeV}/c^2$

Then a vertex fit is applied to the two muons plus the K^+candidate. If the vertex fit is successful, the B^+will be considered a candidate if its fitted variables satisfy the following conditions:

- Secondary vertex probability > 0.001
- $\cos(\Theta) > 0$. Where Θ is the 2D[1] angle between the (fitted) momentum of the B^+candidate and the vector joining the Beam Spot and the SV.
- $4.8\,\text{GeV}/c^2 < m_{Fitted}(B^+) < 5.8\,\text{GeV}/c^2$

Primary Vertex selection

The primary vertex selected for each candidate was based on the 3D pointing angle, whose definition is given by Eq. 5.4.

$$\cos\alpha = \frac{(\vec{SV} - \vec{PV}) \cdot \vec{P}_{B^+}}{|\vec{SV} - \vec{PV}||\vec{P_{B^+}}|} \tag{5.4}$$

Where $\vec{PV}(\vec{SV})$ are the coordinates of the primary(secondary) vertex and $\vec{P_{B^+}}$ is the 3-momentum of the B candidate.

For each vertex of the `offlineSlimmedPrimaryVertices` container we evaluate the $\cos\alpha$. The PV with the highest $\cos\alpha$ is selected and used to evaluate the transverse flight distance (L_{xy}), its significance, and the Proper Decay Length (PDL).

[1] 2D version of the $\cos\alpha$ used in Sec. 5.3.6. For the 2D(3D) evaluation, the Beam Spot(Primary Vertex) is used as a "reference point".

5.3.6 Offline Event Selection

The offline event selection is composed of quality cuts, a multivariate classifier (XGBoost), kinematic cuts, and special selections. The special selections were driven to remove backgrounds observed previously.

The quality cuts that must be met by each candidate, are the following:

- Medium ID muons,
- High purity tracks,
- Number of hits in track ≥ 5,
- Number of pixel hits ≥ 1,

For the Medium ID is selected to reject in-flight decays of kaons and pions to muons. Its performance was tested on the invariant mass of the track and the muon of the opposite sign, both were taken from the final B meson candidate triplet. Two different mass hypotheses were tested:

- the selected μ with the K mass and the track with the π mass,
- the selected μ with the π mass and the track with the K mass,

In Figure 5.4, we show the effect of two identification algorithms, where the Medium ID performs better than the Soft ID in rejecting this background.

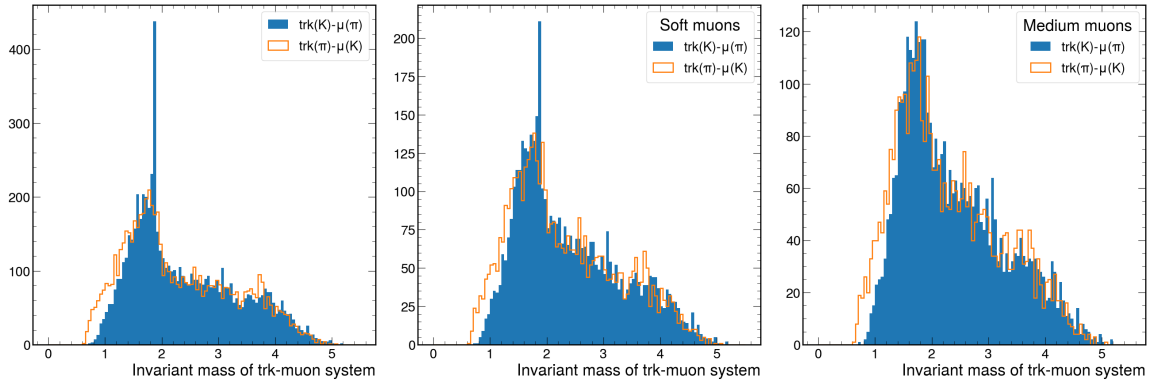

Figure 5.4: The invariant mass distribution for the track and the muon of the opposite sign under two mass hypotheses, and different Muon ID requirements. The plot on the left, show a peak around 1.8 GeV/c^2 , corresponding to the $D0$ mass. The soft muon ID, applied in the middle plot shows a reduction of this peak, but this background is still present. On the last plot, medium ID was required for both muons of the B candidate. From this set of plots, we decided to use the MediumID to remove the background of muons from decays in-flight.

The full description of the Medium ID can be found in this link. However, one of its distinctive features is kink finder variable, which searches for abrupt changes in the tracks.

On the other hand, to define the `highPurity` flag for the tracks, cuts are applied on:

- The track χ^2/DOF,
- The track d_0 to the beam spot,
- The track Δz to the position closest HLT primary vertex,
- The $d_0/\delta d_0$ transverse compatibility with the beam spot, and
- The $\Delta z/\delta z_0$ longitudinal compatibility with the closest HLT vertex.

The description of the algorithm to define the `highPurity` flag and more details can be found elsewhere [108, 109].

Resonance Vetoes

The discrimination between the signal ($B^+ \to K^+\mu^+\mu^-$) and the two resonant channels ($B^+ \to K^+ J/\psi(1S)(\mu^-\mu^+)$and $B^+ \to K^+\psi(2S)'(\mu^-\mu^+)$), is based on a selection in the dimuon invariant mass and its uncertainty from the vertex fit, $m(\mu^+\mu^-), \sigma_{m_\mu^+}\mu^-$, and the B candidate mass.

The selection is used to remove events from the resonances, its main usage is to get a background sample not contaminated by the resonances. This background sample is used in the BDT training. In the remaining analysis, the resonance vetoes are not relevant since the width of the binding is wider than the resonance vetoes.

The resonance veto window is centered around the mass of the resonances given by the PDG[25] (3.0969 GeV/c^2 for $J/\psi(1S)$, and 3.6861 GeV/c^2 for $\psi(2S)'$). We remove events that are close to the resonances, less than 3 ($\psi(2S)'$) and 5 ($J/\psi(1S)$) times the uncertainty on the mass.

- $|m(\mu\mu) - m(J/\psi(1S))_{PDG}| < 5\sigma_{m(\mu\mu)}$,
- $|m(\mu\mu) - m(\psi(2S)')_{PDG}| < 3\sigma_{m(\mu\mu)}$.

In Figure 5.5, we show the effect of the resonance veto on the dimuon invariant mass.

B^+&Ψ veto

This selection served the same purpose as the resonance veto. It was shown by previous and current analyses [110–112] that a rejection of events with $|(m_{B^+PDG}) - m(K\mu\mu)) - (m_{XPDG} - m(\mu\mu))| < \Delta m_X$ can be applied to effectively remove the radiative tail contribution from $J/\psi(1S)$and $\psi(2S)(2S)$ resonances which escape the *resonance veto*, and therefore, leaks to adjacent q^2 bins; namely, bins 3, 5, and 7.

This veto can be seen in the $m(K\mu\mu)$ vs $m(\mu\mu)$ plane as two diagonal stripes as in Figure 5.6, where the parameter Δm_X represents the width of the stripes. This parameter, the width of the stripes, is optimized for each q^2 bin and for each resonance, therefore, the veto is composed of four stripes.

To prevent the *right* stripes from increasing indefinitely, we set an upper threshold on the $m(\mu\mu)$ to be applied to each resonance veto. The value of these thresholds are 3.43 GeV/c^2 and 3.92 GeV/c^2 for the $J/\psi(1S)$and $\psi(2S)(2S)$ resonances, respectively.

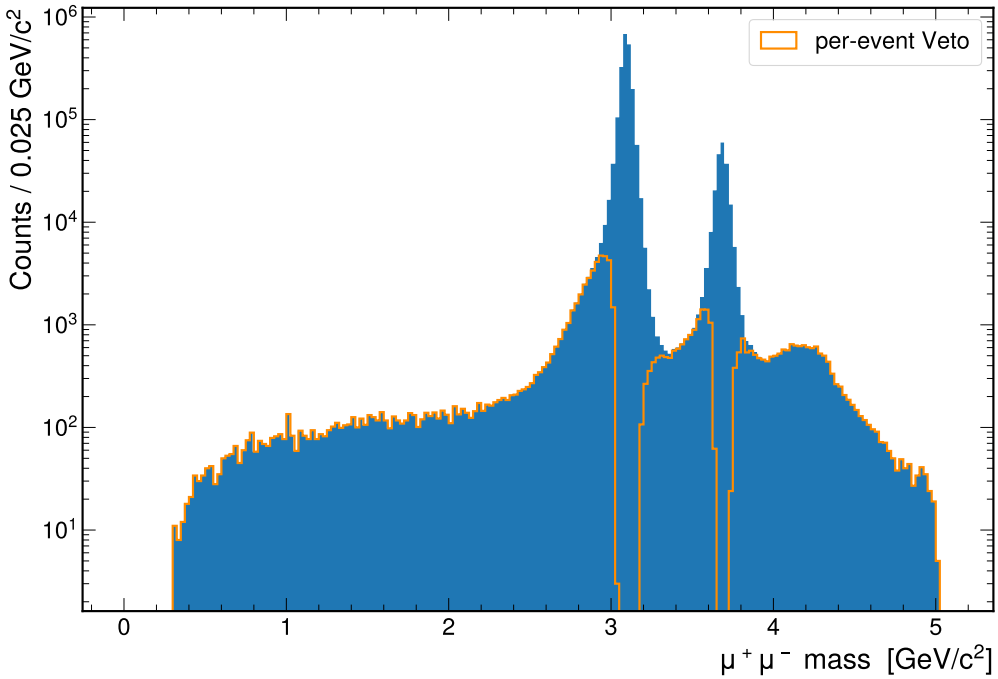

Figure 5.5: Dimuon invariant mass distribution after the multivariate classification (with XGB), before and after the resonance veto. we used a window of 5 sigma window for J/ψ(1S) and 3 sigma window for the ψ(2S)′

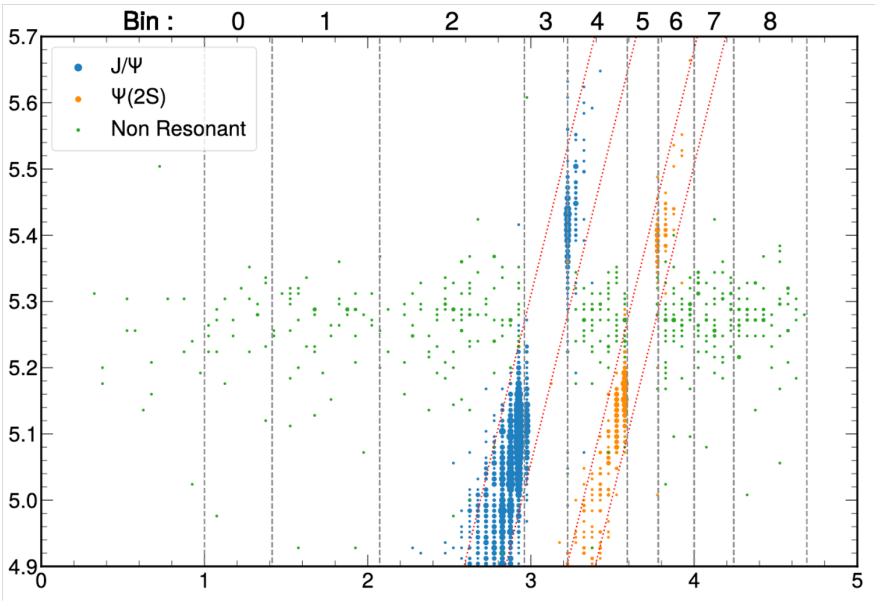

Figure 5.6: Monte Carlo distributions of the non-resonant channel as well as the J/ψ(1S)and ψ(2S)(2S) resonances.

Finally, we have a set of 4 stripes for each of the three q^2 bins of interest. The description of this veto is described in three regions of q^2, as follows:

For m($\mu\mu$) $\leq$ m$_{\mathrm{J}/\psi(1\mathrm{S})\mathrm{PDG}}$:

- $|(\mathrm{m}(\mathrm{K}\mu\mu) - \mathrm{m}_{\mathrm{B^+PDG}}) - (\mathrm{m}(\mu\mu) - \mathrm{m}_{\mathrm{J}/\psi(1\mathrm{S})\mathrm{PDG}})| < 137\,\mathrm{MeV}/c^2$;

For $\mathrm{m}_{\mathrm{J}/\psi(1\mathrm{S})\mathrm{PDG}} < \mathrm{m}(\mu\mu) \leq \mathrm{m}_{\psi(2\mathrm{S})(2S)\mathrm{PDG}}$:

- $|(\mathrm{m}(\mathrm{K}\mu\mu) - \mathrm{m}_{\mathrm{B^+PDG}}) - (\mathrm{m}(\mu\mu) - \mathrm{m}_{\mathrm{J}/\psi(1\mathrm{S})\mathrm{PDG}})| < 134\,\mathrm{MeV}/c^2$ or
- $|(\mathrm{m}(\mathrm{K}\mu\mu) - \mathrm{m}_{\mathrm{B^+PDG}}) - (\mathrm{m}(\mu\mu) - \mathrm{m}_{\psi(2\mathrm{S})(2S)\mathrm{PDG}})| < 97\,\mathrm{MeV}/c^2$ and $(\mathrm{m}(\mu\mu) < 3.43\,\mathrm{GeV}/c^2)$;

For $\mathrm{m}_{\psi(2\mathrm{S})(2S)\mathrm{PDG}} < \mathrm{m}(\mu\mu)$:

- $|(\mathrm{m}(\mathrm{K}\mu\mu) - \mathrm{m}_{\mathrm{B^+PDG}}) - (\mathrm{m}(\mu\mu) - \mathrm{m}_{\psi(2\mathrm{S})(2S)\mathrm{PDG}})| < 44\,\mathrm{MeV}/c^2$ and $(\mathrm{m}(\mu\mu) < 3.92\,\mathrm{GeV}/c^2)$;

The final shape of the veto, with the parameters previously discussed, can be seen in Figure 5.7.

B p_T cut

Candidates with no triggering muons produce a peaking background in the angular observable; an accumulation of events at $\cos\theta_l = \pm 1$ was observed as as can be seen in the right orange histogram of Figure 5.8.

We noticed that a cut on the $\mathrm{B}^+ p_\mathrm{T}$ had a direct effect on this background, and at the same time it does not introduce issues on the B mass fits.

The optimization of this cut was made by a fit to data. The contribution of the signal was modeled by a Johnson's SU distribution and the background component was modeled by a Gaussian plus an exponential. The yields obtained were used to evaluate the Figure of Merit, FOM, $(S/\sqrt{S+B})$. The maximum value was obtained at 12.98 GeV/c , to simplify, a cut on B $p_T > 13.0\,\mathrm{GeV}/c$ is applied.

μ p_T cut

The transverse momentum of the leading muon, in data, has a threshold of around 7 GeV/c , as Figure 5.9 shows, on the other hand, the trailing muon's p_T can get as low as 2 GeV/c in data. We keep events that satisfy the following criteria:

- $\mu_{\mathrm{leading}} > 7\,\mathrm{GeV}/c$
- $\mu_{\mathrm{trailing}} > 3\,\mathrm{GeV}/c$

In Figure 5.9, we show a comparison of the leading and trailing muon p_T distributions on data and Monte Carlo. On the right, is the B mass distribution before and after applying these cuts. The difference in both histograms indicates a uniform effect on the B mass variable.

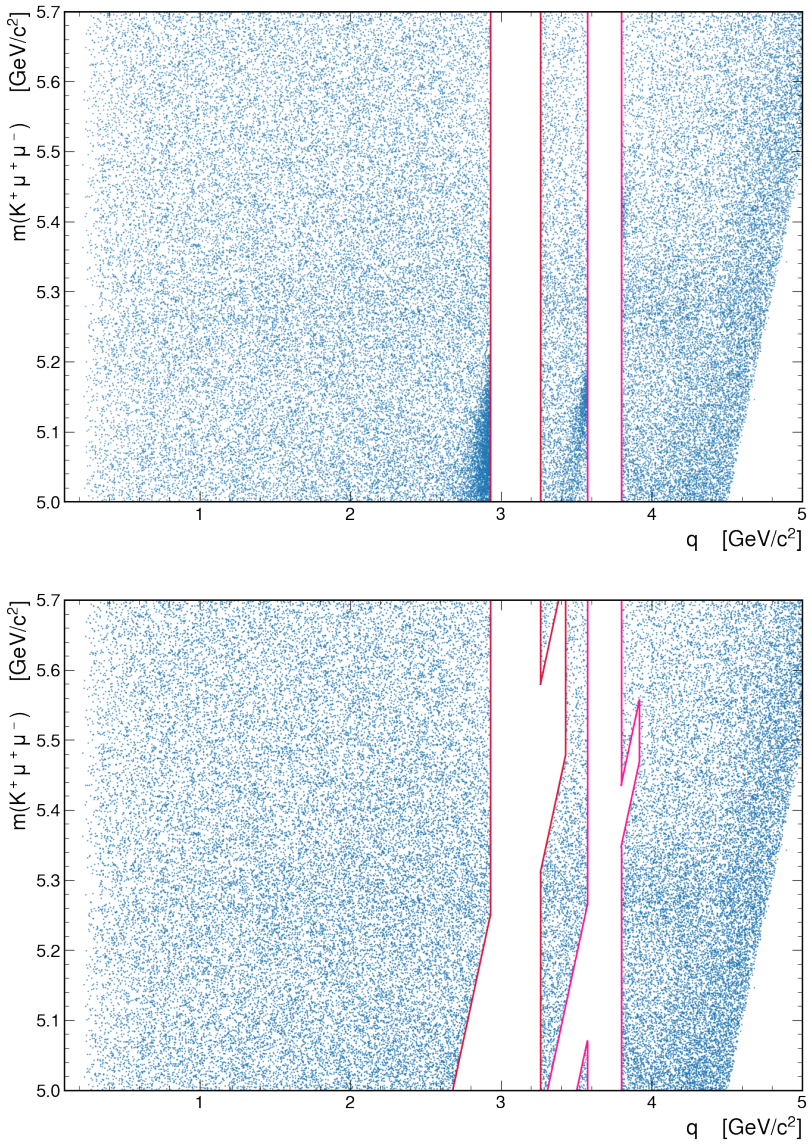

Figure 5.7: Scatter plot of the B mass and Dimuon mass. The diagonal contribution can be seen in the upper plot. Loose cuts on the significance of the L_{xy} displacement and muon ID were applied to show this contribution. On the bottom, the boxes are plotted with the optimized parameters.

XGBoost

To reduce the amount of background we use the XGBoost[113] Classifier within the scikit-learn [114] interface.

The classifier is a Gradient Boosting Algorithm, composed of a large number of decision trees, each of these trees is adjusted iteratively by taking into account the weaknesses of the previous trees. The ensemble of trees provides a set of rules to determine if a given event belongs to one class or another. The information of the cuts in each tree can be encoded as internal weights. The variables used for the classification are referred as input variables, and

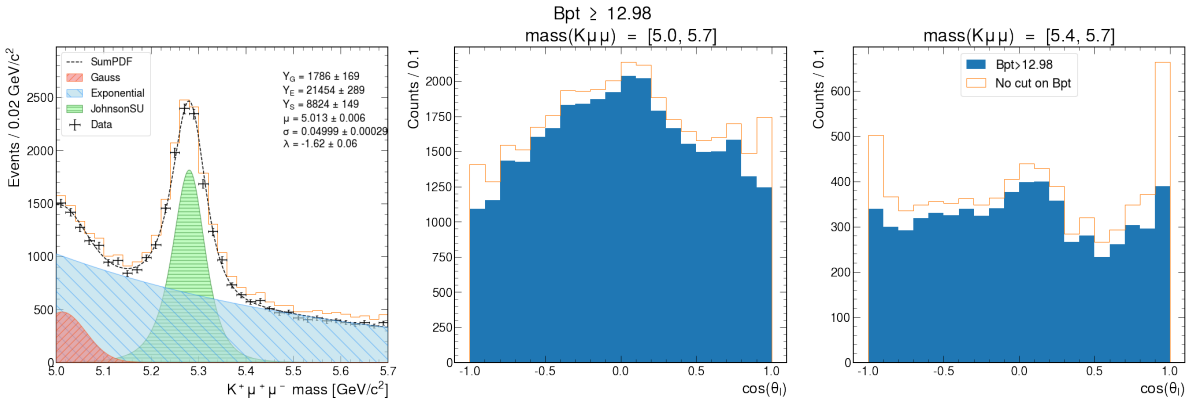

Figure 5.8: Cut optimization on the transverse momentum of the B candidate. On the left, the models used by the fit to data to obtain S and B for the optimization of the FOM. At the center, the distribution of the $\cos\theta_l$ for the complete B meson mass window (5.0 - 5.7 GeV/c^2). On the right, the angular distribution of the right sideband (5.4 - 5.7 GeV/c^2)

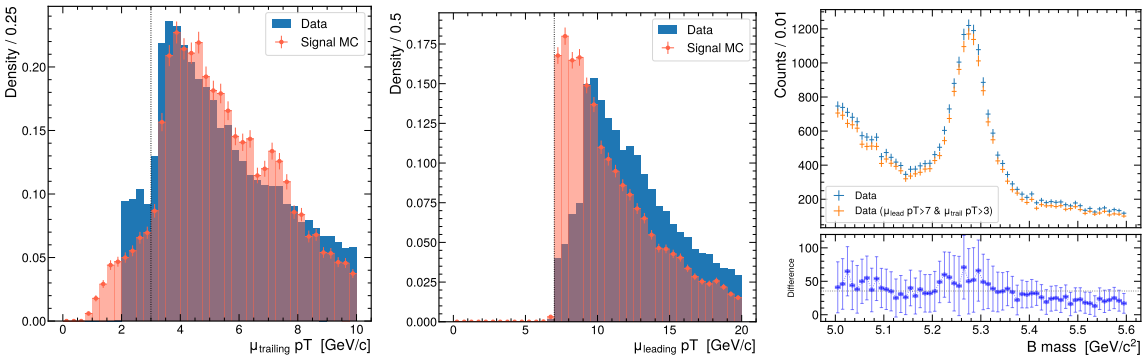

Figure 5.9: Distribution of the transverse momenta of the muons after applying the selection criteria. The signal Monte Carlo exhibits the expected sharp feature at 7 GeV , which reflects the lowest p_T threshold of the single muon triggers: HLT_Mu7_IP4. For data, a smoother distribution is observed due to the non-trivial definition of the trigger menu during data-taking. These distributions support the p_T selection applied to the leading (trailing) muon at 7 (3) GeV . Finally, the plot on the right shows that this selection does not introduce any undesired effect on the invariant mass of the $\mu^+\mu^- K^+$ triplet.

the classifier is then a function of the input variables and parameterized by a set of weights. The output of the classifier runs from 0 to 1, and one can interpret the output as probability.

The input variables are: B p_T, K p_T, Probability of SV, $L_{xy}/\sigma_{L_{xy}}$, 3D pointing angle ($\cos\alpha$), and Proper Decay Length (PDL). Figures 5.10 and 5.11 show a comparison of the input variables in data sidebands and signal MC.

- B p_T: Transverse momentum of the B^+;
- K p_T: Transverse momentum of the K^+;
- signLxy: Significance of the transverse distance from the Primary Vertex to the Secondary Vertex, *i.e.* L_{xy}/σ_{Lxy}, where $L_{xy} = \sqrt{(PV_x - SV_x)^2 + (PV_y - SV_y)^2}$ and its

uncertainty, σ_{Lxy}, is obtained propagating the Secondary Vertex and the PV uncertainties;

- PDL: Proper Decay Length, is defined as: $cl_{xy}\frac{M}{Bp_T}$. Where l_{xy} is the flight distance from the primary vertex to the secondary vertex, projected on the transverse component $\vec{p_T}$ of the B candidate, and M is the mass of the B^+meson given by the PDG;
- prob: Probability of the secondary vertex;
- $\cos(\alpha)$: Cosine of the pointing angle, the definition is given by Eq 5.4.

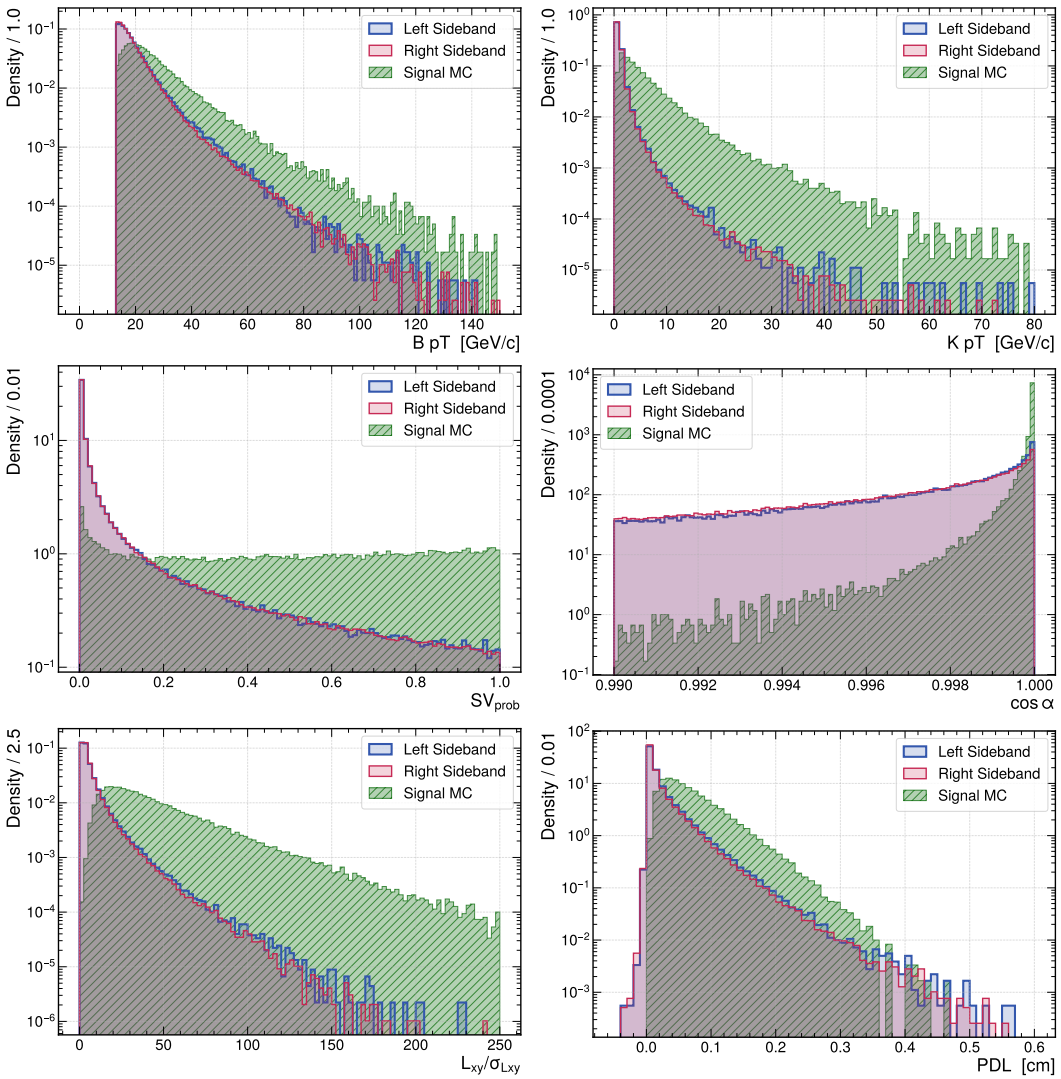

Figure 5.10: Comparison of data sidebands ($B_{mass} \in [5.0, 5.15]\,\mathrm{GeV}/c^2 \cup [5.4, 5.7]\,\mathrm{GeV}/c^2$) and signal distributions. Real Data is taken randomly from the complete dataset. The input or training variables are:$\mathrm{B}^+p_\mathrm{T}, \mathrm{K}^+p_\mathrm{T}, \cos(\alpha)$, probability of secondary vertex , Proper Decay Length and $L_{xy}/\sigma_{L_{xy}}$

.

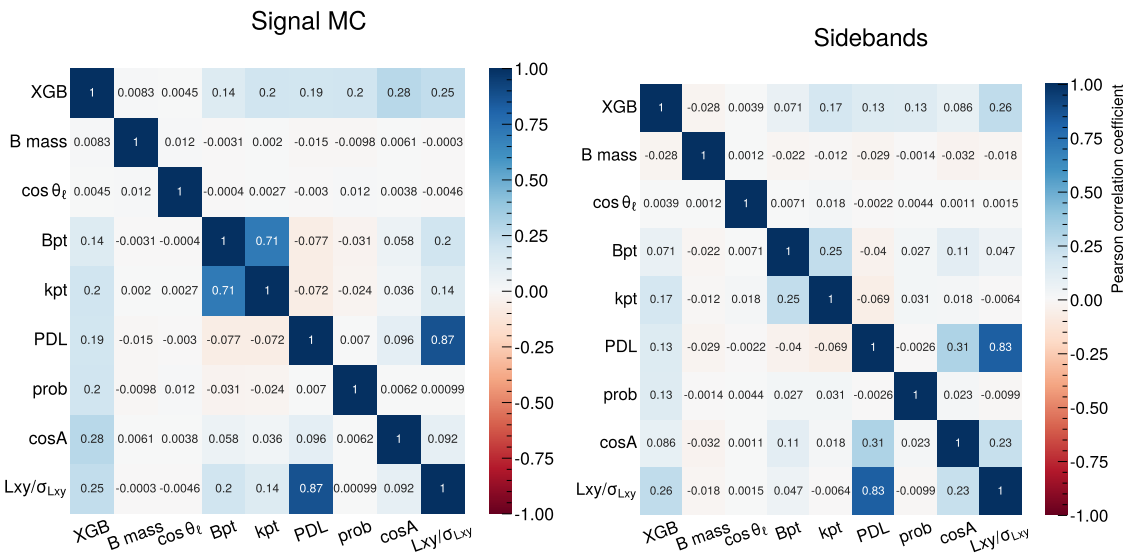

Figure 5.11: Pearson's correlation coefficient for the six variables used to train the XGB classifier.

The internal weights of the classifier are optimized given a differentiable convex cost (or loss) function, that compares the output of the classifier and the original class of a given event. The optimization process is known as training.

We perform the training step with two kinds of events. The first is Monte Carlo events from the BTOSLLBALL official generation, and the other is data sideband events.

The sidebands are defined by a cut in the B mass. Left sideband (5.0 - 5.15 GeV/c^2) and right sideband (5.4 - 5.7 GeV/c^2) events have similar distributions as can be seen from Figure 5.10. Both sidebands are used for the training dataset.

For the background sample used to train the classifier, we randomly selected 4 million events at the NanoAOD level. These events were drawn from both sidebands and from the complete dataset, which contains all eras. The official BTOSLLBALL Monte Carlo sample is used as the signal component. Additionally, the previously mentioned cuts on the transverse momentum of the B candidate and the muons were applied to both the background and signal samples.

In Chapter 5.5.3, we discuss a set of corrections used to replicate the effect of the dynamic nature of the trigger during data acquisition. This effect is absent in the production of the official Monte Carlo, and therefore, if not accounted for, it could introduce bias and hinder the performance of the classifier.

As these corrections are analysis-independent, we apply them at this stage. However, for the sake of simplicity, we only include the Accept/Reject algorithm and do not apply the Scale Factors.

This set of events was later randomly split into 70% for training and 30% for validation. The hyperparameters used for training the classifier can be found in Figure 5.12.

To evaluate the performance of the classifier we use the ROC (Receiver operating characteristic) curve. This curve is created by plotting the true positive rate vs the false positive rate obtained by different thresholds on the XGB output. The true positive rate is the signal

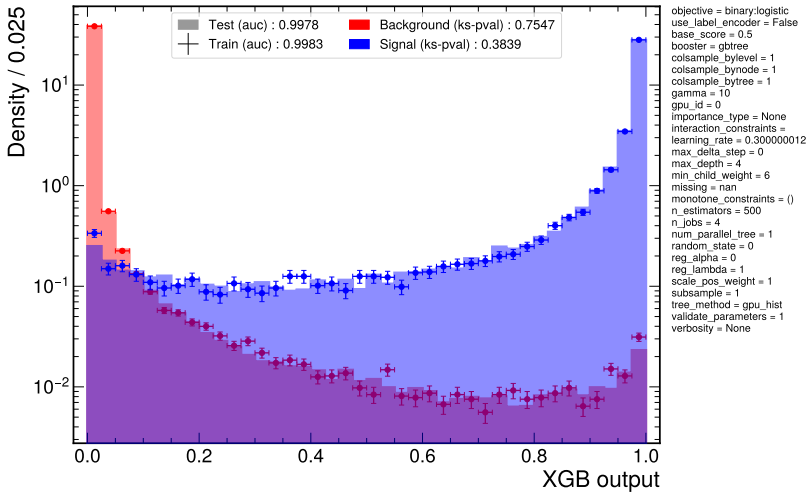

Figure 5.12: Overtraining of the classifier measured by comparing signal and background distributions of the XGBoost output. From the plot it can be seen that the p value of KS test is greater than 0.1 when comparing train and validation datasets. The hyperparameters used for this classifier are shown on the right of the plot.

efficiency (number of accepted signal events divided by the total of signal events S_{pass}/S_{total}) while the false positive rate is the background efficiency (number of accepted background events divided by the total of background events B_{pass}/B_{total}). Background efficiency, that is, the number of background events that pass the selection divided by initial background events is equal to 1 minus the background rejection, the number of rejected background events divided by the number of initial background events.

A random classifier (e.g. tossing a coin) should yield a ROC curve along the line joining the points (0,1) and (0,0), the area of such curve is 0.5. On the other hand, an ideal classification should have signal efficiency equal to 1 and background efficiency equal to 0, that is accepting all signal events while rejecting all background events. The ideal classification should be located at the right top corner, giving signal efficiency and background rejection equal to 1. Therefore, a measure of the performance is given by the area under the ROC curve (*auc*), the greater the *auc*, the greater the discriminating power. Figure 5.13 shows the ROC curve for test and train samples, and its comparison with a straight line representing the random choice. The x axis is plotted in log scale for the sake of visualization.

The overfitting is evaluated by a comparison of the XGB output distributions for signal and background train samples *w.r.t.* test samples. A Kolmogorov-Smirnov test is applied to signal and background distributions, and we accept the null hypothesis with a p-value greater than 0.10. Additionally, the overtraining can be measured by comparing the *auc* of the test and training ROC curve, the model had a variation of 0.01% of the training vs. test *auc*.

Once the training has been completed, a cut on the classifier output must be determined. This cut is called a working point (WP). To define the working point, we used a sample of 5% of the complete dataset and fit a model to the B mass variable. The model was an extended version of a signal plus background model. The signal component is a Gaussian

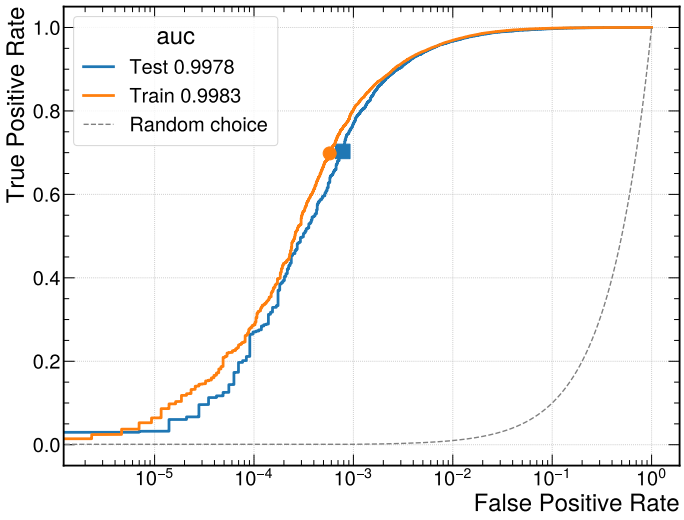

Figure 5.13: Comparison of the ROC curve evaluated in test and train datasets. In the x-axis is the False Positive Rate, or 1 minus the Background Rejection. In the y-axis is the True Positive Rate, or Signal Efficiency. The markers represent the best cut or Working Point, as optimized by the FOM ($S/\sqrt{(T)}$).

and the background is a sum of a Gaussian plus an exponential. The NLL fit is carried out using Minuit and only converged minimizations are considered.

The selection of the working point was driven by the FOM ($S/\sqrt{T}$), where S is the signal yield integrated into the signal region (from 5.15 to 5.4 GeV/c^2) and T is the total number of events inside the same window. In Figure 5.14, the FOM, with the propagated uncertainties is displayed on the right. The marker on each curve represents the WP.

The signal efficiency for this working point measured in the BTOSLL official generation is 70.3% and 69.8% for test and train datasets. Finally, the importance (or gain) of each variable is shown in Figure 5.15.

Triggering muons

After all selection criteria, events with at least one triggering muon are the most common, in Table 5.9, we show the fraction of the number of events with zero, one, or two matched triggering muons. Since it is expected that the events with at least one triggering muon behave differently than events with no triggering muons, we reject the latter. Therefore, we only keep events with at least one triggering muon.

In Figure 5.16, the distribution of the B mass shows a uniform effect due to the selection of triggering events.

The Fake Kaon Veto

After applying the selections described in the previous sections, a background contribution with a large correlation on the $\cos\theta_l$, B mass, and q variables appears as can be seen in Figure 5.17.

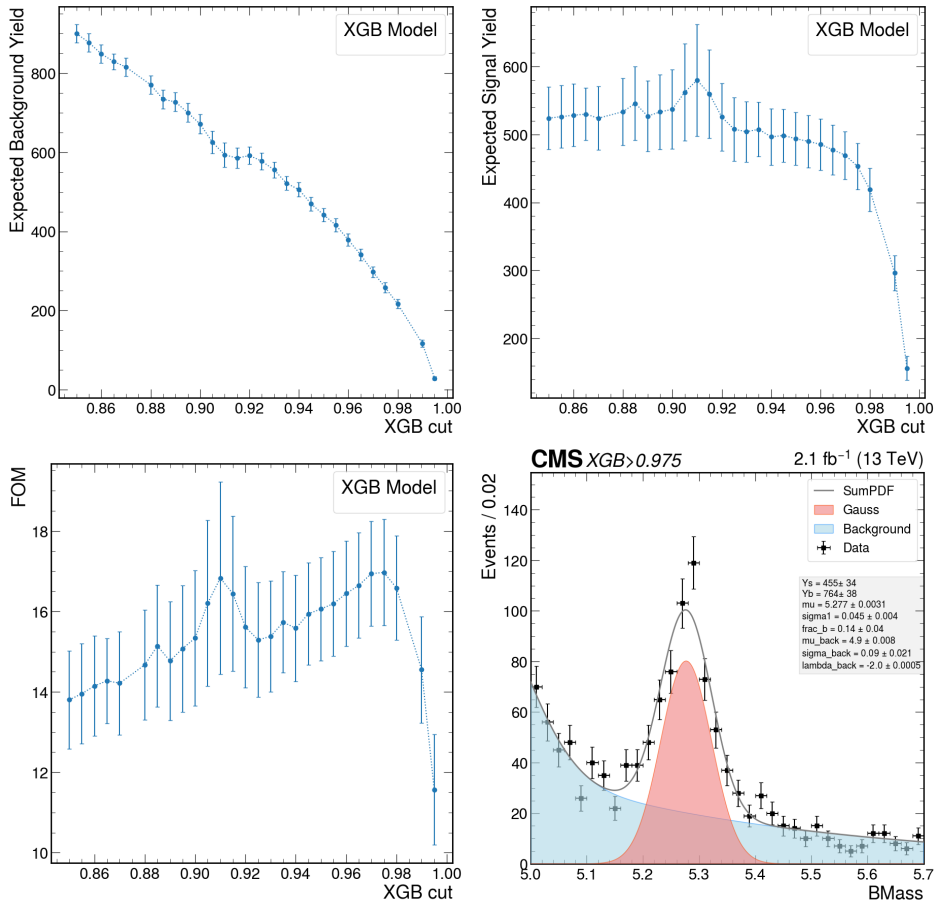

Figure 5.14: Plots on the left and in the middle represent the background and signal yields fitted to a 5% sample of the complete dataset. Yields are integrated inside the signal region. On the right, the FOM is evaluated with the integrated signal yield and the number of data events in the signal region (T). The uncertainties propagated are the error of the integrated signal yield and Poisson uncertainty for T. The best cut is obtained at 0.975.

In Figure 5.17, 2D histograms for $\cos\theta_l$ and B_{mass} variables are plotted for different ranges of q. The background contribution can be seen as an accumulation of events at $(0.0, -0.5, -0.8)$ for increasing q slices. The accumulation can extend to the complete range of B_{mass} as for the lowest q slice.

If the invariant mass of the Kaon and the muon of opposite sign is plotted, a peak can be seen in the J/ψ(1S). This peak becomes narrower when the track related to the Kaon is tested as a muon, that is, the invariant mass of the track -under muon hypothesis- and the muon of opposite sign. This invariant mass is defined as MissID invariant mass. On the right side of Figure5.18 a peak is clearly seen around the J/ψ(1S)mass on the MissID mass distribution for the complete dimuon range.

Events with Miss ID in [3.0, 3.2 GeV/c^2] and the $K^+ p_T < 4.0$ GeV are vetoed.

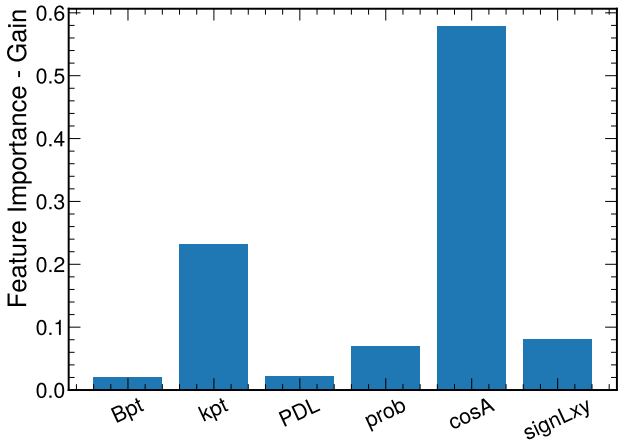

Figure 5.15: The feature score or gain for the trained classifier.

N. triggering muons	Data	PHSP	BTOSLL
0	0.0396	0.0024	0.0018
1	0.8647	0.8189	0.8032
2	0.0957	0.1787	0.1950

Table 5.9: Fraction of the number of events with zero, one or two matched triggering muons, only events with at least one triggering muon will be kept.

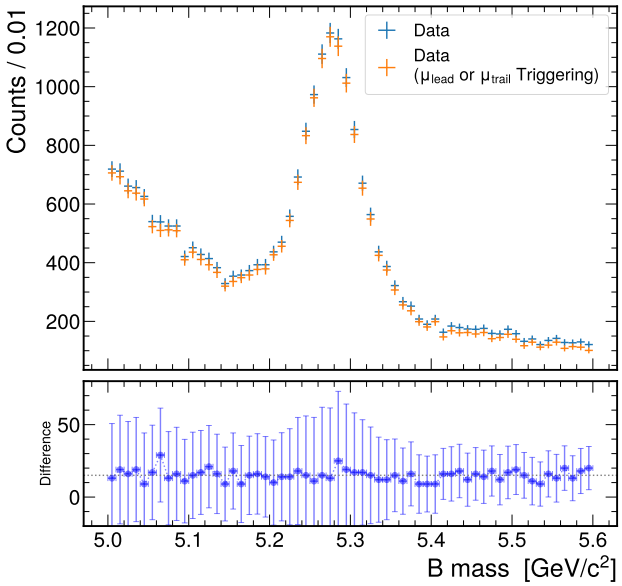

Figure 5.16: The invariant mass distribution of the B meson before and after removing events with no matched triggering muons.

Minimum ΔR cut

In addition to the cut on the MissID invariant mass and $K^+ p_T$, a cut on the angular distance (ΔR) is applied.

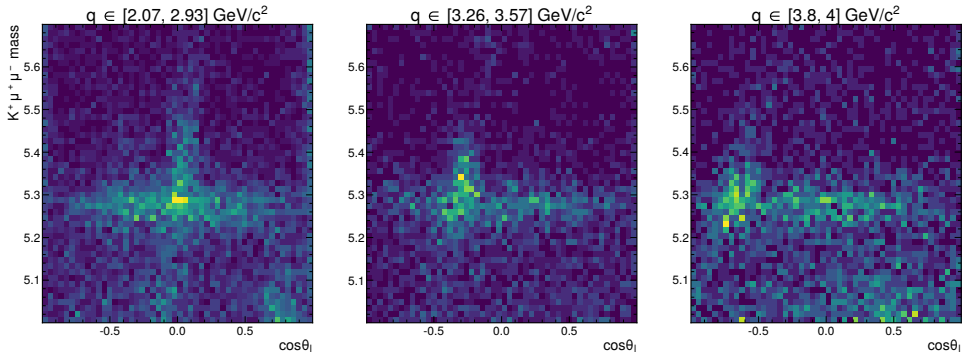

Figure 5.17: Background component coming from a miss identification of Kaons. This background can be seen as a diagonal component on the $B_{mass} - \cos\theta_l$ plane. This component is also correlated with q as can be seen from the projections on different q^2 bins.

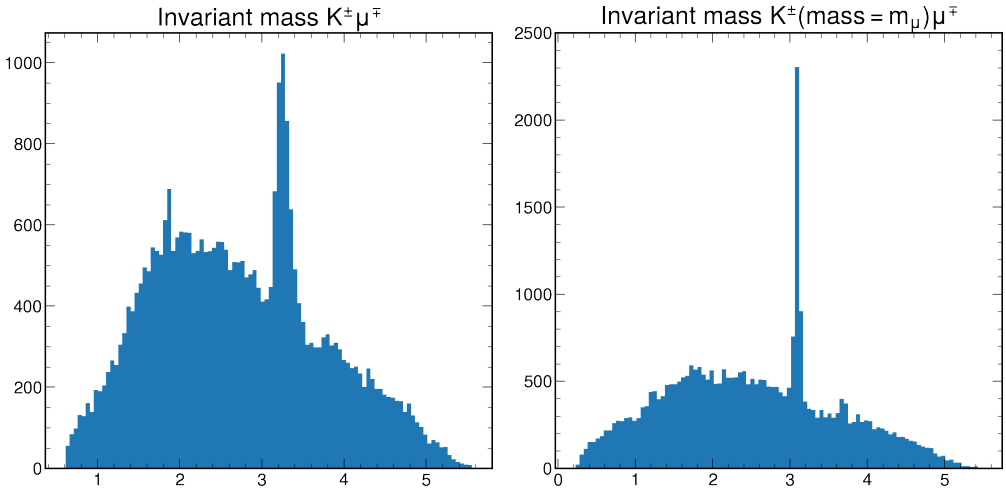

Figure 5.18: On the left, the invariant mass of the Kaon and the muon of opposite sign (which defines the angular observable). On the right, the invariant mass of the track that defines the Kaon, under the muon mass hypothesis and the muon of the opposite sign is plotted. In both it can be seen a large contribution that must come from the J/Ψ resonance.

To remove hadron tracks that are reconstructed also as muons, we evaluate the $min(\Delta R)$ of the hadron track w.r.t. the `innerTrack` of all `trackerMuons`.

The distribution of this variable exhibits a peak close to zero, which is removed with a cut $\Delta R > 0.001$ and is displayed on Figure 5.19 in the upper panel,

in the lower panel we show the overall effect on the angular distribution.

Candidate Selection

After all selection criteria are applied, there are some events with multiple candidates, around 2.6% in data. Most of them (98%) share both muons, an example of this event can be seen in Table 5.10. The remaining 2% only share one muon.

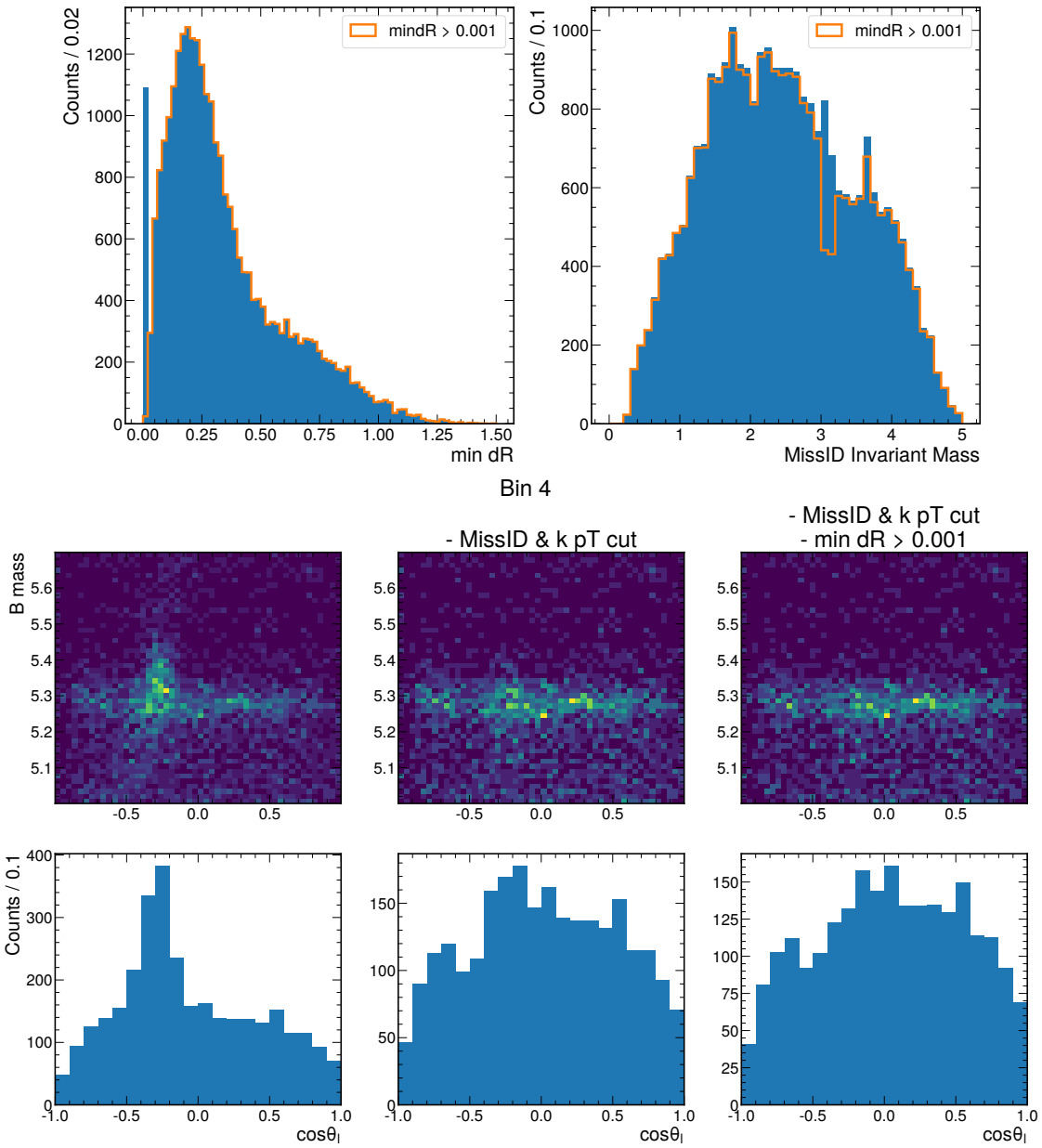

Figure 5.19: Upper panel) Minimum ΔR of the Kaon candidate and all trackerMuons. The evaluation of these distances uses the innerTrack information of the muons. Lower panel) Effect of both Fake Kaon cuts on the angular observable and B mass distributions. Only data from bin 4 is shown.

Therefore, selecting one candidate per event, when necessary, improves the significance of the final selection.

When there are multiple candidates per event, we keep the one with the highest secondary vertex probability. The efficiency of this cut, measured in PHSP Monte Carlo is 99.9%

Candidate	$B^+ p_T$	$\mu_1 p_T$	$\mu_2 p_T$	$K^+ p_T$	SV_{prob}
1	20.3	11.0	3.5	6.5	1.0
2	19.7	11.0	3.5	6.0	0.5
3	19.5	11.0	3.5	5.7	0.4
4	17.6	11.0	3.5	3.9	0.4
5	17.0	11.0	3.5	3.2	0.1
6	16.7	11.0	3.5	2.9	0.5

Table 5.10: Example from an event with multiple candidates, where it can be seen that the only difference is the track used to reconstruct the B^+. This event correspond to the Run:322617, Lumiblock:331, Event:570703179

5.3.7 Final Selection

Cut	Value
Resonance Veto J/ψ(1S)	[2.929, 3.263] GeV/c^2
Resonance Veto ψ(2S)(2S)	[3.574, 3.798] GeV/c^2
B^+& J/ψ(1S) Low Stripe (Δm_1)	137 MeV/c^2
B^+& J/ψ(1S) High Stripe (Δm_2)	134 MeV/c^2
B^+& J/ψ(1S) High Stripe (c)	3.43 GeV/c^2
B^+& ψ(2S)(2S) Low Stripe (Δm_1)	97 MeV/c^2
B^+& ψ(2S)(2S) High Stripe (Δm_2)	44 MeV/c^2
B^+& ψ(2S)(2S) High Stripe (c)	3.92 GeV/c^2
XGBoost Classifier	> 0.975
B p_T	> 13.0 GeV/c
$\mu_{leading}$ p_T	> 7.0 GeV/c
$\mu_{trailing}$ p_T	> 3.0 GeV/c
Fake Kaon (Miss ID invariant mass)	[3.0, 3.2] GeV/c^2
	&
Fake Kaon (K p_T)	< 4.0 GeV/c
Minimum $\Delta R(\mu_{leading}, \mu_{trailing}, K^+)$	> 0.001
Candidate Selection	Highest SV prob (if multiple candidates per event).
Triggering muons	At least one muon must be matched with any HLT_MuX_IPY trigger object.

Table 5.11: Complete selection cuts applied to the $K^+\mu^+\mu^-$ candidates.

A final selection is obtained by applying all the cuts discussed previously to the complete dataset. To obtain the yield of the signal for the complete dimuon mass window, an extended maximum likelihood fit to data was performed. The model for the signal component was a Johnson's SU distribution [115] while for background, an exponential plus Gaussian was considered. The shape of the Johnson's SU distribution is obtained from Signal MC, and all its parameters remain fixed, except the *location parameter* μ parameter. A signal yield of 7264±123 is achieved with this final selection as shown in Figure 5.20.

5.4 Analysis Strategy

As already stated, the present analysis aims to measure the forward-backward asymmetry (A_{FB}) of the muons and the (pseudo)scalar and tensor contributions to the decay width (F_H)

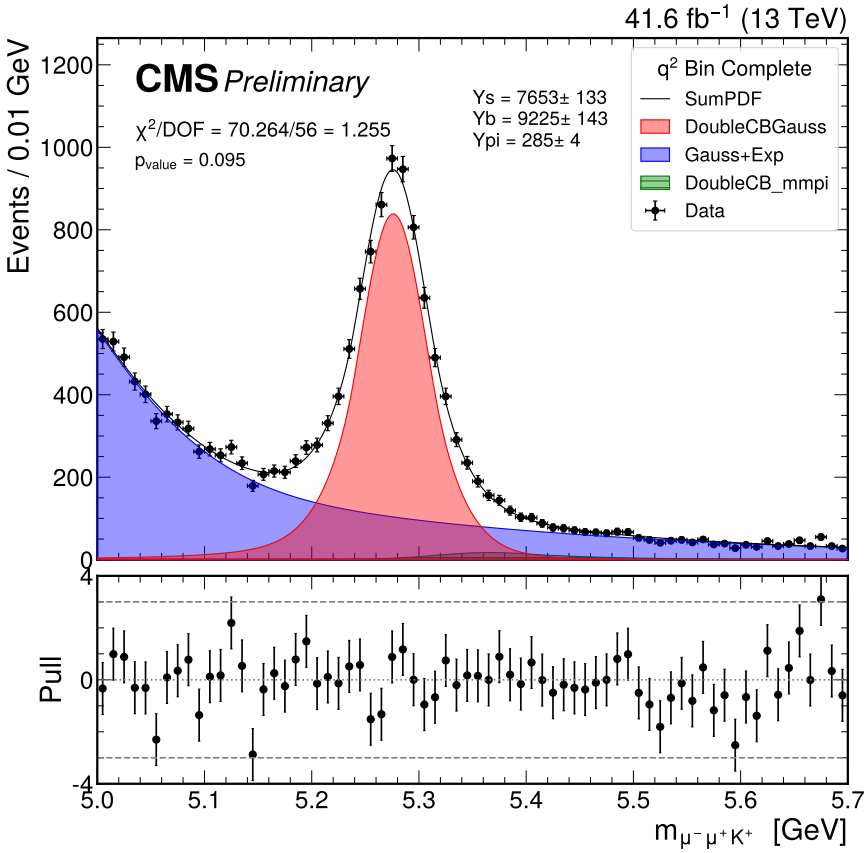

Figure 5.20: B^+invariant mass of data, computed for the whole q^2 spectrum, with the final selection applied.

as a function of q^2. Both parameters are measured from a maximum likelihood estimation on a 2-dimensional pdf for each q^2 bin.

The exact bin definition can be found in Table 5.1. This binning was chosen to match the recent petition to have a common bin definition among experiments performing $b \to s\ell\ell$ analyses.

5.4.1 Probability Density Function

The parameters A_{FB} and F_H define the angular decay width (Equation 5.1). However, the effect of the detector must be taken into account. This is done by multiplying Equation 5.1 by the efficiency of signal detection as a function of $\cos\theta_l$.

The contribution of the background is considered by adding an extra term, which accounts for the background distribution on $\cos\theta_l$.

Each component is then multiplied by the pdfs that define the shapes of the distributions of signal and background events on the $K^+\mu^+\mu^-$invariant mass.

An additional component is included to account for the Cabibbo-suppressed mode $B^+ \to \mu^+\mu^-\pi^+$. The mass and angular distributions are derived from Monte Carlo samples, with its yield fixed to be proportional to the signal yield.

The proportionality constant is obtained as the ratio of the efficiencies and branching fraction of both channels.

Channel	Acceptance from McM (a)	$a \times \epsilon$ [10^{-4}]	BR	$a \times \epsilon \times$ BR [10^{-6}]	Scale (π/K) [%]
$B \to J/\psi(\mu\mu)K$	0.6739 ± 0.0047	20.28 ± 0.26	(1.02 ± 0.19) x 10^{-3}	2.07 ± 0.39	3.34 ± 0.64
$B \to J/\psi(\mu\mu)\pi$	0.0200 ± 0.0200	19.38 ± 0.44	(3.92 ± 0.08) x 10^{-5}	(7.60 ± 0.23) x 10^{-2}	
$B \to \mu\mu K$	0.6272 ± 0.0047	17.30 ± 0.23	(4.53 ± 0.35) x 10^{-7}	(7.84 ± 0.61) x 10^{-4}	3.93 ± 0.72
$B \to \mu\mu\pi$	0.0293 ± 0.0031	17.30 ± 1.80	(1.78 ± 0.23) x 10^{-8}	(3.07 ± 0.51) x 10^{-5}	

Table 5.12: Acceptance, efficiencies and branching ratios to estimate the contribution of the $\mu\mu\pi$ channel with respect to the $\mu\mu K$

The different masses of the final state meson on both channels (K and π) produce different dimuon distributions which result in varying contributions of the Cabibbo-suppressed mode for each q^2 bin. We address this by multiplying the overall constant by the relative contribution in each q^2 bin obtained from the Monte Carlo samples.

The complete pdf is then given by:

$$\text{pdf}_i(m, \cos\theta_l; A_{FB}, F_H) = Y_{S_i} S_i(m) S_i(\theta_l; A_{FB}, F_H)\epsilon_i(\theta_l) + Y_{B_i} B_i(m) B_i(\theta_l) + Y_{\pi_i} B_i^{\pi}(m) B_i^{\pi}(\theta_l) \tag{5.5}$$

The index i indicates the q^2 bin number and:

- Y_{S_i} is the yield of the signal component for the i-th bin.
- Y_{B_i} is yield of the background component for the bin number i.
- Y_{π_i} is yield of the $B^+ \to \pi^+\mu^-\mu^+$ component for the bin number i.
- $S_i(m)$ ($B_i(m), B_i^{\pi}(m)$) is the shape of the distribution for the signal (background, and Cabibbo-suppressed mode) events on the $K^+\mu^+\mu^-$ invariant mass.
- $S_i(\theta_l) = S_i(\cos\theta_l)$ is the angular distribution of the decay width, which is given by Equation 5.1.
- $B_i(\theta_l) = B_i(\cos\theta_l)$ is the shape of the distribution for the background events on the angular variable.
- $B_i^{\pi}(\theta_l)$ is the shape of the distribution for the $B^+ \to \pi^+\mu^-\mu^+$ channel on the angular variable.
- $\epsilon(\theta_l) = \epsilon(\cos\theta_l)$ is the efficiency for signal events of the angular variable.

5.4.2 Components of the Probability Density Function

Before the fitting takes place, we need to obtain each component for the pdf. The mass signal shape and angular efficiency are obtained from the signal MC. The efficiency modeling is described in Section 5.6. For the background component, we used data sidebands, each sideband to obtain angular distributions, and both sidebands to obtain the mass background shapes.

Signal Shape

$S_i(m)$ describes the signal shape as a function of $K^+\mu^+\mu^-$invariant mass. In Figure 5.21 we show the fit plots on signal MC, most parameters of this distribution remain fixed for the final fit as described in Table 5.13.

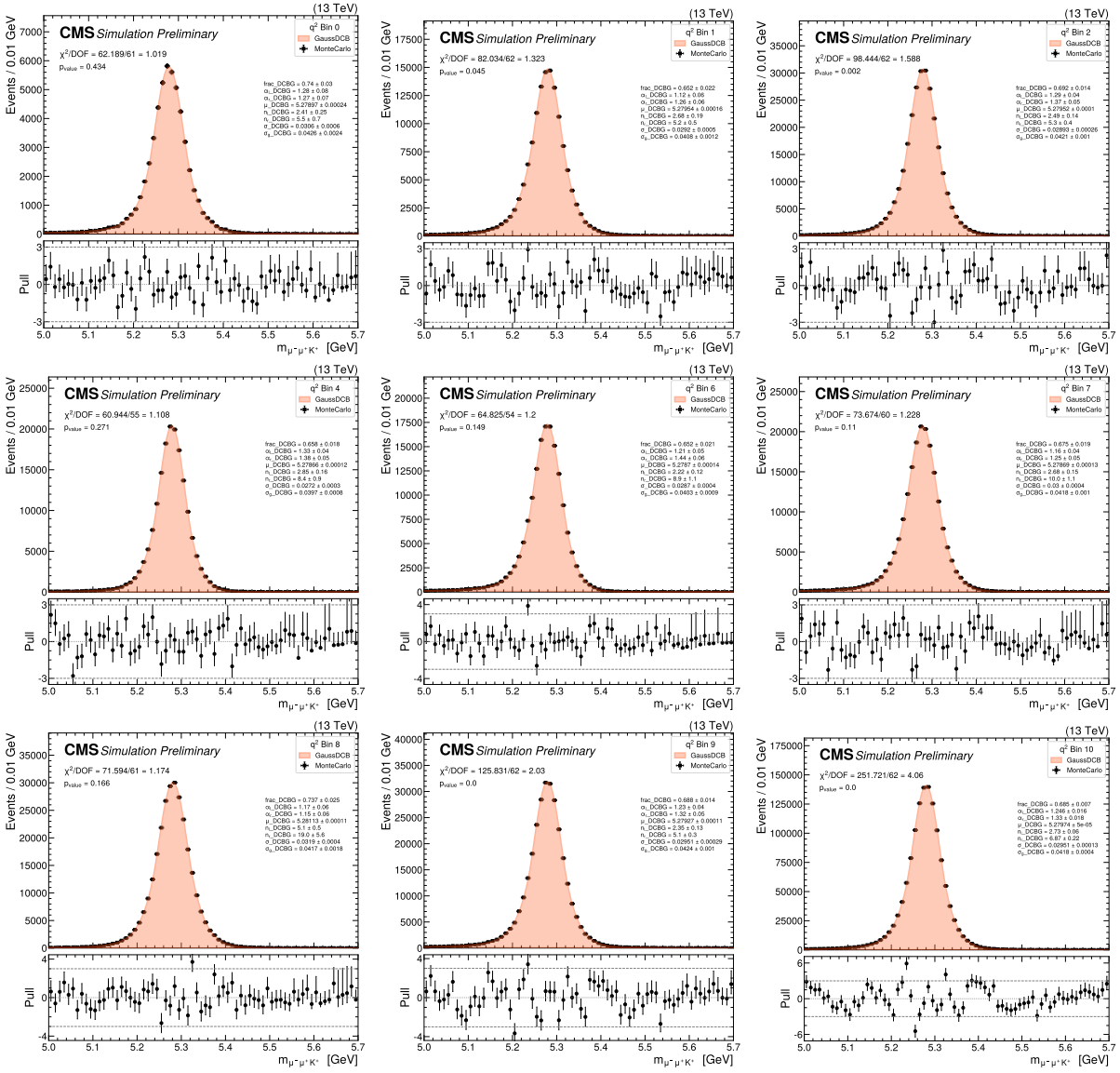

Figure 5.21: B invariant mass of the signal Monte Carlo for each q^2 bin.

Background Shape

The Cabibbo-suppressed mode is included as an extended component of the 2D pdf. This component is modeled using a Crystal Ball function for the mass variable, and Kernel Density Estimation for the angular observable. Both models remain fixed after being obtained from

a fit to MC samples, while the yield is proportional to the signal yield. Figure 5.22 and 5.23 shows the models on the mass and angular variables.

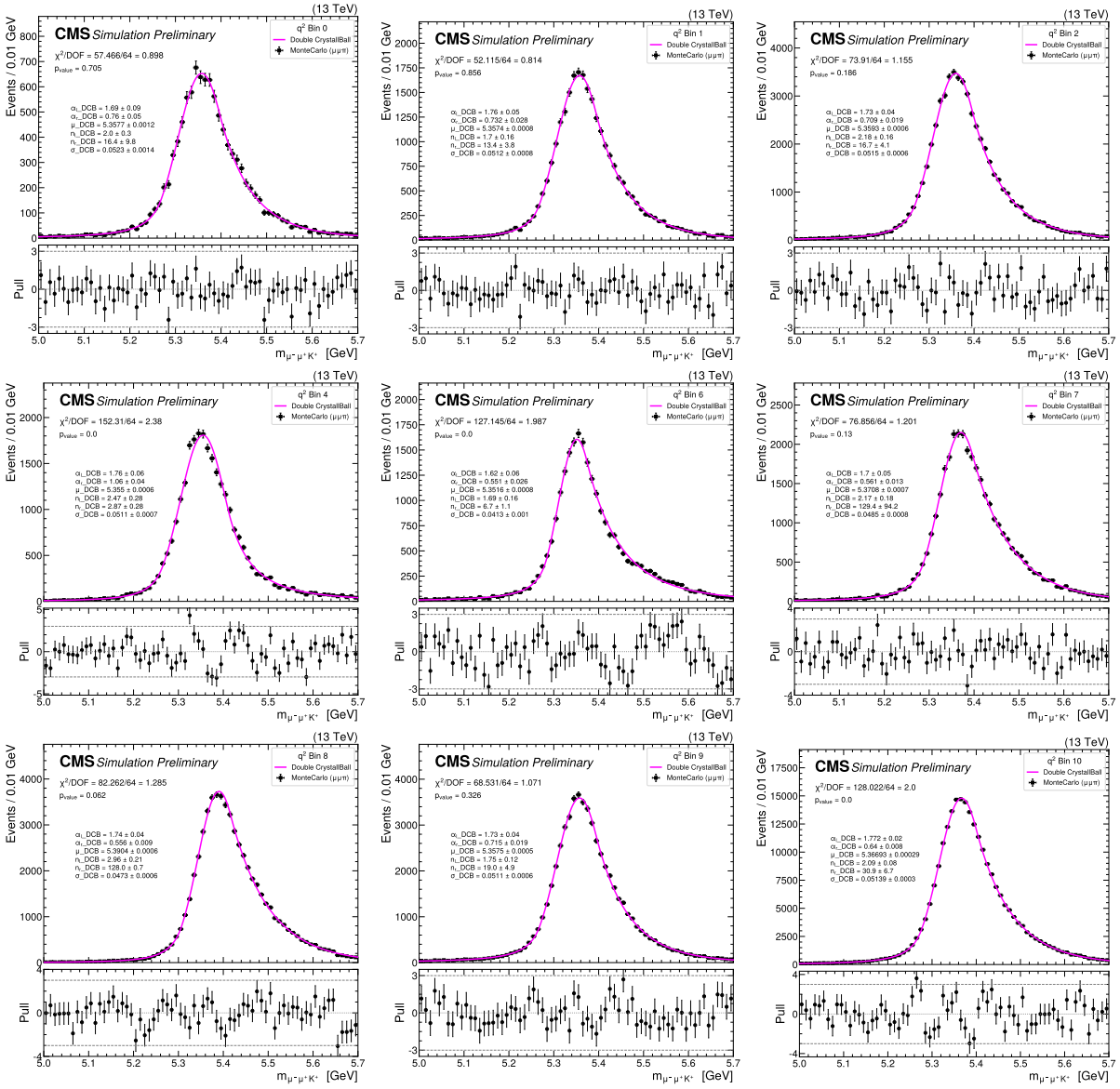

Figure 5.22: $\mu\mu K$ invariant mass for the Cabibbo-suppressed mode in each q^2 bin.

$B_i(m)$ describes the background shape as a function of $K^+\mu^+\mu^-$ invariant mass. The distribution is modeled as an exponential plus a Gaussian, each parameter is shown in Figure 5.24. Only data sidebands are used in this fit.

For the shape of the angular background, we fitted two models, one per sideband. Left side band (5.0,5.15) GeV/c^2 , and right side band (5.4, 5.7) GeV/c^2 . The models are Bernstein polynomials as a function of $\cos(\theta_l)$ for each q^2 bin and for each sideband.

In the low q^2 region (below 8 GeV^2) the angular backgrounds exhibit a different behavior compared to the high q^2 region. For the left sideband, a peaking background contaminates it. This contribution does not extend into the signal region but biases the left sideband

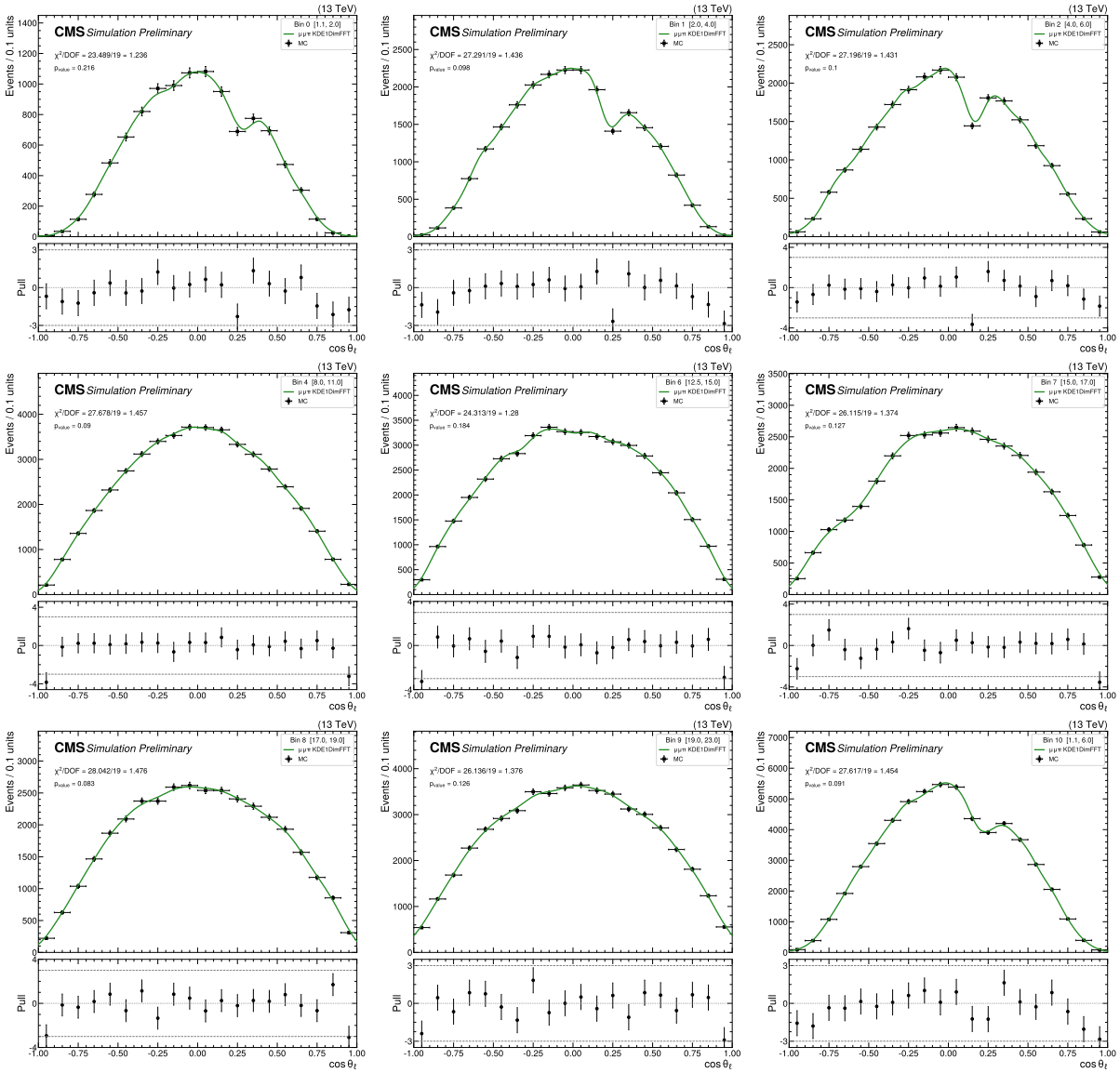

Figure 5.23: $\cos(\theta_\ell)$ distribution for the Cabibbo-suppressed mode in the signal region [5.15 - 5.40 GeV/c^2] for each q^2 bin.

model. To mitigate this bias, we have blinded a small angular region.

The blinded region depends on the q^2 bin and is shown as a vertical grey strip in Figure 5.25, which also displays the fitted angular model. For the right sideband, a peak around ± 0.5 induced the idea to include Gaussian distributions. For these q^2 bins, in addition to the Bernstein polynomials, we added two Gaussian to improve the fit to data. Figure 5.26 shows the angular right sideband models.

To decide the best degree of the Polynomial, we used the F-test, which compares the residuals between data histograms and the fitted model, for different degrees of the polynomial. The null hypothesis of this test is that the model with fewer degrees is as good as the model with more degrees.

Understanding the underlying physics process of the angular background in the signal

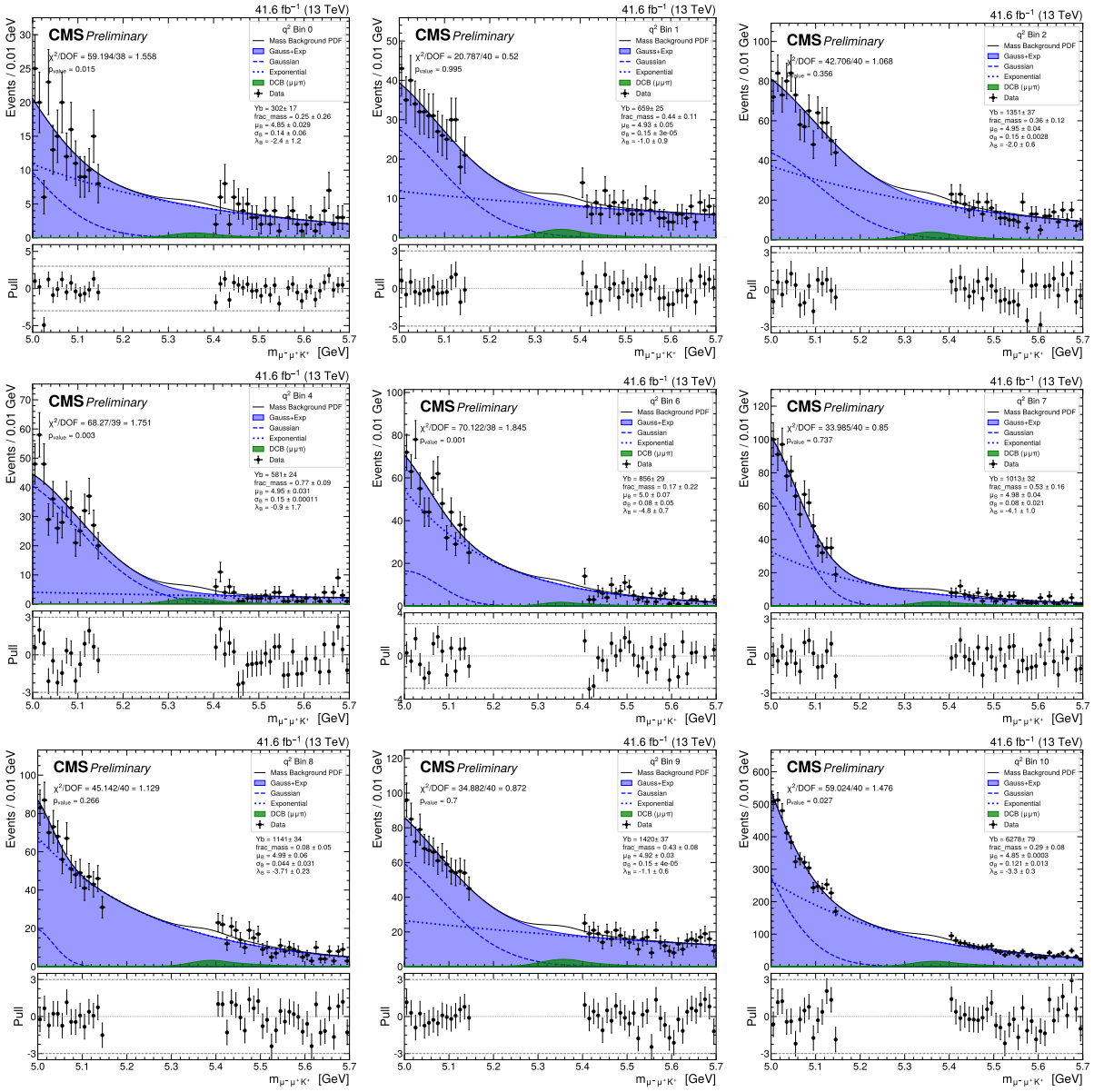

Figure 5.24: B invariant mass of the data sidebands for each q^2 bin. The yield corresponds to the sideband region only.

region, and therefore, predicting precisely how this component distributes, can become a challenging task. Therefore, we adopt a pragmatic approach. We assume that the angular background shape, in the signal region, can be approximated as a weighted sum of both sideband models. This choice allows us to account for the potential contributions from these background components while acknowledging the inherent uncertainty related to their behavior in the signal region.

In this approximation, we treat the fraction of each component as a free nuisance parameter. And it is described mathematically as a sum of two probability distribution functions, one for each sideband:

$$B_i(\theta_\ell) = f \times B_{Left}(\cos\theta_\ell) + (1-f) \times B_{Right}(\cos\theta_\ell), \tag{5.6}$$

where $B_{Left}(\cos\theta_\ell)$ ($B_{Right}(\cos\theta_\ell)$) is the *fixed* pdf for data events from the Left (Right) sideband. And f is the nuisance parameter associated to the modeling of the angular background component in the signal region.

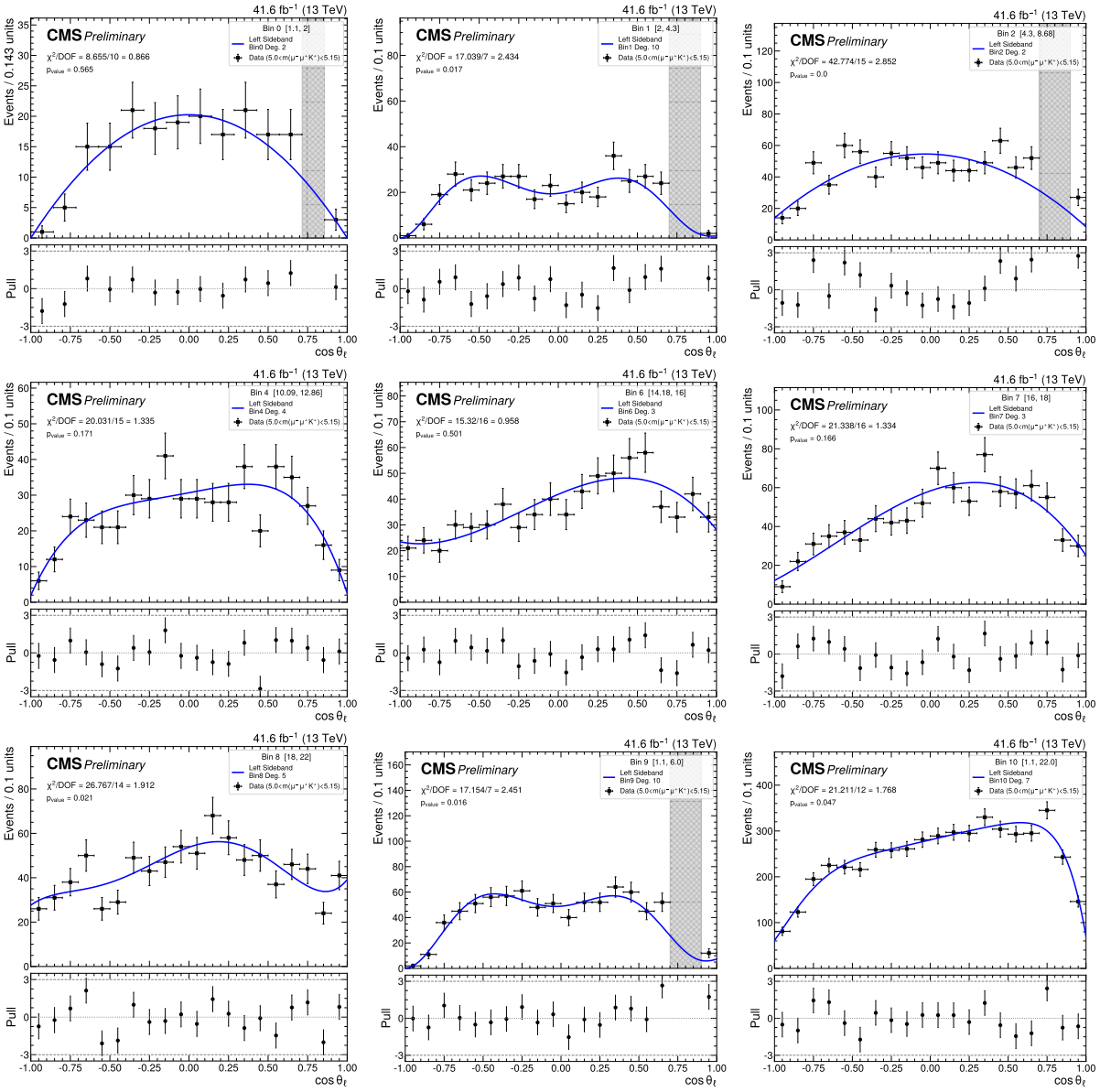

Figure 5.25: $\cos(\theta_\ell)$ distribution for Left sideband [5.0 - 5.15 GeV/c^2] for each q^2 bin.

Summary of the PDF

The complete PDF is a 2D extended model that assumes independence of the mass and angular variables. It is composed of 3 components, one for the signal, one for the combinatorial plus partially reconstructed background, and one for the Cabibbo-suppressed mode

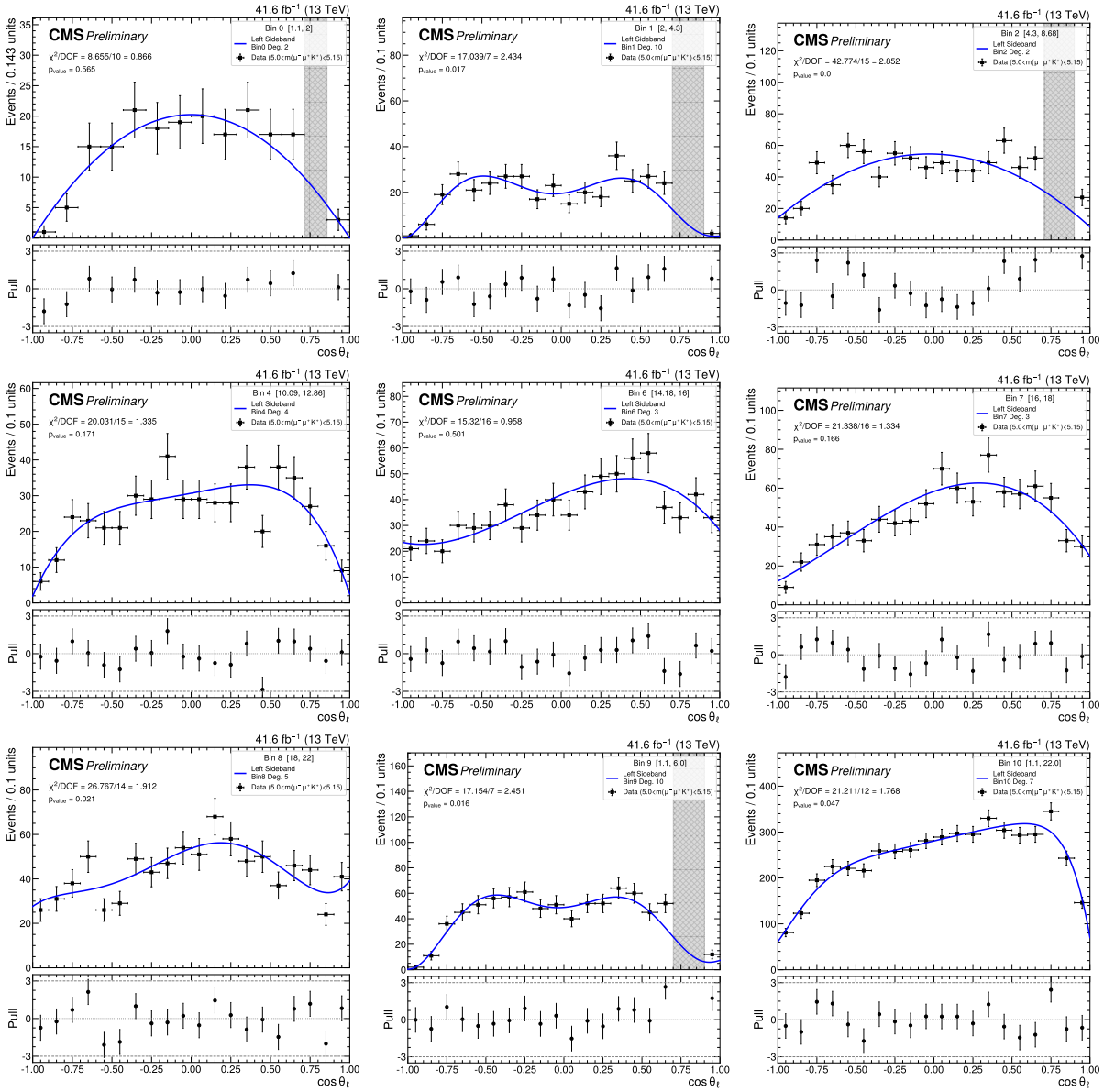

Figure 5.26: $\cos(\theta_\ell)$ distribution for Right sideband [5.4 - 5.7 GeV/c^2] for each q^2 bin.

$B^+ \to \pi^+\mu^-\mu^+$. The partially reconstructed and combinatorial component is constructed with data-driven models using both sidebands for the mass distribution, and independent models for each sideband. The angular sideband models are merged into a single model by summing both contributions using a fraction between them. The signal models are obtained from Monte Carlo; the mass distribution is extracted from the BTOSLLBALL sample, the PHSP is used to get the angular efficiency. For the Cabibbo superseded mode, we used Monte Carlo distributions for modeling the angular and mass distributions.

In Table 5.13 we describe in detail all the 1D components. They are included in the 2D PDF as described by Equation 5.5, and the final fit is carried out in the signal region [5.15, 5.4 GeV/c^2]. The yields of the components are free to float except the $\mu\mu\pi$ component, which is fixed to be proportional to the signal yield as described previously.

Component	Model	Details	Free Parameters
Signal	Mass $S_i(m)$	Double-Sided Crystal Ball plus Gaussian Fitted from MC	μ σ_{CB} σ_{gauss} Gaussian constrained
Signal	Angular $S_i(\theta_l; A_{FB}, F_H)\epsilon_i(\theta_l)$	Decay Rate $\times$ Efficiency. The Efficiency is obtained from the PHSP sample and we use Kernel Density Estimation to model it	A_{FB}, F_H SLSQP constrained
Comb. + Part. Reco.	Mass $B_i(m)$	Gaussian plus exponential Fitted from sidebands	All parameters remain fixed.
Comb. + Part. Reco.	Angular $B_i(\theta_l)$	Sum of Bernstein polynomials for each sideband ($B_{Left}(\cos\theta_\ell)$, $B_{Right}(\cos\theta_\ell)$). Angular sidebands are fitted to Bernstein polynomials. The best degree is selected with the F-test.	f_{SB}: fraction for the sum of the sideband models
$\mu\mu\pi$	Mass $B_i^\pi(m)$	Double-Sided Crystal Ball	All parameters remain fixed.
$\mu\mu\pi$	Angular $B_i^\pi(\theta_l)$	Kernel Density Estimation	All parameters remain fixed.

Table 5.13: The final 2D fit has 8 free parameters with 6 of them being nuisance parameters. The central values of the fixed parameters are obtained from a fit to data sidebands or MC. For the signal model parameters, we use Gaussian constraints on the location and resolution parameters while the remaining are fixed. The SLSQP algorithm employs Lagrange multipliers and we use them to constrain the parameters of interest following equations 5.2 and 5.3.

5.4.3 Fit Sequence

To extract A_{FB} and F_H, we perform an extended likelihood fit in the signal region, that is, the B mass window is restricted from 5.15 to 5.4 GeV/c^2 . The description of the parameters in the final 2D fit is described in Table 5.13.

The fit is carried out using the zfit [116] package. This package uses TensorFlow [117] as the back-end and allows the user to switch between different minimizers. In particular, we use the SLSQP [118] minimization algorithm, implemented on the scipy package [119]. The main advantage of this minimizer over Minuit is that it makes use of Lagrange multipliers and allows for the natural handling of linear constraints. Equations 5.2, 5.3 and Figure 5.3, show the constraints that must be imposed on the parameters of interest (A_{FB} and F_H). The equations are easily implemented in this algorithm and are used for each angular fit.

Fitting Techniques Study

The SLSQP fitting technique was validated with respect to the MINUIT minimizer. The validation was made for each q^2 bin, and 12 points (on the $A_{FB} - F_H$ plane) for each bin were analyzed.

For this exercise, we created pseudo-data with all the parameters fixed as given by the fit on data except the parameters of interest (POIs), which were randomly chosen to be inside the physical region. We considered 6 points near and 6 points far from the physical

boundary. The close points were considered by the region defined by (which is also shown in Figure 5.27):

$$F_H/4 < |A_{FB}| < F_H/2. \tag{5.7}$$

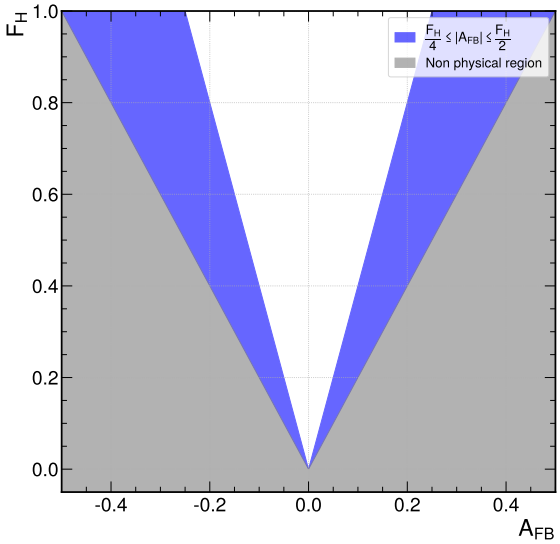

Figure 5.27: In this plot we show the non-physical region for the POI space, as well as a region "close" to the boundary region used for the Fitting Techniques Study.

For each of the 12 points in the physical region, we generated 200 toys and fit each sample with both, SLSQP and MINUIT. For the SLSQP minimizer, we imposed constraints defined by Equation 5.2. For MINUIT we did not impose any constraint or penalty term. The errors used to calculate the pull distributions were obtained from the Hesse routine. For the SLSQP minimizer, it was a custom Hesse routine made by the *zfit* [116] development team.

Points far from the physical region obtained a good agreement between both minimizers. The pull distributions were well-behaved and no bias was introduced by the SLSQP algorithm and custom Hesse routine. Figure 5.28, shows the results for a point far from the physical region.

For points close to the physical boundary and low signal yield, a skewed distribution was obtained for SLSQP, which is mainly a result of the constraints imposed on the minimizer. However, the fitted parameters are always inside the physical region. In Figure 5.29, the results for a point close to the physical boundary on Bin 0, (with lowest signal yield) are displayed along with the pull distributions on the bottom.

From this exercise we validated the fitting technique for points far from the physical region, obtaining similar results as for the MINUIT minimizer. Then, we analyzed the results for points close to the physical boundary, where we verified that SLSQP with constraints produced fits that were completely inside the physical region. Finally, one should be aware that the presence of the boundaries produce non-normal distributions for the fitted parameters, which in turn is a measure of a non-zero bias. This bias should appear independently of the minimizer used, and it is considered as a source of systematic uncertainty which is discussed in Section 5.9.2.

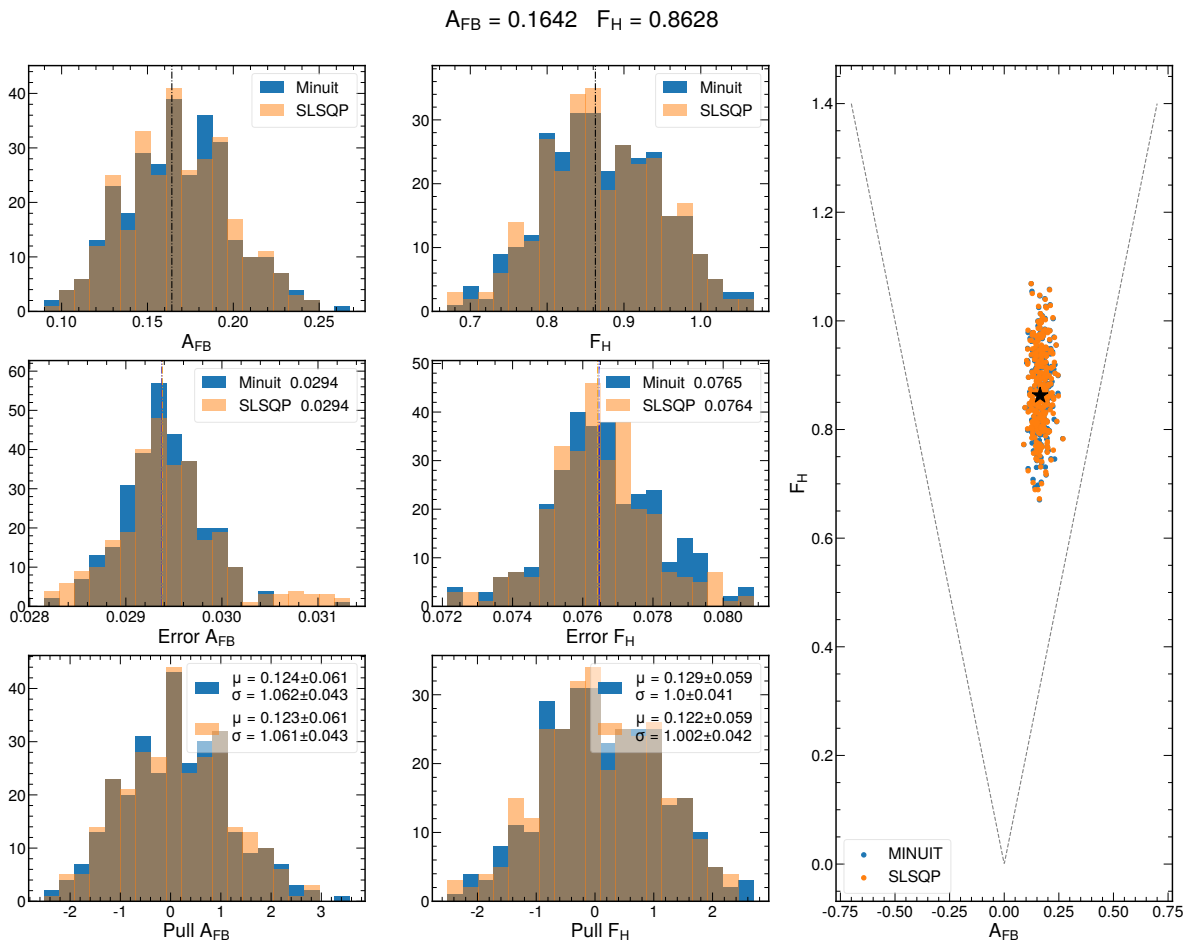

Figure 5.28: Fitting technique study results for Bin 6. The signal yield for this bin is 1533, while for the background is 5539.

Fitting Convergence

We verified the convergence of the fitting technique by creating pseudo-data from the pdf defined in the previous section.

To prove the convergence, we fitted the same pseudo-data 100 times with randomly different initial values of the parameters of interest inside the physical region.

Figures 5.30 and 5.31 show the results of the exercise proving that the convergence of the fitting is well obtained.

5.5 Monte Carlo Correction

In this section, we first compare signal distributions obtained from the Monte Carlo samples with respect to data distributions.

From data, we extract signal distributions using the sPlot technique[120]. This technique returns a set of weights that are used to "subtract the background", and obtain signal-like distributions. The Monte Carlo sample used for the comparison is the BTOSLLBALL

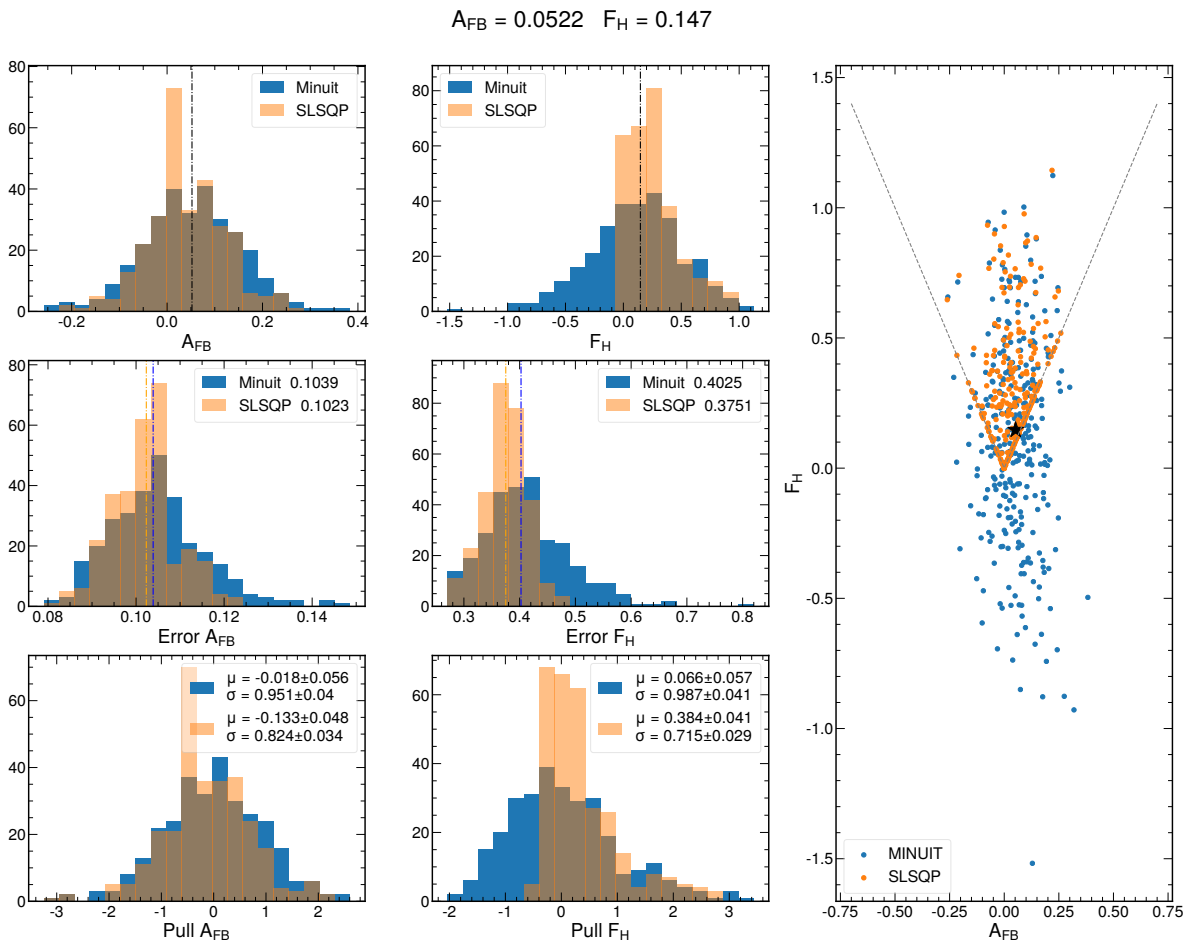

Figure 5.29: Fitting technique study result for Bin 0. Signal yield for this bin is 538, while for the background is 5326.

sample, since the PSHP model is an unrealistic simulation, we avoid *overcorrecting* the Monte Carlo by not comparing to the PHSP distributions.

In the case of the resonant channels, we use the respective physical model from EVTGEN , *i.e.* non-PHSP.

Finally, all the corrections described here are used in the efficiency calculation, which is done in the PHSP sample.

5.5.1 Monte Carlo - Data comparison

After all selection criteria is applied, the data is a mixture of signal and background events, to obtain signal-like distributions we used the sPlot technique to subtract the background.

The so-called sWeights are obtained from the complete mass models shown in Section 5.4.2.

A comparison is then carried out between the signal Monte Carlo distributions to the data background subtracted ones. We then verify if they are consistent by dividing the distributions in normalized histograms.

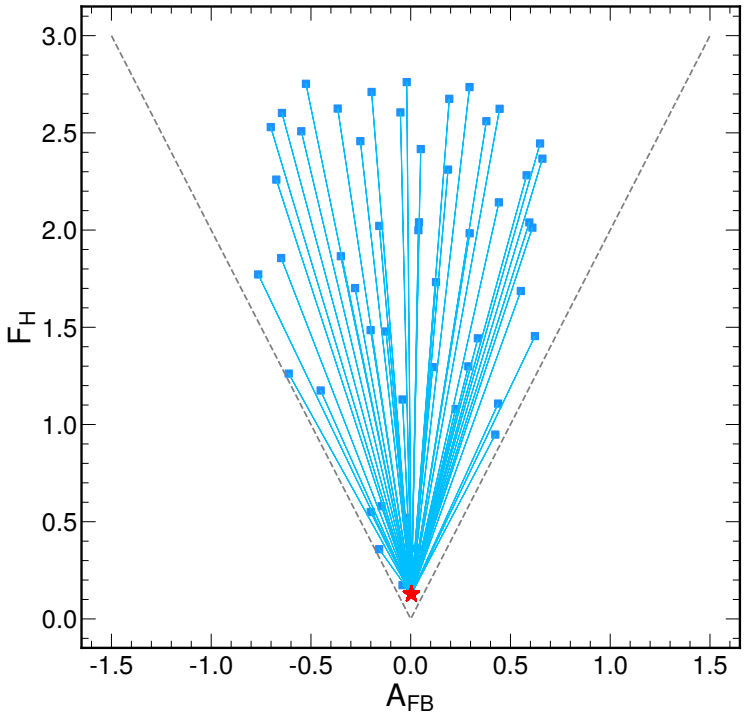

Figure 5.30: Pseudo-data generated with parameters from Bin 6 and $A_{FB} = 0$, $F_H = 0.2$ fitted with 100 different initial values (in blue) inside the physical region, the (red) star stands for the fitted value at each initial point.

.

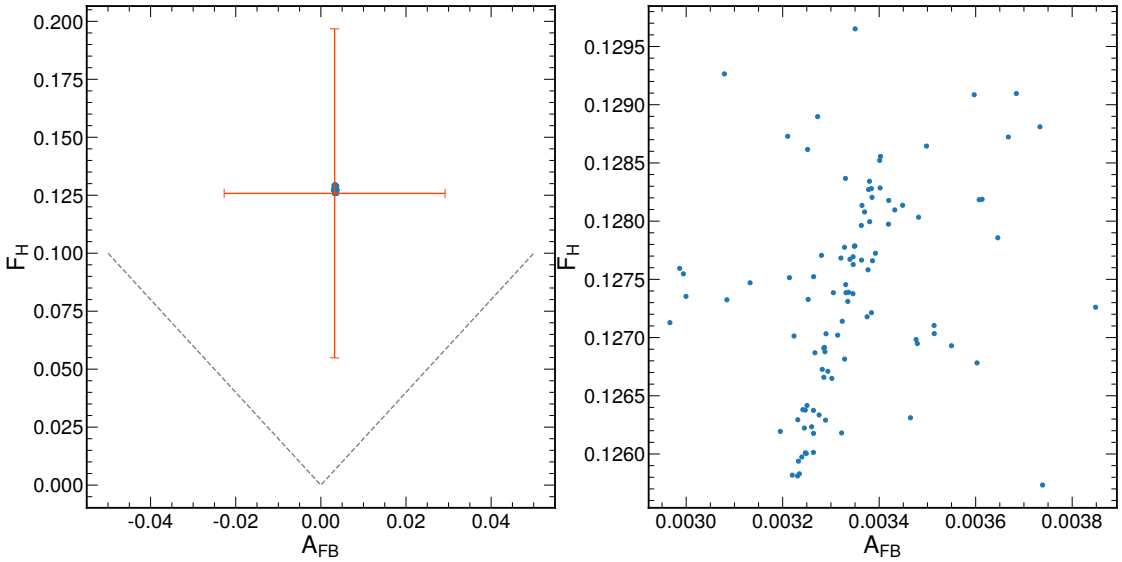

Figure 5.31: The distribution of the fitted parameters. On the left, there is a comparison with the typical errors obtained by the Hesse routine; on the right a zoom showing the actual distribution of the fitted parameters.

In Figure 5.32, a comparison between the p_{T} and IP/σ_{IP} of the leading and trailing muons is shown, a large discrepancy can be seen at low transverse momenta and IP significance.

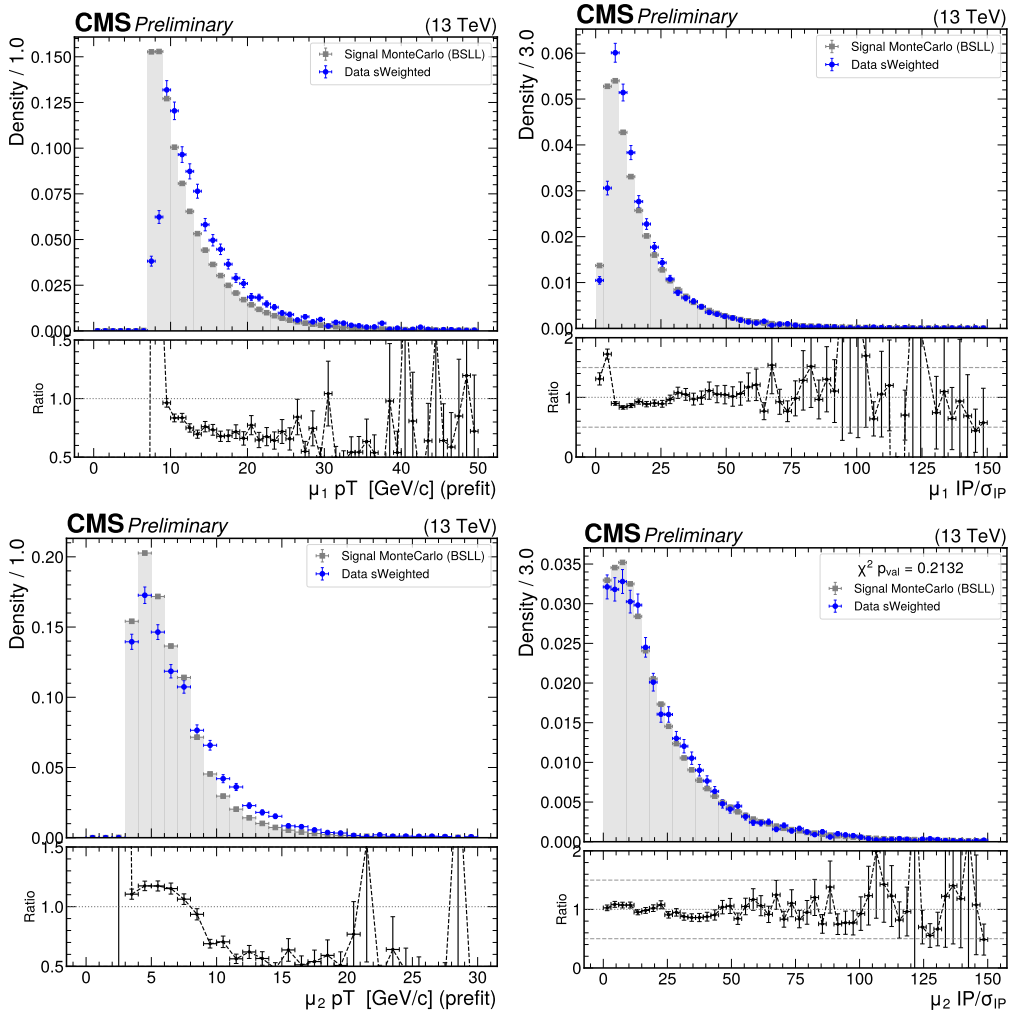

Figure 5.32: Non-corrected Monte Carlo comparison with respect to background subtracted Data.

From these 1-dimensional comparisons, it follows that a correction to the Monte Carlo must be considered.

5.5.2 Medium ID Scale Factors

The Scale Factors (SF) for the muon ID, provided by MUON POG, are used in the present analysis. Since the Medium ID is used in the selection of the muons, we have used the Medium ID Scale Factors provided in the official repository (link). The Table reporting the Scale Factors is shown in Figure 5.33. We obtain an SF per event as the product of the SF for each muon, and in cases where the muon kinematic falls outside the table range (e.g., $p_{\mathrm{T}} > 40\,\mathrm{GeV}$), we use the closest bin.

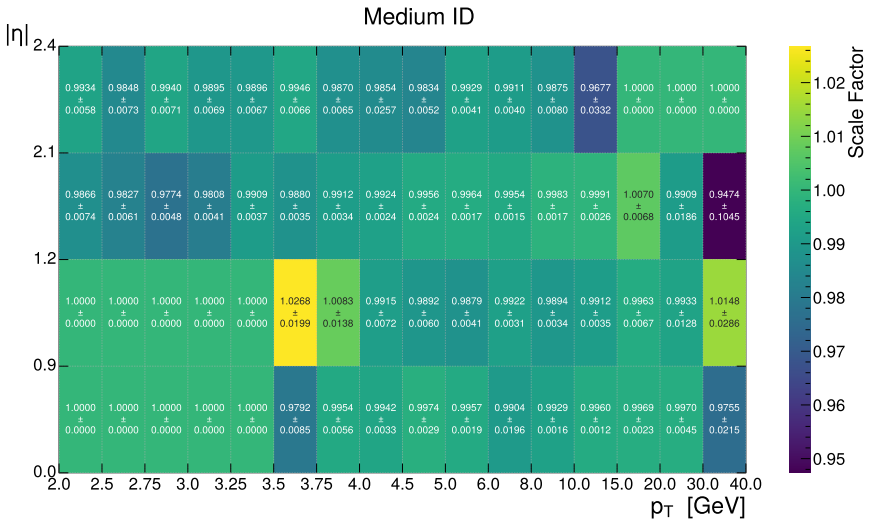

Figure 5.33: Medium ID Scale Factors from MUON POG.

To assess the effect of this correction on the MC distributions, in Figure 5.34 we show a comparison of the uncorrected MC with respect to the MC by applying the Medium ID scale factors on variables of interest.

The first plot shows the distribution of the scale factors, for each muon and the event-per-event scale factor. The plots in the middle and in the right show the effect of this correction on the $(\mu\mu K)$ mass and $\cos\theta_\ell$.

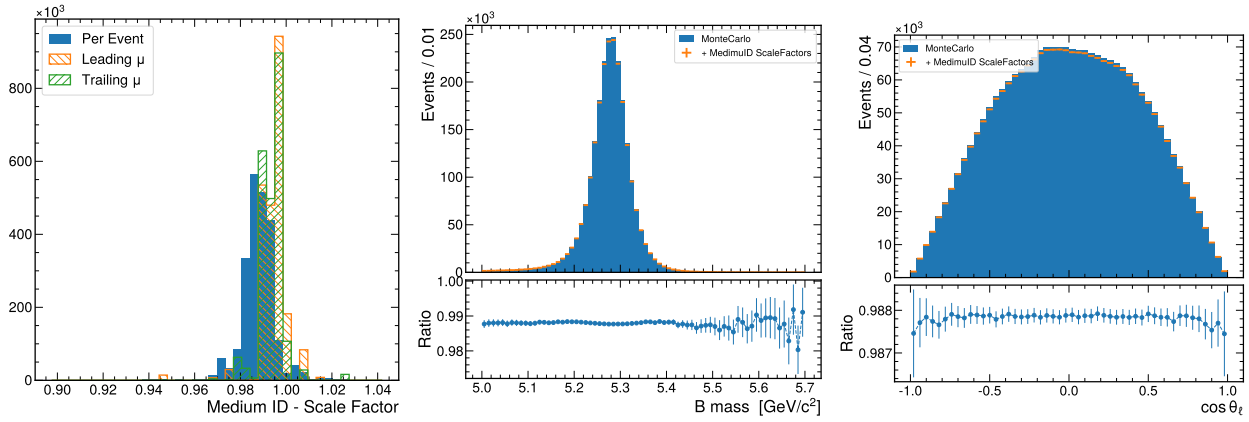

Figure 5.34: The panel on the left shows the distribution of the scale factors per muon, and the per-event SF as the product of both. The plots in the middle and right, display the effect of the per-event scale factor for the MuonID on the two variables to be used for the fitting in this analysis.

5.5.3 Trigger Correction

The trigger menu created for collecting the ParkingBPH dataset consists of several HLT paths with different values on p_{T} and IP significance thresholds. Additionally, these HLT paths

were turned on and off as the instantaneous luminosity fell during a fill. This dynamic nature of the ParkingBPH dataset is not simulated in the MC samples. Therefore, a correction to the MC must be applied.

A scale factor is defined as the ratio between the efficiency measured in data with respect to the efficiency measured in MC samples.

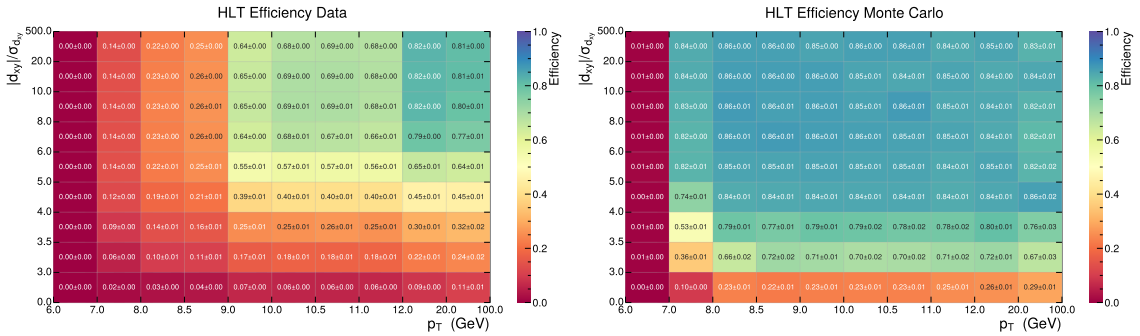

Figure 5.35: Efficiency for the whole BParking dataset measured in Data and MC. Obtained from AN2022_138_v21

The efficiencies for data and Monte Carlo are displayed in Figure 5.35. A per-event efficiency is calculated with the formula:

$$\epsilon_{event} = 1 - (1 - \epsilon_{\mu_1})(1 - \epsilon_{\mu_2}) = \epsilon_{\mu 1} + \epsilon_{\mu 2} - \epsilon_{\mu 1}\epsilon_{\mu 2} \tag{5.8}$$

In the case where a given muon is not triggering, the corresponding efficiency is set to zero. Finally, the Scale Factor is obtained as the ratio of the per-event efficiency from Data over Monte Carlo.

The trigger correction, which involves the scale factors for the HLT efficiency of the "cocktail" of paths, is focused in improving the agreement of the signal channel on MC and data, with particular focus on the variables used in the trigger decision, namely muon's p_{T} and $IP_{significance}$. Figure 5.36 shows one-dimensional comparisons of these corrections for the variables of interest.

5.5.4 Reweighting

The trigger correction improves the closure of the variables related to the trigger such as the transverse momenta of the muons and the significance of the impact parameter. However, other variables used in the selection do not agree between MC and Data. Therefore, we use a further correction to aid this non-closure. Particularly, we use a reweighting to correct kinematic and quality variables.

In this section we discuss the final correction applied sequentially to obtain the corrected angular distribution of the PHSP sample, and consequently, a corrected angular efficiency. The previously discussed corrections are independent of our analysis and can be applied "blindly" to any analysis using the ParkingBPH dataset. However, the reweighting process is fine-tuned for each analysis, with their unique simulation samples and selections playing an important role.

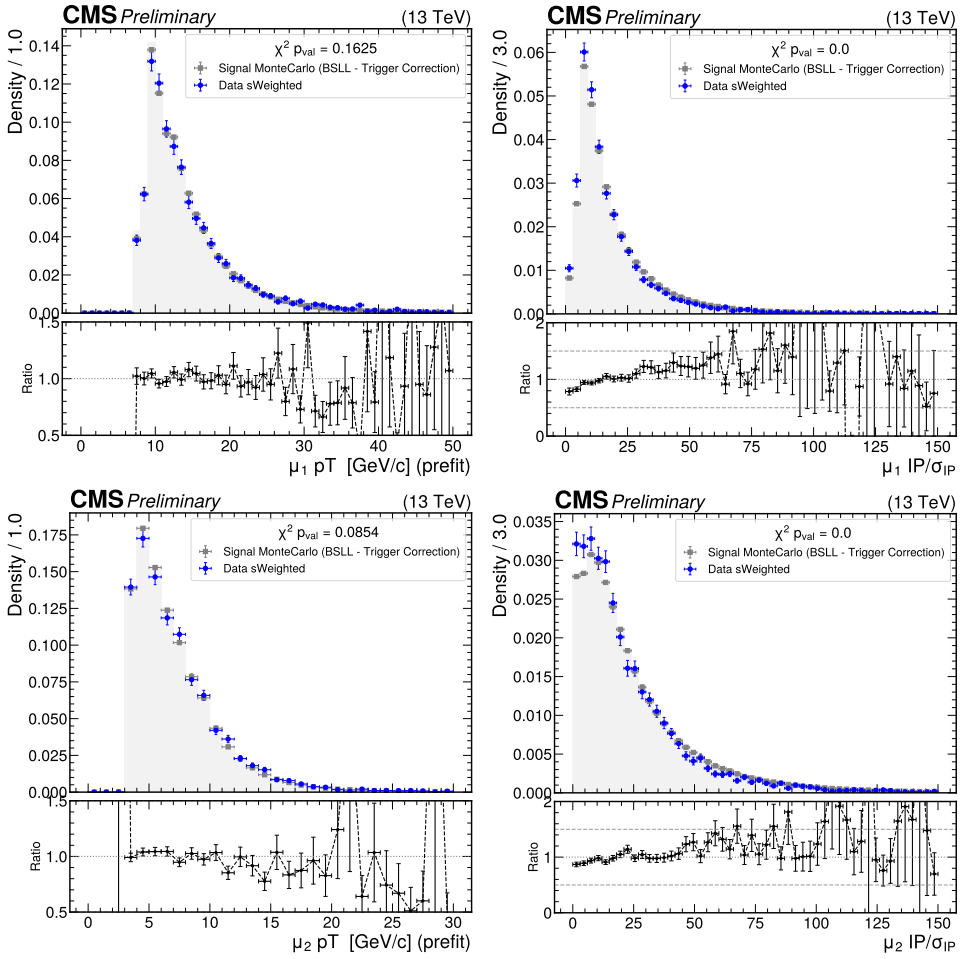

Figure 5.36: Three histograms are displayed in each plot, the original PHSP Monte Carlo is plotted as gray bars, the Trigger Corrected MC in gray error plot, and the Data sWeighted in blue error plot. Trigger correction is performed by the ScaleFactors for the cocktail of trigger paths obtained from EXO-22-019. Data sWeighted is plotted in blue, all uncertainties in the y axis, are the square root of the sum of the squares of the corresponding weights.

Before creating and applying the correction, there are some details to keep in mind. Since the correction is fine-tuned, one should validate its performance on a control sample. The common approach involves using data and simulation from control channels, such as $B^+ \to J/\Psi K^+$ and $B^+ \to \Psi(2S)K^+$. With these two control channels available, we can derive a correction from one and validate it using the second channel. As has become customary within the BPH group, we have selected the J/Ψ to create the correction and the $\Psi(2S)$ to validate it. This approach will be discussed in the next subsection.

Multivariate correction

There are several sources that discuss using multivariate classifiers to correct between different samples, such as Martschei's paper [121] and Rogozhnikov's work [122]. Although both describe slightly different approaches, we found more suitable Martschei's method. The main

idea involves training a classifier to differentiate between Monte Carlo (MC) samples and Real Data (RD). After classification, the output is converted into probabilities indicating whether each event belongs to the Monte Carlo or real data category. Then, the weights for each event are calculated based on these probabilities, as in the following equation:

$$\omega(event) = \frac{RD_{probability}(event)}{MC_{probability}(event)} = \frac{RD_{probability}(event)}{1 - RD_{probability}(event)} \tag{5.9}$$

The output of the classifier depends on the samples and the variables used to train it. The variables we have selected are the same used to train the XGB classifier for background reduction plus kinematic variables of the B meson and the muons.

- signLxy,
- prob,
- PDL,
- kpt,
- Bpt,
- cosA,
- fit_eta,
- mu(1, 2)_IP_sig,
- mu(1, 2)_pt,

Regarding the samples, we have used the high-statistics J/Ψ resonant channel with the corresponding MC sample ($B^+ \to J/\Psi(\mu^+ mu^-)K^+$) to train the classifier. Using this classifier we can obtain weights for any other sample. The first sample we have used is the same ($B^+ \to J/\Psi(\mu^+ mu^-)K^+$) used for the training. The effectiveness of the correction is shown in Figure 5.37. Afterwards, we obtain a set of weights for an independent sample, the $\Psi(2S)$ resonant channel. The effect of the multivariate reweighing is shown in Figure 5.38. Since these corrections produce the desired effect in both control channels, we proceed to apply them to the signal channel.

Finally, the effect of the complete correction, trigger plus multivariate, in the signal channel is shown in Figure 5.39.

A χ^2 test was conducted to compare the Signal Monte Carlo and Data. The χ^2 value was calculated by determining the difference between the normalized counts of both histograms and dividing it by the corresponding uncertainties. These uncertainties were obtained by scaling the uncertainty per bin using the following formula: $\sqrt{\sum_i w_i^2}/C$, where C represents the constant used to normalize the histograms.

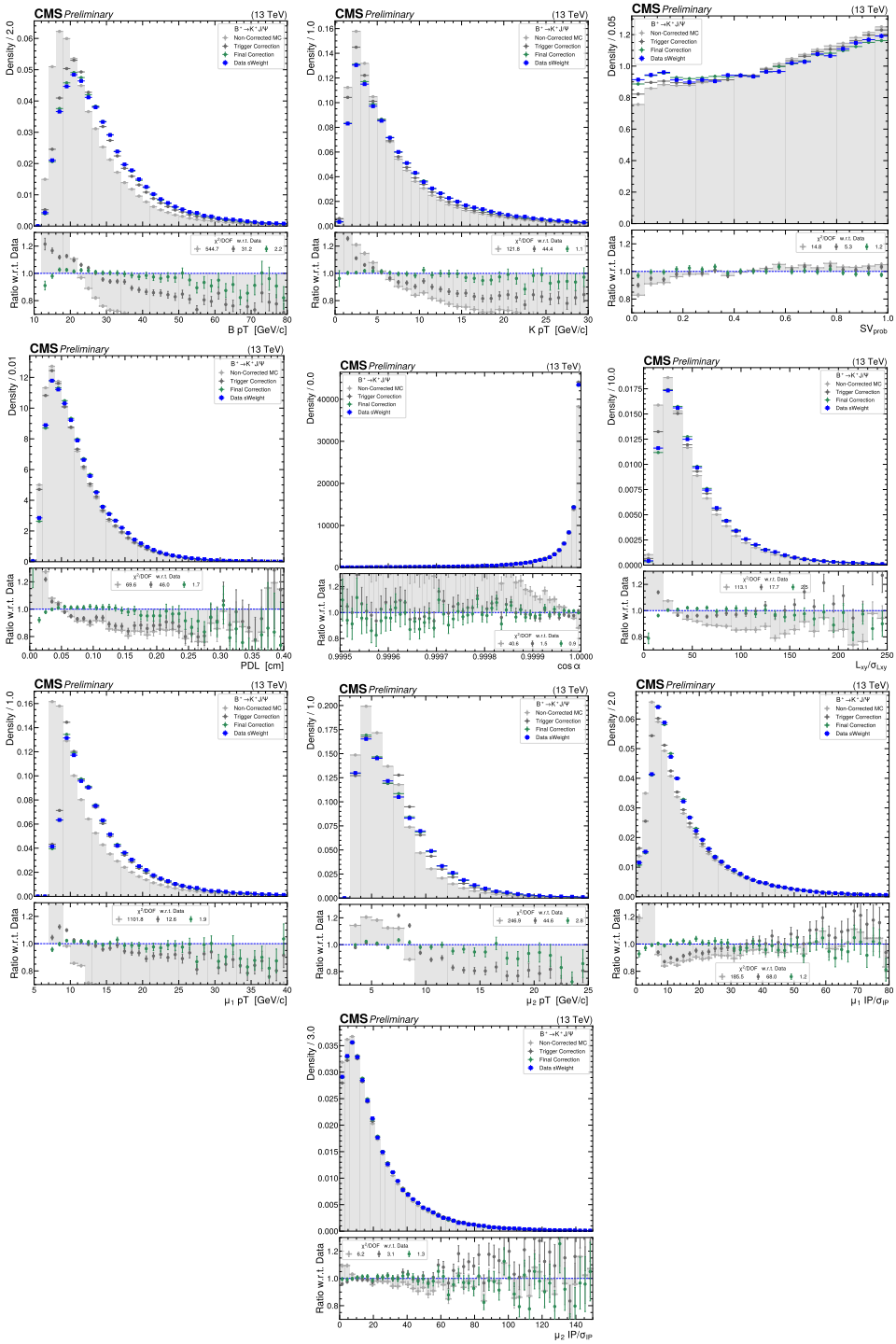

Figure 5.37: The reweighting process for the resonant channel $B^+ \to J/\Psi K^+$ involves training the BDT classifier using only 10% of the complete dataset. In this figure, we present the distribution of the variables used in the BDT training across all correction steps. Each step demonstrates an enhancement, as shown in the ratio and the χ^2 values divided by the number of bins, both with respect to data distributions.

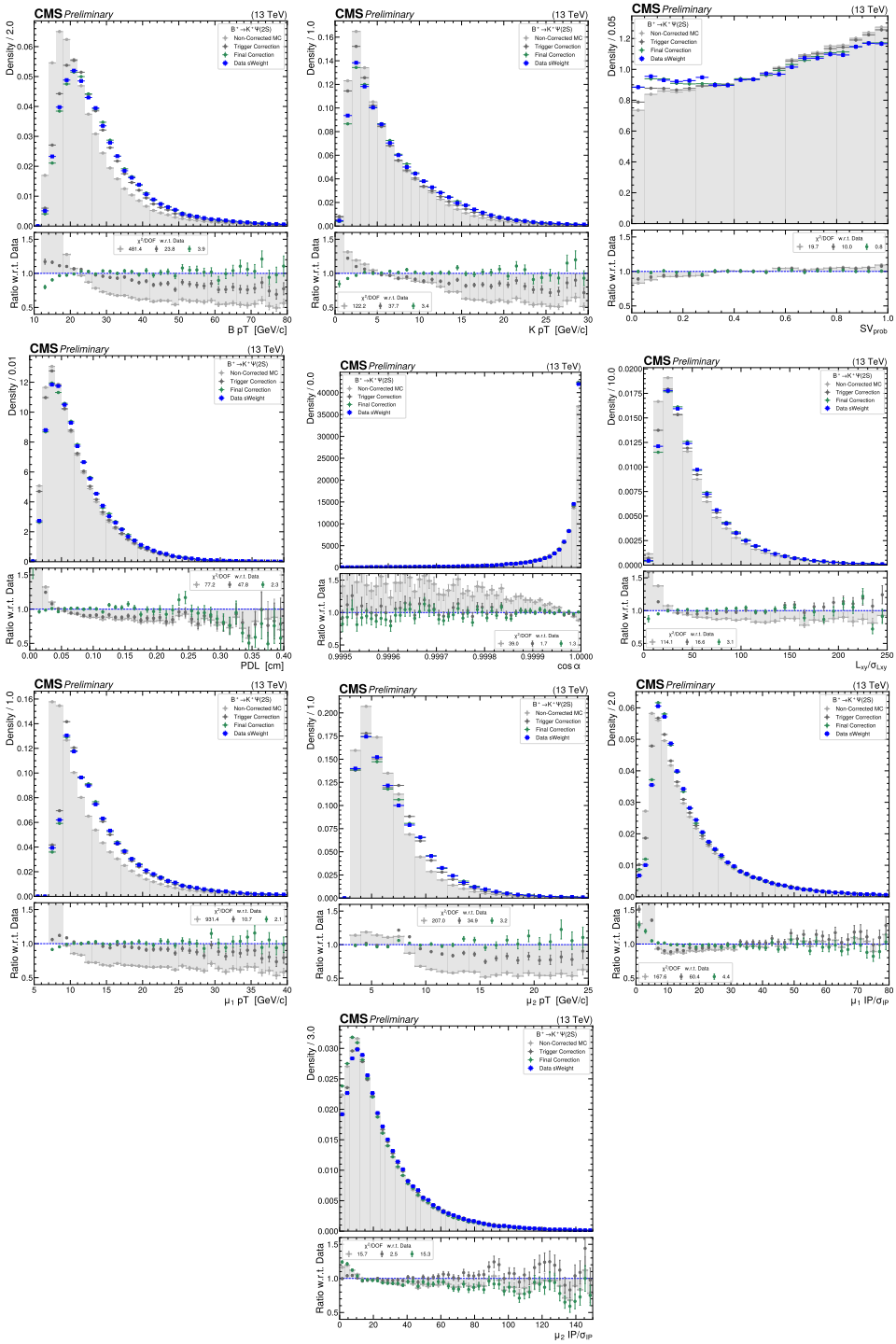

Figure 5.38: The reweighting validation occurred in the $B^+ \to \Psi(2S)K^+$ channel. While there are visible improvements in the variables used for the correction, they are less pronounced as those in the J/Ψ channel. However, we consider this a successful validation, and therefore, the correction is applied to the signal, *i.e.* the non-resonant region.

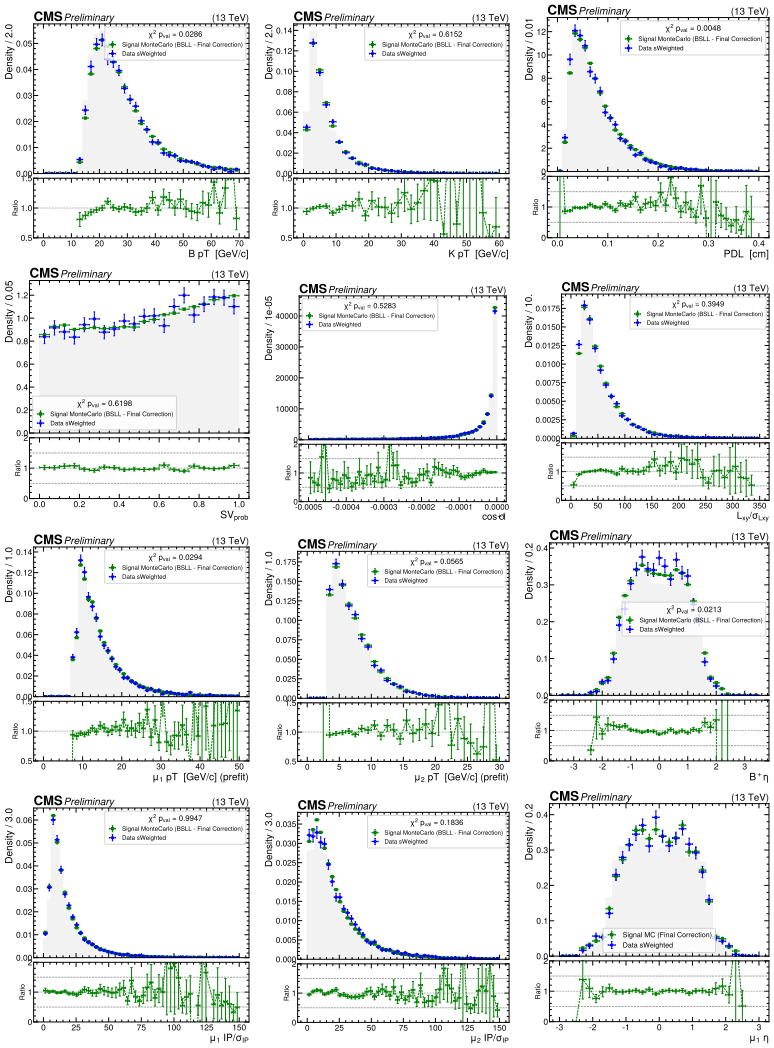

Figure 5.39: Comparison of the corrected Monte Carlo with Scale Factors and multivariate reweighting with respect to data background subtracted via sPlot technique. In green we show the Final correction, which includes multivariate reweight and trigger correction. In blue the signal from data extracted with sPlot and in faint grey the Monte Carlo only trigger corrected, that is without multivariate reweighting.

5.5.5 Effect on the angular distributions

The effect of the trigger correction and the multivariate reweighting on PHSP MC can be seen in Figure 5.41. The Figure shows the comparison between the initial angular distributions and the corrected ones for each q^2 bin, no discrepancy is introduced by the reweighting in high q^2 bins.

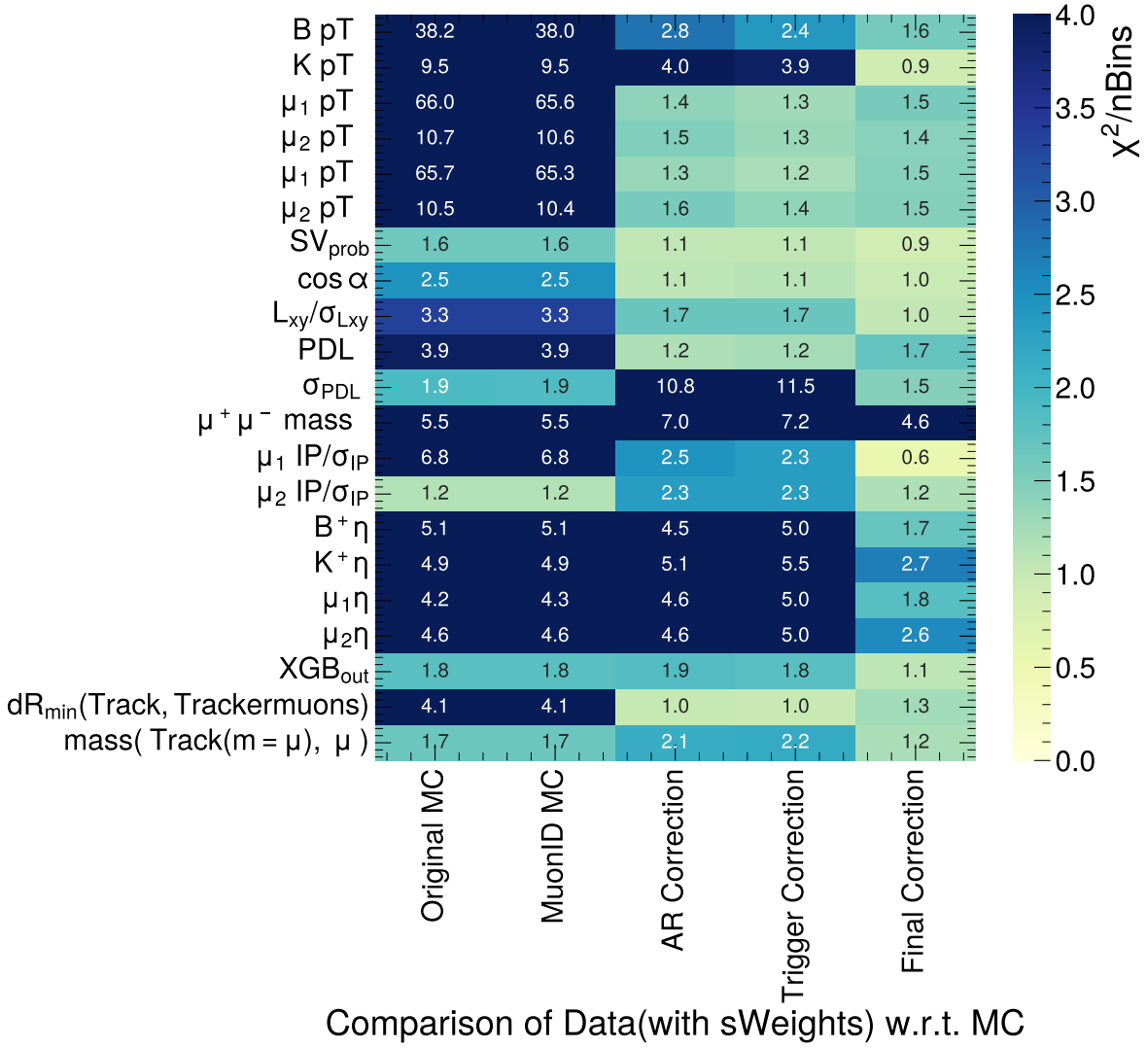

Figure 5.40: Binned χ^2 test comparing Data (using sWeights) with different steps of MC correction. Each column represents the χ^2/DOF at a specific correction step, as described below the plot. The first comparison is against the uncorrected MC, followed by the Trigger Correction, and the Final Correction involves applying a set of weights per event obtained through the multivariate reweighting process described in the text.

5.6 Determination of Angular Efficiency

We evaluate the signal angular efficiency with the distribution of reconstructed events passing the final selection criteria, including corrections described in Section 5.5. The efficiency is obtained for each q^2 bin, and as a function of $\cos(\theta_l)$.

For the calculation of the efficiency, we used the official MC PHSP production, which is described in Section 5.2.2.

By using PHSP we ensure the generation of uniform distributions on $\cos\theta_l$ at the GEN level. Then, the efficiency as a function of the angular variable is given by a fit on the

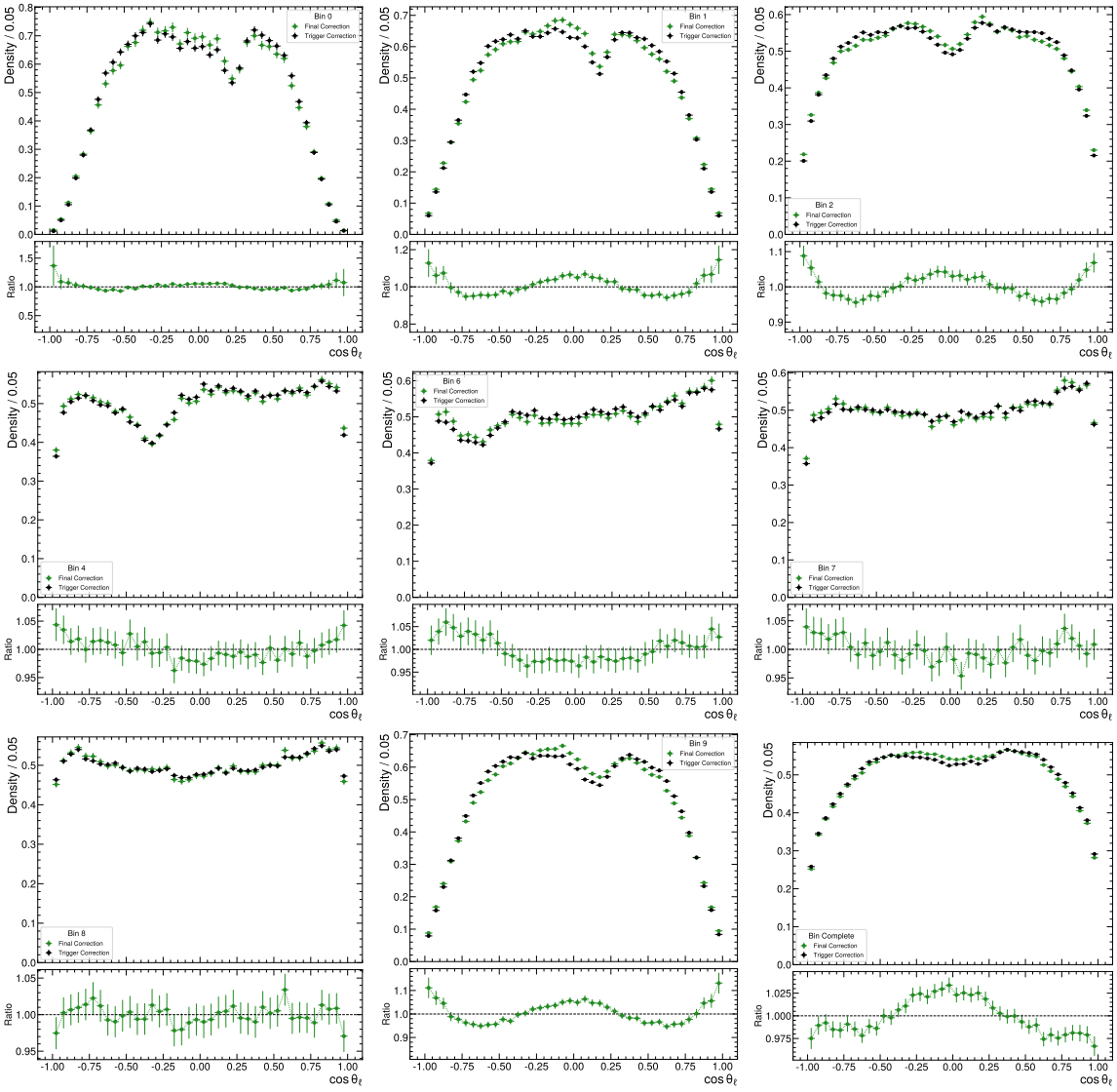

Figure 5.41: Effect of both corrections on the angular observable. Distributions correspond to the Phase Space generation.

angular distribution of reconstructed events passing the final selection criteria, also, the MC correction described in Section 5.5 is considered.

It is worth noting that only the shape of the efficiency is relevant to this analysis, therefore the absolute value of the efficiency is not important.

We opted for Kernel Density Estimation (KDE) with a Gaussian Kernel to model the angular efficiency instead of the Bernstein polynomials used in the angular sidebands.

This decision was motivated by the impact of the Fake Kaon veto on the angular distribution. To have an acceptable fit of the final shape for the PHSP MC, the degree of Bernstein polynomials was greater than 20, which we believed impractical.

Two important parameters of the KDE, are the bandwidth and the mirroring. The bandwidth is the standard deviation of the Gaussian kernel and can be regarded as a smoothing

parameter. The mirroring was introduced to circumvent a problem on the boundaries of the KDE on the angular distribution. This parameter mirrors a fraction of the existing data at the boundaries.

To avoid overfitting, we scanned the bandwidth from 0.1 to 0.01 in steps of 0.005, starting with the highest value. For each bandwidth, we scanned mirroring from 0 (no mirroring) up to the current bandwidth value. We calculated the p-value of the χ^2 test for each combination. If the p-value is lower than the threshold for all models, we continue with the next bandwidth. If a model passes the threshold, we select that model.

In Figure 5.42, the nominal models for the angular signal efficiency are displayed.

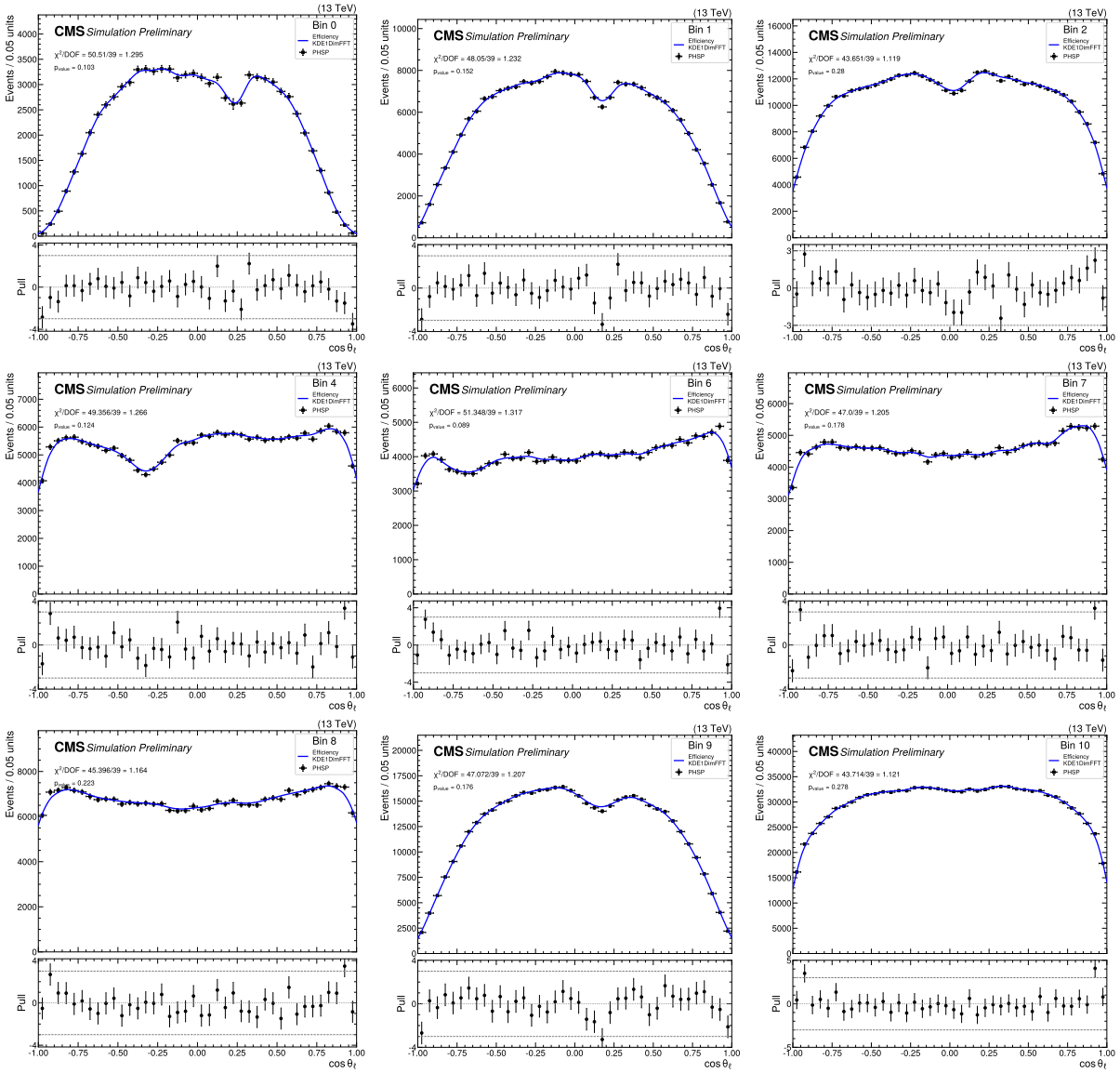

Figure 5.42: Angular distribution for every bin at the final selection level, scale factors and iterative reweighting corrections are applied.

5.7 Cross Checks

Cross-checks are an important part of the analysis in experimental high-energy physics, they can serve to verify any possible biases. In particular, we did a closure test and a validation of the analysis in the resonant/control channels. The closure test compares the fitted parameters of the GEN level distributions of the BTOSLLBALL sample, with respect to the parameters from the RECO level distributions. The GEN level distributions are fitted with the angular pdf Eq. 5.1 only, and the RECO level uses the product of the efficiency and the angular pdf.

The validation on the resonant channels was requested by reviewers of the analysis, and since there are no predictions for the A_{FB}, F_H parameters, we used the result from a fit to GEN level distributions as point of comparison.

5.7.1 Closure Test

A natural cross-check is to compare the parameters obtained from a fit to GEN level and RECO level datasets. In this section, we show this comparison using the official BTOSLLBALL generation.

For the GEN level, we considered radiative corrections via the PHOTOS package, and no filters were applied. For RECO level, we consider the dataset after all selection criteria.

We fit the GEN level dataset by using only the theoretical decay rate model as described by Equation 5.1. For the RECO level, we use the product PDF from the theoretical model and the efficiency description per each q^2 Bin.

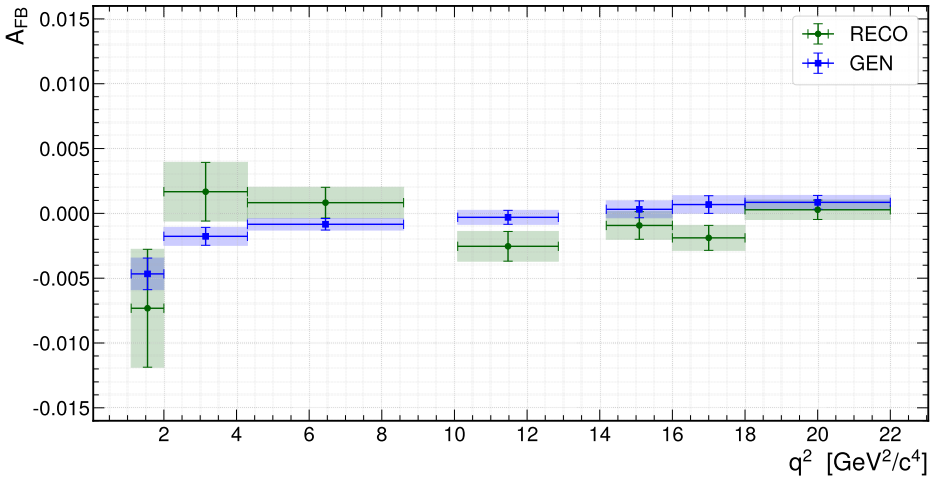

Figure 5.43: Comparison of the fitted A_{FB} at GEN and RECO level. For the RECO level, we only used the theoretical decay width times the efficiency.

Figures 5.43 and 5.44 show the closure test, where the error bars correspond to the *Hessian* uncertainties. Additionally, in Table 5.14 we show the numerical values of the resulting fits. In this comparison, we calculate the difference between the GEN and RECO fits for each q^2 bin, and divide it by the uncertainty at the RECO level. We find that this ratio is less than three for all bins, indicating good agreement between the fits. Since the

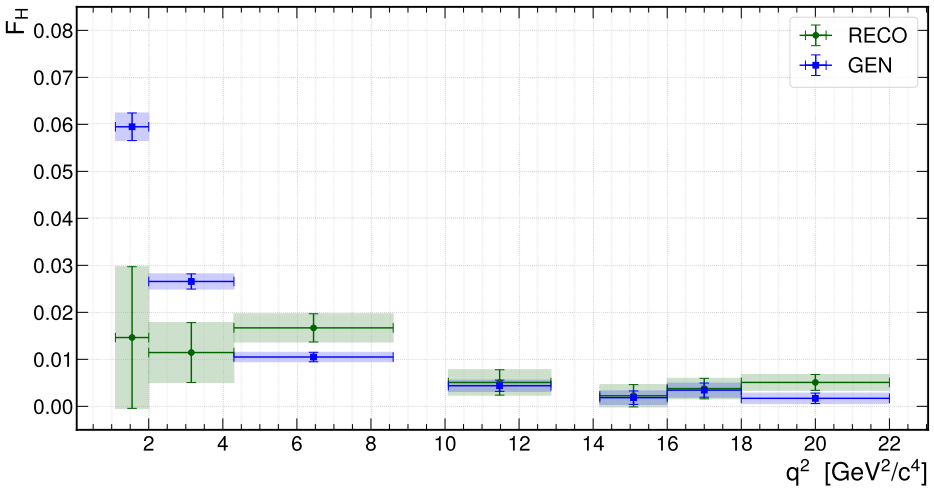

Figure 5.44: Comparison of the fitted F_H at GEN and RECO level. For the RECO level, we only used the theoretical decay width times the efficiency.

ratio of differences to uncertainties is below the threshold of three, we consider the closure test to have passed.

q^2 Bin	$A_{FB_{RECO}}$	$A_{FB_{GEN}}$	$\frac{A_{FB_{RECO}} - A_{FB_{GEN}}}{\sigma}$	$F_{H_{RECO}}$	$F_{H_{GEN}}$	$\frac{F_{H_{RECO}} - F_{H_{GEN}}}{\sigma}$
0	-0.0073 ± 0.0045	-0.0047 ± 0.0012	-0.56	0.0146 ± 0.0151	0.0595 ± 0.0029	-2.92
1	0.0017 ± 0.0023	-0.0018 ± 0.0007	1.46	0.0114 ± 0.0064	0.0266 ± 0.0016	-2.30
2	0.0008 ± 0.0012	-0.0008 ± 0.0004	1.32	0.0167 ± 0.0030	0.0105 ± 0.0010	1.96
4	-0.0025 ± 0.0011	-0.0003 ± 0.0005	-1.77	0.0051 ± 0.0027	0.0044 ± 0.0012	0.24
6	-0.0009 ± 0.0011	0.0003 ± 0.0007	-1.00	0.0023 ± 0.0024	0.0018 ± 0.0014	0.15
7	-0.0019 ± 0.0010	0.0007 ± 0.0007	-2.18	0.0038 ± 0.0022	0.0034 ± 0.0015	0.13
8	0.0003 ± 0.0007	0.0009 ± 0.0005	-0.62	0.0051 ± 0.0017	0.0017 ± 0.0011	1.67

Table 5.14: Results from the closure test. Fitted parameters at GEN and RECO level to BTOSLLBALL MonteCarlo. At GEN level, only theory PDF was used, while at RECO level we multiplied the theory model with the corresponding angular efficiency.

5.7.2 Control channels

The control channels $B^+ \to K^+ J/\psi(1S)(\mu^-\mu^+)$and $B^+ \to K^+\psi(2S)'(\mu^-\mu^+)$provide a useful reference for evaluating the statistical treatment and fitting strategy used for the non-resonant (signal) channel.

In this section, we attempt to replicate the strategy applied to the non-resonant decay for the control channels. However, some changes have been applied, such as modifying the sidebands definition to obtain angular background distributions that are not strongly influenced by the signal component. And the decision to not apply the Fake kaon cut, since the background it is intended to remove, is negligible for the resonant channels.

GEN distributions

Since the angular theoretical model was obtained for the non-resonant channel, the parameters A_{FB} and F_H may not be appropriate to describe the control channels. We have not found previous measurements of these parameters on the control channels. Therefore, we rely on the estimation obtained from Monte Carlo simulations. Our first step on this cross-check was to obtain a fit on the GEN level distribution of the $B^+ \to K^+ J/\psi(1S)(\mu^-\mu^+)$channel.

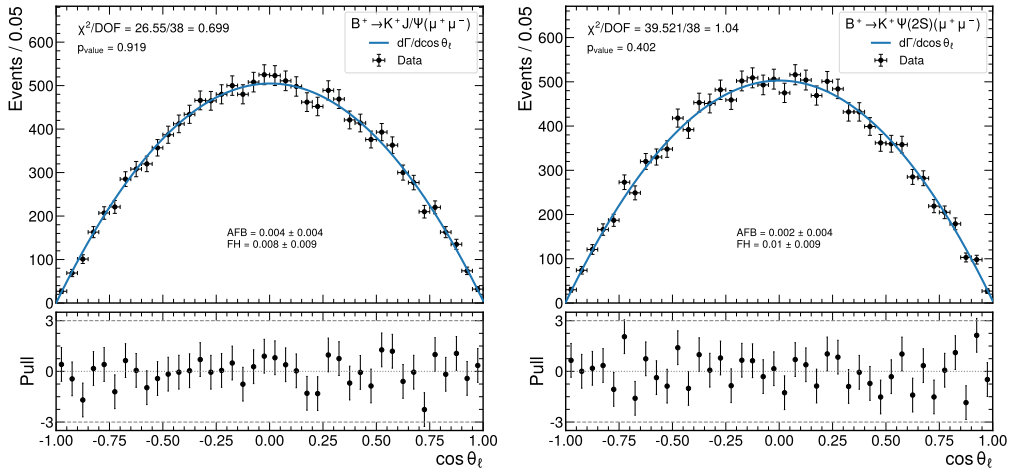

Figure 5.45: GEN level fit on the angular distribution of the $B^+ \to K^+ J/\psi(1S)(\mu^-\mu^+)$and $B^+ \to K^+\psi(2S)'(\mu^-\mu^+)$decay channels using Equation 5.1. Both parameters of interest are consistent with zero. This result serves as our point of reference for the validation of the control channels.

In Figure 5.45, we show the result of the fit to (Unfiltered) GEN level $B^+ \to K^+ J/\psi(1S)(\mu^-\mu^+)$and $B^+ \to K^+\psi(2S)'(\mu^-\mu^+)$decay channels. The result of this fit shows that A_{FB} and F_H are consistent with zero from the simulation.

Final Selection

The complete selection cannot be applied blindly to the control channels, at least the resonant veto and the B^+ & Ψ cut must not be applied. Additionally, our fake kaon veto was applied since, on the non-resonant channel the contribution of this background was relevant. However, in the control channels, the large branching fraction of these decays makes this background negligible as Figure 5.46 shows. Therefore, we decided that the final selection on the resonant channels would not include the Fake Kaon veto.

After applying the final selection, we proceed to obtain a mass fit on each control channel, this fit serves two purposes: first, it gives us a reliable estimation of the signal and background yields, and second, it provides sWeights used for the MC correction used in the evaluation of the angular efficiency.

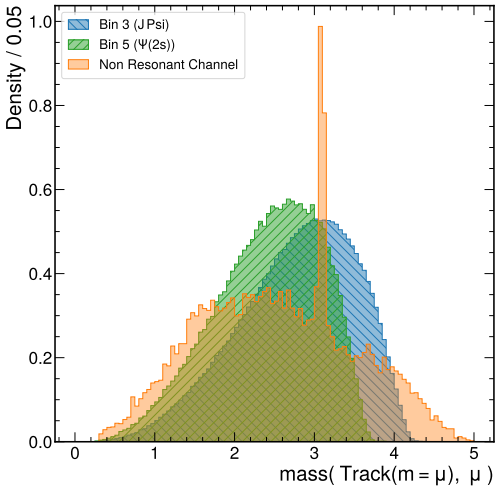

Figure 5.46: Distribution of the invariant mass of the track and the muon of opposite sign. The track is considered under the mass hypothesis of the muon. On the non-resonant channel a clear peak appears around the mass of the J/Ψ, while on the control channels, this contribution is negligible.

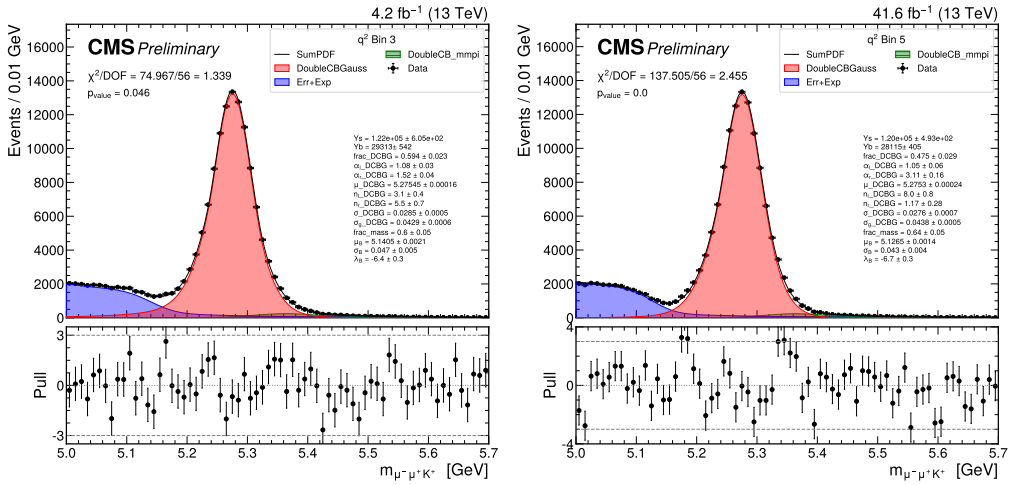

Figure 5.47: Fit on the mass variable to the control channels corresponding to q^2 Bins 3 and 5, J/Ψ and $\Psi(2s)$ resonant channels respectively. From these fits we obtain the measurements of the signal and background yields. From Bin 3, we obtain the sWeights used in the MC correction.

Angular Efficiency

We evaluated the angular efficiency using the same non-resonant MC simulation used for the signal channel. We only took events from the respective q^2 Bin, that is Bin 3 (2.95 - 3.18 GeV/c^2) for J/Ψ, and Bin 5 (3.59 - 3.77 GeV/c^2) for $\Psi(2s)$. The procedure to select the degree of the Bernstein polynomial, and corrections applied to the MC, are the same as for the non-resonant channels and are described in Sections 5.6 and 5.5 respectively.

The selected models for the angular efficiency in each q^2 Bin, are displayed in Figure

5.48. The pull distribution and χ^2/DOF agree on the goodness of the fit to the simulated data.

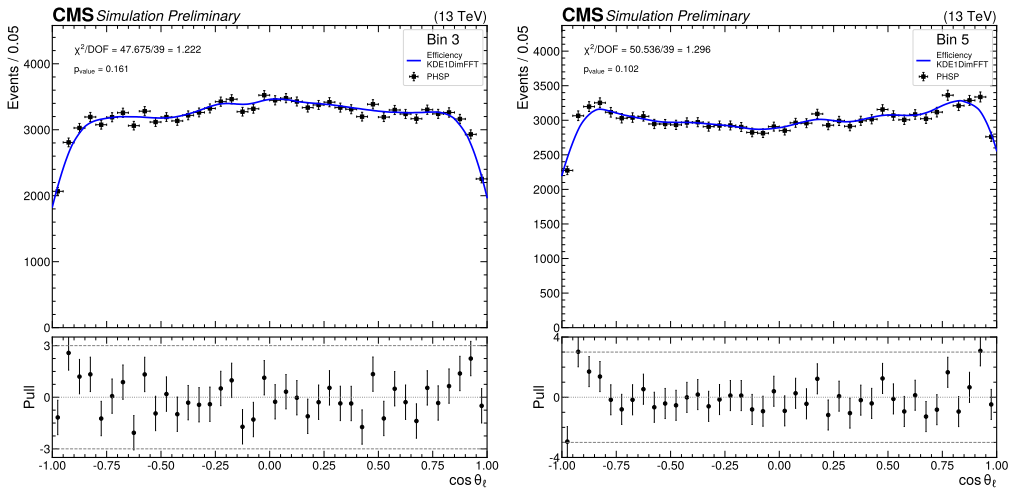

Figure 5.48: Angular distribution for q^2 bins 3 and 5, corresponding to the control channels. The complete selection for the control channels have been applied as well as the trigger and iterative correction.

Angular Background

The definition of the sidebands has been constant throughout the analysis, 5.0 - 5.15 GeV/c^2 for the left sideband, and 5.4 - 5.7 GeV/c^2 for the right sideband. However, as can be seen from Figure 5.47, in the resonant channel, these sidebands have a significant contribution of the signal component. This contribution could bias the shape of the angular background in each region. Therefore, we modified the sideband definition for the resonant channels as (5.0 - 5.1 GeV/c^2) and (5.5 - 5.7 GeV/c^2) for each sideband.

Figures 5.49 and 5.50 show the angular distribution on the left and right sidebands in q^2 Bins 3 and 5.

Similarly, as with the non-resonant channel, the model for the angular background in the signal region is modeled by:

$$B_i(\theta_l) = \frac{1}{2}(B_{Left}(\cos\theta_l) + B_{Right}(\cos\theta_l)), \tag{5.10}$$

Angular Fit and Projections

The final fit is done in the signal region defined by the mass of the B candidate (5.15 - 5.4 GeV/c^2). The signal and background yields were interpolated from the value obtained in Figure 5.47, and were kept fixed at the final fit. All mass parameters are fixed from the same values in Figure 5.47, as well as the fraction described in the previous section to define the model of the angular background. The mass projections in that region are shown in Figure 5.51, and the angular projections, after the angular fit, in Figure 5.52.

The values obtained for the POIs are displayed in the table 5.15.

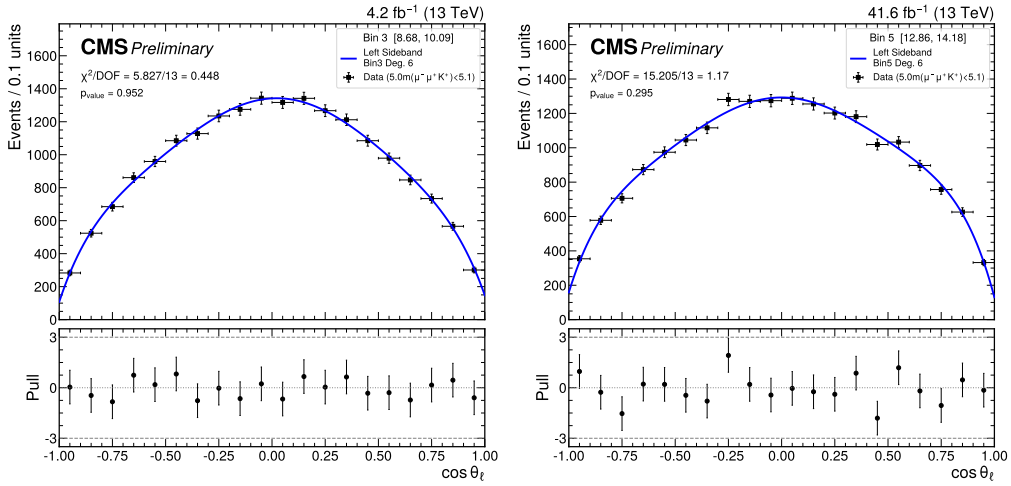

Figure 5.49: $\cos(\theta_l)$ distribution for left sideband [5.0 - 5.1 GeV/c^2] for each q^2 bin.

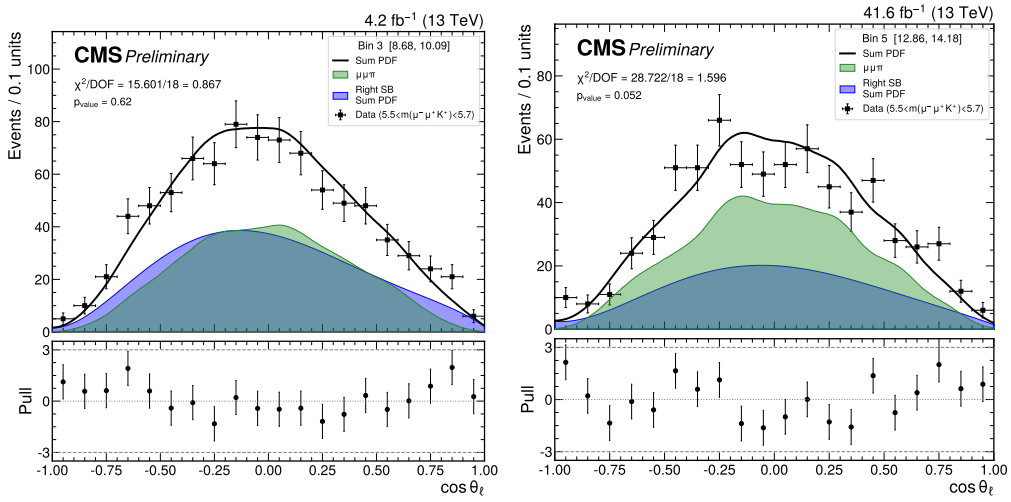

Figure 5.50: $\cos(\theta_l)$ distribution for right sideband [5.5 - 5.7 GeV/c^2] for each q^2 bin.

q^2 Bin	[(GeV/c^2)^2]	A_{FB}	F_H
J/Ψ	(8.68, 10.09)	-0.0011 ± 0.0016	0.0116 ± 0.0039
$\Psi(2s)$	(12.86, 14.18)	-0.0037 ± 0.0014	0.0073 ± 0.0034

Table 5.15: Angular parameters of the control channels obtained by a 2D fit on the mass and angular variables. The floating parameters in this fit were: A_{FB}, F_H, Y_B, Y_S, and f_{SB}.

5.8 Statistical Error Estimation using the Feldman-Cousins Method

The presence of the physical boundaries defined by equations 5.2 and 5.3 complicates the estimation of the confidence intervals of a fit result that may lie close to the Physical boundary. The Feldman-Cousins (FC) approach gives a reliable method to obtain the corresponding

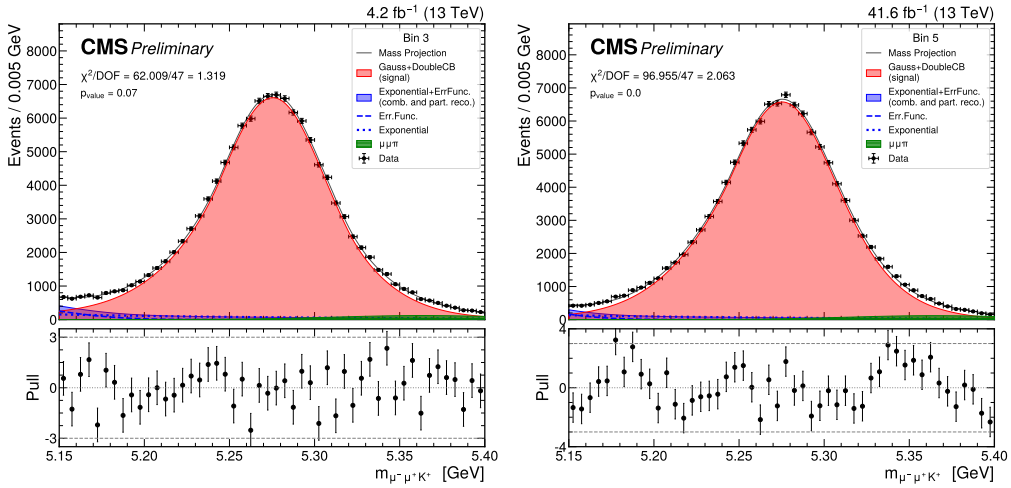

Figure 5.51: Mass projections of the two-dimensional model used to extract the angular parameters. On the left, q^2 Bin 3, corresponds to the $B^+ \to K^+ J/\psi(1S)(\mu^-\mu^+)$resonant decay. On the right, q^2 Bin 5, corresponds to the $B^+ \to K^+\psi(2S)'(\mu^-\mu^+)$resonant decay.

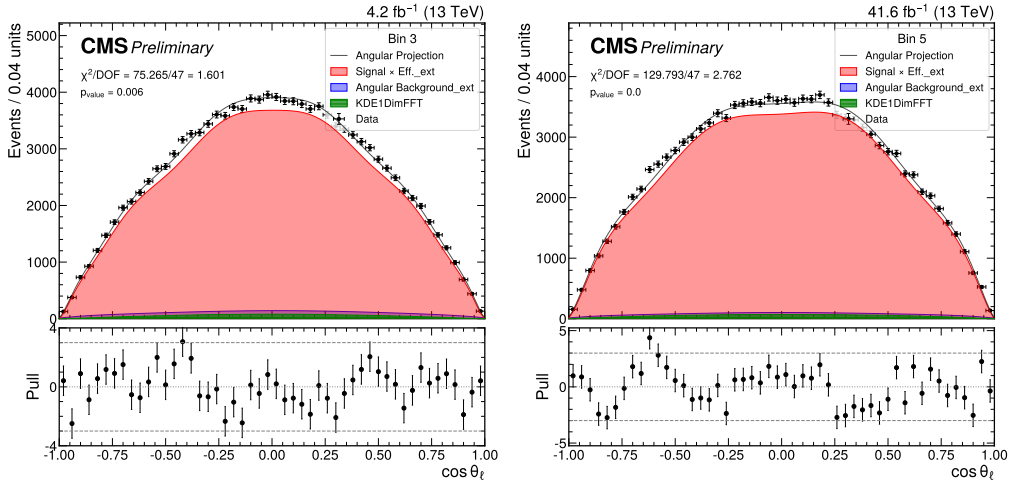

Figure 5.52: Angular projections of the two-dimensional model used to extract the angular parameters. On the left, q^2 Bin 3, corresponds to the $B^+ \to K^+ J/\psi(1S)(\mu^-\mu^+)$resonant decay. On the right, q^2 Bin 5, corresponds to the $B^+ \to K^+\psi(2S)'(\mu^-\mu^+)$resonant decay.

intervals which also ensures the correct coverage for the confidence intervals.

5.8.1 2D Contours

A 2-dimensional confidence region can be obtained by considering both parameters of interest simultaneously. In this case, the 1-CL method as described by Karbach [123] is applied. This method starts by considering a pair of true parameters $(A_{FB_{True}}, F_{H_{True}})$ and generate toy experiments. Then, for each toy, it is computed the negative logarithm of the likelihood ratio $(\Delta\chi^2_{Toy})$ Eq. 5.11, Where $\vec{\alpha}$ stands for the nuisance parameters and $\vec{\alpha_0}$ are the fitted nuisance parameters with $A_{FB_{True}}$ and $F_{H_{True}}$ fixed. The Best parameters are the ones that

minimize the negative-log likelihood and are inside the physical region.

$$R(m,\theta,A_{FB_{True}},F_{H_{True}}) = \frac{P(m,\theta|A_{FB_{True}},F_{H_{True}}\vec{\alpha_0})}{P(m,\theta|A_{FB_{Best}},F_{H_{Best}},\vec{\alpha_0})} \qquad (5.11)$$
$$\Delta\chi^2 = -log\left(R(m,\theta,A_{FB_{True}},F_{H_{True}})\right)$$

Then, the Negative Logarithm of the Likelihood ratio for data is calculated ($\Delta\chi^2_{Data}$) and the 1-CL value is given by the fraction of toys that have $\Delta\chi^2_{Toy} > \Delta\chi^2_{Data}$. A complete contour is drawn by scanning all possible values for the parameters (inside the physical region) and for a given CL. For example, for the case of the 2D contour, a CL = 39.3% corresponds to a 1σ region. Although this is very computing-intensive, a first estimate of the contour can be obtained by means of the likelihood profile or the prob-method (proposed by Karbach) reducing the computing time. Results are blinded for the moment.

We applied this method with the complete pdf as defined in Section 5.4.3, for all q^2 bins. We generated injection MC with the same yield as obtained from real data, taking the signal component from the BTOSLLBALL generation. Figure 5.53 shows the contour for different confidence levels.Injection MC is obtained by adding a toy MC from the 2D background pdf, and a sample from the BTOSLLBALL MC, both numbers of events are the same as the yield obtained from a fit to data.

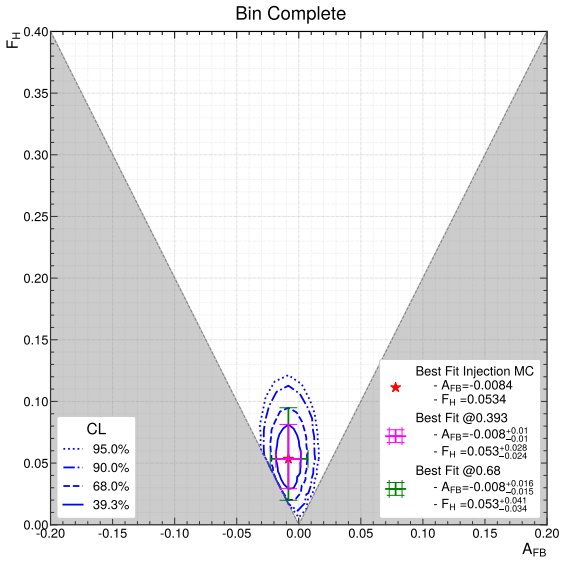

Figure 5.53: Contour at different confidence levels for Injection Monte Carlo corresponding to Bin Complete. The contours for all q^2 Bins are shown in Appendix **??**

In Tables 5.16 and 5.17, we compare the projections of the 39.3% contours with respect to the Hessian uncertainty obtained from the NLL fit. In cases where the best fit lies far from the boundary, the uncertainties agree in both methods. On the other hand, for best fits on the boundary, the projection of the uncertainties can be less than 50% of the Hessian uncertainty.

q^2 Bin	Nominal Fit	$\sigma_{\mathrm{AFB}up}$	$\sigma_{\mathrm{AFB}low}$	Hesse
0	-0.0654	+0.0841	-0.1081	0.0957
1	-0.0000	+0.0346	-0.0279	0.0457
2	0.0102	+0.0367	-0.0361	0.0260
4	0.0195	+0.0364	-0.0364	0.0243
6	0.0154	+0.0250	-0.0299	0.0258
7	0.0016	+0.0263	-0.0276	0.0184
8	-0.0734	+0.0263	-0.0278	0.0243
9	-0.0000	+0.0189	-0.0106	0.0317
10	0.0083	+0.0132	-0.0150	0.0097
Complete	-0.0085	+0.0158	-0.0146	0.0101

Table 5.16: Statistical uncertainty estimation with Injection MC for A_{FB}.

q^2 Bin	Nominal Fit	$\sigma_{\mathrm{FH}up}$	$\sigma_{\mathrm{FH}low}$	Hesse
0	0.1308	+0.2874	-0.1252	0.3511
1	0.0000	+0.0880	-0.0000	0.1431
2	0.0679	+0.1134	-0.0650	0.0747
4	0.1275	+0.0992	-0.0795	0.0648
6	0.0307	+0.0810	-0.0303	0.0638
7	0.0746	+0.0743	-0.0532	0.0461
8	0.1467	+0.0571	-0.0471	0.0630
9	0.0000	+0.0434	-0.0000	0.0972
10	0.0457	+0.0400	-0.0297	0.0255
Complete	0.0522	+0.0415	-0.0336	0.0270

Table 5.17: Statistical uncertainty estimation with Injection MC for F_H.

5.9 Systematic Uncertainties

The physical boundaries affect the uncertainties, therefore the evaluation of the systematic uncertainties needs the unblinding of the results. To get an estimation of the uncertainties, we used an injection Monte Carlo technique, this technique allowed us to obtain an expected uncertainty in any place of the physical space, with the same statistics as the real data.

5.9.1 Injection Monte Carlo

A reference injection Monte Carlo is used to estimate the systematic and statistical uncertainties while the analysis remains in the current blinding status. The results of the systematic uncertainties for the reference injection will be shown in this section. To create an injection sample we use the 2D background component of the complete PDF to produce a toy MC then, we *inject* signal events from the signal BTOSLLBALL MC generation, produced with the BTOSLLBALL evtgen routine. The sampling on the Signal MC is done with replacement, and the number of events for each sample is the same as the integer part of the yields obtained from the complete 2D fit.

5.9.2 Fitting Bias

The presence of the boundaries on the parameter space induces a bias on the MLE estimator of the parameters of interest. The bias is expected to be larger when the *true* values lie on, or close, to the boundaries. We take the fitting bias as a source of systematic uncertainty and measure it in two different ways.

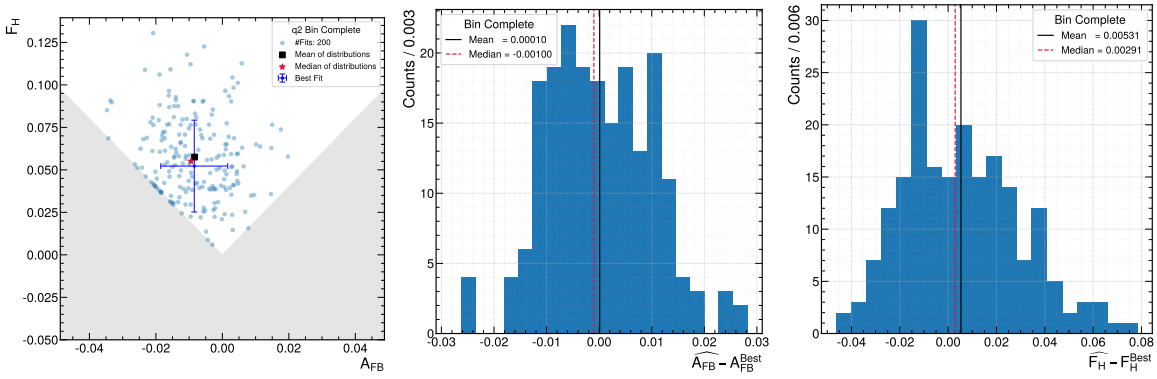

Figure 5.54: On the left, we show a scatter plot of the fitted parameters where the mean and median are displayed as black squares and red stars respectively. The best fit is also shown with its Hessian errors for comparison. The middle and right plots show the histograms of the difference with respect to the reference values (best fit).

For the first one, we generated 200 toys MC from the complete PDF, with A_{FB}, F_H, and all other nuisance parameters as obtained by the 2D fit to reference data. The bias in each parameter is used as a source of systematic uncertainty and is evaluated by the mean of the fitted POIs minus the reference value.

The plots in Figure 5.54 show the scatter of all fitted parameters for the complete q^2 Bin, as well as the histograms for each parameter of interest. The black solid line represents the mean of the distribution, which is used as an estimation of the fitting bias.

The sampling of the injection MC allows us to evaluate the effect of the presence of the modeled background. First, we fit the signal angular model with the signal component of the injection MC. The signal model is the product of the angular efficiency times the theoretical distribution from Eq. 5.1. Then, the signal plus background 2D model is fitted to the complete injection. The values of the parameters from each fit are indexed with S and $S+B$. In figure 5.55, we show the scatter plot of both sets of fitted parameters, as well as the distributions of their difference, $\hat{\theta}_{S+B} - \hat{\theta}_S$. We use the mean of these distributions as the estimation of the systematic uncertainty on the fitting bias due to the presence of the background.

5.9.3 Limited size of Monte Carlo Sample

The limited size of the Monte Carlo used to obtain the efficiency model induces a systematic uncertainty. To estimate this uncertainty, we use the angular signal efficiency from Section 5.6 and its covariance matrix from the fit result.

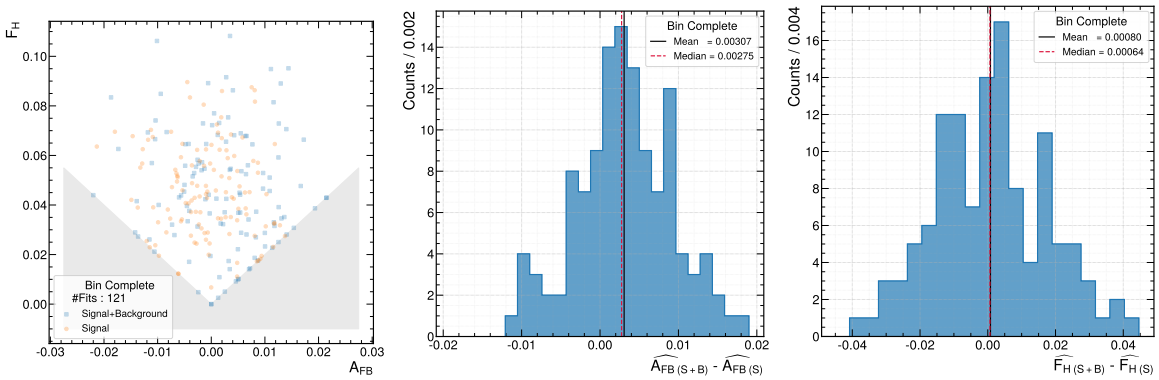

Figure 5.55: On the left, the dispersion of the fitted parameters on injection Monte Carlo, using the complete data (blue squares) and the signal component only (orange circles). The plots in the middle and on the right, show the distribution of the difference between these sets of parameters. The mean of these distributions is used as an estimation of the fitting bias due to the presence of the background.

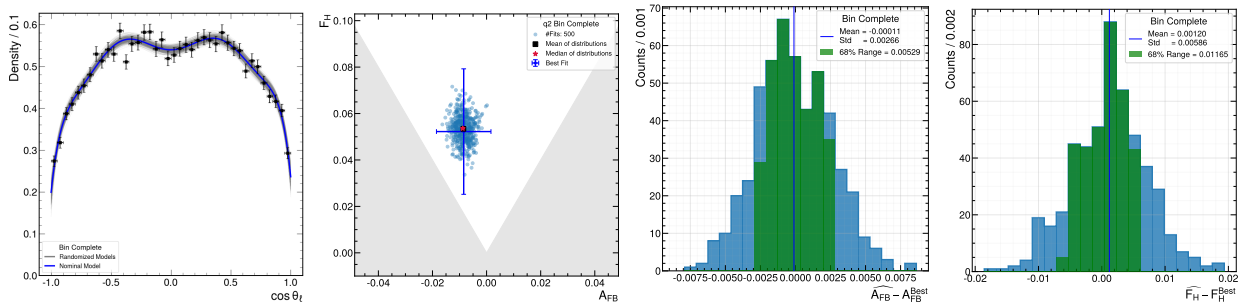

Figure 5.56: From left to right. The first plot shows the nominal efficiency model in blue and its variation from the covariance matrix in gray, the data used for this fit (unfiltered and corrected PHSP MC) is shown in the histogram. The second plot shows the scatter plot of the fitted parameters and the best fit with Hessian errors for comparison. Finally, the third and fourth plots show the histograms of the difference of the fitted parameters with respect to the reference value. The blue line shows the mean of the distribution and the green histograms, show the 68% of parameters that are closer to the reference value. The standard deviation of the complete distribution is used as an estimation of the systematic uncertainty due to the limited size of the MC sample.

The covariance matrix is fed into an n-dimensional Gaussian to draw random vectors. These vectors are used as coefficients to produce randomized efficiency models. Since the efficiency is modeled by a Bernstein Polynomial with positive coefficients, we only take random vectors that are positive in all entries.

For each variation of the efficiency, we perform a two-dimensional fit to the same reference data. The standard deviation of the fitted parameters is used as an estimation of the uncertainty.

In Figure 5.56, the variation of the signal efficiency model used to estimate the systematic uncertainty of the limited size of the Monte Carlo sample is shown in gray. In blue, the

nominal model is plotted. The histograms on the right show the distribution of the fitted parameters around the reference value, its standard deviation is used as the systematic uncertainty induced by the limited size of the MC sample.

5.9.4 Degree of Bernstein Model

Angular distributions have been modeled using Bernstein polynomials. The selection of each polynomial's degree is based on the F test. The F test tends to select the most simple model that describes the data, however, a model with more parameters could produce a better fit. We associate a systematic uncertainty due to the selection of the Bernstein polynomial for each angular model. The standard deviation of all models with the greatest number of parameters than the nominal is used as an estimation of this systematic uncertainty.

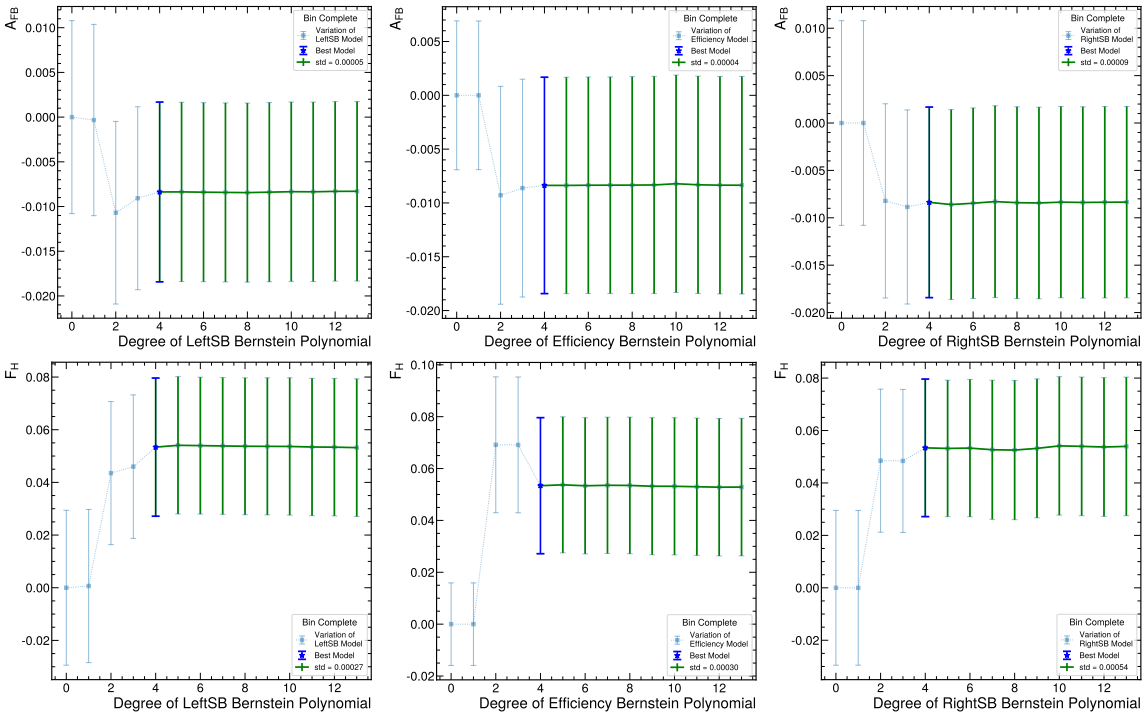

Figure 5.57: Variation on the fitted parameters as a function of the degree of the Bernstein Polynomial, the blue error bar corresponds to the nominal model selected by the F test, while the green bars are the models used to estimate the systematic uncertainty associated with the selection of the degree of the model. The standard deviation of the green models is shown in the legend of each plot. Each column corresponds to a given model, Left Sideband, Efficiency, and Right Sideband. The first row shows the results for A_{FB} and the second one contains the results for F_H.

5.9.5 Signal mass peak

We considered an alternative PDF (Double Crystal-Ball) to the nominal one (Johnson's SU), to evaluate the complete 2D fit. The alternative PDF, was evaluated just as the nominal

one. First, from a fit to signal Monte Carlo we obtain all parameters for the signal PDF. Then, we perform the 2D fit in the signal region, and the location parameter, A_{FB}, F_H, and signal yield are free to float.

The Double Crystal-Ball is defined in Equation 5.12, and the definition of the constants A and B are in Equations 5.13 and 5.14.

$$f(x;\mu,\sigma,\alpha_L,n_L,\alpha_R,n_R) = \begin{cases} A_L \cdot (B_L - \frac{x-\mu}{\sigma})^{-n}, & \text{for } \frac{x-\mu}{\sigma} < -\alpha_L \\ \exp(-\frac{(x-\mu)^2}{2\sigma^2}), & \text{for } -\alpha_L \leq \frac{x-\mu}{\sigma} \leq \alpha_R \\ A_R \cdot (B_R - \frac{x-\mu}{\sigma})^{-n}, & \text{for } \alpha_R < \frac{x-\mu}{\sigma} \end{cases} \tag{5.12}$$

$$A_{L/R} = \left(\frac{n_{L/R}}{|\alpha_{L/R}|}\right)^n_{L/R} \cdot \exp\left(-\frac{|\alpha_{L/R}|^2}{2}\right) \tag{5.13}$$

$$B_{L/R} = \frac{n_{L/R}}{|\alpha_{L/R}|} - |\alpha_{L/R}| \tag{5.14}$$

The difference of the fitted parameters between the alternative and the nominal ($\hat{\theta}_{Nominal} - \hat{\theta}_{Alternative}$) is considered as the estimation of the systematic uncertainty associated with the selection of the signal mass peak.

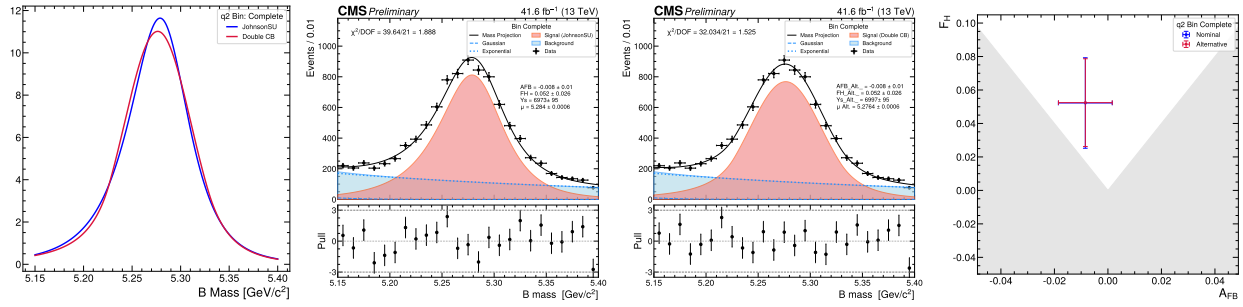

Figure 5.58: A comparison of the signal models only, appears in the first plot from left to right. The plots in the middle show the projections for each mass signal model. Finally, the plot on the right shows the parameters of inters fitted using both mass models.

In Figure 5.58, the mass of the 2d fits can be seen for both models for the complete bin of the dimuon mass squared (q^2). We also show a comparison of the nominal versus the alternative mass model. The plot on the right shows both fits in the $A_{FB} - F_H$ plane with the Hessian uncertainties.

5.9.6 Background mass shape

For the background mass distribution, we considered an alternative PDF (error function plus exponential) to evaluate the complete fit. The difference between the nominal (Gaussian plus exponential) against the alternative's fit results are considered as the estimation of the systematic uncertainty associated with the selection of the background mass distribution.

The error function used in this estimation, has two free parameters, location (μ) and scale (σ). That is, in the error function, the variable was transformed as $x \to (x - \mu)/\sigma$.

Just as with the signal mass shape, the difference of the fitted parameters $(\hat{A_{FB}}, \hat{F_H})$ between the alternative and the nominal PDF is considered as the estimation of the systematic uncertainty associated to the selection of the background mass shape.

In Figure 5.59, the mass projections can be seen for both models for the reference data on the complete q^2 Bin, as well as a comparison of the mass background models and the fitted parameters with their Hessian uncertainties.

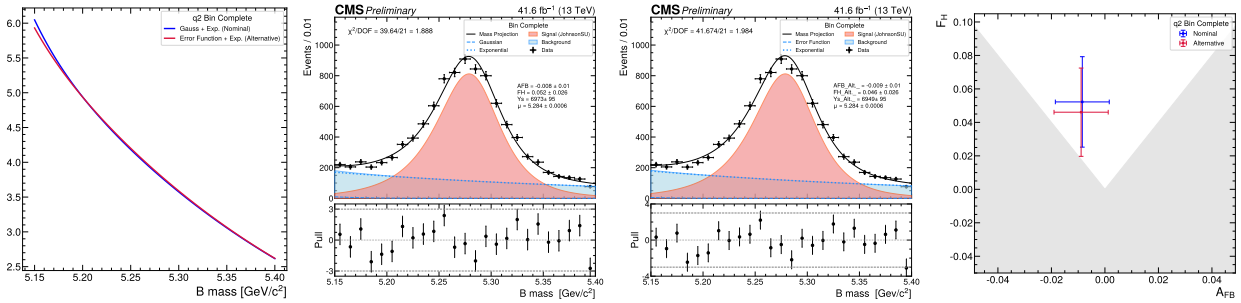

Figure 5.59: A comparison of the background mass models appears in the first plot from left to right. The plots in the middle show the projections for each mass background model. Finally, the plot on the right shows the parameters of interest fitted using both mass models.

5.9.7 Final Systematic Uncertainty

Here we show all systematic uncertainties being evaluated so far. For each q^2 Bin, and for each parameter of interest. The total uncertainty is evaluated as the root square of the sum of squares for each Bin.

Systematic uncertainties × 100

$q^2 Bin$	0	1	2	4	6	7	8	9	10	Complete
FittingBiasBackground	3.15	1.43	2.07	0.61	1.71	0.45	1.71	1.04	-0.10	0.08
FittingBiasToys	11.20	7.10	1.16	0.86	2.70	1.15	1.89	4.54	0.22	0.53
LimitedSize	1.77	0.09	1.37	1.67	0.78	1.19	1.23	0.00	0.57	0.59
BernsteinRightSB	3.19	0.00	0.08	0.94	0.16	0.08	0.39	0.00	0.08	0.05
BernsteinLeftSB	0.73	0.00	2.85	0.08	0.07	0.05	0.04	0.00	0.03	0.03
BernsteinEfficiency	0.07	0.00	0.31	0.18	0.02	0.03	0.04	0.00	0.05	0.03
MassModelSignal	-0.88	-0.00	-0.12	-0.03	-0.16	0.05	-0.05	-0.00	0.03	0.02
MassModelBackground	4.06	3.09	4.96	0.17	-0.97	-0.51	-0.59	1.29	-0.96	-0.61
Total	12.90	7.88	6.35	2.20	3.44	1.79	2.92	4.83	1.15	1.01

Table 5.18: Systematic uncertainties for F_H.

Systematic uncertainties × 100

$q^2 Bin$	0	1	2	4	6	7	8	9	10	Complete
FittingBiasBackground	-0.36	0.18	0.78	0.25	0.62	0.01	-0.31	-0.02	0.34	0.31
FittingBiasToys	1.64	0.52	-0.38	0.22	-0.35	0.04	0.35	0.30	-0.11	0.01
LimitedSize	0.88	0.05	0.68	0.73	0.42	0.53	0.62	0.00	0.26	0.27
BernsteinRightSB	1.59	0.00	0.04	0.14	0.08	0.02	0.20	0.00	0.01	0.01
BernsteinLeftSB	0.36	0.00	0.33	0.04	0.04	0.02	0.02	0.00	0.01	0.00
BernsteinEfficiency	0.04	0.00	0.04	0.02	0.01	0.01	0.02	0.00	0.00	0.00
MassModelSignal	0.44	0.00	0.12	-0.01	-0.08	0.03	0.03	0.00	-0.02	0.00
MassModelBackground	-2.03	1.55	-0.18	0.03	-0.49	-0.13	0.29	0.64	-0.05	-0.04
Total	3.25	1.64	1.17	0.82	0.97	0.55	0.85	0.71	0.44	0.41

Table 5.19: Systematic uncertainties for A_{FB}.

5.10 Results and Conclusions

For the moment we are using Injection MC to evaluate the statistical and systematic uncertainties. Here we will summarize the values obtained from these studies, and once we unblind the results in data, we will also update the uncertainties.

q^2 Bin	A_{FB}	F_H
0	$-0.065^{+0.084}_{-0.108} \pm 0.033$	$0.131^{+0.287}_{-0.125} \pm 0.129$
1	$-0.000^{+0.035}_{-0.028} \pm 0.016$	$0.000^{+0.088}_{-0.000} \pm 0.079$
2	$0.010^{+0.037}_{-0.036} \pm 0.012$	$0.068^{+0.113}_{-0.065} \pm 0.064$
4	$0.020^{+0.036}_{-0.036} \pm 0.008$	$0.128^{+0.099}_{-0.080} \pm 0.022$
6	$0.015^{+0.025}_{-0.030} \pm 0.010$	$0.031^{+0.081}_{-0.030} \pm 0.034$
7	$0.002^{+0.026}_{-0.028} \pm 0.006$	$0.075^{+0.074}_{-0.053} \pm 0.018$
8	$-0.073^{+0.026}_{-0.028} \pm 0.008$	$0.147^{+0.057}_{-0.047} \pm 0.029$
9	$-0.000^{+0.019}_{-0.011} \pm 0.007$	$0.000^{+0.043}_{-0.000} \pm 0.048$
10	$0.008^{+0.013}_{-0.015} \pm 0.004$	$0.047^{+0.040}_{-0.030} \pm 0.011$
Complete	$-0.008^{+0.016}_{-0.015} \pm 0.004$	$0.053^{+0.041}_{-0.034} \pm 0.010$

Table 5.20: Final result for the MC injection study.

5.10.1 Previous Results

In this section, we include a comparison of the low and high q^2 Bins from the most recent measurements.

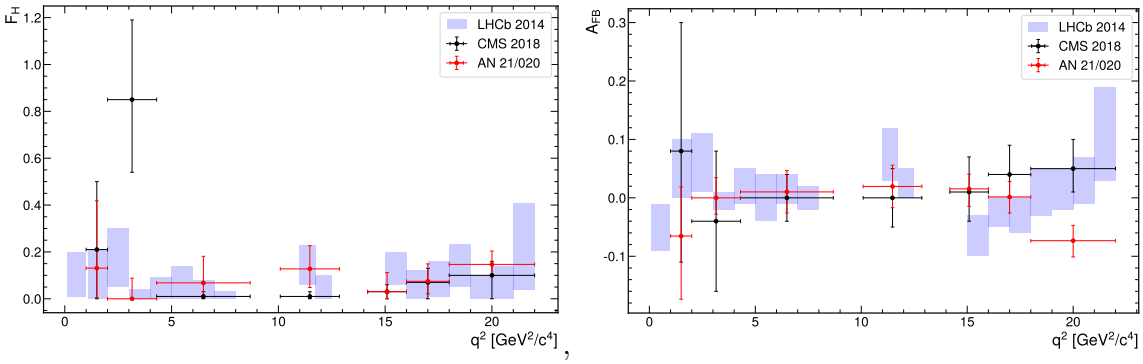

Figure 5.60: Comparison with previous measurements, from CMS (2018) [100] and LHCb (2014) [99]. For the current blinding status, we show results for the reference Injection MC. Only statistical uncertainties are shown for all measurements, and our uncertainties are obtained from the projection of the confidence contours from Table 5.16.

q^2 Range $[(\,\mathrm{GeV}/c^2)^2]$	A_{FB}	F_H
CMS (1.00 - 6.00)	$-0.14^{+0.07}_{-0.06} \pm 0.03$	$0.38^{+0.17}_{-0.21} \pm 0.09$
LHCb (1.10 - 6.00)	$0.005 \pm 0.015 \pm 0.01$	$0.03 \pm 0.03 \pm 0.02$
CMS (14.18 - 16.00)	$0.01^{+0.06}_{-0.05} \pm 0.02$	$0.03^{+0.03}_{-0.03} \pm 0.07$
CMS (16.00 - 18.00)	$0.04^{+0.05}_{-0.04} \pm 0.03$	$0.07^{+0.06}_{-0.07} \pm 0.07$
CMS (18.00 - 22.00)	$0.05^{+0.05}_{-0.04} \pm 0.02$	$0.10^{+0.06}_{-0.10} \pm 0.09$
LHCb (15.00 - 22.00)	$-0.005 \pm 0.025 \pm 0.01$	$0.035 \pm 0.035 \pm 0.02$

Table 5.21: Most recent results from CMS (2018) [100] and LHCb (2014) [99] at low and high q^2. Numbers are written in the same format for better comparison. LHCb results were given as intervals, here we used the midpoint and half its length as estimates of the best point and statistical uncertainty respectively.

q^2 Range $[(\,\mathrm{GeV}/c^2)^2]$	A_{FB}	F_H
CMS (1.00 - 6.00)	$[\,0.08, 0.21] \pm 0.03$	$[0.17, 0.55] \pm 0.09$
LHCb (1.10 - 6.00)	$[-0.01, 0.02] \pm 0.01$	$[0.00, 0.06] \pm 0.02$
CMS (14.18 - 16.00)	$[-0.04, 0.07] \pm 0.02$	$[0.00, 0.06] \pm 0.07$
CMS (16.00 - 18.00)	$[\,0.00, 0.09] \pm 0.03$	$[0.00, 0.13] \pm 0.07$
CMS (18.00 - 22.00)	$[\,0.01, 0.10] \pm 0.02$	$[0.00, 0.16] \pm 0.09$
LHCb (15.00 - 22.00)	$[-0.03, 0.02] \pm 0.01$	$[0.00, 0.07] \pm 0.02$

Table 5.22: Most recent results from CMS (2018) [100] and LHCb (2014) [99] at low and high q^2. Numbers are written in the same format for better comparison. CMS results were given as a best-fit value and asymmetric uncertainties, we transformed these results into an interval.

Chapter 6

Conclusions

We have used B mesons to perform precision measurements and as a probe for the study of nuclear modifications.

The former was studied via a rare decay, namely the flavor-changing neutral current decay $B^+ \to K^+\mu^+\mu^-$. In this study, the angular parameters A_{FB} and F_H were measured as a function of the momentum transfer from the b to the s quark, $q^2 = m(\mu^+\mu^-)$. The expected values from the Operator Product Expansion of the Weak-Effective Hamiltonian are known with great precision. In particular, the forward-backward asymmetry (A_{FB}) of the dimuon system is expected to be zero up to small corrections ($(m_e/m_b)^2$), and the F_H parameter is predicted to be of the order of $(m_e/m_b)^2$ and decreasing as the recoil energy increases. However, for the current experimental precision, any significative deviation from zero would be an indicator of new physics. As of the writing of this thesis, the analysis is still under review by the CMS collaboration. The measurements will contribute to the understanding of the Flavour Anomalies that emerged during the early 2010s, in which the so-called P5prime, RK, and branching fractions of rare b decays were, and some still, in tension with the SM.

On the other hand, the study of QGP is of great interest since it explores another region of the SM that can be achieved in high energy collisions; high (extreme) temperatures. Studies at smaller systems, such as pp and pPb, are being analyzed to understand the collectivity effects in heavy ion collisions. However, even in these small systems, collectivity effects are observed. The results reported in this analysis show no significant effect on the nuclear modification factor in multiplicity classes, and as a function of transverse momenta, for the production of BJPSIK. An important feature of this work is that the number of collisions is not obtained from the Glauber model, instead, it uses the premise that the Z^0 production is not sensible to the (colored) collectivity effects, and the missing factor is just the ratio of the Z^0 production for the same classes as its counterpart with B mesons. This approach has the potential to set a new standard in the measurement of collective effects in high-energy collisions.

The study of B mesons is an active area of research that has the potential to unveil unknown effects and help to build and improve the knowledge of the Standard Model. The present work showed two different approaches in this area, one with preliminary results but competitive uncertainties, and the other showing a nuclear modification factor consistent with unity in pPb collisions, within current experimental uncertainties.

Appendix A

Efficiencies for all multiplicity classes

The efficiency is an important aspect of the cross-section measurement. In this appendix, we report the total efficiency, reconstruction, and acceptance efficiencies for each multiplicity class. The reconstruction efficiencies consider the weights obtained in the iterative method.

A.1 Acceptance

The efficiency dependencies at generator level are shown for pPb (left) and Pbp (right) samples in (p_T, $N_{\mathrm{trk}}^{\mathrm{gen}}$) bins. Generator-level efficiency is defined as the ratio of events passing pre-filter cuts to the number of generated events.

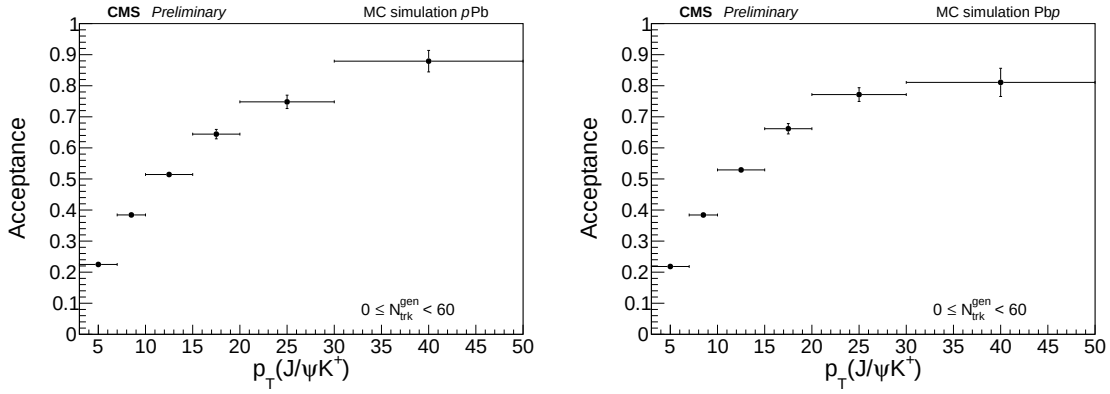

Figure A.1: The efficiency dependencies at the generator level are shown for pPb (left) and Pbp (right) samples in p_T bins for the 0-60 multiplicity class.

A.2 Reconstruction Efficiency

The reconstruction efficiency dependencies are shown for pPb (left) and Pbp (right) samples in p_T bins for all multiplicity classes are shown in Figures A.5 - A.8.

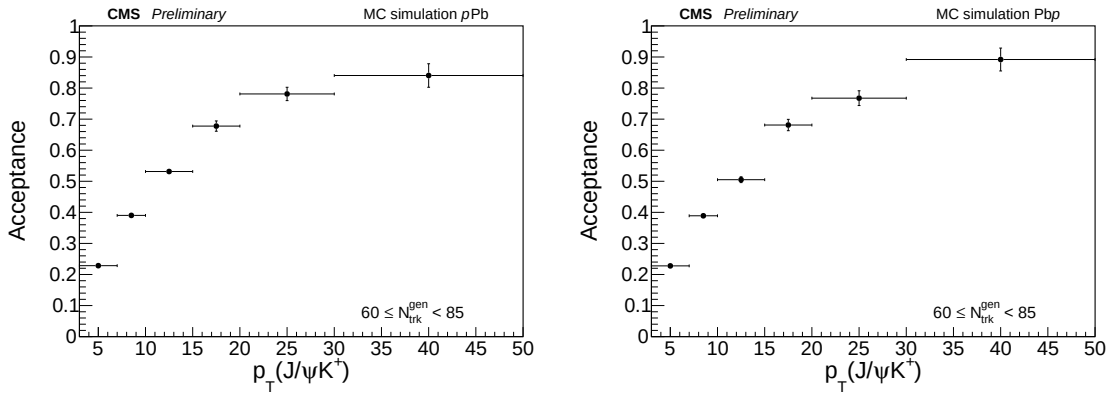

Figure A.2: The efficiency dependencies at the generator level are shown for pPb (left) and Pbp (right) samples in p_T bins for the 60-85 multiplicity class.

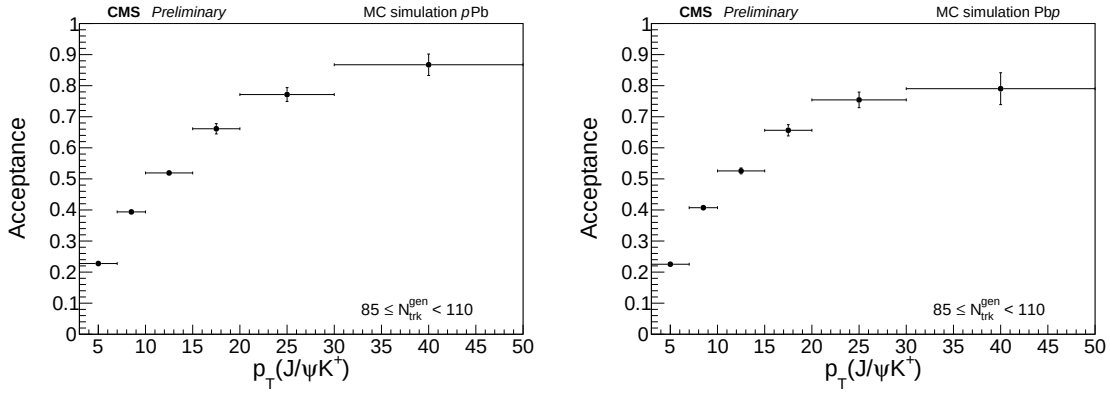

Figure A.3: The efficiency dependencies at the generator level are shown for pPb (left) and Pbp (right) samples in p_T bins for the 85-110 multiplicity class.

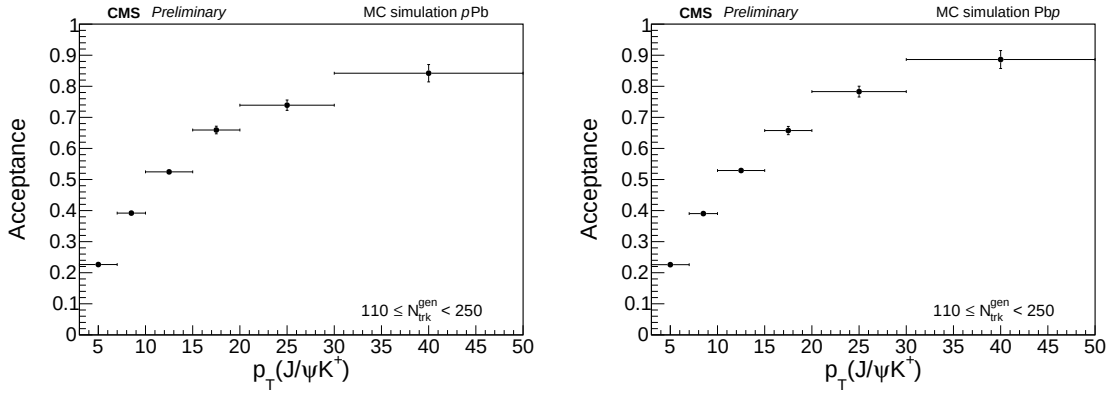

Figure A.4: The efficiency dependencies at the generator level are shown for pPb (left) and Pbp (right) samples in p_T bins for the 110-250 multiplicity class.

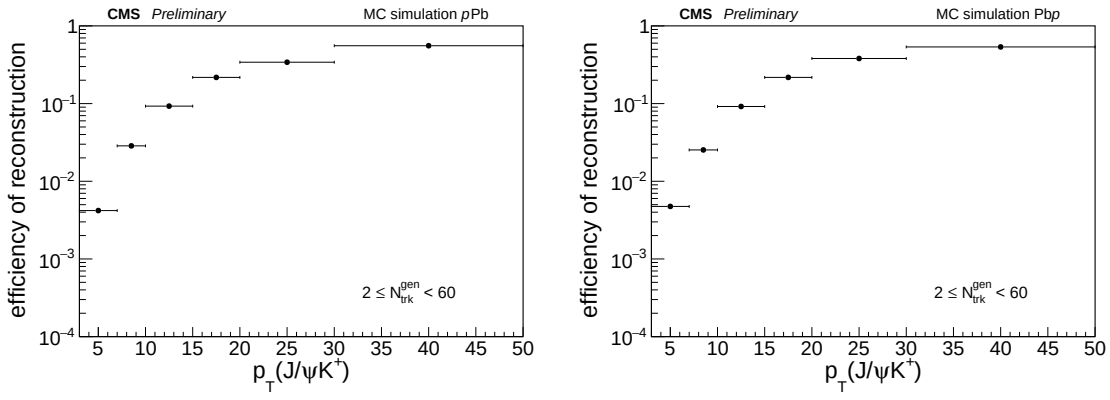

Figure A.5: The reconstruction efficiency dependencies are shown for pPb (left) and Pbp (right) samples in p_T bins for the 2-60 multiplicity class. Reconstruction efficiency is defined as the ratio of reconstructed events in a sample of MC events that include pre-filter cuts with respect to the number of generated events in the same sample.

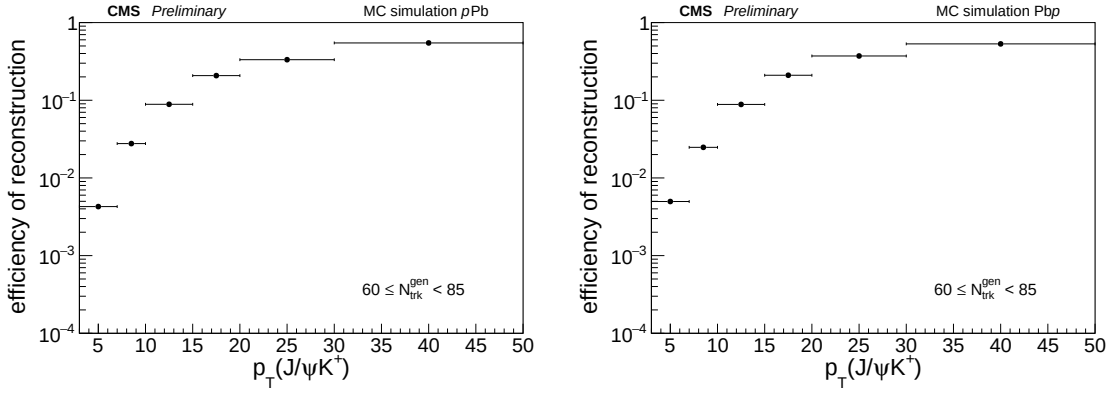

Figure A.6: The reconstruction efficiency dependencies are shown for pPb (left) and Pbp (right) samples in p_T bins for the 60-85 multiplicity class. Reconstruction efficiency is defined as the ratio of reconstructed events in a sample of MC events that include pre-filter cuts with respect to the number of generated events in the same sample.

A.3 Total Efficiency

Table A.1: The numerical values obtained for the prefilter efficiency, the reconstruction efficiency and the total efficiency are shown in the table as transverse momentum bins of the B^+ candidates, in pPb collisions for samples in (p_T ,N_{trk}^{gen}) bins, with $2 \leq N_{trk}^{gen} < 60$.

p_T (B^+) (GeV)	Pre-Filter	Reco	Total
3 – 7	0.22483 ± 0.00254	0.00420 ± 0.00003	0.00094 ± 0.00001
7 – 10	0.38421 ± 0.00517	0.02857 ± 0.00011	0.01098 ± 0.00015
10 – 15	0.51429 ± 0.00768	0.09280 ± 0.00024	0.04772 ± 0.00072
15 – 20	0.64429 ± 0.01513	0.21745 ± 0.00064	0.14010 ± 0.00332
20 – 30	0.74815 ± 0.02152	0.34106 ± 0.00108	0.25517 ± 0.00739
30 – 50	0.87912 ± 0.03458	0.55598 ± 0.00236	0.48877 ± 0.01934

Table A.2: The numerical values obtained for the prefilter efficiency, the reconstruction efficiency and the total efficiency are shown in the table as transverse momentum bins of the B^+ candidates, in Pbp collisions for samples in (p_T ,N_{trk}^{gen}) bins, with $2 \leq N_{trk}^{gen} < 60$.

p_T (B^+) (GeV)	Pre-Filter	Reco	Total
3 – 7	0.21827 ± 0.00271	0.00475 ± 0.00003	0.00104 ± 0.00001
7 – 10	0.38404 ± 0.00561	0.02532 ± 0.00010	0.00972 ± 0.00015
10 – 15	0.52911 ± 0.00837	0.09179 ± 0.00024	0.04857 ± 0.00078
15 – 20	0.66167 ± 0.01669	0.21741 ± 0.00064	0.14386 ± 0.00365
20 – 30	0.77159 ± 0.02212	0.38083 ± 0.00110	0.29384 ± 0.00846
30 – 50	0.81081 ± 0.04536	0.53644 ± 0.00235	0.43495 ± 0.02441

Table A.3: The numerical values obtained for the prefilter efficiency, the reconstruction efficiency and the total efficiency are shown in the table as transverse momentum bins of the B^+ candidates, in pPb collisions for samples in (p_T ,N_{trk}^{gen}) bins, with $60 \leq N_{trk}^{gen} < 85$.

p_T (B^+) (GeV)	Pre-Filter	Reco	Total
3 – 7	0.22837 ± 0.00296	0.00428 ± 0.00004	0.00098 ± 0.00002
7 – 10	0.39019 ± 0.00595	0.02769 ± 0.00013	0.01080 ± 0.00017
10 – 15	0.53141 ± 0.00851	0.08874 ± 0.00028	0.04716 ± 0.00077
15 – 20	0.67762 ± 0.01659	0.20763 ± 0.00072	0.14069 ± 0.00348
20 – 30	0.78108 ± 0.02146	0.33282 ± 0.00119	0.25996 ± 0.00720
30 – 50	0.84043 ± 0.03784	0.54697 ± 0.00246	0.45969 ± 0.02080

Table A.4: The numerical values obtained for the prefilter efficiency, the reconstruction efficiency and the total efficiency are shown in the table as transverse momentum bins of the B^+ candidates, in Pbp collisions for samples in (p_T ,N_{trk}^{gen}) bins, with $60 \leq N_{trk}^{gen} < 85$.

p_T (B^+) (GeV)	Pre-Filter	Reco	Total
3 – 7	0.22772 ± 0.00325	0.00497 ± 0.00004	0.00113 ± 0.00002
7 – 10	0.38894 ± 0.00644	0.02477 ± 0.00012	0.00963 ± 0.00017
10 – 15	0.50509 ± 0.00936	0.08839 ± 0.00028	0.04464 ± 0.00084
15 – 20	0.68105 ± 0.01826	0.20990 ± 0.00071	0.14295 ± 0.00386
20 – 30	0.76752 ± 0.02379	0.37169 ± 0.00120	0.28528 ± 0.00889
30 – 50	0.89189 ± 0.03682	0.53182 ± 0.00243	0.47432 ± 0.01970

Table A.5: The numerical values obtained for the prefilter efficiency, the reconstruction efficiency and the total efficiency are shown in the table as transverse momentum bins of the B^+ candidates, in pPb collisions for samples in (p_T ,N_{trk}^{gen}) bins, with $85 \leq N_{trk}^{gen} < 110$.

p_T (B^+) (GeV)	Pre-Filter	Reco	Total
3 – 7	0.22758 ± 0.00306	0.00429 ± 0.00004	0.00098 ± 0.00002
7 – 10	0.39379 ± 0.00616	0.02681 ± 0.00014	0.01056 ± 0.00017
10 – 15	0.51918 ± 0.00878	0.08509 ± 0.00028	0.04418 ± 0.00076
15 – 20	0.66133 ± 0.01658	0.20324 ± 0.00074	0.13441 ± 0.00341
20 – 30	0.77143 ± 0.02240	0.32202 ± 0.00120	0.24842 ± 0.00727
30 – 50	0.86735 ± 0.03453	0.52868 ± 0.00250	0.45855 ± 0.01838

Table A.6: The numerical values obtained for the prefilter efficiency, the reconstruction efficiency and the total efficiency are shown in the table as transverse momentum bins of the B^+ candidates, in Pbp collisions for samples in (p_T ,N_{trk}^{gen}) bins, with $85 \leq N_{trk}^{gen} < 110$.

p_T (B^+) (GeV)	Pre-Filter	Reco	Total
3 – 7	0.22531 ± 0.00333	0.00484 ± 0.00004	0.00109 ± 0.00002
7 – 10	0.40727 ± 0.00674	0.02377 ± 0.00013	0.00968 ± 0.00017
10 – 15	0.52567 ± 0.00946	0.08466 ± 0.00028	0.04451 ± 0.00081
15 – 20	0.65643 ± 0.01812	0.20394 ± 0.00073	0.13387 ± 0.00373
20 – 30	0.75427 ± 0.02508	0.35794 ± 0.00122	0.26998 ± 0.00903
30 – 50	0.79032 ± 0.05128	0.50390 ± 0.00248	0.39824 ± 0.02591

Table A.7: The numerical values obtained for the prefilter efficiency, the reconstruction efficiency and the total efficiency are shown in the table as transverse momentum bins of the B^+ candidates, in pPb collisions for samples in (p_T ,N_{trk}^{gen}) bins, with $110 \leq N_{trk}^{gen} < 250$.

p_T (B^+) (GeV)	Pre-Filter	Reco	Total
3 – 7	0.22633 ± 0.00235	0.00478 ± 0.00004	0.00108 ± 0.00001
7 – 10	0.39188 ± 0.00461	0.02830 ± 0.00011	0.01109 ± 0.00014
10 – 15	0.52461 ± 0.00649	0.08513 ± 0.00022	0.04466 ± 0.00056
15 – 20	0.65930 ± 0.01225	0.20127 ± 0.00056	0.13270 ± 0.00249
20 – 30	0.73919 ± 0.01665	0.32303 ± 0.00090	0.23878 ± 0.00542
30 – 50	0.84210 ± 0.02792	0.53649 ± 0.00180	0.45178 ± 0.01506

Table A.8: The numerical values obtained for the prefilter efficiency, the reconstruction efficiency and the total efficiency are shown in the table as transverse momentum bins of the B^+ candidates, in Pbp collisions for samples in (p_T ,N_{trk}^{gen}) bins, with $110 \leq N_{trk}^{gen} < 250$.

p_T (B^+) (GeV)	Pre-Filter	Reco	Total
3 – 7	0.22587 ± 0.00259	0.00558 ± 0.00004	0.00126 ± 0.00002
7 – 10	0.39030 ± 0.00509	0.02497 ± 0.00010	0.00975 ± 0.00013
10 – 15	0.52892 ± 0.00720	0.08529 ± 0.00022	0.04511 ± 0.00062
15 – 20	0.65757 ± 0.01324	0.20321 ± 0.00056	0.13362 ± 0.00272
20 – 30	0.78292 ± 0.01737	0.35741 ± 0.00091	0.27983 ± 0.00625
30 – 50	0.88618 ± 0.02895	0.51287 ± 0.00179	0.45450 ± 0.01493

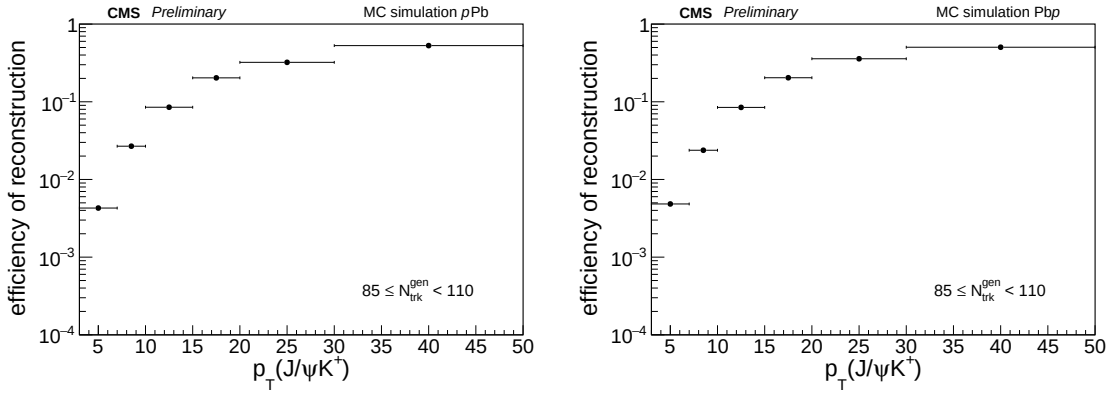

Figure A.7: The reconstruction efficiency dependencies are shown for pPb (left) and Pbp (right) samples in p_T bins for the 85-110 multiplicity class. Reconstruction efficiency is defined as the ratio of reconstructed events in a sample of MC events that include pre-filter cuts with respect to the number of generated events in the same sample.

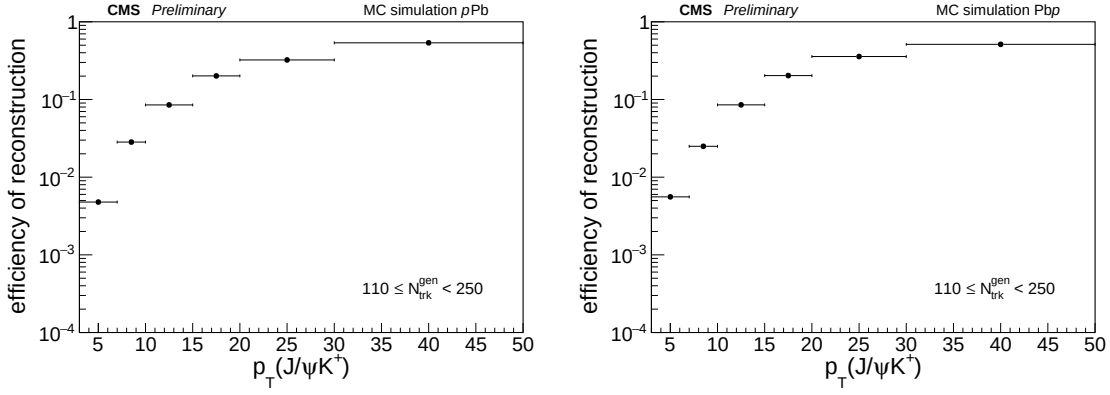

Figure A.8: The reconstruction efficiency dependencies are shown for pPb (left) and Pbp (right) samples in p_T bins for the 110-250 multiplicity class. Reconstruction efficiency is defined as the ratio of reconstructed events in a sample of MC events that include pre-filter cuts with respect to the number of generated events in the same sample.

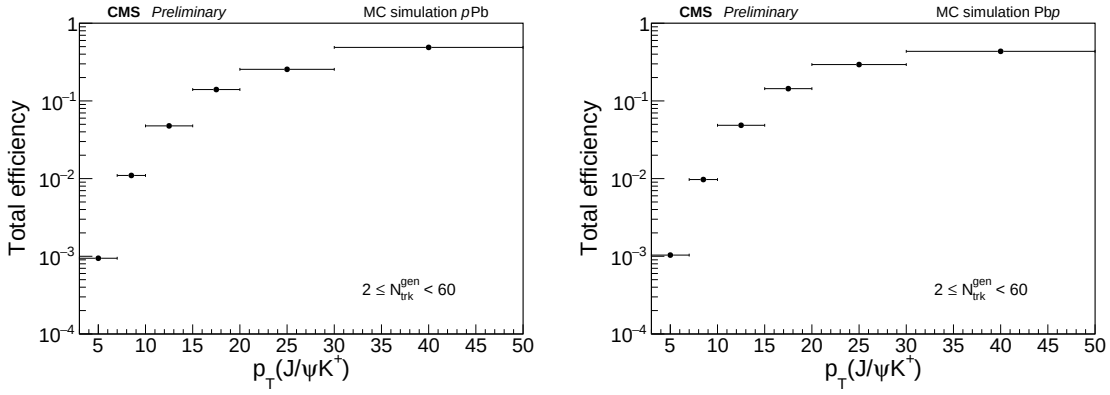

Figure A.9: The total efficiency distributions are shown for pPb (left) and Pbp (right) samples in (p_T, $N_{\mathrm{trk}}^{\mathrm{gen}}$) bins. The total efficiency is defined as the product of generator level efficiency with reconstruction efficiency.

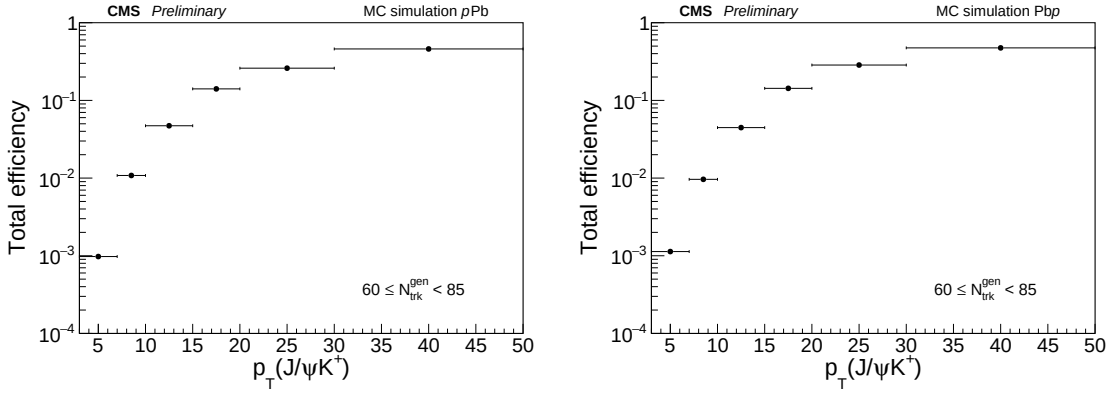

Figure A.10: The total efficiency distributions are shown for pPb (left) and Pbp (right) samples in (p_T, $N_{\mathrm{trk}}^{\mathrm{gen}}$) bins. The total efficiency is defined as the product of generator-level efficiency with reconstruction efficiency.

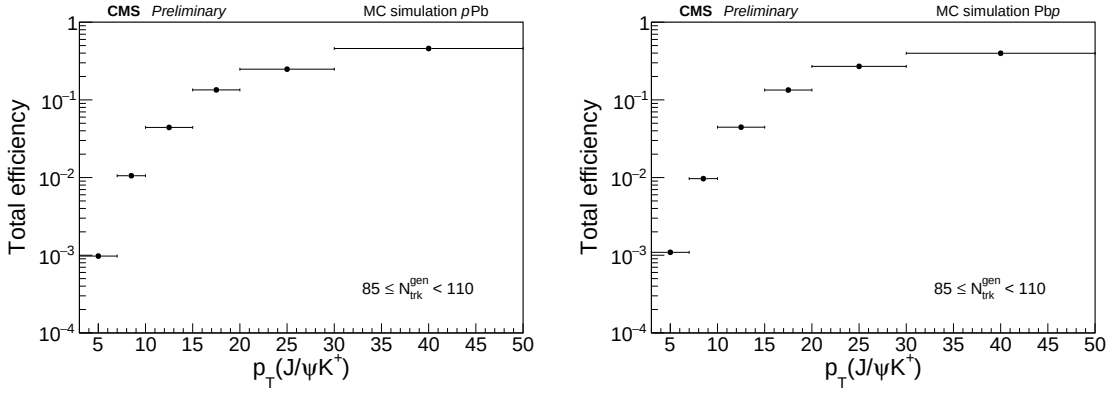

Figure A.11: The total efficiency distributions are shown for pPb (left) and Pbp (right) samples in (p_T, $N_{\mathrm{trk}}^{\mathrm{gen}}$) bins. The total efficiency is defined as the product of generator level efficiency with reconstruction efficiency.

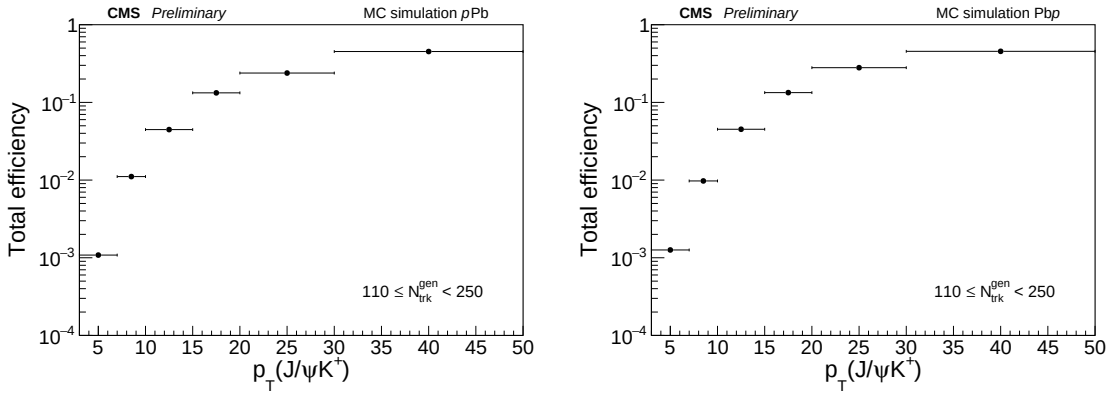

Figure A.12: The total efficiency distributions are shown for pPb (left) and Pbp (right) samples in (p_T, $N_{\mathrm{trk}}^{\mathrm{gen}}$) bins. The total efficiency is defined as the product of generator-level efficiency with reconstruction efficiency.

Appendix B

Raw yields for each multiplicity class

Raw yields as obtained from a Maximum Likelihood Estimator, using the nominal models described in Section 4.4.6. These raw yields are another ingredient for the cross-section measurements.

Table B.1: The raw yields obtained and efficiencies computed are shown with their respective statistical uncertainties in (p_{T} , $N_{\mathrm{trk}}^{\mathrm{corrected}}$) bins, with $2 \leq N_{\mathrm{trk}}^{\mathrm{corrected}} < 60$. The value of $\mathrm{d}\sigma/\mathrm{dp_T}$is computed directly from these results. For $\mathrm{d}\sigma/\mathrm{dp_T}$, just the yield error propagation is present.

p_{T} (GeV)	B^+ Yield	B^+ Efficiency	$\mathrm{d}\sigma/\mathrm{dp_T}(\mu\mathrm{b/GeV})$
3 – 7	26 ± 6	0.00100 ± 0.00001	305.42 ± 71.08
7 – 10	99 ± 12	0.01017 ± 0.00011	151.95 ± 17.89
10 – 15	239 ± 17	0.04827 ± 0.00056	46.34 ± 3.23
15 – 20	153 ± 13	0.14251 ± 0.00263	10.05 ± 0.87
20 – 30	124 ± 12	0.27996 ± 0.00604	2.07 ± 0.20
30 – 50	49 ± 7	0.45427 ± 0.01712	0.25 ± 0.04
3 – 50	689 ± 29	0.01440 ± 0.00009	47.67 ± 2.66

Table B.2: The raw yields obtained and efficiencies computed are shown with their respective statistical uncertainties in (p_{T} , $N_{\mathrm{trk}}^{\mathrm{corrected}}$) bins, with $60 \leq N_{\mathrm{trk}}^{\mathrm{corrected}} < 85$. The value of $\mathrm{d}\sigma/\mathrm{dp_T}$is computed directly from these results. For $\mathrm{d}\sigma/\mathrm{dp_T}$, just the yield error propagation is present.

p_{T} (GeV)	B^+ Yield	B^+ Efficiency	$\mathrm{d}\sigma/\mathrm{dp_T}(\mu\mathrm{b/GeV})$
3 – 7	34 ± 7	0.00108 ± 0.00001	372.18 ± 74.82
7 – 10	81 ± 11	0.01005 ± 0.00012	126.10 ± 16.72
10 – 15	227 ± 17	0.04554 ± 0.00060	46.77 ± 3.45
15 – 20	179 ± 15	0.14214 ± 0.00277	11.78 ± 0.97
20 – 30	142 ± 13	0.27619 ± 0.00626	2.41 ± 0.21
30 – 50	58 ± 8	0.46907 ± 0.01467	0.29 ± 0.04
3 – 50	721 ± 30	0.01584 ± 0.00011	45.33 ± 2.33

Table B.3: The raw yields obtained and efficiencies computed are shown with their respective statistical uncertainties in (p_{T} , $N_{\mathrm{trk}}^{\mathrm{corrected}}$) bins, with $85 \leq N_{\mathrm{trk}}^{\mathrm{corrected}} < 110$. The value of $\mathrm{d}\sigma/\mathrm{dp_T}$is computed directly from these results. For $\mathrm{d}\sigma/\mathrm{dp_T}$, just the yield error propagation is present.

p_{T} (GeV)	B^+ Yield	B^+ Efficiency	$\mathrm{d}\sigma/\mathrm{dp_T}(\mu\mathrm{b/GeV})$
3 – 7	33 ± 7	0.00105 ± 0.00001	367.28 ± 78.97
7 – 10	87 ± 11	0.01000 ± 0.00012	135.45 ± 17.10
10 – 15	189 ± 16	0.04439 ± 0.00059	39.93 ± 3.28
15 – 20	150 ± 13	0.13406 ± 0.00268	10.48 ± 0.92
20 – 30	131 ± 12	0.26224 ± 0.00635	2.33 ± 0.22
30 – 50	69 ± 9	0.41989 ± 0.01787	0.39 ± 0.05
3 – 50	659 ± 29	0.01566 ± 0.00011	41.92 ± 2.13

Table B.4: The raw yields obtained and efficiencies computed are shown with their respective statistical uncertainties in (p_{T} , $N_{\mathrm{trk}}^{\mathrm{corrected}}$) bins, with $110 \leq N_{\mathrm{trk}}^{\mathrm{corrected}} < 250$. The value of $\mathrm{d}\sigma/\mathrm{dp_T}$is computed directly from these results. For $\mathrm{d}\sigma/\mathrm{dp_T}$, just the yield error propagation is present.

p_{T} (GeV)	B^+ Yield	B^+ Efficiency	$\mathrm{d}\sigma/\mathrm{dp_T}(\mu\mathrm{b/GeV})$
3 – 7	39 ± 9	0.00120 ± 0.00001	383.87 ± 87.31
7 – 10	154 ± 15	0.01023 ± 0.00010	234.27 ± 23.49
10 – 15	340 ± 21	0.04495 ± 0.00045	70.76 ± 4.45
15 – 20	271 ± 18	0.13329 ± 0.00196	19.04 ± 1.26
20 – 30	251 ± 17	0.26510 ± 0.00445	4.43 ± 0.30
30 – 50	82 ± 10	0.45352 ± 0.01099	0.42 ± 0.05
3 – 50	1128 ± 38	0.01694 ± 0.00009	66.33 ± 3.79

References

[1] S. Chatrchyan et al. "Observation of a new boson at a mass of 125 GeV with the CMS experiment at the LHC". In: *Physics Letters B* 716.1 (2012), pp. 30–61. ISSN: 0370-2693. DOI: https://doi.org/10.1016/j.physletb.2012.08.021. URL: https://www.sciencedirect.com/science/article/pii/S0370269312008581.

[2] G. Aad et al. "Observation of a new particle in the search for the Standard Model Higgs boson with the ATLAS detector at the LHC". In: *Physics Letters B* 716.1 (2012), pp. 1–29. ISSN: 0370-2693. DOI: https://doi.org/10.1016/j.physletb.2012.08.020. URL: https://www.sciencedirect.com/science/article/pii/S037026931200857X.

[3] D. J. Gross and F. Wilczek. "Asymptotically Free Gauge Theories. I". In: *Phys. Rev. D* 8 (10 Nov. 1973), pp. 3633–3652. DOI: 10.1103/PhysRevD.8.3633. URL: https://link.aps.org/doi/10.1103/PhysRevD.8.3633.

[4] H. David Politzer. "Asymptotic freedom: An approach to strong interactions". In: *Physics Reports* 14.4 (1974), pp. 129–180. ISSN: 0370-1573. DOI: https://doi.org/10.1016/0370-1573(74)90014-3. URL: https://www.sciencedirect.com/science/article/pii/0370157374900143.

[5] P. W. Higgs. "Broken Symmetries and the Masses of Gauge Bosons". In: *Phys. Rev. Lett.* 13 (16 Oct. 1964), pp. 508–509. DOI: 10.1103/PhysRevLett.13.508. URL: https://link.aps.org/doi/10.1103/PhysRevLett.13.508.

[6] E. V. Shuryak. "Theory of Hadronic Plasma". In: *Sov. Phys. JETP* 47 (1978), pp. 212–219.

[7] J. C. Collins and M. J. Perry. "Superdense Matter: Neutrons Or Asymptotically Free Quarks?" In: *Phys. Rev. Lett.* 34 (1975), p. 1353. DOI: 10.1103/PhysRevLett.34.1353.

[8] A. Bazavov et al. "Equation of state in (2+1)-flavor QCD". In: *Physical Review D* 90.9 (Nov. 2014). ISSN: 1550-2368. DOI: 10.1103/physrevd.90.094503. URL: http://dx.doi.org/10.1103/PhysRevD.90.094503.

[9] A. Bazavov et al. "Chiral crossover in QCD at zero and non-zero chemical potentials". In: *Physics Letters B* 795 (2019), pp. 15–21. ISSN: 0370-2693. DOI: https://doi.org/10.1016/j.physletb.2019.05.013. URL: https://www.sciencedirect.com/science/article/pii/S0370269319303223.

[10] A. Bazavov et al. "Chiral and deconfinement aspects of the QCD transition". In: *Phys. Rev. D* 85 (5 Mar. 2012), p. 054503. DOI: 10.1103/PhysRevD.85.054503. URL: https://link.aps.org/doi/10.1103/PhysRevD.85.054503.

[11] A. Hansen. "Pseudorapidity dependence of anisotropic azimuthal flow with the ALICE detector". In: 2015. URL: https://api.semanticscholar.org/CorpusID:125387349.

[12] J.-Y. Ollitrault. "Anisotropy as a signature of transverse collective flow". In: *Phys. Rev. D* 46 (1 July 1992), pp. 229–245. DOI: 10.1103/PhysRevD.46.229. URL: https://link.aps.org/doi/10.1103/PhysRevD.46.229.

[13] A. Adare et al. "Detailed measurement of the e+e- continuum in pp and AuAu collisions sqrt(sNN)=200 GeV and implications for direct photon production". In: *Physical Review C* 81.3 (Mar. 2010). ISSN: 1089-490X. DOI: 10.1103/physrevc.81.034911. URL: http://dx.doi.org/10.1103/PhysRevC.81.034911.

[14] W. Busza, K. Rajagopal, and W. van der Schee. "Heavy Ion Collisions: The Big Picture and the Big Questions". In: *Annual Review of Nuclear and Particle Science* 68.Volume 68, 2018 (2018), pp. 339–376. ISSN: 1545-4134. DOI: https://doi.org/10.1146/annurev-nucl-101917-020852. URL: https://www.annualreviews.org/content/journals/10.1146/annurev-nucl-101917-020852.

[15] M. L. Miller, K. Reygers, S. J. Sanders, and P. Steinberg. "Glauber Modeling in High-Energy Nuclear Collisions". In: *Annual Review of Nuclear and Particle Science* 57.Volume 57, 2007 (2007), pp. 205–243. ISSN: 1545-4134. DOI: https://doi.org/10.1146/annurev.nucl.57.090506.123020. URL: https://www.annualreviews.org/content/journals/10.1146/annurev.nucl.57.090506.123020.

[16] B. Alver et al. "High Transverse Momentum Triggered Correlations over a Large Pseudorapidity Acceptance in Au + Au Collisions at $\sqrt{s_{NN}} = 200$ GeV". In: *Phys. Rev. Lett.* 104 (6 Feb. 2010), p. 062301. DOI: 10.1103/PhysRevLett.104.062301. URL: https://link.aps.org/doi/10.1103/PhysRevLett.104.062301.

[17] S. Chatrchyan et al. "Observation and studies of jet quenching in PbPb collisions at $\sqrt{s_{NN}} = 2.76$ TeV". In: *Phys. Rev. C* 84 (2 Aug. 2011), p. 024906. DOI: 10.1103/PhysRevC.84.024906. URL: https://link.aps.org/doi/10.1103/PhysRevC.84.024906.

[18] K. Adcox et al. "Suppression of Hadrons with Large Transverse Momentum in Central $Au + Au$ Collisions at $\sqrt{s_{\mathrm{NN}}} = 130$GeV". In: *Phys. Rev. Lett.* 88 (2 Dec. 2001), p. 022301. DOI: 10.1103/PhysRevLett.88.022301. URL: https://link.aps.org/doi/10.1103/PhysRevLett.88.022301.

[19] W. T. Ford, A. Lemonick, U. Nauenberg, and P. A. Piroué. "Comparison of the K^+ and K^- Decay Rates into the τ and $K_{\mu 2}$ modes". In: *Phys. Rev. Lett.* 18 (26 June 1967), pp. 1214–1218. DOI: 10.1103/PhysRevLett.18.1214. URL: https://link.aps.org/doi/10.1103/PhysRevLett.18.1214.

[20] S. L. Glashow, J. Iliopoulos, and L. Maiani. "Weak Interactions with Lepton-Hadron Symmetry". In: *Phys. Rev. D* 2 (7 Oct. 1970), pp. 1285–1292. DOI: 10.1103/PhysRevD.2.1285. URL: https://link.aps.org/doi/10.1103/PhysRevD.2.1285.

[21] J. J. Aubert et al. "Experimental Observation of a Heavy Particle J". In: *Phys. Rev. Lett.* 33 (23 Dec. 1974), pp. 1404–1406. DOI: 10.1103/PhysRevLett.33.1404. URL: https://link.aps.org/doi/10.1103/PhysRevLett.33.1404.

[22] J. .-. Augustin et al. "Discovery of a Narrow Resonance in e^+e^- Annihilation". In: *Phys. Rev. Lett.* 33 (23 Dec. 1974), pp. 1406–1408. DOI: 10.1103/PhysRevLett.33.1406. URL: https://link.aps.org/doi/10.1103/PhysRevLett.33.1406.

[23] M. Kobayashi and T. Maskawa. "CP-Violation in the Renormalizable Theory of Weak Interaction". In: *Progress of Theoretical Physics* 49.2 (Feb. 1973), pp. 652–657. ISSN: 0033-068X. DOI: 10.1143/PTP.49.652. eprint: https://academic.oup.com/ptp/article-pdf/49/2/652/5257692/49-2-652.pdf. URL: https://doi.org/10.1143/PTP.49.652.

[24] S. W. Herb et al. "Observation of a Dimuon Resonance at 9.5 GeV in 400-GeV Proton-Nucleus Collisions". In: *Phys. Rev. Lett.* 39 (5 Aug. 1977), pp. 252–255. DOI: 10.1103/PhysRevLett.39.252. URL: https://link.aps.org/doi/10.1103/PhysRevLett.39.252.

[25] P. D. Group et al. "Review of Particle Physics". In: *Progress of Theoretical and Experimental Physics* 2020.8 (Aug. 2020). 083C01. ISSN: 2050-3911. DOI: 10.1093/ptep/ptaa104. eprint: https://academic.oup.com/ptep/article-pdf/2020/8/083C01/34673722/ptaa104.pdf. URL: https://doi.org/10.1093/ptep/ptaa104.

[26] M. S. Alam et al. "Exclusive hadronic B decays to charm and charmonium final states". In: *Phys. Rev. D* 50 (1 July 1994), pp. 43–68. DOI: 10.1103/PhysRevD.50.43. URL: https://link.aps.org/doi/10.1103/PhysRevD.50.43.

[27] H. Albrecht et al. "B meson decays into charmonium states". In: *Physics Letters B* 199.3 (1987), pp. 451–456. DOI: https://doi.org/10.1016/0370-2693(87)90952-X. URL: https://www.sciencedirect.com/science/article/pii/037026938790952X.

[28] A. J. Bevan et al. "The Physics of the B Factories". In: *The European Physical Journal C* 74.11 (Nov. 2014). ISSN: 1434-6052. DOI: 10.1140/epjc/s10052-014-3026-9. URL: http://dx.doi.org/10.1140/epjc/s10052-014-3026-9.

[29] K. Abe, K. Abe, and R. Abe. "Observation of the Decay $B \to K\ell^+\ell^-$". In: *Phys. Rev. Lett.* 88 (2 Dec. 2001), p. 021801. DOI: 10.1103/PhysRevLett.88.021801. URL: https://link.aps.org/doi/10.1103/PhysRevLett.88.021801.

[30] B. Aubert. *Evidence for the Flavor Changing Neutral Current Decays B to K l+ l- and B to K l+ l-*. 2002. arXiv: hep-ex/0207082 [hep-ex]. URL: https://arxiv.org/abs/hep-ex/0207082.

[31] R. Aaij et al. "Test of Lepton Universality Using $B^+ \to K^+\ell^+\ell^-$ Decays". In: *Phys. Rev. Lett.* 113 (15 Nov. 2014), p. 151601. DOI: 10.1103/PhysRevLett.113.151601. URL: https://link.aps.org/doi/10.1103/PhysRevLett.113.151601.

[32] J.-T. Wei et al. "Measurement of the Differential Branching Fraction and Forward-Backward Asymmetry for $B \to K^{(*)}l^+l^-$". In: *Phys. Rev. Lett.* 103 (17 Nov. 2009), p. 171801. DOI: 10.1103/PhysRevLett.103.171801. URL: https://link.aps.org/doi/10.1103/PhysRevLett.103.171801.

[33] J. P. Lees et al. "Measurement of branching fractions and rate asymmetries in the rare decays $B \to K^{(*)}\ell^+\ell^-$". In: *Phys. Rev. D* 86 (3 Aug. 2012), p. 032012. DOI: 10.1103/PhysRevD.86.032012. URL: https://link.aps.org/doi/10.1103/PhysRevD.86.032012.

[34] R. Aaij et al. "Measurements of the S-wave fraction in $B^0 \to K^+\pi^-\mu^+\mu^-$ decays and the$B^0 \to K^*(892)^0\mu^+\mu^-$ differential branching fraction". In: *Journal of High Energy Physics* 2016.11 (Nov. 2016), p. 47. ISSN: 1029-8479. DOI: 10.1007/JHEP11(2016)047. URL: https://doi.org/10.1007/JHEP11(2016)047.

[35] R. Aaij et al. "Differential branching fraction and angular analysis of $\Lambda_b^0 \to \Lambda\mu^+\mu^-$ decays". In: *Journal of High Energy Physics* 2015.6 (June 2015), p. 115. ISSN: 1029-8479. DOI: 10.1007/JHEP06(2015)115. URL: https://doi.org/10.1007/JHEP06(2015)115.

[36] R. Aaij, B. Adeva, M. Adinolfi, A. Affolder, Z. Ajaltouni, and T. L. collaboration. "Differential branching fractions and isospin asymmetries of $B \to K(*)\mu^+\mu^-$ decays". In: *Journal of High Energy Physics* 2014.6 (June 2014), p. 133. ISSN: 1029-8479. DOI: 10.1007/JHEP06(2014)133. URL: https://doi.org/10.1007/JHEP06(2014)133.

[37] R. Aaij, B. Adeva, and M. Adinolfi. "Measurement of Form-Factor-Independent Observables in the Decay $B^0 \to K^{*0}\mu^+\mu^-$". In: *Phys. Rev. Lett.* 111 (19 Nov. 2013), p. 191801. DOI: 10.1103/PhysRevLett.111.191801. URL: https://link.aps.org/doi/10.1103/PhysRevLett.111.191801.

[38] A. Sirunyan et al. "Measurement of angular parameters from the decay $B^0 \to K^{*0}\mu^+\mu^-$ in proton–proton collisions at s=8TeV". In: *Physics Letters B* 781 (2018), pp. 517–541. ISSN: 0370-2693. DOI: https://doi.org/10.1016/j.physletb.2018.04.030. URL: https://www.sciencedirect.com/science/article/pii/S0370269318303149.

[39] B. Collaboration et al. *Lepton-Flavor-Dependent Angular Analysis of $B \to K^*\ell^+\ell^-$*. 2016. arXiv: 1612.05014 [hep-ex]. URL: https://arxiv.org/abs/1612.05014.

[40] M. Aaboud, G. Aad, B. Abbott, O. Abdinov, and T. A. collaboration. "Angular analysis of $B_d^0 \to K^{*0}\mu^+\mu^-$ decays in pp collisions at $\sqrt{s} = 8$ TeV with the ATLAS detector". In: *Journal of High Energy Physics* 2018.10 (Nov. 2018), p. 47. ISSN: 1029-8479. DOI: 10.1007/JHEP10(2018)047. URL: https://doi.org/10.1007/JHEP10(2018)047.

[41] R. Aaij et al. "Angular analysis of the $B^0 \to K^{*0}\mu^+\mu^-$ decay using 3 fb^{-1} of integrated luminosity". In: *Journal of High Energy Physics* 2016.2 (Feb. 2016), p. 104. ISSN: 1029-8479. DOI: 10.1007/JHEP02(2016)104. URL: https://doi.org/10.1007/JHEP02(2016)104.

[42] C. Bobeth, G. Hiller, and G. Piranishvili. "Angular distributions of $B \to K\ell\ell$ decays". In: *Journal of High Energy Physics* 2007.12 (Dec. 2007), pp. 040–040. ISSN: 1029-8479. DOI: 10.1088/1126-6708/2007/12/040. URL: http://dx.doi.org/10.1088/1126-6708/2007/12/040.

[43] C. Bouchard, G. P. Lepage, C. Monahan, H. Na, and J. Shigemitsu. "Standard Model Predictions for $B \to K\ell^+\ell^-$ with Form Factors from Lattice QCD". In: *Phys. Rev. Lett.* 111 (16 Nov. 2013), p. 162002. DOI: 10.1103/PhysRevLett.111.162002. URL: https://link.aps.org/doi/10.1103/PhysRevLett.111.162002.

[44] F. Landua. "The CERN accelerator complex layout in 2022. Complexe des accélérateurs du CERN en janvier 2022". In: (2022). General Photo. URL: https://cds.cern.ch/record/2813716.

[45] W. Herr and B. Muratori. "Concept of luminosity". In: (2006). DOI: 10.5170/CERN-2006-002.361. URL: https://cds.cern.ch/record/941318.

[46] S. Baird. *Accelerators for pedestrians; rev. version*. Tech. rep. Geneva: CERN, 2007. URL: https://cds.cern.ch/record/1017689.

[47] M. Benedikt, P. Collier, V. Mertens, J. Poole, and K. Schindl. *LHC Design Report*. CERN Yellow Reports: Monographs. Geneva: CERN, 2004. DOI: 10.5170/CERN-2004-003-V-3. URL: http://cds.cern.ch/record/823808.

[48] J. M. Jowett and M. Schaumann. "Overview of Heavy Ions in LHC Run 2". In: (2019), pp. 15–25. URL: https://cds.cern.ch/record/2750273.

[49] *Public CMS Luminosity Information*. https://twiki.cern.ch/twiki/bin/view/CMSPublic/LumiPublicResults. Accessed: 2024-08-20.

[50] T. Sakuma. "Cutaway diagrams of CMS detector". In: (2019). URL: https://cds.cern.ch/record/2665537.

[51] G. L. Bayatian et al. *CMS Physics: Technical Design Report Volume 1: Detector Performance and Software*. Technical design report. CMS. There is an error on cover due to a technical problem for some items. Geneva: CERN, 2006. URL: http://cds.cern.ch/record/922757.

[52] A. Hayrapetyan et al. "Development of the CMS detector for the CERN LHC Run 3." In: *JINST* 19.05 (2024). Replaced with the published version. Added the journal reference and the DOI. All the figures and tables can be found at http://cms-results.web.cern.ch/cms-results/public-results/publications/PRF-21-001 (CMS Public Pages), P05064. DOI: 10.1088/1748-0221/19/05/P05064. arXiv: 2309.05466. URL: https://cds.cern.ch/record/2870088.

[53] V. Klyukhin. "Design and Description of the CMS Magnetic System Model". In: *Symmetry* 13.6 (2021). 17 pages, 9 figures, 67 references, p. 1052. DOI: 10.3390/sym13061052. arXiv: 2201.10478. URL: https://cds.cern.ch/record/2773274.

[54] *The CMS magnet project: Technical Design Report*. Technical design report. CMS. Geneva: CERN, 1997. DOI: 10.17181/CERN.6ZU0.V4T9. URL: https://cds.cern.ch/record/331056.

[55] W. Adam et al. "The CMS Phase-1 Pixel Detector Upgrade". In: *JINST* 16.02 (2021), P02027. DOI: 10.1088/1748-0221/16/02/P02027. arXiv: 2012.14304. URL: https://cds.cern.ch/record/2748381.

[56] *The Phase-2 Upgrade of the CMS Tracker*. Tech. rep. Geneva: CERN, 2017. DOI: 10.17181/CERN.QZ28.FLHW. URL: http://cds.cern.ch/record/2272264.

[57] T. C. Collaboration et al. "The CMS experiment at the CERN LHC". In: *Journal of Instrumentation* 3.08 (Aug. 2008), S08004. DOI: 10.1088/1748-0221/3/08/S08004. URL: https://dx.doi.org/10.1088/1748-0221/3/08/S08004.

[58] P. K. Siddireddy. *The CMS ECAL Trigger and DAQ system: electronics auto-recovery and monitoring*. Tech. rep. 7 pages, 6 figues, 1 table, conference record. 2018. arXiv: 1806.09136. URL: http://cds.cern.ch/record/2630618.

[59] *The CMS hadron calorimeter project: Technical Design Report*. Technical design report. CMS. Geneva: CERN, 1997. URL: https://cds.cern.ch/record/357153.

[60] A. Sirunyan et al. "Performance of the CMS muon detector and muon reconstruction with proton-proton collisions at $\sqrt{s} = 13$ TeV". In: *JINST* 13.06 (2018). Replaced with the published version. Added the journal reference and the DOI. All the figures and tables can be found at http://cms-results.web.cern.ch/cms-results/public-results/publications/MUO-16-001 (CMS Public Pages), P06015. DOI: 10.1088/1748-0221/13/06/P06015. arXiv: 1804.04528. URL: https://cds.cern.ch/record/2313130.

[61] T. A. Bawej et al. *The New CMS DAQ System for Run 2 of the LHC*. Tech. rep. Geneva: CERN, 2015. DOI: 10.1109/RTC.2014.7097437. URL: http://cds.cern.ch/record/1711011.

[62] A. Sirunyan et al. "Performance of the CMS Level-1 trigger in proton-proton collisions at sqrt(s) = 13 TeV". In: *Journal of Instrumentation* 15.10 (Oct. 2020), P10017–P10017. ISSN: 1748-0221. DOI: 10.1088/1748-0221/15/10/p10017. URL: http://dx.doi.org/10.1088/1748-0221/15/10/P10017.

[63] C. Collaboration. *Enriching the physics program of the CMS experiment via data scouting and data parking*. 2024. arXiv: 2403.16134 [hep-ex]. URL: https://arxiv.org/abs/2403.16134.

[64] J. Adam et al. "Centrality Dependence of the Charged-Particle Multiplicity Density at Midrapidity in Pb-Pb Collisions at $\sqrt{s_{NN}} = 5.02$ TeV". In: *Phys. Rev. Lett.* 116 (22 June 2016), p. 222302. DOI: 10.1103/PhysRevLett.116.222302. URL: https://link.aps.org/doi/10.1103/PhysRevLett.116.222302.

[65] V. Khachatryan et al. "Evidence for Collective Multiparticle Correlations in p-Pb Collisions". In: *Phys. Rev. Lett.* 115.1 (2015), p. 012301. DOI: 10.1103/PhysRevLett.115.012301. arXiv: 1502.05382 [nucl-ex].

[66] A. M. Sirunyan et al. "Observation of Correlated Azimuthal Anisotropy Fourier Harmonics in *pp* and $p + Pb$ Collisions at the LHC". In: *Phys. Rev. Lett.* 120.9 (2018), p. 092301. DOI: 10.1103/PhysRevLett.120.092301. arXiv: 1709.09189 [nucl-ex].

[67] A. M. Sirunyan et al. "Measurement of prompt and nonprompt J/ψ production in pp and pPb collisions at $\sqrt{s_{\mathrm{NN}}} = 5.02$ TeV". In: *Eur. Phys. J. C* 77.4 (2017), p. 269. DOI: 10.1140/epjc/s10052-017-4828-3. arXiv: 1702.01462 [nucl-ex].

[68] M. Aaboud et al. "Correlated long-range mixed-harmonic fluctuations measured in pp, p+Pb and low-multiplicity PbPb collisions with the ATLAS detector". In: *Phys. Lett. B* 789 (2019), pp. 444–471. DOI: 10.1016/j.physletb.2018.11.065. arXiv: 1807.02012 [nucl-ex].

[69] S. Acharya et al. "Multiplicity dependence of light-flavor hadron production in pp collisions at $\sqrt{s} = 7$ TeV". In: *Phys. Rev. C* 99.2 (2019), p. 024906. DOI: 10.1103/PhysRevC.99.024906. arXiv: 1807.11321 [nucl-ex].

[70] B. B. Abelev et al. "Multiplicity Dependence of Pion, Kaon, Proton and Lambda Production in p-Pb collisions at $\sqrt{s_{\mathrm{NN}}} = 5.02$ TeV". In: *Phys. Lett. B* 728 (2014), pp. 25–38. DOI: 10.1016/j.physletb.2013.11.020. arXiv: 1307.6796 [nucl-ex].

[71] A. Tumasyan et al. "Probing Charm Quark Dynamics via Multiparticle Correlations in Pb-Pb collisions at $\sqrt{s_{\mathrm{NN}}} = 5.02\,\mathrm{TeV}$". In: *Phys. Rev. Lett.* 129 (2022), p. 022001. DOI: 10.1103/PhysRevLett.129.022001. arXiv: 2112.12236 [hep-ex].

[72] A. M. Sirunyan et al. "Observation of prompt J/ψ(1S) meson elliptic flow in high-multiplicity pPb collisions at $\sqrt{s_{\mathrm{NN}}} = 8.16\,\mathrm{TeV}$". In: *Phys. Lett. B* 791 (2019), p. 172. DOI: 10.1016/j.physletb.2019.02.018. arXiv: 1810.01473 [hep-ex].

[73] S. Acharya et al. "Azimuthal correlations of prompt Dmesons with charged particles in pp and p-Pb collisions at $\sqrt{s_{\mathrm{NN}}} = 5.02\,\mathrm{TeV}$". In: *Eur. Phys. J. C* 80.10 (2020), p. 979. DOI: 10.1140/epjc/s10052-020-8118-0. arXiv: 1910.14403 [nucl-ex].

[74] A. Andronic et al. "Heavy-flavour and quarkonium production in the LHC era: from proton–proton to heavy-ion collisions". In: *Eur. Phys. J. C* 76.3 (2016), p. 107. DOI: 10.1140/epjc/s10052-015-3819-5. arXiv: 1506.03981 [nucl-ex].

[75] X. Dong, Y.-J. Lee, and R. Rapp. "Open Heavy-Flavor Production in Heavy-Ion Collisions". In: *Ann. Rev. Nucl. Part. Sci.* 69 (2019), pp. 417–445. DOI: 10.1146/annurev-nucl-101918-023806. arXiv: 1903.07709 [nucl-ex].

[76] L. Apolinário, Y.-J. Lee, and M. Winn. "Heavy quarks and jets as probes of the QGP". In: *Prog. Part. Nucl. Phys.* 127 (2022), p. 103990. DOI: 10.1016/j.ppnp.2022.103990. arXiv: 2203.16352 [hep-ph].

[77] R. Aaij et al. "Measurement of Pbp, Pbd and Lambdab production in *pPb* collisions at sqrt(sNN)=8.16 TeV ". In: *Phys. Rev. D* 99.5 (2019), p. 052011. DOI: 10.1103/PhysRevD.99.052011. arXiv: 1902.05599 [hep-ex].

[78] Particle Data Group, M. Tanabashi, et al. "Review of Particle Physics". In: *Phys. Rev. D* 98 (2018), p. 030001. DOI: 10.1103/PhysRevD.98.030001.

[79] M. Cacciari et al. "Theoretical predictions for charm and bottom production at the LHC." In: *J. High Energ. Phys.* (2012), p. 137. DOI: 10.1007/JHEP10(2012)137. URL: https://doi.org/10.1007/JHEP10(2012)137.

[80] M. Cacciari, S. Frixione, and P. Nason. "The pT spectrum in heavy-flavour photoproduction". In: *Journal of High Energy Physics* 2001.03 (Mar. 2001), pp. 006–006. DOI: 10.1088/1126-6708/2001/03/006. URL: https://doi.org/10.1088/1126-6708/2001/03/006.

[81] M. Cacciari, M. Greco, and P. Nason. "The pT spectrum in heavy-flavour hadroproduction". In: *Journal of High Energy Physics* 1998.05 (May 1998), pp. 007–007. DOI: 10.1088/1126-6708/1998/05/007. URL: https://doi.org/10.1088/1126-6708/1998/05/007.

[82] *cms luminosity measurement using 2016 proton-nucleus collisions at nucleon-nucleon center-of-mass energy of 8.16 TeV*. CMS Physics Analysis Summary CMS-PAS-LUM-17-002. CERN, 2018. URL: https://cds.cern.ch/record/2628652?ln=es.

[83] *HITracking*. CERN CMS. code. 2016. URL: https://github.com/cmsHiTracking/TrackingCode/tree/master/pileUpFilter.

[84] *HiCentralityAlgos*. CERN CMS. code. 2016. URL: https://github.com/CmsHI/cmssw/blob/forest_CMSSW_10_3_1/RecoHI/HiCentralityAlgos/plugins/CentralityProducer.cc#L331-L397.

[85] S. Chatrchyan et al. "Description and performance of track and primary-vertex reconstruction with the CMS tracker". In: *JINST* 9 (2014), P10009. DOI: 10.1088/1748-0221/9/10/P10009. arXiv: 1405.6569 [physics.ins-det].

[86] *Tracker reco-to-sim association*. CERN. twiki. 2015. URL: https://twiki.cern.ch/twiki/bin/view/CMSPublic/SWGuideTrackMCTruth.

[87] CMS Heavy Ion Physics group. *Studies of two-particle correlations in pPb collisions at 5 TeV*. CMS Note AN-12-352., 2012. URL: https://cms.cern.ch/iCMS/user/noteinfo?cmsnoteid=CMS%20AN-2012/352.

[88] CMS Heavy Ion Physics group. *Multiplicity and pt dependence of dihadron correlations and multiparticle cumulant harmonics in pPb*. CMS Note AN-13-031., 2013. URL: https://cms.cern.ch/iCMS/user/noteinfo?cmsnoteid=CMS%20AN-2013/031.

[89] *Tracking POG results for pion efficiency with the D* meson using data from 2016 and 2017*. CMS Detector Performance Report CMS-DP-2018-050. CERN, 2018. URL: http://cds.cern.ch/record/2634940.

[90] L. Fano and V. Mariani and D. Pedrini and Y. Yang. *Measurement of prompt open charm production cross-sections in pp collisions at* $\sqrt{s} = 13$ *TeV with the CMS detector*. CMS Note AN-17-166. INFN and DESY, 2017. URL: https://cms.cern.ch/iCMS/user/noteinfo?cmsnoteid=CMS%20AN-2017/166.

[91] N. L. Johnson. "Systems of frequency curves generated by methods of translation". In: *Biometrika* 36 (1949), p. 149. DOI: 10.1093/biomet/36.1-2.149.

[92] S. Jackman. *Bayesian analysis for the social sciences*. New Jersey, USA: John Wiley & Sons, 2009. DOI: 10.1002/9780470686621.

[93] S. Chatrchyan et al. "Study of Z Boson Production in PbPb Collisions at $\sqrt{s_{NN}} = 2.76$ TeV". In: *Phys. Rev. Lett.* 106 (21 May 2011), p. 212301. DOI: 10.1103/PhysRevLett.106.212301. URL: https://link.aps.org/doi/10.1103/PhysRevLett.106.212301.

[94] Z. Citron. "Z Boson Production in 5.02 TeV pp, p + Pb and Pb + Pb Collisions with ATLAS". In: *Nuclear Physics A* 967 (2017). The 26th International Conference on Ultra-relativistic Nucleus-Nucleus Collisions: Quark Matter 2017, pp. 305–308. ISSN: 0375-9474. DOI: https://doi.org/10.1016/j.nuclphysa.2017.05.070. URL: https://www.sciencedirect.com/science/article/pii/S0375947417301951.

[95] A. Aaij et al. "Measurement of the Z boson production cross-section in proton-lead collisions at $\sqrt{s_{NN}}$= 8.16 TeV". In: *Journal of High Energy Physics* 2023.6 (June 2023), p. 22. ISSN: 1029-8479. DOI: 10.1007/JHEP06(2023)022. URL: https://doi.org/10.1007/JHEP06(2023)022.

[96] A. Aaij et al. "Measurement of the Z boson production cross-section in proton-lead collisions at $\sqrt{s_{NN}}$= 8.16 TeV". In: *Journal of High Energy Physics* 2023.6 (June 2023), p. 22. ISSN: 1029-8479. DOI: 10.1007/JHEP06(2023)022. URL: https://doi.org/10.1007/JHEP06(2023)022.

[97] A. Ali, P. Ball, L. T. Handoko, and G. Hiller. "Comparative study of the decays $\vec{B}$ $(K, K^*)l^+l^-$ in the standard model and supersymmetric theories". In: *Phys. Rev. D* 61 (7 Mar. 2000), p. 074024. DOI: 10.1103/PhysRevD.61.074024. URL: https://link.aps.org/doi/10.1103/PhysRevD.61.074024.

[98] D. M. Straub. *flavio: a Python package for flavour and precision phenomenology in the Standard Model and beyond*. 2018. DOI: 10.48550/ARXIV.1810.08132. URL: https://arxiv.org/abs/1810.08132.

[99] R. Aaij et al. "Angular analysis of charged and neutral B →Kmu +mu -decays". In: *Journal of High Energy Physics* 2014.5 (2014), p. 82. DOI: 10.1007/JHEP05(2014)082. URL: https://doi.org/10.1007/JHEP05(2014)082.

[100] A. M. Sirunyan et al. "Angular analysis of the decay $B^+ \to K^+\mu^+\mu^-$ in proton-proton collisions at $\sqrt{s} = 8$ TeV". In: *Phys. Rev. D* 98 (11 Dec. 2018), p. 112011. DOI: 10.1103/PhysRevD.98.112011. URL: https://link.aps.org/doi/10.1103/PhysRevD.98.112011.

[101] J. .-. Wei et al. "Measurement of the Differential Branching Fraction and Forward-Backward Asymmetry for $B \to K^{(*)}\ell^+\ell^-$". In: *Phys. Rev. Lett.* 103 (2009), p. 171801. DOI: 10.1103/PhysRevLett.103.171801. arXiv: 0904.0770 [hep-ex].

[102] B. Aubert et al. "Measurements of branching fractions, rate asymmetries, and angular distributions in the rare decays $B \to K\ell^+\ell^-$ and $B \to K^*\ell^+\ell^-$". In: *Phys. Rev. D* 73 (2006), p. 092001. DOI: 10.1103/PhysRevD.73.092001. arXiv: hep-ex/0604007.

[103] T. Aaltonen et al. "Measurements of the Angular Distributions in the Decays $B \to K^{(*)}\mu^+\mu^-$ at CDF". In: *Phys. Rev. Lett.* 108 (2012), p. 081807. DOI: 10.1103/PhysRevLett.108.081807. arXiv: 1108.0695 [hep-ex].

[104] *BRIL Work Suite*. 2021. URL: https://cms-service-lumi.web.cern.ch/cms-service-lumi/brilwsdoc.html (visited on 03/20/2021).

[105] T. Sjöstrand, S. Mrenna, and P. Skands. "A brief introduction to PYTHIA 8.1". In: *Computer Physics Communications* 178.11 (June 2008), pp. 852–867. ISSN: 0010-4655. DOI: 10.1016/j.cpc.2008.01.036. URL: http://dx.doi.org/10.1016/j.cpc.2008.01.036.

[106] D. Lange. "The EvtGen particle decay simulation package". In: *Nucl. Instrum. Meth. A* 462 (2001). Ed. by S. Erhan, P. Schlein, and Y. Rozen, pp. 152–155. DOI: 10.1016/S0168-9002(01)00089-4.

[107] "Recording and reconstructing 10 billion unbiased b hadron decays in CMS". In: (Oct. 2019). URL: http://cds.cern.ch/record/2704495.

[108] P. Azzurri and B. Mangano. "Optimal filtering of fake tracks". In: (Apr. 2008). URL: https://cds.cern.ch/record/1364938.

[109] T. C. Collaboration. "Description and performance of track and primary-vertex reconstruction with the CMS tracker". In: *Journal of Instrumentation* 9.10 (Oct. 2014), P10009–P10009. ISSN: 1748-0221. DOI: 10.1088/1748-0221/9/10/p10009. URL: http://dx.doi.org/10.1088/1748-0221/9/10/P10009.

[110] M. Dinardo and K. Stenson. *Angular analysis and differential branching fraction of the decay* $B^0 \to K^{*0}\mu^+\mu^-$. CMS Note 2014/129. 2014. URL: %7Bhttps://cms.cern.ch/iCMS/user/noteinfo?cmsnoteid=CMS%20AN-2014/129%7D.

[111] A. Boletti, M. Dinardo, P. Dini, S. Fiorendi, S. Lacaprara, L. Li, and D. Wang. *Full angular analysis of decay* $B_0 \to K * mumu$ *at 13 TeV*. CMS Note 2018/138. 2018. URL: %7Bhttps://cms.cern.ch/iCMS/user/noteinfo?cmsnoteid=CMS%20AN-2018/138%7D.

[112] Y. Ban et al. *Measurement of angular observables in the decay B+→ K+mu + mu - from proton-proton collisions at sqrt(s)=8 TeV*. CMS Note 2014/244. 2014. URL: %7Bhttps://cms.cern.ch/iCMS/user/noteinfo?cmsnoteid=CMS%20AN-2014/244%7D.

[113] T. Chen and C. Guestrin. "XGBoost: A Scalable Tree Boosting System". In: *Proceedings of the 22nd ACM SIGKDD International Conference on Knowledge Discovery and Data Mining*. KDD '16. San Francisco, California, USA: ACM, 2016, pp. 785–794. ISBN: 978-1-4503-4232-2. DOI: 10.1145/2939672.2939785. URL: http://doi.acm.org/10.1145/2939672.2939785.

[114] F. Pedregosa et al. "Scikit-learn: Machine Learning in Python". In: *Journal of Machine Learning Research* 12 (2011), pp. 2825–2830.

[115] N. L. Johnson. "Systems of Frequency Curves Generated by Methods of Translation". In: *Biometrika* 36.1/2 (1949), pp. 149–176. ISSN: 00063444. URL: http://www.jstor.org/stable/2332539.

[116] J. Eschle, A. Puig Navarro, R. Silva Coutinho, and N. Serra. "zfit: Scalable pythonic fitting". In: *SoftwareX* 11 (2020), p. 100508. ISSN: 2352-7110. DOI: https://doi.org/10.1016/j.softx.2020.100508. URL: http://www.sciencedirect.com/science/article/pii/S2352711019303851.

[117] Martín Abadi et al. *TensorFlow: Large-Scale Machine Learning on Heterogeneous Systems*. Software available from tensorflow.org. 2015. URL: https://www.tensorflow.org/.

[118] K. D. *A software package for sequential quadratic programming*. Tech. rep. DFVLR-FB 88-28. Institute for Flight Mechanics, Koln, Germany., 1998.

[119] P. Virtanen et al. "SciPy 1.0: Fundamental Algorithms for Scientific Computing in Python". In: *Nature Methods* 17 (2020), pp. 261–272. DOI: 10.1038/s41592-019-0686-2.

[120] M. Pivk and F. Le Diberder. ": A statistical tool to unfold data distributions". In: *Nuclear Instruments and Methods in Physics Research Section A: Accelerators, Spectrometers, Detectors and Associated Equipment* 555.1-2 (Dec. 2005), pp. 356–369. ISSN: 0168-9002. DOI: 10.1016/j.nima.2005.08.106. URL: http://dx.doi.org/10.1016/j.nima.2005.08.106.

[121] D. Martschei, M. Feindt, S. Honc, and J. Wagner-Kuhr. "Advanced event reweighting using multivariate analysis". In: *Journal of Physics: Conference Series* 368.1 (June 2012), p. 012028. DOI: 10.1088/1742-6596/368/1/012028. URL: https://dx.doi.org/10.1088/1742-6596/368/1/012028.

[122] A. Rogozhnikov. "Reweighting with Boosted Decision Trees". In: *Journal of Physics: Conference Series* 762.1 (Oct. 2016), p. 012036. DOI: 10.1088/1742-6596/762/1/012036. URL: https://dx.doi.org/10.1088/1742-6596/762/1/012036.

[123] T. M. Karbach. *Feldman-Cousins Confidence Levels - Toy MC Method*. 2011. arXiv: 1109.0714 [physics.data-an].